IntechOpen

Bismuth

Advanced Applications and Defects Characterization

Edited by Ying Zhou, Fan Dong and Shengming Jin

BISMUTH - ADVANCED APPLICATIONS AND DEFECTS CHARACTERIZATION

Edited by **Ying Zhou, Fan Dong** and **Shengming Jin**

Bismuth - Advanced Applications and Defects Characterization
http://dx.doi.org/10.5772/intechopen.71174
Edited by Ying Zhou, Fan Dong and Shengming Jin

Contributors

Susana Devesa, Manuel Pedro Graça, Luís Costa, Jerzy Dryzek, Minh Thang Le, Yanhua Luo, Shuen Wei, Mingjie Ding, Desheng Fan, Gang-Ding Peng, Jianxiang Wen, Andrea Goforth, Hayden Winter, Anna Brown, Jin Chen, Yiyan Song, Syed Rizwan Hussain, Sabeen Fatima, William Wilson Anku, Samuel Oppong, Penny Govender, Simona Condurache-Bota, Phuoc Huu Le, Nguyen Van Chien

Notice

First published in London, United Kingdom, 2018 by IntechOpen
eBook (PDF) Published by IntechOpen, 2019
IntechOpen is the global imprint of INTECHOPEN LIMITED, registered in England and Wales, registration number: 11086078, The Shard, 25th floor, 32 London Bridge Street
London, SE19SG – United Kingdom
Printed in Croatia

British Library Cataloguing-in-Publication Data
A catalogue record for this book is available from the British Library

Additional hard and PDF copies can be obtained from orders@intechopen.com

Bismuth - Advanced Applications and Defects Characterization
Edited by Ying Zhou, Fan Dong and Shengming Jin

p. cm.

Print ISBN 978-1-78923-262-2

Online ISBN 978-1-78923-263-9

eBook (PDF) ISBN 978-1-83881-528-8

Meet the editors

Ying Zhou received his BSc and MSc degrees from Central South University and Chinese Academy of Sciences, respectively. In 2010, he received his PhD degree from the University of Zurich (UZH) under the supervision of Prof. Greta R. Patzke. He then continued his work with a postdoctoral Forschungskredit grant from UZH. He was also awarded a fellowship by the Alexander von Humboldt Foundation at Karlsruhe Institute of Technology with Prof. Jan-Dierk Grunwaldt and was a visiting professor at Kyoto University. He currently holds a professorship at Southwest Petroleum University. His research interest is in the clean utilization of oil and gas and environmental remediation materials as well as the related in situ characterization techniques.

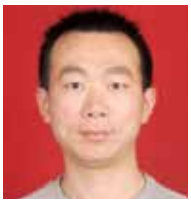

Dr. Fan Dong, born in 1982, received his PhD degree in 2010 from Zhejiang University. Currently, he is a full professor at Chongqing Key Laboratory of Catalysis and New Environmental Materials, Chongqing Technology and Business University. He was a visiting scholar from 2009 to 2010 at Hong Kong Polytechnic University. His research interests include nanostructured materials for photocatalysis and supercapacitors. He has coauthored more than 150 papers on renowned journals and has an H index of 38.

Dr. Shengming Jin , is currently an associate professor in Central South University. He received his MSc and PhD degrees from the Hunan University in 1998 and Central South University in 2001, respectively. He was a visiting scholar at Alberta University from 2013 to 2014. His research interest mainly includes bismuth oxide-based functional materials, solid waste recycling and SiC matrix composites. Dr. Jin has published two books in the field of new inorganic materials and relative inorganic experiments.

Contents

Preface

Bismuth (Bi) is a posttransition metal element with the atomic number of 83, which belongs to the pnictogen group elements with As and Sb . It is located between Pb and Po in Period 6 in the elemental periodic table, having an electron configuration $[Xe]4f^{14}5d^{10}6s^{2}6p^{3}$. Bi is a heavy metal with a standard atomic weight of 208.98. Among several isotopes, ^{209}Bi is the primordial isotope with the abundance of 100%. Nevertheless, as a heavy metal, the hazard of Bi is unusually low in contrast to its neighbors Pb, Sb (highly poisonous) and Po (highly radioactive). Though recently it is confirmed that Bi is weakly radioactive, it has the longest alpha-decay half-time (ca. 1.9×10^{19} years), which is a billion times of the estimated age of the universe. Therefore, Bi could be considered as the heaviest stable and non-toxic metal mostly. Such property, along with other typical characteristics like strong diamagnetism and low thermal conductivity, makes Bi attractive in industrial applications.

Usually, Bi resource mainly coexisted with lead, copper or tungsten ore and is extracted as a byproduct. The largest country for bismuth production is China, followed by Mexico, Canada, Bolivia and Peru. There are more than 100 bismuth products in the industry, including high-purity bismuth, bismuth alloy, bismuth oxide, bismuth oxychloride, bismuth nitrite, bismuth potassium citrate, bismuth subsalicylate, bismuth subgallate, bismuth aluminate and so on. Accordingly, commercial applications of Bi materials could be summarized from two categories: Bi metal or alloy and Bi compounds.

For Bi metal, it could be used as the substitution of Pb. Due to the small density variation between Bi and Pb (9.78 vs. 11.32 g cm^{-3}), Bi metal could replace Pb for ballistic applications like hunting bullet. Besides, Bi with high atomic weight could also replace Pb as the shields of X-ray in medical uses. On the other hand, benefited from its low melting point (271.5 °C), Bi could form fusible alloys with other elements like Sn and Cd, such as the famous Wood's metal (Bi-Pb-Sn-Cd), which is widely used in the field of safety device fuse and solders for electronics. In addition, Bi will expand 3.3% during the solidifying process, which could compensate the contraction of other metals in the alloy and avoid the deformation or cracking of the alloy.

Besides elemental Bi, Bi compounds also have a wide range of applications, and the amount of Bi compounds accounts for more than a half of total Bi production. In the medical field, bismuth compounds, for example, bismuth subsalicylate, bismuth subcitrate and bismuth subgallate, are used as the active ingredients in some pharmaceuticals for the treatment of stomach disorders such as diarrhea, colitis, peptic ulcers and the like. Other applications of bismuth compounds include fields of semiconductors, superconductors, cosmetics, pigments and more. For instance, Bi_2O_3 is used as an important additive in electronic ceramics, a potential electrolyte in solid fuel cell as well as a catalyst for oxidation reactions in chemi-

cal industry. Bi-Te-Se is an excellent thermoelectric cooling semiconductor, which could decrease the temperature to less than 200 K and can be used for laser cooler in military and aerospace industry. Bismuth strontium calcium copper oxide (BSCCO) is one of the most studied high-temperature superconductors. BiOCl is sometimes used as the additives in cosmetics like lipsticks due to its pearlescent quality as well as water retention property. Bismuth vanadate, as a well-known yellow pigment and paint with good UV-light resistance, could take the place of cadmium sulfide, chromates and other toxic pigments.

Based on the good applications of Bi materials above, this book goes further and mainly focuses on the potential uses of Bi materials. According to the various application areas, the book has been divided into six sections: in Section 1, bismuth-based nanoparticles, in special bismuth ferrites, bismuth vanadate and bismuth telluride, are discussed for photocatalytic hydrogen evolution and CO_2 reduction, organic degradation, photoelectrochemical water splitting and thermoelectric applications; in Section 2, bismuth is introduced for X-ray contrast and shielding, as well as radiation therapy in medical uses; in Section 3, Bismuth Based Dielectric Materials like a series of bismuth niobate doped with europium were prepared and their dielectric constants were measured; in Section 4, bismuth oxide prepared by different physical vapor deposition methods and bismuth oxychloride were adopted for humidity sensing and heavy metal detection as well as antibiosis, respectively; in Section 5, a series of post-treatments on bismuth-doped and bismuth/erbium-co-doped optical fibers were carried out to improve their performance and stability; in Section 6, recent development of bismuth molybdate-based catalysts for selective oxidation of hydrocarbons in organic industry is summarized; Section 7 is a little different from the other sections, in which the powerful characterization method positron annihilation spectroscopy is introduced to study the defects and vacancies in bismuth. However, we are aware that the division of the ten chapters into seven sections might be arbitrary, and there is some cross-linking of the chapters in different sections.

We really acknowledge all the authors of this book, who come from all over the world: Australia, China, Pakistan, Poland, Portugal, Romania, South Africa, the USA and Vietnam. Without their hard work in every step, the publication of this book could not be so smooth. We wish them a bright future in the scientific research field. Finally, we want to thank the editorial staff for the tedious proofreading and the patient communication between the authors and editor during the whole process.

Prof. Ying Zhou
Southwest Petroleum University
China

Prof. Fan Dong
Chongqing Technology and Business University
China

Prof. Shengming Jin
Central South University
China

Section 1

Bismuth Materials for Energy Conversion and Organics Degradation

Chapter 1

Bismuth Ferrites/Graphene Nanoplatelets Nanohybrids for Efficient Organic Dye Removal

Syed Rizwan and Sabeen Fatima

Additional information is available at the end of the chapter

http://dx.doi.org/10.5772/intechopen.75807

Abstract

The doped bismuth ferrites have got tremendous attraction owing to its ideal properties for photocatalysis application. We have fabricated the novel lanthanum and manganese co-doped $BiFeO_3$ (namely BLFMO)/graphene nanoplatelets (GNPs) nanohybrid for photocatalysis with easy and effective synthesis routes namely the co-precipitation (C-hybrid) and hydrothermal (H-hybrid) processes. The H-hybrid showed crystalline structure with lower band-gap than the C-hybrid samples. However, C-hybrid showed higher dye degradation (92%) due its higher surface area (55 m^2/g) and the fine incorporation of BLFMO nanoparticles into the GNPs which enhanced the surface adsorption. This is verified from more degradation in dark conditions for these samples. The proposed nanohybrids are novel for photocatalytic application fabricated through the low cost routes which show higher efficiency for practical applications.

Keywords: graphene nanoplatelets, nanohybrid, photocatalysis, co-precipitation, adsorption

1. Introduction

1.1. Bismuth ferrite

Bismuth ferrite $BiFeO_3$ also called BFO is the only naturally existing magnetoelectric materials. BFO possess a perovskite structure with ABO_3 type atoms where A and B represent the cations and O is the oxygen atoms or anions. A are corner atoms, B are the body centered and O are the atoms attach to the faces of the unit cell as shown in **Figure 1**.

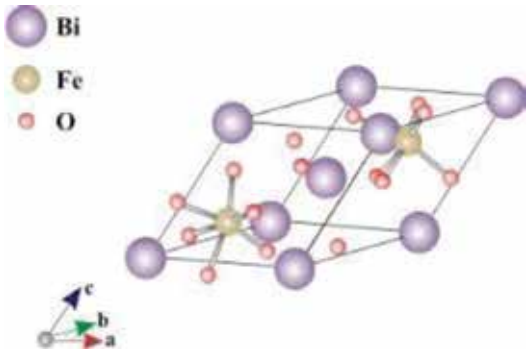

Figure 1. Perovskite structure [1].

The perovskite structures are of great interest due to their magnetic, multiferroic and photocatalytic properties. These properties are beneficial for different applications such as in non-volatile memories [2], photochemical cells [3], thin films capacitors [4] and non-linear optics [5]. Perhaps BFO is the only perovskite material representing both strong ferroelectric and magnetic effect at room temperature [6]. The BFO is doped with various elements due to which its structural, electrical and magnetic properties are improved. This enhancement in properties provides a great use of doped BFO particles in different industrial and medical applications.

1.2. Carbon-based 2D materials

Carbon is an important element of our nature and is approximately present in all living forms. In nature carbon is available in many allotropic forms with different chemical and physical properties. Important crystalline forms of carbon are fullerene (0D), carbon nanotube (2D), graphene (2D), graphite and diamond (3D).

1.2.1. Graphene

Graphene is a two dimensional (2D) allotrope of carbon in which carbon atoms are hexagonally arranged in a single layer pattern. Graphene being lighter in weight, flexible and strongest material is getting more popular day by day. In these years graphene spell has

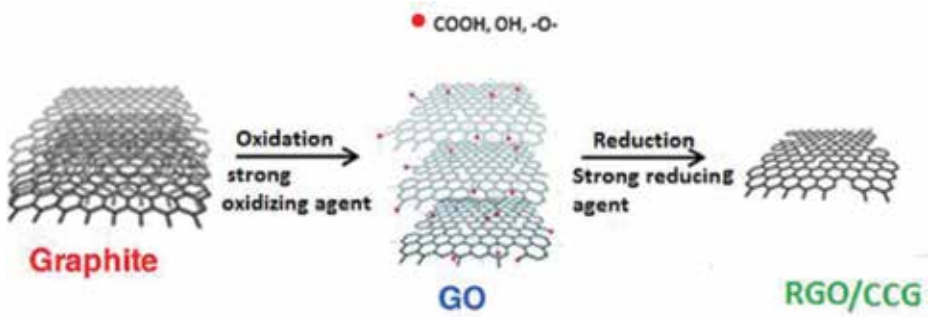

Figure 2. Chemically converted graphene by chemical exfoliation [10].

covered the complete industry and due to its extraordinary optical [7], mechanical, electronic and magnetic properties [8] it is considered to be the most important material for whole optical and electronic media. Single layer graphene is unstable and is difficult to prepare. The first stable single layer of graphene was made by Geim and Novoselov [9]. The easiest and cheapest way to synthesize graphene is its chemical exfoliation in which graphite is used as the starting material. By oxidation and reduction of graphite with the help of suitable oxidizing and reducing agents we reached to multilayer graphene called chemically converted graphene (CCG) or reduced graphene oxide (rGO) as shown in **Figure 2**.

1.2.2. Graphene nanoplatelets

Nanoplatelets are particles in platelet form at nanoscale. Different functional groups like carboxyls, hydroxyls or ethers are naturally attached to the edges of nanoparticles and the wt% of these group varies as the particle size is changed [11]. Graphene nanoplatelets (GNP's) are a few disk shaped round graphene sheets stacked (more than 10 layers). together as shown in **Figure 3**.

Actually GNP's are the flakes of graphene so called the GNF's. It is difficult to make GNP's even during the artificial synthesis process. So, if GNF's are not round they are still marked as graphene nanoplatelets. They have a thin but wide aspect ratio (ranging in thousand). Sometimes, the GNP's are also called graphite nanoplatelets when there are more stacked layers (about 38 layers [13]). GNP's are easy to prepare as there is no separate need of reduction. They have better conductivity with less defects. At the nanoscale GNPs are prepared by thermal exfoliation of naturally available graphite flakes [14]. Commercially, graphene nanoplatelets xGNPs (shown in **Figure 4**) are prepared with the help of intercalation process of graphite with acids, metal ions or different alkali metals with thicknesses of 1–15 nm [14].

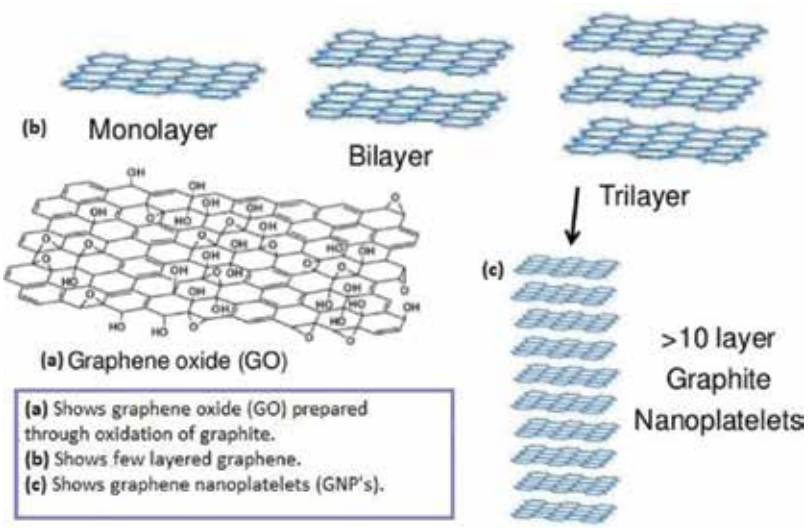

Figure 3. Difference in between GO, graphene and GNP's [12].

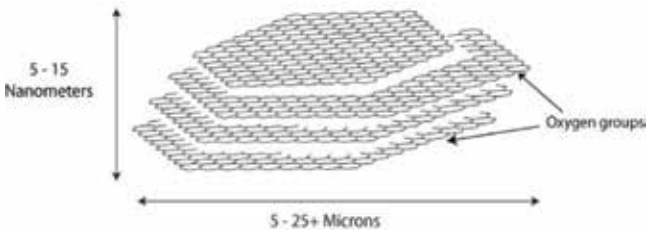

Figure 4. A typical graphene nanoplatelets (xGNPs) [15].

1.2.3. Graphene-based nanocomposites

A nanocomposite is a blend of two materials in such a way so that we can get the best properties of these materials. A nanocomposite is a hybrid structure of any two materials and among these each of these materials should have its dimension in nanoscale (less than 100 nm) [16]. It is a multiphase material in which one phase consists of a matrix while the other one is a discontinuous or reinforcing phase (usually in the form of sheets, particles or fibers). Nanocomposite materials are emerging as a suitable alternative for overcoming all the limitations which are faced by microcomposites in different applications.

Graphene nanocomposites are common and simplest hybrid structures which are prepared by adding its small amount to polymers, ceramics or metals [13]. These nanocomposites will be much stronger, heat resistive and conductive due to the addition of graphene. By combining graphene nanoplatelets with a material in a hybrid, one can improve the composite stiffness, abrasion resistance, tensile strength, corrosion resistance and lubricant properties. The nanocomposites of GNP's with other materials help in modifying the mechanical properties and conductivity of the hybrid structures.

In combination of graphene and graphene nanoplatelets in a composite form with different magnetic materials or ferrites, one can use these hybrid structures into different applications like band gap engineering, sensors, desorption, antibacterial activity, oil spilling, photocatalytic activity etc [17].

1.3. Photocatalytic activity

Photocatalytic activity involves the degradation of the pollutants present in water with the help of suitable photocatalysts. In start semiconductor oxides like ZnO, SnO_2 and TiO_2 were used as good photocatalysts due to their higher catalytic activity, excellent ultra violet (UV) absorbency, low cost, chemical stability and non-toxicity [18]. Photocatalysts perform their action by oxidizing the organic pollutants or molecules under UV light and result in carbon dioxide (CO_2) and water (H_2O) as by-products. In TiO_2, the recombination rate of photo-generated charge carriers were found to be fast and hence, making it a less efficient photocatalyst [19, 20]. Since, the solar energy is available as an abundant natural source of electromagnetic radiation and most of it consists of visible light, the best way is to use it in purification of water and hence, to find a photocatalyst that can work efficiently in the presence of visible light. Recently, it has been investigated that BFO also responses actively under visible light. BFO nanoparticles represent a significant photocatalytic activity due

to stability of crystal structure, large surface area and small energy bandgap [21]. It is possible to degrade the organic molecules within a short period of time by preparing the particles with smaller diameters or larger surfaces. The separation between electrons and holes plays a vital role in this oxidation process and hence, in photocatalysis. If this separation cannot be maintained, charge carriers will recombine resulting in no oxidation. Graphene in a hybrid structure with BFO gives an efficient way of enhancing photocatalytic activity by promoting the separation between the photo-generated pairs of electrons and holes [22, 23]. Hence, the thirst for searching new graphene-based hybrid nanocomposites with large surface area and small energy band-gap is an ever-demanding field of research.

2. Material synthesis

The material synthesis scheme for pure Bismuth ferrites, and its composites are shown in **Figures 5–7**, respectively. The visual changes occur during the hybrid preparation in co-ppt and hydrothermal synthesis are shown in the given **Figure 8**.

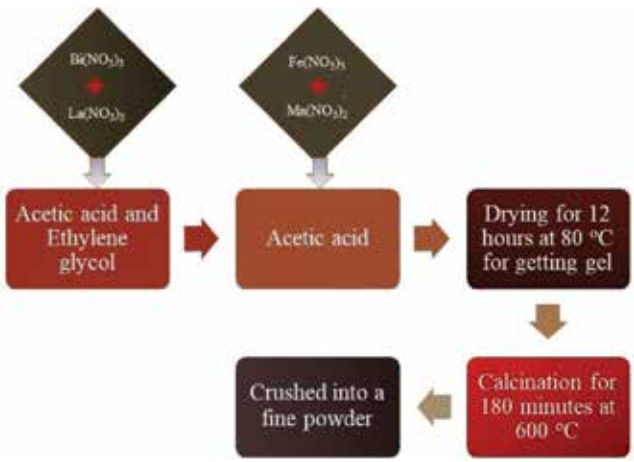

Figure 5. Sol–gel synthesis of BLFO and BLFMO nanoparticles.

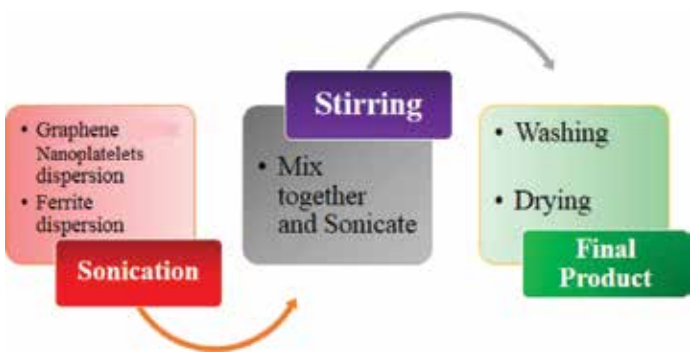

Figure 6. Ferrite-GO/GNP hybrids through Co-ppt method.

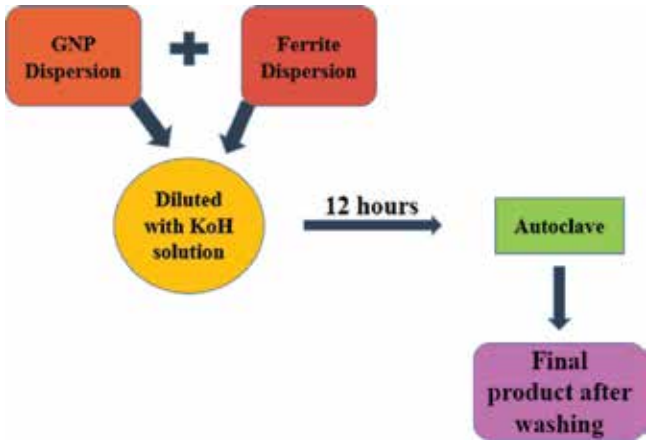

Figure 7. Hydrothermal synthesis of BLFMO/GNP nanohybrids.

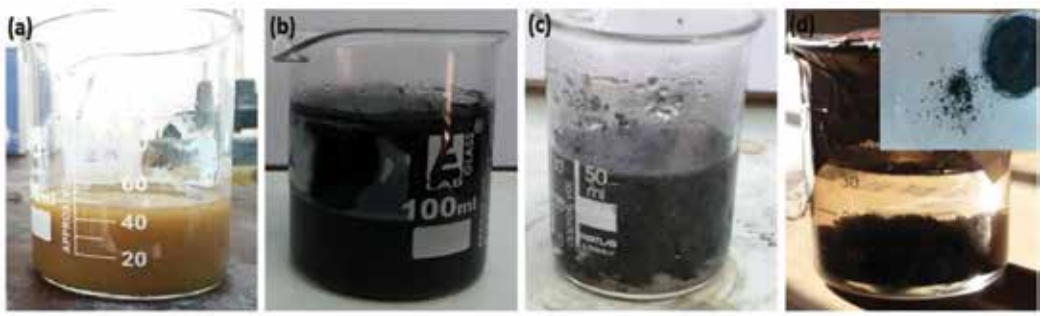

Figure 8. (a) Ferrite dispersion, (b) GNP dispersion, (c) hybrid formation, (d) sedimentation; the inset is the final dried form of hybrid structure.

3. Enhanced catalytic activity of La, Mn co-doped $BiFeO_3$/GNP nanohybrids

3.1. C-series structural analysis

The x-ray diffraction pattern was obtained by irradiating Cu-Kα rays (λ = 1.54 nm) over the sample with scanning angle ranging from 20 to 60°. The recorded XRD patterns of graphene nanoplatelets (GNP) and graphite is shown in **Figure 9**. One peak is appeared at 26.4° in graphite referring highly stacked structure with an interlayer spacing of 0.34 Å for graphite with a calculated particle size of approximately 145 nm by using Scherrer's formula [24]. This peak also appears inside GNP is referred to same graphite primitive plane (002) with a d-spacing of 3.37 Å. The intensity of the peak is very low as compared to graphite. This low intensity is due to the small number of layers present inside GNP with a thickness of ~1 nm and the calculated particle size was 35 nm which corresponds to 24 graphene sheet inside one GNP particle.

The XRD of C-series (BLFO/GNP and BLFMO/GNP) nanohybrids are shown in **Figure 10**. The labeled peak of BLFO (**Figure 10a**) are referred to as the primitive hkl planes (012), (104), (110), (006), (202), (024), (116), (112), (018) and (214) of bismuth ferrite BFO corresponding to the JCPDS card no. 20-0169. The perovskite rhomboidal structure of bismuth ferrite distort due to the addition of lanthanum due to which the intensity of peaks is reduced [25]. A small peak of an impurity $Bi_2Fe_4O_9$ is also appeared in BLFO/GNP which is not present inside BLFO/GNP with the introduction of graphene nanoplatelets. As these peaks in hybrid structure are broadened also with the decreased intensity which is representing the disorderedness introduced in hybrid structure with the addition of graphene sheets and hence, the low crystallinity. An extra peak also appeared in hybrid structure of hkl (002) plane which is a clear proof of formation of BLFO/GNP nanohybrid. With the introduction of manganese (5–25%) the Bi/Fe deficiencies were compensated and the impurity peak has been completely removed as the Mn amount was increased as shown in **Figure 10b–f**. The crystal structure of co-doped bismuth ferrite is transformed completely from rhombohedral to orthorhombic with the addition on Mn [26] and this is why the peaks are overlapped. As inter-planar spacing is inversely proportional to diffraction angle, a positive shift in peak was appeared up to Mn = 15% which showed a decrease in lattice constant. This decrement in lattice constant is due to the replacement of Fe with Mn-atoms which has a lower atomic radii than Fe [27]. With a further increase in Mn percentage (BLFMO-20 and BLFMO-25), negative peak shift is observed due to creation of compressive strain inside crystal structure. With the introduction of Mn in hybrid structure (BLFMO-5/GNP to BLFMO-25/GNP), there is a same trend of peak broadening and decreased intensity as was in BLFO/GNP representing complete incorporation of graphene layers inside BLFMO nanoparticles. The (002) peak of graphitic structure is also present showing graphene presence inside the nanohybrid. The particle sizes are also calculated by using Scherrer's formula [24] ranging from 19.3 to 23.5 nm. A small amount of impurity ($Bi_2Fe_4O_9$) is also present in BLFMO-25/GNP. There is more disorderedness in C-series nanohybrids crystal structure due to enhanced fusion of GNP sheets inside BLFO and BLFMO nanoparticles.

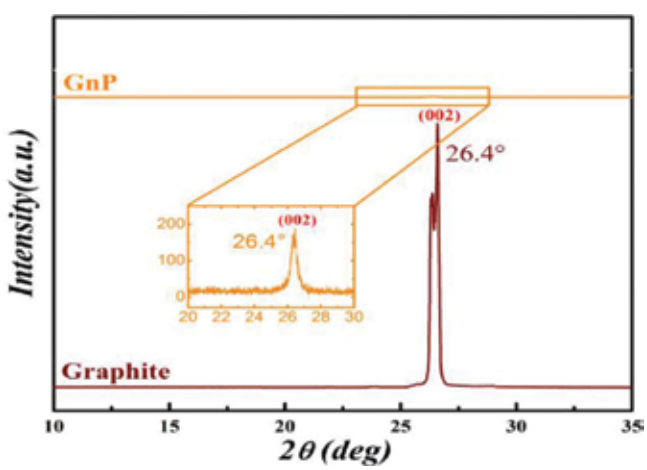

Figure 9. X-ray diffraction pattern of graphite (dark brown) and graphene nanoplatelets GNP (yellow).

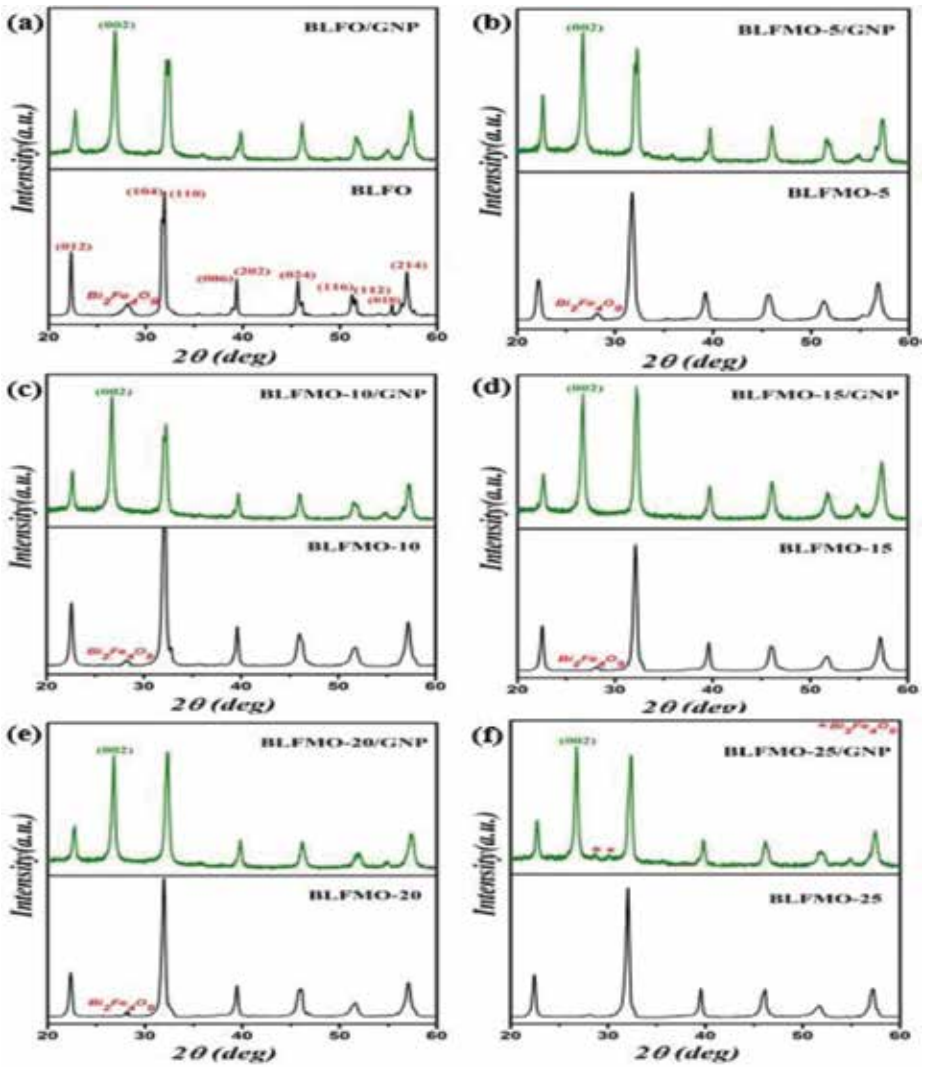

Figure 10. XRD patterns of C-series nanohybrids respectively as (a) BLFO/GNP, (b) BLFMO-5/GNP, (c) BLFMO-10/GNP, (d) BLFMO15/GNP, (e) BLFMO-20/GNP, (f) BLFMO-25/GNP.

3.2. C-series morphological analysis

Scanning electron microscope image of graphene nanoplatelets (GNP) is shown in **Figure 11**. Flat and smooth graphene sheets with sharp corners are clearly seen in SEM image. The commercial grade graphene layers (up to 24) are stacked together in the form of flakes inside GNP and are shown thick and darker in appearance.

Figure 12 shows the SEM micrographs of hybrid structures representing the mixed morphology of BLFO or BLFMO nanoparticles (white granular part) and graphene sheets (dark layered part). BLFO and BLFMO nanoparticles were not even attached with the edge atoms covalently but also adsorbed by the surface of graphene layers inside GNPs. The GNP consists of stacked

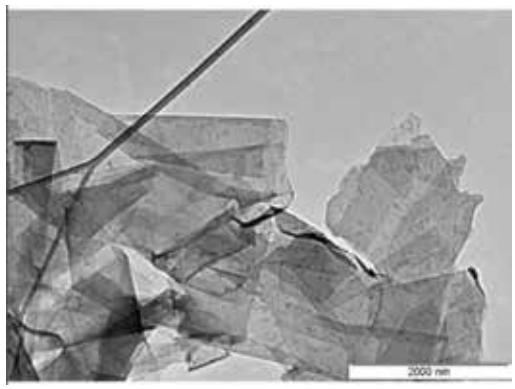

Figure 11. SEM image of graphene nanoplatelets (GNP) representing sheet structure of graphene.

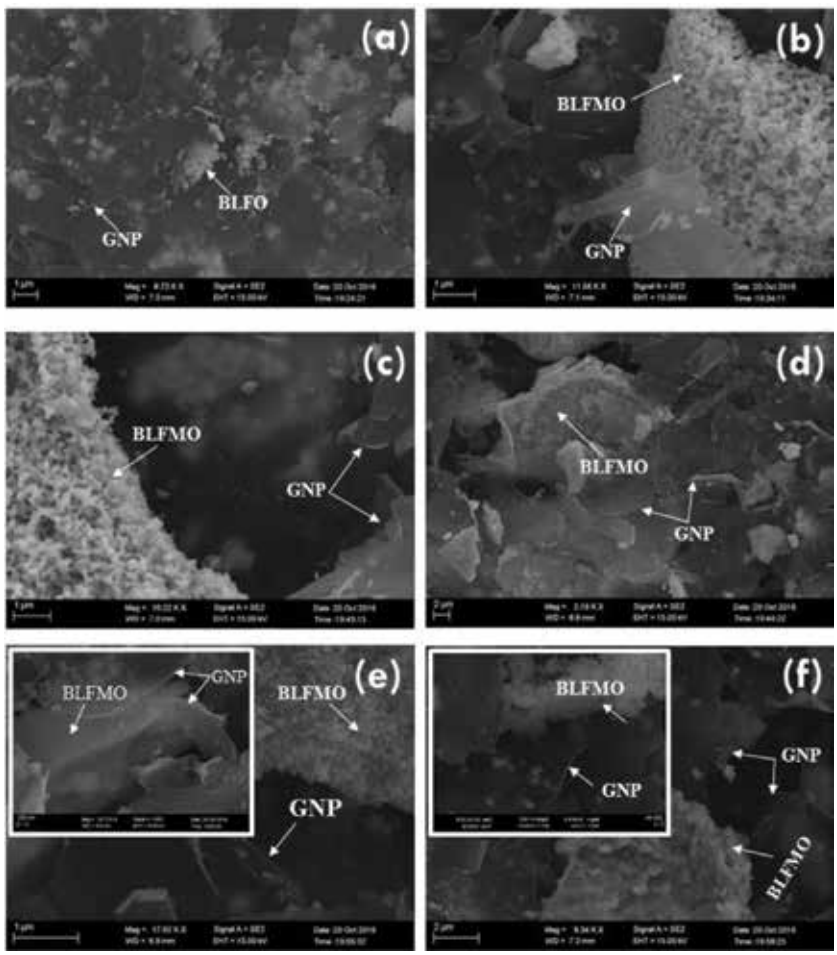

Figure 12. SEM micrographs of (a) BLFO/GNP, (b) BLFO-5/GNP, (c) BLFMO-10/GNP, (d) BLFMO-15/GNP, (e) BLFMO-20/GNP, (f) BLFMO25/GNP nanohybrids showing mixed morphology of both nanoparticles and graphene sheets; inset: shows big clusters of agglomerated particles.

graphene layers in the flake form and adsorbance of particles provides a sandwiched structure of layers in-between the nanoparticles. The particle adsorbancy gives an icy transparent effect to hybrid structures due to which the nanoparticles are clearly visible through the layers in SEM images. The rapid growth of particles over graphene layers provides a damage to the graphene sheets inside GNP resulting more disordered hybrid structures which is consistent with the XRD results. There is also an agglomeration of nanoparticles inside GNP and can be seen in the form of clusters of particles in SEM images.

The TEM micrographs are shown in **Figure 13** representing the BLFMO nanoparticles (dark part) and the light graphene sheets. Spherical BLFMO nanoparticles are not even connected to interface but are also distributed over the surface of graphene sheets in the form of small clusters. Due to overlapping of nanoparticles over the sheets, it is hard to distinguish a separate particle inside the hybrid structures. The estimated average particle size from the TEM micrographs using image-J software is ~ 31 nm.

3.3. X-ray photoluminescence of C-series

Figure 14 represents the X-ray Photoluminescence (XPS) spectra of C-series nanohybrids which helps in analyzing the detailed chemical composition of hybrid structures. The given peaks of bismuth (Bi), iron (Fe), lanthanum (La), manganese (Mn), oxygen (O) and carbon (C) at their corresponding binding energies of 159.1, 711, 837.5, 641.5, 529.8 and 284.7 eV are shown which are already reported before [28–30]. The main peaks verifying both the material's (BFO and graphene) elemental composition are also shown in **Figure 14b-d**. The Bi and O represents two peaks for Bi4f (**Figure 14b** and **c**) while C shows only one peak (**Figure 14d**) representing a network of C-C atoms. There are three main peaks in pristine GNP [31] which corresponds to C1s (a high intensity peak), O1s (a low intensity peak) and OKLL (oxygen vacancies created due to reduction process). The high intensity peak of Oxygen is due to the introduction of O atoms of BFO inside the hybrid material. There is no additional peak of other functional groups like C-H, COOR and C-O present inside BLFMO/GNP nanohybrid as they are eliminated during the reduction process of GNPs. There is peak of OKLL at 970 eV

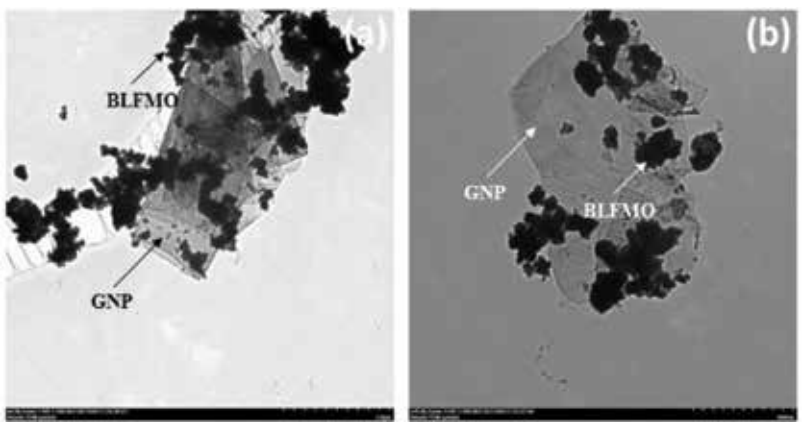

Figure 13. TEM images of BLFMO/GNP nanohybrids of C-series at (a) 1 μm and (b) 500 nm, resolution.

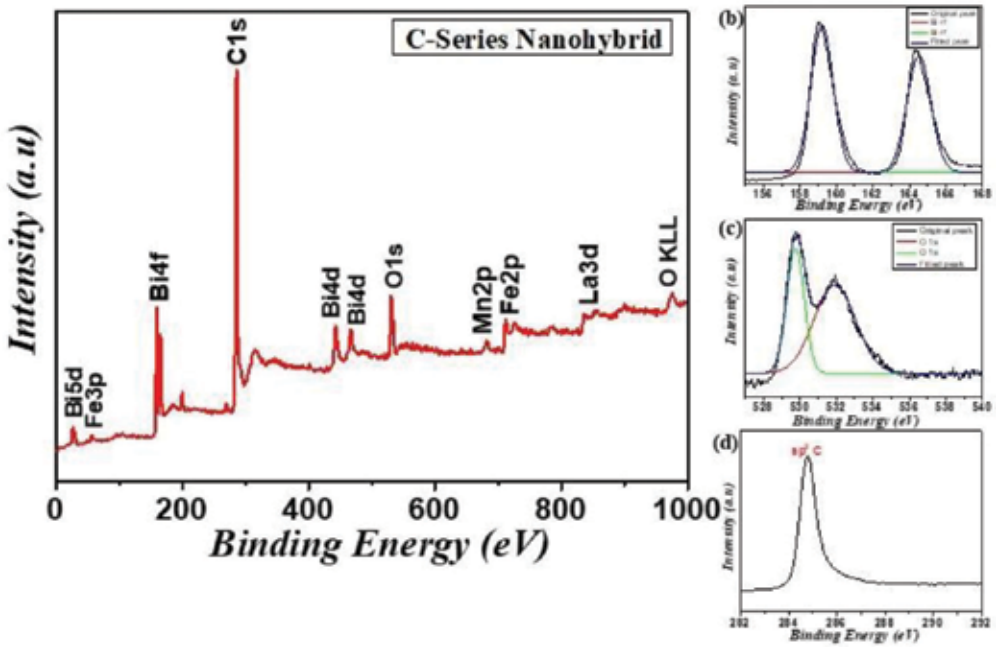

Figure 14. X-ray photoluminescence spectra of C-series nanohybrid.

which corresponds to both, GNP and BFO as oxygen vacancies are produced inside BFO during charge compensation and inside the graphene during reduction.

3.4. H-series structural analysis

The X-ray diffraction pattern of H-series nanohybrids is shown in **Figure 15**. The BLFO XRD pattern with its hybrid form of BLFO/GNP is shown in **Figure 14a**. All labeled peaks represent the bismuth ferrite (BFO) hkl planes (012), (104),(110), (006), (202), (024), (116), (112), (018) and (214), respectively. Peaks are broadened as compared to pure BFO which is due to the rhombohedral crystal structure distortion of BLFO with the introduction of Lanthanum. An impurity peak of $Bi_2Fe_4O_9$ is also appeared inside BLFO with the La addition which is disappeared in BLFO/GNP nanohybrid. The peaks inside the BLFO/GNP hybrid are broadened due to low periodicity in crystal structure with the incorporation of graphene sheets inside BLFO nanoparticles. An extra peak of (002) graphitic plane is also appeared in BLFO/GNP hybrid representing the successful fabrication of hybrid structure. The addition of manganese inside BLFO crystal structure is completely transformed from rhombohedral to orthorhombic and the overlapping of peaks is giving a clear proof of this transformation as shown in **Figure 16b-f**. The positive peak shift up to Mn = 15% is due to decrease of lattice constant as interlayer spacing is inversely related with the diffraction angle. The replacement of iron atoms with Mn-atoms causes the decrease in d-spacing because Mn have low atomic radii than iron. The impurity peak is first decreased and then disappeared with the increase amount of Mn (up to 25%) because of the compensation of bismuth-iron deficiencies. A negative peak shift is also occurred as Mn doping is increase above 15% which is due to the compressive strain produced

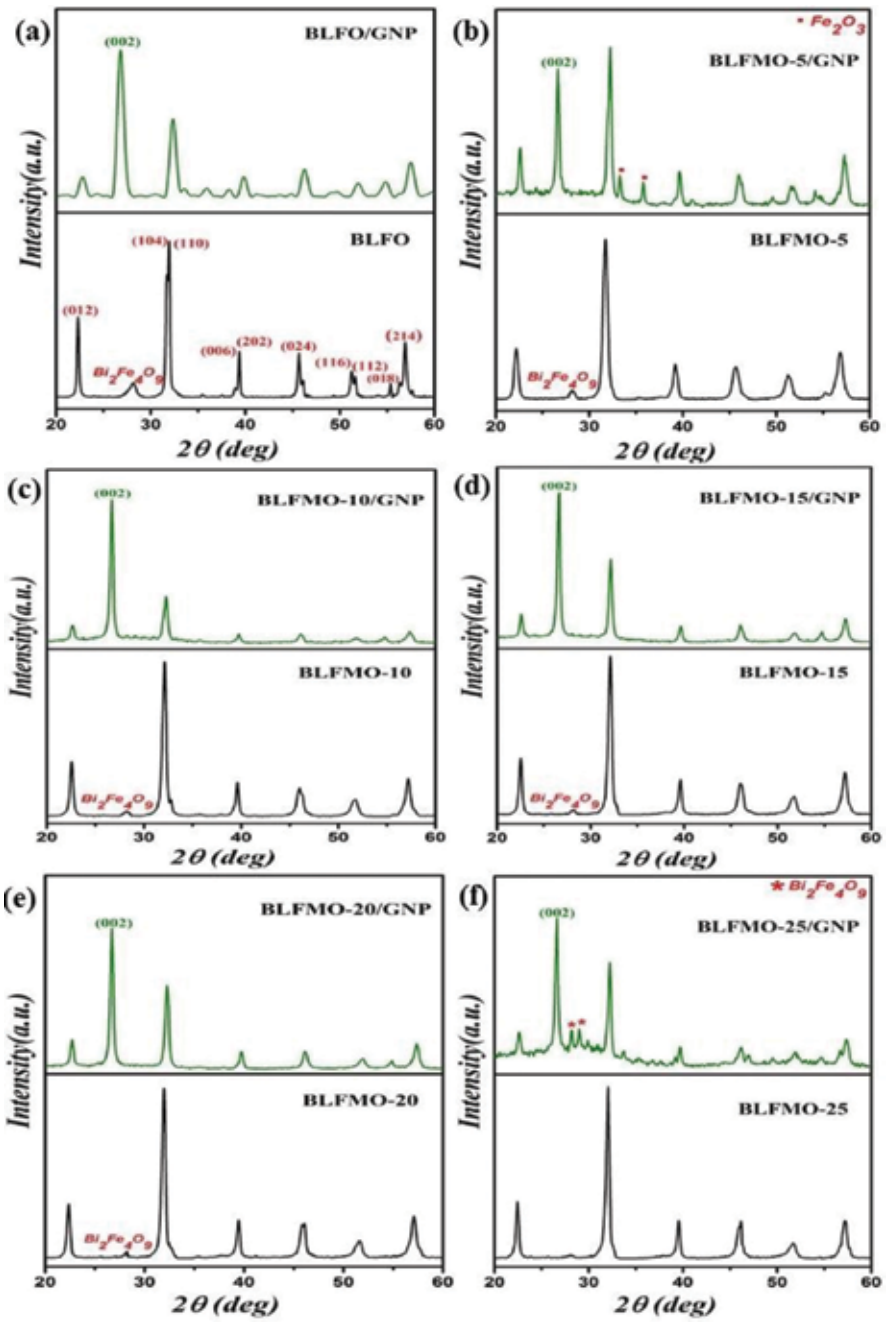

Figure 15. XRD patterns of H-series nanohybrids respectively (a) BLFO/GNP, (b) BLFMO-5/GNP, (c) BLFMO-10/GNP, (d) BLFMO15/GNP, (e) BLFMO-20/GNP, and (f) BLFMO-25/GNP.

inside the crystal structure. The broadening of peaks inside BLFMO-20 and BLFMO-25 is due to the surface defects and Mn-atoms trapped inside the crystals [32]. With the introduction of Mn atoms in hybrid structure from BLFMO-5/GNP to BLFMO-25/GNP, the peaks become

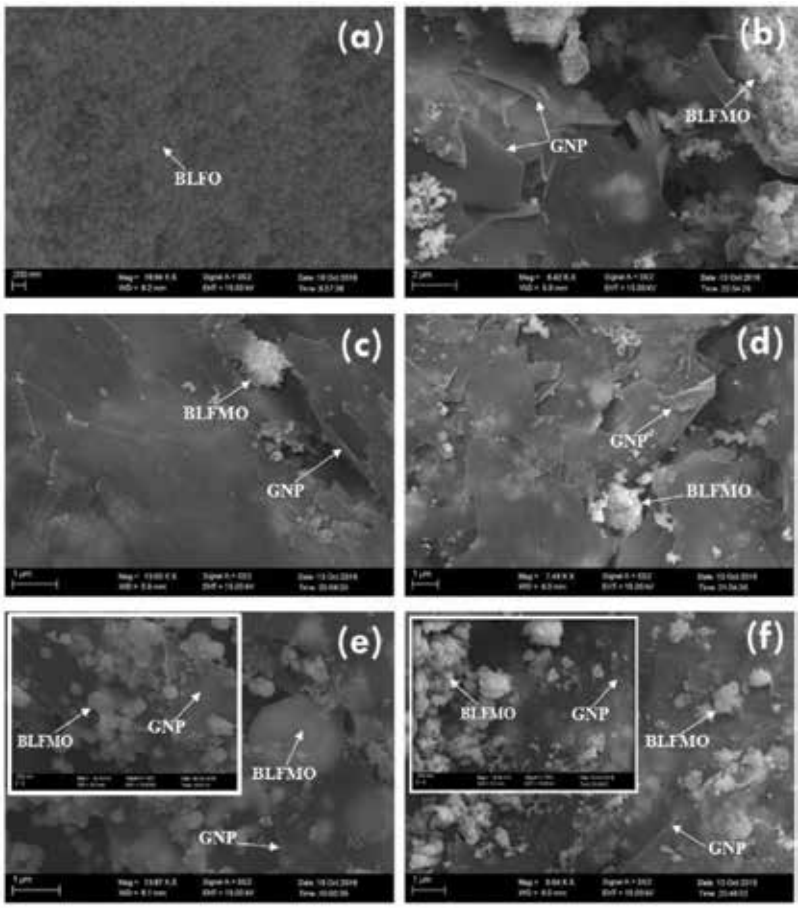

Figure 16. SEM micrographs of (a) BLFO/GNP, (b) BLFO-5/GNP, (c) BLFMO-10/GNP, (d) BLFMO-15/GNP, (e) BLFMO-20/GNP, (f) BLFMO25/GNP nanohybrids showing both, nanoparticles and graphene sheets morphology together. Inset: Uniform distribution of nanoparticles over graphene sheets.

more narrower and intensity of peaks is also increased which shows more crystallinity and periodicity inside the hybrid structure.

In hydrothermal method under controlled conditions of temperature and pressure, stable and good quality fine crystals can easily be grown with having a good control over hybrid composition. As the structure is more crystalline and ordered, small amount of impurities ($Bi_2Fe_4O_9$ and Fe_2O_3) are also appeared inside crystal structure of BLFMO/GNP nanohybrids. A positive shift in (002) peak is also observed inside the hybrid structures which can be occurred due to produced tensile strain with the introduction of uniformly distributed BLFO or BLFMO particles inside GNP layers [33]. The crystallite sizes are also calculated using Scherrer's formula which ranges from 22.5 to 26 nm.

3.5. H-series morphological analysis

Figure 16 shows SEM micrographs of H-series representing both, nanoparticle and sheet morphologies inside hybrid structures. In **Figure 16a**, the GNP sheets are not very much visible

as the whole surface of graphene sheets is covered with the adsorbed BLFO nanoparticles. As the GNPs are efficient nanofillers in nanohybrid synthesis and form a good dispersion, well dispersed and uniformly distributed BLFMO nanoparticles over the smooth surface of graphene nanoplatelets can be clearly seen in SEM images (**Figure 16b-f**).

Hydrothermal fabrication is a controlled growth synthesis process under high pressure and temperature conditions which enables graphene sheets to be more focused towards nucleation centers and thus, more uniform nanohybrids are formed. Mesoporous BLFMO particles are well embedded inside and over the graphene sheets inside GNP and are more visible in inset of SEM images. A transparency effect shown in SEM micrographs is due to the surface adsorption of BLFMO nanoparticles over graphene sheets. These sheets are stacked over one another inside GNP or in other words, are sandwiched in between the BLFMO nanoparticles which is why particles can be seen through the transparent graphene layers.

The H-series and C-series hybrids are further subjected to the photocatalytic experiments and measurement.

3.6. Photocatalytic activity

The photocatalytic activity is checked by measuring the degradation efficiency of hybrid structure in removal of the organic dye congo red (CR). The absorption spectra measured at a specific wavelength λ was compared with the maximum absorption at λ = 496 nm. The diffused reflectance spectra (DRS) of BLFO/GNP and BLFMO/GNP hybrids is shown in **Figure 17**. There is low optical absorption of hybrid structures in UV region as compared to the pure bismuth ferrite and then an overlap is occurred and optical absorption increases for the visible region (550 nm-700 nm). This increase in optical absorption enables the BLFMO/GNP nanohybrids as an efficient photocatalyst under visible light irradiation.

The optical absorption coefficient is related to the given Kubelka-Munk function (Eq. (1)) which is actually responsible for edge absorption.

$$(\alpha h\upsilon) = A\left(h\upsilon - E_g\right)^{n/2} \tag{1}$$

Here, Eg is bandgap energy, A and n are constants respectively, υ and h are light frequency and plank's constant [34].

Optical band gap of BLFO/GNP and BLFMO/GNP were also calculated by drawing a graph in between photon energy and $(\alpha h\upsilon)^2$ and are compared with the pure bismuth ferrite as shown in **Figure 18**. A straight line drawn over the $(\alpha h\upsilon)^2$ vs. energy plot till the point where it goes to zero provides the approximate band gap of hybrid structure. The obtained band gap of BLFMO-20/GNP hybrid structure is significantly reduced to 1.40 eV in comparison to BFO (2.04 eV). Here in all hybrid structures with small changes in optical absorption for visible range, it is slightly difficult to measure the onset of decreasing amount in optical absorption. A decrease in band gap illustrates that there are more chances of an efficient charge transfer and hence an enhanced photocatalytic activity.

The photocatalytic degradation efficiency of the hybrid structures was measured by checking the degradation rate of congo red organic dye under visible light. The obtained plots for

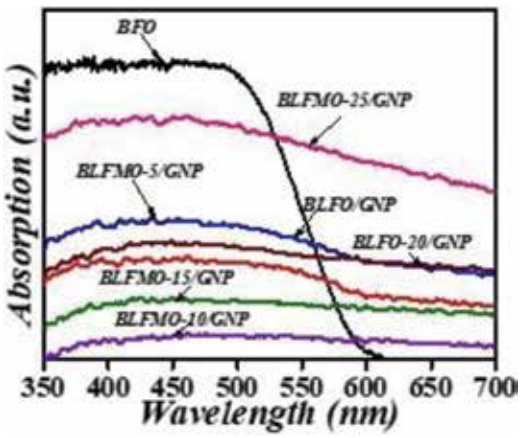

Figure 17. UV-visible absorption spectrum of pure BFO, BLFO/GNP and BLFMO/GNP hybrid structures.

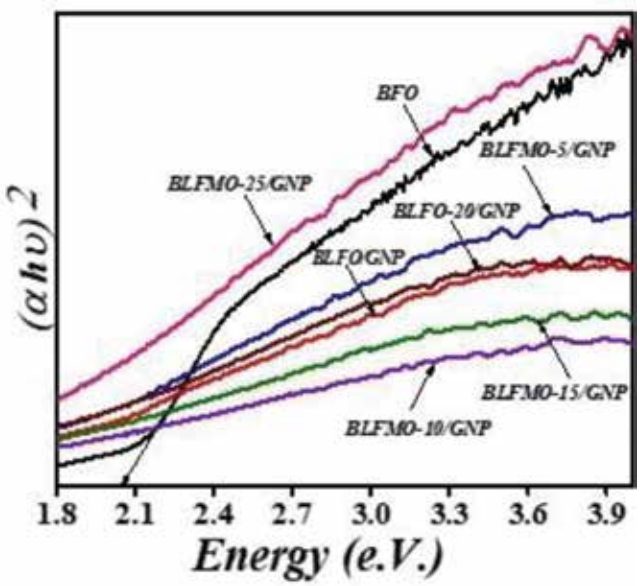

Figure 18. Measurement of the optical band gaps of the BFO, BLFO/GNP and BLFMO/GNP nanohybrids.

photocatalytic degradation are shown in **Figure 19**. The total photocatalytic degradation efficiency of pure BFO is 40% as shown in **Figure 19a** (H-series nanohybrids). The overall catalytic activity of H-series nanohybrids depends upon two factors: (i) adsorption of dye over material surface and (ii) degradation of dye under visible light irradiation. The surface adsorption of dye for BLFMO-15/GNP, BLFMO-20/GNP and BLFMO-25/GNP is 36, 65 and 54% while the photodegradation of dye is about 19, 11 and 9%, respectively. The total dye removal for BLFMO15/GNP, BLFMO-20/GNP and BLFMO-25/GNP nanohybrids is 55, 76 and 63%. C-series nanohybrids catalytic activity is shown in **Figure 19b**. The surface adsorption of dye for BLFO/GNP, BLFMO-5/GNP, BLFMO-15/GNP and BLFMO-25/GNP is 92, 70, 67 and 62% while the

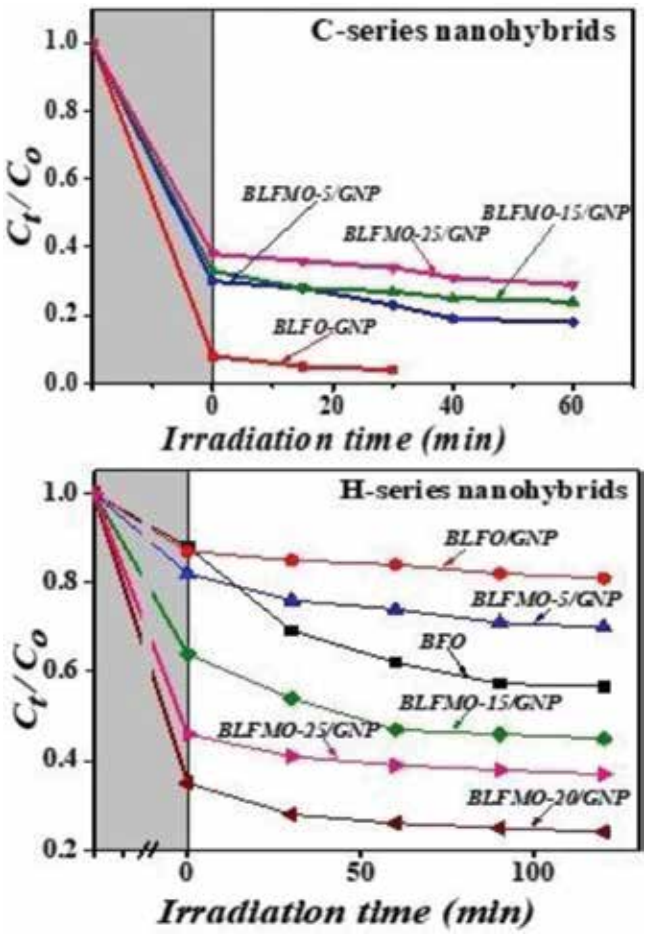

Figure 19. Photocatalytic efficiencies of BFO and BLFMO/GNP nanohybrids degrading the CR under visible light.

photo-degradation of dye is about 4, 12, 9 and 8%, respectively. The total dye removal for BLFO/GNP, BLFMO-5/GNP, BLFMO-15/GNP and BLFMO-25/GNP nanohybrids is 96, 82, 76 and 70%, respectively. The time taken by H-series hybrid structures to remove the whole dye from the aqueous solution was 120 min while it was 30 min for the C-series BLFO/GNP nanohybrid. The more dye removal due to surface adsorption is due to enhanced incorporation of GNP sheets inside BLFO nanoparticles. As co-ppt synthesis took more time for GNP sonication so there will be more yield of graphene due to exfoliation of sheets inside GNP. Graphene inclusion inside a nanohybrid helps in enhancing its specific surface area which causes more surface adsorption inside the material. In the following section, Brunauer Emmett Teller and photoluminescence measurement are performed to support the catalytic results.

3.7. Brunauer Emmett Teller measurements for C-series nanohybrid

To measure the specific surface area, BET measurement was performed and the obtained Nitrogen adsorption–desorption curve is shown in **Figure 20**. The observed curve is of type IV

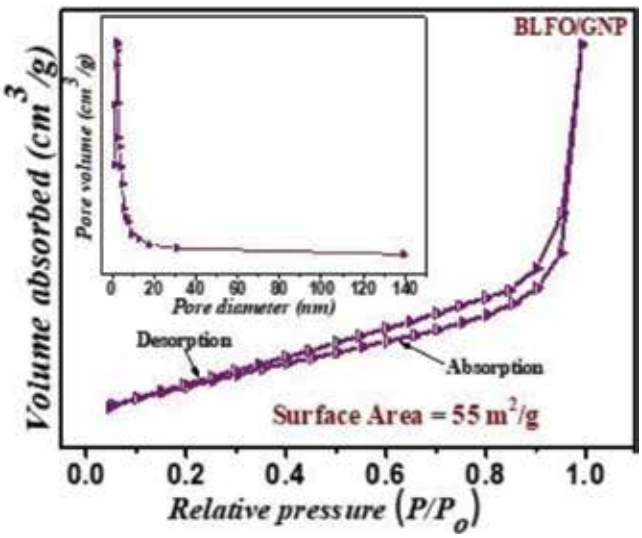

Figure 20. Nitrogen adsorption-desorption curve for surface area measurements of C-series BLFO/GNP nanohybrid.

(H3 hysteresis) with mesopore existence [35]. The average pore diameter and total pore volume for BLFO/GNP is 13.32 nm and 0.184 cm^3/g, respectively. The surface area of pristine BFO is 3.3 m^2/g [36] while the surface area for BLFO/GNP is enhanced up to 55 m^2/g due to the GNP loading inside BLFO nanoparticles. The enhanced surface area is representing the presence of multichannel structure inside BLFO/GNP nanohybrid which permits rapid mass movement and more intake of light harvesting due to increased absorption and multiple light reflections with gas diffusion inside the material's pores [37, 38]. The existence of mesopores with macro-channel structure attribute to more trapping of dye molecules over the material's surface Hence both adsorption over the surface and multiple light reflections together attribute in enhancing the photocatalytic activity of the nanohybrid which results in fast dye degradation.

3.8. Photoluminescence spectra of C-series nanohybrids

In photoluminescence measurement, electron-hole recombination rate is checked which promotes the efficient charge separation inside the photocatalytic material. The low PL intensity gives us low carrier recombination rate and hence, easily promotes the charge carriers over material surface for photo-degradation of dye [39]. The loading of graphene usually reduces the PL intensity due to graphene being a good trapping site for electrons and hence, easy charge transfer over catalyst surface [40]. **Figure 21** represents photoluminescence spectra of Pure BFO and C-series. Pristine BFO has larger band gap as compared to hybrid structures which is why the PL has high intensity for pure BFO showing more recombination rate The peak intensity is low for BLFMO-5/GNP and BLFMO-15/GNP as compared to BLFO/GNP and BLFMO-25/GNP. The low peak intensity refers to low recombination rate of charge carriers and hence more dye degradation under visible light. Hence, BLFMO-5/GNP (12%), BLFMO-15/GNP (9%) show more dye-degradation under visible light as compared to BLFO/GNP (4%) and BLFMO-25/GNP (8%).

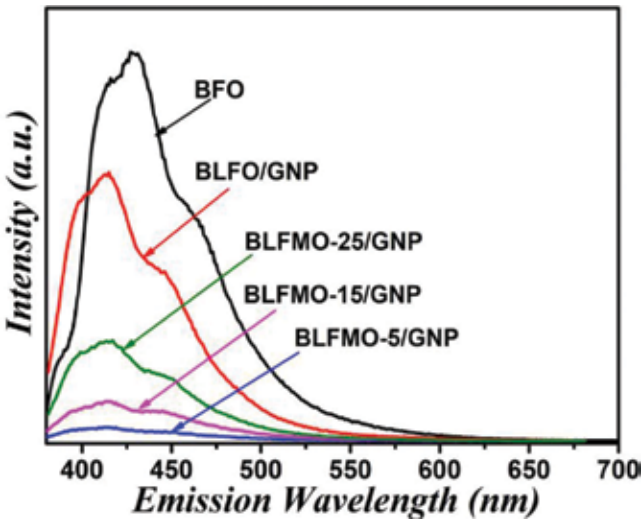

Figure 21. Photoluminescence spectra of C-series nanohybrids.

4. Conclusion

Here using sol-gel method lanthanum (La) and manganese (Mn) doped BFO nanoparticles were prepared and named as BLFO and BLFMO nanoparticles. These nanoparticles were further process to the coprecipitation and hydrothermal routes for synthesizing nanohybrids with graphene nanoplatelets (GNP). As synthesized BLFO/GNP and BLFMO/GNP nanohybrids via different routes were named as C and H series, respectively. Further nanohybrids were undergo structural and morphological analysis using XRD and SEM which show that the H-series nanohybrids are showing more crystallinity as compared to the C-series nanohybrids. The energy level introduced with the addition of Mn into BFO nanoparticles reduces the band-gap of nanohybrids. The detailed elemental composition of nanohybrids was checked using XPS which verified the bonding between nanoparticles and GNP. The BET shows that surface area is greatly enhanced from 3.3 m^2/g (for pure BFO) to 55 m^2/g (for C-series nanohybrid) which then contributes in fast dye removal as a result of both surface adsorption and photo-degradation. Hence C-series nanohybrids are more efficient as catalysts rather than H-series and showed 96% dye removal in only 30 min. The catalytic activity mainly depends upon the adsorption of dye over catalyst surface under dark conditions. These nanohybrids are very much applicable for commercial applications as they are fabricated via an easy and cost effective route and provide a fast and efficient dye removal from aqueous solution.

Acknowledgements

The authors are thankful to Higher Education Commission (HEC) of Pakistan for providing research funding under the Project No.: 6040/Federal/NRPU/R&D/HEC/2016 and

HEC/USAID for financial support under the Project No.: HEC/R&D/PAKUS/2017/783. The author also thanks School of Natural Sciences (SNS) at National University of Science & Technology (NUST), Islamabad, Pakistan for partial financial support.

Notes/thanks/other declarations

Special thanks to Dr. S. Irfan Ali at Tsinghua University, China for providing all technical assistance and guidance for the project.

Conflict of interest

I declare that there is no conflict of interest for the content added in this chapter.

Author details

Syed Rizwan* and Sabeen Fatima

*Address all correspondence to: syedrizwanh83@gmail.com

Department of Physics, School of Natural Sciences (SNS), National University of Sciences and Technology (NUST), Islamabad, Pakistan

References

[1] http://www.nature.com/nmat/journal/v11/n5/images_article/nmat3318-f2.jpg

[2] http://www.reade.com/images/product_images/ferrite_compounds/bismuth_ferrite_structure.jpg

[3] Zaleski M. Thermally stimulated processes related to photochromism of scandium doped sillenites. Journal of Applied Physics. 2000;**87**:4279-4284. DOI: 10.1063/1.373066

[4] Borse PH, Joshi UA, Ji SM, Jang JS, Jeong ED, Kim HG, Lee JS. Band gap tuning of lead-substituted $BaSnO_3$ for visible light photocatalysis. Applied Physics Letters. 2007; **90**:034103-034105. DOI: 10.1063/1.2430932

[5] Nippolainen E, Kamshilin AA, Prokofiev VV, Jaskelainen T. Combined formation of a self-pumped phase-conjugate mirror and spatial subharmonics in photorefractive sillenites. Applied Physics Letters. 2001;**78**:859-861. DOI: 10.1063/1.1344570

[6] Catalan G, Scott JF. Physics and applications of bismuth ferrite. Advanced Materials. 2009; **21**:2463-2485. DOI: 10.1002/adma.200802849

[7] Falkovsky LA. Optical properties of graphene. Journal of Physics: Conference Series. 2008;**129**:1-7

[8] Choi W, Lee JW. Graphene: Synthesis and Applications. USA: CRC Press; 2016. vii p. ISBN: 9781439861875. DOI: 10.1088/1742-6596/129/1/012004

[9] http://www.rsc.orgejNR2012c2nr30605kc2nr30605k-s1.gif

[10] Wolf EL. Applications of Graphene: An Overview. Dordrecht London: Springer Science & Business Media; 2014. 19 p. ISBN: 978-3-319-03946-6

[11] http://www.slideshare.net/NCSRCommunications/graphenemanchester-beyondthe-sticky-tape

[12] https://www.slideshare.net/BusinessGrowthHub/prof-ian-kinloch-presentation-graphene-week-25th-june

[13] Mertens R. The Graphene Handbook. lulu.com; 2016. 16 p. ISBN: 9781365707674

[14] Geng Y, Wang SJ, Kim JK. Preparation of graphite nanoplatelets and graphene sheets. Journal of Colloid and Interface Science. 2009;**336**:592-598. DOI: 10.1016/j.jcis.2009.04.005

[15] http://xgsciences.us/aboutxgnp.html

[16] Okpala C. C., "Nanocomposites—An overview", International Journal of Engineering Research and Development. 2013:17-23. ISSN: 2278-800X

[17] Adrian MTS, Sonia ACC. Advances in Carbon Nanostructures. Croatia, Europe: InTech; 2016. 3 p. DOI: 10.5772/61730

[18] Jing LQ, Zhou W, Tian GH, Fu HG. Surface tuning for oxide-based nanomaterials as efficient photocatalysts. Chemical Society Reviews. 2013;**42**:9509-9549. DOI: 10.1039/C3CS60176E

[19] Stengl V, Popelkova D, Vlacil P. TiO_2-graphene nanocomposite as high performance photo catalysts. Journal of Physical Chemistry C. 2011;**115**:25209-25218. DOI: 10.1021/jp207515z

[20] Liang YY, Wang HL, Casalongue HS, Chen Z, Dai HJ. TiO_2 nanocrystals grown on graphene as advanced photocatalytic hybrid materials. Nano Research. 2010;**3**:701-705. DOI: 10.1007/s12274-010-0033-5

[21] Gao F, Chen XY, Yin KB, Dong S, Ren ZF, Yuan F, Yu T, Liu JM. Visible-light photocatalytic properties of weak magnetic $BiFeO_3$ nanoparticles. Advanced Materials. 2007; **19**:2889-2892. DOI: 10.1002/adma.200602377

[22] An J, Zhu L, Wang N, Song Z, Yang Z, Du D, Tang H. Photo-Fenton like degradation of tetrabromobisphenol A with graphene single bond $BiFeO_3$ composite as a catalyst. Chemical Engineering Journal. 2013;**219**:225-237. DOI: 10.1016/j.cej.2013.01.013

[23] Li Z, Shen Y, Yang C, Lei Y, Guan Y, Lin Y, Liu D, Nana CW. Significant enhancement in the visible light photocatalytic properties of $BiFeO_3$-graphene nanohybrids. Journal of Materials Chemistry A. 2013;**1**:823-829. DOI: 10.1039/C2TA00141A

[24] Kaelble EF. Handbook of X-Rays. USA: McGraw-Hill Education; 1967

[25] Garciaa FG, Riccardi CS, Simoes AZ. Lanthanum doped $BiFeO_3$ powders: Syntheses and characterization. Journal of Alloys and Compounds. 2010;**501**:25-29. DOI: 10.1016/j.jallcom.2010.04.049

[26] Irfan S, Rizwan S, Shen Y, Tomovska R, Zulfiqar S, Sarwar MI, Nan CW. Mesoporous template-free gyroid-like nanostructures based on La and Mn co-doped bismuth ferrites with improved photocatalytic activity. RSC Advances. 2016;**6**:114183-114189. DOI: 10.1039/C6RA23674J

[27] Gupta S, Sharma A, Tomar M, Gupta V, Pal M, Guo R, Bhalla A. Piezoresponse force microscopy and vibrating sample magnetometer study of single phased Mn induced multiferroic $BiFeO_3$ thin film. Journal of Applied Physics. 2012;**111**:064110-064116. DOI: 10.1063/1.3699021

[28] Li Y, Sheng CM, Wang DW, Yuan J. High-efficiency and dynamic stable electromagnetic wave attenuation for La doped bismuth ferrite at elevated temperature and gigahertz frequency. RSC Advances. 2015;**5**:77184-77191. DOI: 10.1039/C5RA15458H

[29] Xu Q, Sheng Y, Khalid M, Cao Y, Wang Y, Qiu X, Zhang W, He M, Wang S, Zhou S, Li Q, Wu D, Zhai Y, Liu W, Wang P, Xu YB, Du J. Magnetic interactions in $BiFe_{0.5}Mn_{0.5}O_3$ films and $BiFeO_3$/$BiMnO_3$ superlattices. Scientific Reports. 2015;**5**:1-8. DOI: 10.1038/srep09093

[30] Wang F, Drzal LT, Qin Y, Huang Z. Effects of functionalized graphene nanoplatelets on the morphology and properties of epoxy resins. High Performance Polymers. 2015;**28**:1-11. DOI: 10.1177/0954008315588983

[31] Sun R, Yao H, Zhang HB, Li YWMY, Yu ZZ. Decoration of defect-free graphene nanoplatelets with alumina for thermally conductive and electrically insulating epoxy composites. Composites Science and Technology. 2016;**137**:1-9. DOI: 10.1016/j.compscitech.2016.10.017

[32] Arya GS, Negi NS. Effect of In and Mn co-doping on structural, magnetic and dielectric properties of $BiFeO_3$ nanoparticles. Journal of Physics D: Applied Physics. 2013;**46**:1-8. DOI: 10.1088/0022-3727/46/9/095004

[33] Qiu B, Zhou Y, Ma Y, Yang X, Sheng W, Xing M, Zhang J. Facile synthesis of the Ti^{3+} self-doped TiO_2-graphene nanosheet composites with enhanced photocatalysis. Scientific Reports. 2015;**5**:1-6. DOI: 10.1038/srep08591

[34] Kubelka P, Munk F. Ein beitrag zur optik der farbanstriche. Technical Physics. 1931; **12**:593-601

[35] Chieng BW, Ibrahim NA, Yunus WMZW, Hussein MZ, Silverajah VSG. Graphene nanoplatelets as novel reinforcement filler in poly(lactic acid)/epoxidized palm oil green nanocomposites: Mechanical properties. International Journal of Molecular Sciences. 2012;**13**:10920-10934. DOI: 10.3390/ijms130910920

[36] Irfan S, Rizwan S, Shen Y, Liangliang L, Asfandiyar, Butt S, Nan CW. The gadolinium (Gd^{3+}) and Tin (Sn^{4+}) co-doped BiFeO3 nanoparticles as new solar light active Photocatalyst, Scientific Reports, 2017;**7**:1-12. DOI:10.1038/srep42493

[37] Zhao T, Liu Z, Nakata K, Nishimoto S, Murakami T, Zhao Y, Jiang L, Fujishima A. Multichannel TiO_2 hollow fibers with enhanced photocatalytic activity. Journal of Materials Chemistry. 2010;**20**:5095-5099. DOI: 10.1039/C0JM00484G

[38] Fang B, Bonakdarpour A, Reilly K, Xing Y, Taghipour F, Wilkinson DP. Large-scale synthesis of TiO_2 microspheres with hierarchical nanostructure for highly efficient photodriven reduction of CO_2 to CH_4. ACS Applied Materials & Interfaces. 2014;**6**:15488-15498. DOI: 10.1021/am504128t

[39] Arshad A, Iqbal J, Siddiq M, Mansoor Q, Ismail M, Mehmood F, Ajmal M, Abid Z. Graphene nanoplatelets induced tailoring in photocatalytic activity and antibacterial characteristics of MgO/graphene nnanoplatelets nanocomposites. Journal of Applied Physics. 2017;**121**:1-10. DOI: 10.1063/1.4972970

[40] Worajittiphon P, Pingmunag K, Inceesungvorn B, Phanichphant S. Enhancing the photocatalytic activity of ZnO nanoparticles for efficient rhodamine B degradation by functionalized graphene nanoplatelets. Ceramics International. 2015;**41**:1885-1889. DOI: 10.1016/j.ceramint.2014.09.023

Chapter 2

Bismuth-Based Nanoparticles as Photocatalytic Materials

William W. Anku, Samuel O.B. Oppong and Penny P. Govender

Additional information is available at the end of the chapter

http://dx.doi.org/10.5772/intechopen.75104

Abstract

Bismuth-based nanoparticles are a unique category of materials that possess interesting properties such as excellent chemical, electrical, optical and catalytic activities among others. The application of bismuth-based nanoparticles as photocatalytic materials has caught the interest of the scientific community in recent times due to these unique properties. Consequently, a number of data have been generated in relation to the photocatalytic application of these nanoparticles. This chapter intends to organise and provide the recently generated information on the use of bismuth-based nanoparticles in photocatalytic degradation processes. A detailed discussion is provided on bismuth-based nanoparticles including bismuth chalcogenides, bismuth vanadate, bismuth oxyhalides and other bismuth-related nanoparticles. Attention was also paid to the modification of these nanoparticles to improve their photocatalytic activities. The application of the modified nanoparticles in various photocatalytic processes with emphasis on water treatment, waste gas treatment, hydrogen production and air purification has also been thoroughly discussed.

Keywords: bismuth-based nanoparticles, photocatalytic degradation, hydrogen generation, carbon dioxide reduction, water treatment, pharmaceutical products, organic pollutants

1. Introduction

Photocatalysis is gradually becoming a dependable technological approach in many industries due to its cost-effective and environmentally friendly nature. This technique has the tendency to convert light energy into chemical energy under mild reaction conditions [1].

Subsequently, the technology has had successful application in many areas and is seen as a possible solution to the ever-increasing environmental and energy shortage issues.

Recent advancement in population growth coupled with the expansion of industrialisation has brought about serious environmental pollution and energy shortages. This has necessitated the rising demands for environmental remediation, the alternative supply of energy and novel methods for pollution eradication by researchers [2]. A lot of methods have been employed to degrade complex toxic pollutants to less toxic compounds. Among them are the convention ones (coagulation, oxidation, ion exchange, membrane filtration and flocculation) [2]. These methods are, however, considered ineffective by a lot of researchers due to their severe disadvantages including producing a large volume of sludge and operating at a very high cost [3]. Photocatalysis using semiconductors has been recommended as a potential method for environmental clean-up because it is economical and degrades pollutants by using artificial or natural sunlight which is cheap and abundant worldwide. Besides, there is no formation of sludge, and the catalyst can be reused after the process since it remains unchanged [4].

A number of semiconductors (TiO_2, ZnO, Fe_2O_3, CdS and ZnO) have been employed for varied photocatalytic activities due to their unique properties such as excellent electronic structure and light absorption, degradation of pollutants, thermal stability, less toxicity, low cost and inertness [5]. However, these semiconductors suffer two serious drawbacks. These drawbacks include large energy band gap which is too wide to absorbed visible light [6]. Thus, these semiconductors are only photoactive in UV range. The second limitation is the rate at which the photo-generated electrons and holes recombine; a phenomenon that reduces the effectiveness of photodegradation process [7]. Hence, for a semiconductor to attain its maximum potential as an efficient photocatalyst, some effective modifications that can enhance its photosensitivity in the visible light range and also retard the recombination of the electrons and holes [8] are required. Thus, the development of a novel photocatalyst that has potential to eliminate the environmental pollutants is an essential requirement for photocatalysis process.

Documented reports on bismuth-related nanoparticles including BiOCOOH, Bi_2WO_6, $(BiO)_2CO_3$, $BiVO_4$, $BiPO_4$, Bi_2O_3 and BiOCl [9], have been found to attract considerable attention because of their proficient photocatalytic performance, cost-effectiveness, low toxicity and high stability. Modification of bismuth-related nanoparticles with metals and non-metal, carbonaceous materials and biopolymers is reported to further endow these catalysts with exceptionally high visible light responsivity and efficient photocatalytic performances [10]. Modified bismuth-related nanoparticles have been efficaciously utilised in many photocatalytic processes including antifogging, self-cleaning, disinfection, carbon dioxide reduction, organic pollutant degradation in water, hydrogen generation, air purification and so on.

This chapter discusses bismuth as a metal and its related nanoparticles. It also dwells on the modification of bismuth-based nanoparticles for enhanced photocatalytic activity and finally elaborated on the various photocatalytic applications/processes that these nanoparticles have been successfully applied to.

1.1. Bismuth

Bismuth (Bi) occurs naturally as a diamagnetic element with atomic number 83. It is a pentavalent transition metal and its oxides and sulphides represent significant commercial ore. It has

low thermal conductivity, high Hall coefficient and high electrical resistivity [11]. Deposition of a thin layer of bismuth on the surfaces of materials causes it to behave as a semiconductor [12]. Again, bismuth is reported to be denser in its liquid phase than the solid phase and expands about 3% during solidification. This property enables it to be used as a component of alloys so that it can compensate for the contraction of other components of the alloy [12]. Bismuth is relatively non-toxic and has a relatively low melting point (271 C). Approximately, 63% bismuth is used to produce cosmetics, pigments and pharmaceuticals. 26% of it is also used in the field of metallurgy for galvanising and casting [13]. 7% is used in bismuth alloys, solders and ammunition and the 4% also are used in research fields [13].

1.2. Bismuth-based nanoparticles

The use of bismuth-based nanoparticles instead of the traditional bismuth-containing bulk materials/compounds for application in various advanced technological areas has received greater attention recently. This widespread interest in bismuth-based nanoparticles is as a result of the fact that the nanoparticles possess peculiar properties that are absent in the bulk solid materials. These unique features which include high optical, electrical, thermal, photocatalytic and magnetic properties are mainly dependent on the nanoparticles' large specific surface area and small sizes [14]. Fortunately, opportunities exist, through colloidal chemistry, to synthesis bismuth-based nanoparticles. This process involves utilisation of bismuth salts as precursors with the addition of surface modifiers and reducing agents to produce size controllable and highly crystalline bismuth-based nanoparticles. Among the bismuth-based nanoparticles of interest are Bismuth chalcogenides, Bismuth vanadate, Bismuth oxyhalides and other bismuth-related nanoparticles.

1.2.1. Bismuth chalcogenides

Bismuth chalcogenides are a class of photoelectric compounds consisting of bismuth and group VI elements. These compounds are generally represented as Bi_2E_3 (E = O, S, Se, Te) and consist of bismuth oxide (Bi_2O_3), bismuth sulphide (Bi_2S_3), bismuth selenide (Bi_2Se_3) and bismuth telluride (Bi_2T_3). These class of compounds are technologically important semiconductors owing to their peculiar properties and have been applied in different industries. A recent study in bismuth chalcogenides' visible-light-responsive properties and enhanced photocatalytic activities has stimulated a great research interest in their nanomaterials.

Bi_2O_3 is a p-type semiconductor with six crystallographic polymorphs which are represented as α-, β-, γ-, ω-, ε-, and δ-Bi_2O_3. Monoclinic α-Bi_2O_3 is the phase present at room temperature. This phase can transition to the face-centred cubic δ-Bi_2O_3 phase when heated. The other phases of Bi_2O_3 include tetragonal β-Bi_2 phase, body-centred cubic γ- Bi_2O_3, orthorhombic ε-Bi_2O_3 and triclinic ω- Bi_2O_3 phases [15]. Bi_2O_3 has high refractive index, narrow energy band gap (2.40–2.80), dielectric permittivity and outstanding photoconductivity [16]. Bi_2O_3 is also considered as an amphoteric semiconductor as there are reports of the material exhibiting both p and n-type conductivity based on the methods of synthesis [16]. These properties enable Bi_2O_3 to be used as a sensor and electrochromic materials, optical coating and photocatalyst.

Bi_2S_3 possesses interesting optical and electronic properties and a direct band gap ranging from 1.3 to 1.7 eV. These qualities enable Bi_2S_3 to be applied in various fields including thermoelectric

transport for the fabrication of optoelectronic, photovoltaic and thermoelectric devices [17] and photocatalysis. Various morphologies of Bi_2S_3 have been fabricated through different routes of synthesis. These one-dimensional nanostructures which include nanowires, nanotubes, nanorods and nanoflowers are considered to be the most appropriate for the above-named applications of Bi_2S_3 because of quantum confinement effect which subsequently enhances the thermoelectric efficiencies of the materials [18].

Bi_2Se_3 has a stacked layered laminated structure. Each layer is about 0.96 nm thick and contains five atoms which are bonded covalently along the z-axis in the following order: Se-Bi-Se-Bi-Se [19] (**Figure 1**). As a result of the weak interlayer forces of attraction, exfoliation of Bi_2Se_3 into few-layer nanosheets is possible [19]. Being a narrow band gap semiconductor (0.3 eV) with a high charge carrier mobility, Bi_2Se_3 has high potential application in photoelectrochemical and thermoelectrical devices as well as optical recording systems and photocatalysis [20].

Bismuth telluride (Bi_2Te_3), is a semiconductor with a band gap of 0.15 eV. It has a trigonal structure and a high melting point of 585°C. When alloyed with antimony or selenium, Bi_2Te_3 becomes a highly efficient thermoelectric material at room temperature [21]. Because of these interesting properties, Bi_2Te_3 has been applied in thermoelectric power generation and refrigeration [22, 23].

1.2.2. Bismuth vanadate

Bismuth vanadate ($BiVO_4$) exists in three main phases. These phases include tetragonal scheelite, monoclinic scheelite and tetragonal zircon. The monoclinic phase has high visible light activity due to the narrow nature of its band gap (2.4 eV) [24]. This visible light absorption behaviour has stimulated a lot of research investigation into its application in environmental remediation through photocatalysis. Again, $BiVO_4$ has advantages over lots of its related semiconductors such as being environmentally friendly, highly resistant to photocorrosion, non-toxic and low cost [24].

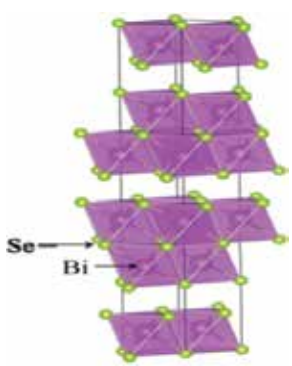

Figure 1. Structure of bismuth selenide [21].

1.2.3. Bismuth oxyhalides (BiOX)

BiOX, with the X representing either Br, Cl or I, are layered semiconductor materials that are crystallised in a tetragonal matlockite form [25]. The layered structure is arranged in such a way that each bismuth atom is encircled by four oxygen and halogen atoms resulting in an asymmetric tetrahedral symmetry (X-Bi-O-Bi-X) [25]. This arrangement enables BiOX to possess remarkable optical, mechanical, electrical and catalytic properties. As a result, BiOX has been utilised in selective oxidation of alcohols, organic synthesis, water splitting, indoor-gas purification and photodegradation of organic pollutants in wastewater [26].

Bismuth oxychloride (BiOCl), a p-type semiconductor, exhibits excellent ionic conduction, optical, catalytic and electrical properties. It is made up of chlorine ions (Cl^-), bismuth ions (Bi^{3+}) and oxygen ions (O^{2-}) that pile up in tetragonal layered [Cl-Bi-O-Bi-Cl]n structure forming non-bonding attractions via the chlorine atoms (Cl) along C-axis. The four Bi-Cl and four Bi-O are arranged opposite to one another in a tetragonal pyramidal phase with the Bi in the centre of the structure (**Figure 2**). BiOCl is active in UV range with experimental band gap range of 3.1 to 3.5 eV while the theoretical values range from 2.8 to 2.9 eV [27].

Bismuth oxybromide (BiOBr) nanoparticle is also a p-type semiconductor and a promising photocatalyst due to its excellent optical properties, chemical stability and effective photocatalytic activity. Its layered tetragonal structure and appropriate indirect band gap bequeathed it with high visible light activity and the ability to efficiently separate electrons and hole leading to its pollutant degradation tendency [26].

Bismuth oxyiodide (BiOI) has a stacked tetragonal structure that contains alternate $[Bi_2O_2]^{2+}$ and I slabs. It is one of the attractive nanoparticles for visible light photocatalytic applications owing to its relatively narrow band gap (1.6 to 1.9 eV) which endowed it with high visible light activity. Photo-generated electrons and holes are also perfectly separated in BiOI as a result of the presence of strong intralayer and weak van der Waals interlayer

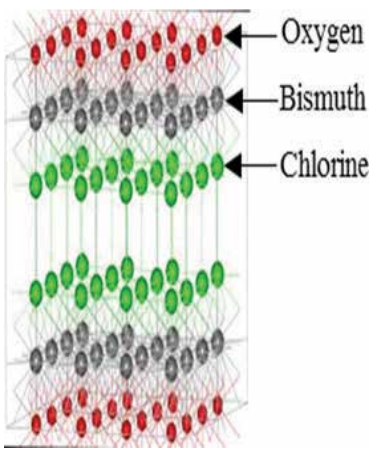

Figure 2. Structure of bismuth oxychloride [27].

bonding in its structure [28]. As a result, BiOI has been successfully applied in some photocatalytic processes including organic pollutant degradation, CO_2 conversion and hydrogen generation.

1.2.4. Other bismuth-related nanoparticles

1.2.4.1. Bismuth (III) phosphate ($BiPO_4$) and bismuth niobate (Bi_3NbO_7)

$BiPO_4$ is an intrinsic p-type semiconductor with two polymorphic phases. These phases include the stable monazite-type structure (known as low-temperature monoclinic phase (LBP)) and high-temperature monoclinic phase (HBP). The HBP polymorph is obtained by heating LBP at higher temperatures. $BiPO_4$ nanoparticles are known to be non-toxic and have low costs of production [29]. They possess high thermal and chemical stability, redox active species, and high photocatalytic activity [29]. Consequently, these materials have been used for Li-ion batteries, sensors and as photocatalysts for disinfection of water and photodegradation of organic pollutants in water [30].

Bi_3NbO_7 is noted for its favourable properties resulting in its use as electrochemical controllers, a catalyst for photolytic water splitting, selective oxidation of hydrocarbons and as oxygen sensors [31]. It exists in cubic and tetragonal phases and has the ability to undergo a reversible transition between tetragonal phase at 800°C to the cubic phases at 900°C and back to tetragonal phase. The cubic phase has defective fluorite-structure (Fm3m, a = 0.548), while the bismuth and niobium atoms are dispersed over similar crystallographic locations. [31].

2. Modified bismuth-based nanoparticles and their photocatalytic applications

2.1. Modified bismuth-based nanoparticles

Bismuth-based nanoparticles are receiving substantial consideration as promising photocatalysts as a result of their comparatively narrow band gaps. They are non-toxic and have the potential to resist corrosion. They are environmentally friendly and relatively cheap [32]. There are a number of available reports regarding the efficient visible light activities of these nanoparticles, and their use for water disinfection and organic pollutants degradation [33]. Their effectiveness as photocatalysts for production of hydrogen gas from water as well as carbon dioxide conversion to useful hydrocarbon products has also been studied. Notwithstanding all these advantages, bismuth-based nanoparticles have some disadvantages that limit their practical application as effective photocatalysts. For example, they have small specific surface areas which impair their photocatalytic activities. They also experience recombination of the photogenerated electrons and holes [34] and thus reduce their effectiveness as photocatalysts.

Attempts to overcome these problems and improve the efficiency of these nanoparticles have culminated in the use of different approaches/techniques to modify them. These approaches comprise the use of carbon-based materials and modification with biopolymers [35], doping

with metals and non-metal [36], and the use of heterostructures/mixed metal oxides [37]. The modified bismuth-based nanoparticles are reported to display higher photocatalytic activities compared to their bare/pure counterparts. Some of the photocatalytic processes to which these materials have been applied are discussed in the subsequent sections.

2.2. Photocatalytic applications of modified bismuth-based nanoparticles

2.2.1. Application in water treatment

A number of publications are available on the use of modified bismuth-based nanoparticle for water treatment through the degradation of organic pollutants and removal of bacteria. This section presents some of the research works that have been performed in this regard.

2.2.1.1. Degradation of organic pollutants

Harmful organic contaminants in water can be degraded or mineralised into innocuous/inoffensive products (CO_2 and H_2O) through a photocatalytic reaction involving photo-generated electrons and holes and reactive oxygen species. Photodegradation of organic contaminants through the use of bismuth-based nanoparticles occurs when the photocatalyst absorbs light of appropriate wavelength from sunlight or illuminated light source. This light energy excites and promotes electrons in the photocatalyst's valence band to its conduction band. This results in the creation of positive charges (holes) and negative charges (electrons) on the valence and conduction bands respectively leading to the creation of electron-hole pairs. The hole oxidise water molecule into hydrogen gas and hydroxyl radical while the electron reduces oxygen molecules into superoxide radicals. The hydroxyl and the superoxide radicals then attack the pollutants and degrade them into harmless products [38]. These hydroxyl ions and superoxide radicals are also responsible for inactivation of bacteria through degradation of their cell walls [38]. The mechanism of the photodegradation process is presented in **Figure 3**.

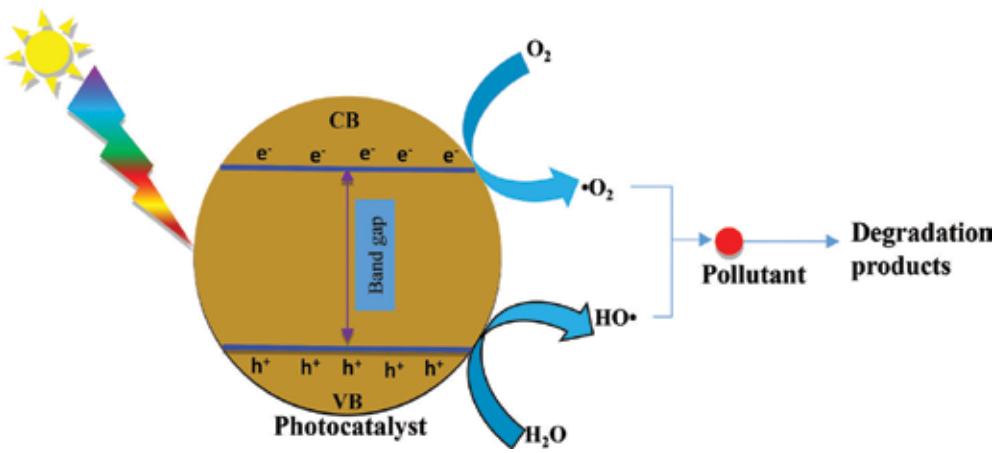

Figure 3. Mechanism of photocatalytic degradation of organic polluting.

2.2.1.2. Degradation of textile dyes

A modified bismuth-based nanocomposite consisting of α-BiO_3, silver (Ag) and graphene oxide (GO) (Ag/GO/α-Bi_2O_3), has been synthesised by [39] and deployed in photodegradation of crystal violet and rhodamine 6G dyes by visible light illumination. The Ag/GO/α-Bi_2O_3 exhibited six times photocatalytic activity compared to Degussa-P25. It degraded both dyes at a higher efficiency than the bare α-BiO_3 and achieved about 90% degradation of the crystal violet and rhodamine 6G dyes in 40 minutes and 150 minutes respectively. Nickel doped Bi_2S_3 has also been applied in the degradation of congo red and rose bengal dyes by visible light illumination with successful results [40]. A nanocomposite consisting of $BiVO_4$, Ag and reduced graphene oxide (rGO) was also synthesised and used to degrade rhodamine B dye [41]. They identified the composite to possess more photocatalytic reaction sites because of enhanced charge carriers separation ability of the $BiVO_4$, electron transfer property of the silver nanoparticles and surface plasmon effect. The composite showed enhanced visible light activity and exhibited higher degradation efficiency of the dye compared to the bare $BiVO_4$ and the $BiVO_4$-rGO composite.

Qu and Huanyan [42] synthesised a $BiOCl_xBr_{1-x}$ photocatalysts consisting of BiOCl, BiOBr, $BiOCl_{0.5}Br_{0.5}$, $BiOCl_{0.75}Br_{0.25}$ and $BiOCl_{0.25}Br_{0.75}$. The photocatalytic degradation abilities of the catalysts were assessed by applying them to degrade methyl orange under ultraviolet light. $BiOCl_{0.5}Br_{0.5}$ was identified to be the best photocatalyst for the degradation of 5 mg/L of the dye at pH 7 with 90% degradation efficiency within 90 min. In addition, BiOI-graphene nanocomposite's photodegradation ability was tested on methyl orange. The BiOI-graphene was found to degrade the dye at a faster rate than BiOI. The enhanced photodegradation efficiency of the BiOI-graphene composite was credited to its ability to effectively separate and transport the generated electrons and holes owing to the bonding between graphene and BiOI, the increase light adsorption and the high dye adsorption [43]. Studies on the photocatalytic degradation ability of Bi_2WO_6-rGO nanocomposite was performed by Rajagopal et al. [44] with impressive results. The improved performance of the catalyst against the degradation of rhodamine B was assigned to the fact that the catalyst possessed a large surface area, as well as the capability to reduce the rate at which the electrons and holes recombined as a result of the inclusion of rGO. Similarly, $Bi_2O_2CO_3/ZnWO_4$ nanocomposite was synthesised and used to degrade methylene blue [45]. Compared to the individual $ZnWO_4$ and $Bi_2O_2CO_3$, the $Bi_2O_2CO_3/ZnWO_4$ demonstrated excellent ability to photocatalytically degrades the dye [45]. This was as a result of the existence of a heterojunction in the composite. The presence of the heterojunction favoured the separation of the holes and electrons [45].

2.2.1.3. Degradation of pharmaceutical products (antibiotics)

The occurrence and accumulation of pharmaceutical products in water bodies can be injurious to humans as well as aquatic organisms. Hence the need for an appropriate technology for the removal of this pollutants becomes paramount. Scientists have been studying photocatalysis as a suitable means to remove these pollutants. As a result, a number of photocatalytic degradation studies using bismuth-based nanoparticles have been carried out. Some of these research works have been discussed here.

In their study, [46] synthesised a Bi_2WO_6/Fe_3O_4 heterojunction through the hydrothermal process and supported it over graphene sand composite by in situ wet impregnation method. The tendency of the composite (Bi_2WO_6/Fe_3O_4/GSC) to photocatalytically degrade pharmaceutical waste was tested by its application in the degradation of oxytetracycline and ampicillin. They obtained a high degradation efficiency of the antibiotics into CO_2, H_2O and NO_3^- under solar light irradiation due to high adsorption property of the composite. The magnetic nature of the catalyst ensured its easy separation and recyclability [46]. Tetracycline degradation with $BiFeO_3$ prepared through hydrothermal method was also undertaken with successful results [47]. BiOBr modified with chelating agents (citric acid and ethylenediaminetetraacetic acid) was reported to have been used in the degradation of norfloxacin with high photocatalytic efficiency [48]. The chelating agents modified BiOBr was noted to be more photoactive and displayed higher degradation efficiency compared to the bare BiOBr. Again, a successfully prepared BiOBr-activated peroxymonosulfate system (BiOBr/PMS) demonstrated exceptional visible-light-responsive activities for photodegradation of Ciprofloxacin [49] and carbamazepine [50] respectively. A mesoporous Bi_2WO_6 prepared by hydrothermal technique was used to degrade tetracycline in water, further endorsing the visible-light-driven photodegradation of pharmaceutical wastes using bismuth-based nanoparticles [51]. About 97% of the pollutant (20 mg/L) was degraded after 120 minutes of simulated solar light irradiation.

2.2.1.4. Water disinfection (removal of bacteria)

The need for cost-effective and non-toxic antibacterial agents for an effective water treatment has become urgent due to the life-threatening consequences of water pollution with various species of bacteria. The use of nanoparticles as disinfection systems for water treatment is gaining recognition due to its effectiveness. Bismuth-based nanoparticles are among the category of nanoparticles that are being tested for water disinfection. Some of the progress that has been made so far with respect to the use of bismuth-based nanoparticle for bacterial inactivation in water is discussed below:

Inactivation of *Escherichia coli* was determined through the use of Z-scheme photocatalyst of $AgI/BiVO_4$ synthesised through chemical deposition precipitation [52]. The catalyst could inactivate 7.0 × 107 CFU/mL of the bacteria species within 50 minutes under visible light. Superoxide radical ($\bullet O_2$) and holes (h^+) were identified to be responsible for the photocatalytic disinfection process. In much the same manner, *Escherichia coli* inactivation under visible light was performed by using $Ag/BiVO_4$ nanocomposite with impressive results [53]. There was a total inactivation of the bacterial cell (107 CFU mL^{-1}) within 120 minutes. They assigned the effectiveness of the composite for the bacterial inactivation to the presence of the metallic silver nanoparticle in the composite. The silver nanoparticle trapped the generated electrons and hence promoted charge carriers separation for the creation of the necessary reactive oxygen species. Zhang et al. [54] reported the application of AgBr−Ag − Bi_2WO_6 nanocomposite in photodisinfection of *Escherichia coli* K-12 by visible light illumination. The AgBr−Ag − Bi_2WO_6 was more effective than the other catalysts i.e. Bi_2WO_6 superstructure, Ag-Bi2WO_6 and AgBr-Ag-TiO_2 used in this experiment. The AgBr−Ag − Bi_2WO_6 nanocomposite was able to completely disinfect 5 x 107 cfu mL^{-1} of the *Escherichia coli* K-12 under 15 minutes through the influence of hydroxyl radicals (•OH).

A Bi_2O_3 and $NiFe_2O_4/Bi_2O_3$ photocatalysts with different concentration of $NiFe_2O_4$ were fabricated and applied in a comparative photocatalytic degradation of tetracycline in water [55]. The $NiFe_2O_4/Bi_2O_3$ was more efficient that Bi_2O_3 in the visible light degradation process with $NiFe_2O_4/Bi_2O_3$ (50%$NiFe_2O_4$) being the most efficient catalyst. This catalyst demonstrated a high degradation efficiency of 90.78 within 90 minutes. The catalyst was easily recovered and recycled due to its magnetic nature [55]. The destruction of bacteria cells (*Escherichia coli* K-12) using Bi_2MoO_6 –rGO was also noted to achieve high efficiency [56]. In all these cases, large surface area for enhanced pollutant adsorption, improved electron-hole reparation and the subsequent generation of sufficient oxygen reactive species were identified to be responsible for the impressive photocatalytic performance of the composites.

2.2.2. Application in waste gas treatment (reduction of carbon dioxide)

The release of carbon dioxide (CO_2) into the atmosphere resulting mainly from fossil fuels combustion is contributing significantly to the global climate change. This phenomenon necessitates the need for appropriate strategies to abate the increasing level of CO_2 in the atmosphere. An appropriate approach to reducing the level of atmospheric CO_2 is its conversion into useful chemicals. Photocatalytic reduction of CO_2 to useful chemicals as a way of recycling it to a fuel feedstock is receiving attention as an appropriate substitute for fossil fuels combustion [57].

The mechanism of CO_2 photoreduction to hydrocarbon fuels is similar to that of organic pollutants degradation. This process also involves illumination of the semiconductor photocatalyst with a photon of appropriate energy resulting in the creation of electron and hole pairs on the conduction and valence bands respectively. The generated electrons must have greater energy than the reduction potential of CO_2 i.e. the conduction band potential of the catalyst should have higher negative value than the reduction potential of CO_2. At the same time, the valence band potential of the catalyst must have higher positive value than water oxidation potential. In other words, the hole must have the potential to oxidise water to produce hydrogen ion (H^+) [58]. The notable thing about this process is that the type of hydrocarbon produced depends on the number of protons present in the reaction system. The possible reactions involved in the reduction/conversion of CO_2 to various hydrocarbon products are presented in Eqs. 1 to 4 [59]:

The presence of two protons (H^+) in the system leads to the conversion of CO_2 to Carbon monoxide (CO) i.e.:

$$CO_2 + 2H^+ + 2e^- \rightarrow CO + H_2O \quad (1)$$

Methanol (CH_3OH) is produced when six protons are available in the reaction system:

$$CO_2 + 6H^+ + 6e^- \rightarrow CH_3OH + H_2O \quad (2)$$

The availability of eight and twelfth protons results in the production of methane and ethanol respectively:

$$CO_2 + 8H^+ + 8e^- \rightarrow CH_4 + H_2O \quad (3)$$

$$2CO_2 + 12\,H^+ + 12\,e^- \rightarrow C_2H_5OH + H_2O \quad (4)$$

In this section, we discuss some of the achievement made so far as the use of bismuth-based nanocomposites in CO_2 photoconversion to useful hydrocarbon products is concerned.

A comparative study on CO_2 photocatalytic conversion using titanium oxide (TiO_2) nanotubes and palladium decorated bismuth titanate was conducted by Raja et al. [60]. The experiment was executed through light illumination of the catalyst in a CO_2 saturated sulphuric acid solution. Formic acid (HCOOH) was the resultant product. According to their result, the palladium decorated bismuth titanate nanocomposite was the better of the two catalysts as it produced about two times formic acid than that produced by the TiO_2 nanotubes composite. They attributed the effectiveness of the palladium decorated bismuth titanate to effective charge carriers' separation. In addition, a $Bi_4O_5Br_xI_{2-x}$, $Bi_4O_5Br_2$ and $Bi_4O_5I_2$ composite solutions which were prepared by the molecular precursor method were applied in CO_2 photocatalytic reduction experiment [61]. The results showed that the $Bi_4O_5Br_xI_{2-x}$ composite exhibited the highest photocatalytic activity with the Bi_4O_5BrI (x = 1) being the best catalyst. This catalyst (Bi_4O_5BrI) was able to convert CO_2 to carbon monoxide (CO) at the rate of 22.85 μmol $h^{-1}g^{-1}$CO generation. High CO_2 adsorption tendency and excellent electron-hole separation were identified to be the reason for the effectiveness of this catalyst for the reduction of CO_2 to CO.

Again, different structures of Bi_2S_3 (nanoparticles and microsphere hierarchical nanostructure) prepared by Chen et al. [62] through facile and template-free solvothermal route were used to convert CO_2. The microsphere composite exhibits a better visible light photocatalytic CO_2 conversion activity than the Bi_2S_3 nanoparticle. The CO_2 was reduced to formate in methanol. Excellent light harvesting ability, profound permeability and the unique hierarchical structure are the factors that accounted for the effectiveness of the Bi_2S_3 microsphere hierarchical nanostructure. Palanichamy et al. [63] also showed the trend in the photocatalytic performance of $BiVO_4$, and Cu_2BiVO_4 in the CO_2 conversion to methanol. The percentage CO_2 conversion efficiencies of the $BiVO_4$ and Cu_2BiVO_4 were 2.78% and 2.50% respectively within 80 minutes under the same conditions.

2.2.3. Application in hydrogen production (reduction of water)

The ever-increasing air pollution as a result of fossil fuels combustion has heightened the need to develop alternative fuel sources. One of the alternative sources is hydrogen gas production through photocatalytic splitting of water [64]. In order to achieve an economically feasible hydrogen generation through photocatalysis, the photocatalyst must be visible light active so as to effectively utilise the limitless and readily available visible light [64]. Bismuth-based nanocomposites are highly active under visible light owing to their narrow band gaps. Consequently, generation of hydrogen gas using bismuth-based nanoparticles/composites with visible light is regarded as one of the promising approaches. The mechanism of this process is discussed as follows [59]:

Similar to the mechanism of photodegradation of organic compounds, electron and hole are produced on the conduction and valence bands of the photocatalyst when it is exposed to light with energy greater than or equal its band gap. Modification of the catalyst enhances its ability to minimise the recombination of the holes and the electrons upon generation.

The holes in the valence band directly oxidise the chemisorbed water molecule on the catalyst's surface resulting in the generation of four hydrogen ions (H^+) and oxygen molecules (O_2):

$$2H_2O \rightarrow 4H^+ + O_2 \quad (5)$$

The conduction band electrons then reduce the hydrogen ions to produce hydrogen gas:

$$4H^+ + 4e^- \rightarrow 2H_2 \quad (6)$$

A number of experimental results on the utilisation of visible light active bismuth-based nanocomposite for production of hydrogen through water splitting have been published. Some of these published results are discussed in this section.

The ability of a bismuth-based catalyst, $Cr_2O_3/Pt/RuO_2{:}Bi_2O_3$, to photocatalytically split water into hydrogen gas was studied in the presence of a sacrificial hole scavenger (oxalic acid) by Hsieh et al. [65]. According to their result, the photocatalyst showed a high ability to generate hydrogen gas from water at a rate of 17.2 μmol g^{-1} h^{-1}. In their experiment, Adhikari et al. [66] carried out the synthesis and characterisation of visible light active bismuth-based photocatalysts (Ta_2O_5/Bi_2O_3, TaON/Bi_2O_3, and Ta_3N_5/Bi_2O_3). They then evaluate their tendency to generate hydrogen from water under visible light using water-methanol solution. The result showed enhanced hydrogen generation potential of the catalysts. The composites showed significant hydrogen production in comparison to the individual component (Ta_2O_5, Bi_2O_3, TaON and Ta_3N_5) as a result of the existence of heterojunction in the composites. The heterojunction enhanced separation of the electrons and holes. In addition, the synthesis, characterisation and the photocatalytic hydrogen gas production tendency of Pt-Bi_2O_3/RuO_2 under visible light was also assessed [67]. The experiment was performed by adding 0.3 M Na_2SO_3 and 0.03 M $H_2C_2O_4$ as sacrificial agents. The presence of Na_2SO_3 and $H_2C_2O_4$ assisted the catalyst to increase hydrogen production at the rates of 11.6 mol g^{-1} h^{-1} (Na_2SO_3) and 14. 5 mol g^{-1} h^{-1} ($H_2C_2O_4$) [67].

2.2.4. Application in air purification

The desire to purify urban or indoor air by removing nitrogen oxide pollutants (NO_X) and volatile organic compounds (VOCs) from it particularly in public places including schools, churches, shopping mall and so on, has become an issue of high necessity. This is due to the health consequences associated with these groups of pollutants which are mostly released into the air through vehicular emissions, building materials, personal care products, office equipment, cleaning agents etc. [68]. Photocatalysis has been identified as an appropriate technology for the removal of these pollutants from the air because of the technique's tendency to completely mineralise these pollutants [68].

The principle behind the photocatalytic degradation of the NO_X and VOCs in the air is similar to that described in the previous sections: The holes generated after excitation of electrons from the valence band to the conduction band due to illumination of the catalyst oxidise water molecules in the air to for •OH. The •OH then attach the organic pollutants in air and mineralise them through the destruction of their molecular bonds.

Bismuth-based photocatalysts are among the catalysts that have been tested for effective air purification experiments. Some results of these experiments are discussed here:

The successful application of Bi nanoparticles modified TiO_2 (Degussa P25) with mixed anatase and rutile phase in the photocatalytic removal of NO from the air at ppb level was undertaken by Zhao et al. [69]. The Bi-TiO_2 was noted to outperform the pure TiO_2 in the NO photocatalytic removal process. Among the catalysts used, Bi-TiO_2 with Bi nanoparticles diameters ranging from 5 to 8 demonstrated excellent photocatalytic activity as this diameter range acted as an excellent visible light active site with improved charge separation [69]. The improved performance of this catalyst was assigned to the movement of the electrons, which were generated through plasmonic activation of the Bi nanoparticles, between the conduction band of the anatase and rutile phases of TiO_2; thus reducing their rate of recombination with the holes. In their experiment, Ai et al. [70] compared the ability of a hierarchial BiOBr microsphere, BiOBr bulk, Degussa TiO_2 and C doped TiO_2 to photocatalytically remove NO from indoor air (400 ppb level). According to their result, the BiOBr microsphere performed extremely well compared to the other catalysts as a result of its unique hierarchical structure which enhanced the diffusion of intermediates and NO oxidation final product leading to the efficient removal of the NO. NO removal from air at ppb levels through visible light photocatalysis has also been studied by [71, 72] using N-$Bi_2O_2CO_3$-graphene quantum dot and Br-BiOCOOH respectively with excellent results.

Photocatalytic decomposition experiment was also performed to remove toluene from air. The experiment was conducted comparatively using V_2O_5/$BiVO_4$/TiO_2, V_2O_5/$BiVO_4$ and TiO_2 photocatalysts through illumination with visible light. The V_2O_5/$BiVO_4$/TiO_2 was identified to be the best catalyst for the decomposition of toluene due to enhanced charge carriers separation across the multiple interfaces of the ternary nanojunctions [73]. Similarly, toluene removal from air through photocatalysis using BiOI/TiO_2, pure TiO_2 and Degussa P25 was carried out by Boonprakob et al. [74]. They observed that the highest toluene photodecomposition activity (*ca*. 68%) was exhibited by BiOI/TiO_2 as a result of its excellent visible light activity and efficient charge carriers separation. In their study, Xu et al. [75] synthesised Bi_2O_3/TiO_2 nanocomposite and tested its ability to photocatalytically decompose 4-chlorophenol in air. They noted that the Bi_2O_3/TiO_2 catalyst effectively removed the pollutant from air compared to the pure TiO_2 and Degussa P25 owing to the narrow band gap of α- Bi_2O_3 which improved on the visible light activity of the composite.

3. Conclusion

The necessity to develop more efficient photocatalysts for effective water treatment, carbon dioxide conversion, hydrogen reduction and air purification so as to alleviate the increasing energy crisis, air pollution, and to make clean and potable water readily available cannot be overemphasised. The use of bismuth-based nanoparticles/nanocomposite in this regard has been organised in this chapter. The chapter also provided recently generated information on the use of bismuth-based nanoparticles in various photocatalytic degradation processes. A detailed discussion was provided on bismuth as an element/metal, and bismuth-based

nanoparticles including bismuth chalcogenides, bismuth vanadate, bismuth oxyhalides and other bismuth-related nanoparticles. Attention was also paid to the modification of these nanoparticles to improve their photocatalytic activities. The application of the modified nanoparticles in various photocatalytic processes with emphasis on water treatment, waste gas treatment, hydrogen production and air purification has also been thoroughly discussed.

Author details

William W. Anku*, Samuel O.B. Oppong and Penny P. Govender

*Address all correspondence to: williamanku85@gmail.com

Department of Applied Chemistry, University of Johannesburg, South Africa

References

[1] Oller I, Malato S, Sánchez-Pérez J. Combination of advanced oxidation processes and biological treatments for wastewater decontamination—A review. Science of the Total Environment. 2011;**409**(20):4141-4166. DOI: 10.1016/j.scitotenv.2010.08.061

[2] Asiagwu A. Sorption model for the removal of m-anisidine dye from aqueous solution using beaker's yeast (*Saccharomuces cerevisiae*). International Journal of Research and Reviews in Applied Sciences. 2012;**13**:617-625

[3] Anjaneyulu Y, Chary NS, Raj DSS. Decolourization of industrial effluents–available methods and emerging technologies–a review. Reviews in Environmental Science and Bio/Technology. 2005;**4**(4):245-273. DOI: 10.1007/s11157-005-1246-z

[4] Beach ES, Malecky RT, Gil RR, Horwitz CP, Collins TJ. Fe-TAML/hydrogen peroxide degradation of concentrated solutions of the commercial azo dye tartrazine. Catalysis Science & Technology. 2011;**1**(3):437-443

[5] Hoffmann MR, Martin ST, Choi W, Bahnemann DW. Environmental applications of semiconductor photocatalysis. Chemical Reviews. 1995;**95**(1):69-96. DOI: 10.1021/cr00033a004

[6] Linsebigler AL, Lu G, Yates JT Jr. Photocatalysis on TiO_2 surfaces: Principles, mechanisms, and selected results. Chemical Reviews. 1995;**95**(3):735-758

[7] Choy J-H, Lee H-C, Jung H, Hwang S-J. A novel synthetic route to TiO_2-pillared layered titanate with enhanced photocatalytic activityElectronic supplementary information (ESI) available: XRD patterns and crystallographic data for pristine layered caesium titanate and its proton exchanged form, and XRD pattern of the anatase TiO_2 nano-sol used as pillaring agent. Journal of Materials Chemistry. 2001;**11**(9):2232-2234. DOI: 10.1039/B104551M

[8] Yoo D-H, Cuong TV, Pham VH, Chung JS, Khoa NT, Kim EJ, Hahn SH. Enhanced photocatalytic activity of graphene oxide decorated on TiO_2 films under UV and visible irradiation. Current Applied Physics. 2011;**11**(3):805-808. DOI: 10.1016/j.cap.2010.11.077

[9] Wu Y-C, Chaing Y-C, Huang C-Y, Wang S-F, Yang H-Y. Morphology-controllable Bi_2O_3 crystals through an aqueous precipitation method and their photocatalytic performance. Dyes and Pigments. 2013;**98**(1):25-30. DOI: 10.1016/j.dyepig.2013.02.006

[10] Wang Z, Luo W, Yan S, Feng J, Zhao Z, Zhu Y, Li Z, Zou Z. $BiVO_4$ nano–leaves: Mild synthesis and improved photocatalytic activity for O_2 production under visible light irradiation. CrystEngComm. 2011;**13**(7):2500-2504. DOI: 10.1039/C0CE00799D

[11] Khaghani S, Ghanbari D, Khaghani S. Green synthesis of iron oxide-palladium nanocomposites by pepper extract and its application in removing of Colored pollutants from water. Journal of Nanostructures. 2017;**7**(3):175-182

[12] Jones H. The theory of the galvomagnetic effects in bismuth. Proceedings of the Royal Society of London. Series A: Mathematical and Physical Sciences. 1936;**155**(886):653-663. DOI: 10.1098/rspa.1936.0126

[13] Pistofidis N, Vourlias G, Konidaris S, Pavlidou E, Stergiou A, Stergioudis G. The effect of bismuth on the structure of zinc hot-dip galvanized coatings. Materials Letters. 2007;**61**(4):994-997. DOI: 10.1016/j.matlet.2006.06.029

[14] Kargin YF, Ivicheva S, Buslaeva EY, Kuvshinova T, Volodin V, Yurkov GY. Preparation of bismuth nanoparticles in opal matrices through reduction of bismuth compounds with supercritical isopropanol. Inorganic Materials. 2006;**42**(5):487-490. DOI: 10.1134/S002016850

[15] Liu G, Li S, Lu Y, Zhang J, Feng Z, Li C. Controllable synthesis of α-Bi_2O_3 and γ-Bi_2O_3 with high photocatalytic activity by α-Bi_2O_3→γ-Bi_2O_3→ α-Bi_2O_3 transformation in a facile precipitation method. Journal of Alloys and Compounds. 2016;**689**:787-799. DOI: 10.1016/j.jallcom.2016.08.047

[16] Valant M, Suvorov D. Dielectric characteristics of bismuth oxide solid solutions with a fluorite-like crystal structure. Journal of the American Ceramic Society. 2004;**87**(6):1056-1061. DOI: 10.1111/j.1551-2916.2004.01056.x

[17] Yousefia M, Salavati-Niasarib M, Gholamiand F, Ghanbarie D, Aminifazl A. Polymeric nanocomposite materials: Synthesis and thermal degradation of acrylonitrile–butadiene–styrene/tin sulfide (ABS/SnS). Inorganica Chimica Acta. 2011;**371**:1-5

[18] Shi L, Gu D, Li W, Han L, Wei H, Tu B, Che R. Synthesis of monodispersed ultrafine Bi_2S_3 nanocrystals. Journal of Alloys and Compounds. 2011;**509**(38):9382-9386. DOI: 10.1016/j.jallcom.2011.07.049

[19] Sun Y, Cheng H, Gao S, Liu Q, Sun Z, Xiao C, Wu C, Wei S, Xie Y. Atomically thick bismuth selenide freestanding single layers achieving enhanced thermoelectric energy harvesting. Journal of the American Chemical Society. 2012;**134**(50):20294-20297. DOI: 10.1021/ja3102049

[20] Taskin A, Sasaki S, Segawa K, Ando Y. Manifestation of topological protection in transport properties of epitaxial Bi_2Se_3 thin films. Physical Review Letters. 2012;**109**(6):066803. DOI: 10.1103/PhysRevLett.109.066803

[21] Teweldebrhan D, Goyal V, Balandin AA. Exfoliation and characterization of bismuth telluride atomic quintuples and quasi-two-dimensional crystals. Nano Letters. 2010;**10**(4):1209-1218. DOI: 10.1021/nl903590b

[22] Goldsmid HJ. The electrical conductivity and thermoelectric power of bismuth telluride. Proceedings of the Physical Society. 1958;**71**(4):633. DOI: 10.1088/0370-1328/71/4/312

[23] Yamashita O, Tomiyoshi S, Makita K. Bismuth telluride compounds with high thermoelectric figures of merit. Journal of Applied Physics. 2003;**93**(1):368-374. DOI: 10.1063/1.1525400

[24] Liu Z, Yan F. The application of bismuth-based oxides in organic-inorganic hybrid photovoltaic devices. Journal of the American Ceramic Society. 2012;**95**(6):1944-1948. DOI: 10.1111/j.1551-2916.2012.05088.x

[25] Peng H, Chan CK, Meister S, Zhang XF, Cui Y. Shape evolution of layer-structured bismuth oxychloride nanostructures via low-temperature chemical vapor transport. Chemistry of Materials. 2008;**21**(2):247-252. DOI: 10.1021/cm802041g

[26] Zhang J, Shi F, Lin J, Chen D, Gao J, Huang Z, Ding X, Tang C. Self-assembled 3-D architectures of BiOBr as a visible light-driven photocatalyst. Chemistry of Materials. 2008;**20**(9):2937-2941. DOI: 10.1021/cm7031898

[27] Zhang K-L, Liu C-M, Huang F-Q, Zheng C, Wang W-D. Study of the electronic structure and photocatalytic activity of the BiOCl photocatalyst. Applied Catalysis B: Environmental. 2006;**68**(3):125-129. DOI: 10.1016/j.apcatb.2006.08.002

[28] Liu Q-C, Ma D-K, Hu Y-Y, Zeng Y-W, Huang S-M. Various bismuth oxyiodide hierarchical architectures: Alcohothermal-controlled synthesis, photocatalytic activities, and adsorption capabilities for phosphate in water. ACS Applied Materials & Interfaces. 2013;**5**(22):11927-11934. DOI: 10.1021/am4036702

[29] Duo F, Wang Y, Mao X, Zhang X, Wang Y, Fan C. A $BiPO_4$/BiOCl heterojunction photocatalyst with enhanced electron-hole separation and excellent photocatalytic performance. Applied Surface Science. 2015;**340**:35-42. DOI: 10.1016/j.apsusc.2015.02.175

[30] Zhu Y, Liu Y, Lv Y, Ling Q, Liu D, Zhu Y. Enhancement of photocatalytic activity for $BiPO_4$ via phase junction. Journal of Materials Chemistry A. 2014;**2**(32):13041-13048. DOI: 10.1039/C4TA01807A

[31] Ling CD, Johnson M. Modelling, refinement and analysis of the "type III" δ-Bi_2O_3-related superstructure in the Bi_2O_3–Nb_2O_5 system. Journal of Solid State Chemistry. 2004;**177**(6):1838-1846

[32] Sayama K, Nomura A, Arai T, Sugita T, Abe R, Yanagida M, Oi T, Iwasaki Y, Abe Y, Sugihara H. Photoelectrochemical decomposition of water into H_2 and O_2 on porous

$BiVO_4$ thin-film electrodes under visible light and significant effect of Ag ion treatment. The Journal of Physical Chemistry B. 2006;**110**(23):11352-11360. DOI: 10.1021/jp057539+

[33] Xu L, Wei Y, Guo W, Guo Y, Guo Y. One-pot solvothermal preparation and enhanced photocatalytic activity of metallic silver and graphene co-doped $BiVO_4$ ternary systems. Applied Surface Science. 2015;**332**:682-693. DOI: 10.1016/j.apsusc.2015.01.235

[34] Zhang L, Tan G, Wei S, Ren H, Xia A, Luo Y. Microwave hydrothermal synthesis and photocatalytic properties of TiO_2/$BiVO_4$ composite photocatalysts. Ceramics International. 2013;**39**(8):8597-8604. DOI: 10.1016/j.ceramint.2013.03.106

[35] Mahmoud WE, Al-Ghamdi A. Synthesis and properties of bismuth oxide nanoshell coated polyaniline nanoparticles for promising photovoltaic properties. Polymers for Advanced Technologies. 2011;**22**(6):877-881. DOI: 10.1002/pat.1591

[36] Raza W, Bahnemann D, Muneer M. A green approach for degradation of organic pollutants using rare earth metal doped bismuth oxide. Catalysis Today. 2018;**300**:89-98. DOI: 10.1016/j.cattod.2017.07.029

[37] Cho M, Chung H, Choi W, Yoon J. Linear correlation between inactivation of *E. coli* and OH radical concentration in TiO_2 photocatalytic disinfection. Water Research. 2004;**38**(4):1069-1077. DOI: 10.1016/j.watres.2003.10.029

[38] Dalrymple OK, Stefanakos E, Trotz MA, Goswami DY. A review of the mechanisms and modeling of photocatalytic disinfection. Applied Catalysis B: Environmental. 2010;**98**(1):27-38. DOI: 10.1016/j.apcatb.2010.05.001

[39] Som T, Troppenz GV, Wendt R, Wollgarten M, Rappich J, Emmerling F, Rademann K. Graphene oxide/α-Bi_2O_3 composites for visible-light photocatalysis, chemical catalysis, and solar energy conversion. ChemSusChem. 2014;**7**(3):854-865. DOI: 10.1002/cssc.201300990

[40] Kulsi C, Ghosh A, Mondal A, Kargupta K, Ganguly S, Banerjee D. Enhanced photo catalytic performance of nickel doped bismuth selenide under visible light irradiation. Materials Research Express. 2017;**4**(3):035902. DOI: 10.1088/2053-1591/aa61ad

[41] Du M, Xiong S, Wu T, Zhao D, Zhang Q, Fan Z, Zeng Y, Ji F, He Q, Xu X. Preparation of a microspherical silver-reduced graphene oxide-bismuth vanadate composite and evaluation of its photocatalytic activity. Materials. 2016;**9**(3):160. DOI: 10.3390/ma9030160

[42] Qu T, Huanyan X. Photocatalytic degradation of methyl orange over BiOClxBr1-x (0≤x≤1) solid solutions. International Conference on Mechatronics, Electronic, Industrial and Control Engineering (MEIC); 2014

[43] Liu H, Cao W-R, Su Y, Chen Z, Wang Y. Bismuth oxyiodide–graphene nanocomposites with high visible light photocatalytic activity. Journal of Colloid and Interface Science. 2013;**398**:161-167. DOI: 10.1016/j.jcis.2013.02.007

[44] Rajagopal R, Krishnan R, Ramasubbu A, Kamaludeen BA, editors. Synthesis of Bi_2WO_6-RGO Nanocomposite for Photocatalytic Application. Smart Sensors and Systems (IC-SSS), International Conference on. IEEE; 2015

[45] Tian N, Huang H, Zhang Y, He Y. Enhanced photocatalytic activities on $Bi_2O_2CO_3$/$ZnWO_4$ nanocomposites. Journal of Materials Research. 2014;**29**(5):641-648. DOI: 10.1557/jmr.2014.29

[46] Raizada P, Kumari J, Shandilya P, Dhiman R, Singh VP, Singh P. Magnetically retrievable Bi_2WO_6/Fe_3O_4 immobilized on graphene sand composite for investigation of photocatalytic mineralization of oxytetracycline and ampicillin. Process Safety and Environment Protection. 2017;**106**:104-116. DOI: 10.1016/j.psep.2016.12.012

[47] Xue Z, Wang T, Chen B, Malkoske T, Yu S, Tang Y. Degradation of tetracycline with $BiFeO_3$ prepared by a simple hydrothermal method. Materials. 2015;**8**(9):6360-6378. DOI: 10.3390/ma8095310

[48] Yan DY-S, Lam FL. Development of a novel photocatalyst for the advanced antibiotic oxidation of wastewater. SpringerPlus. 2015;**4**(S2):O7. DOI: 10.1186/2193-1801-4-S2-O7

[49] Zhang X, Li R, Jia M, Wang S, Huang Y, Chen C. Degradation of ciprofloxacin in aqueous bismuth oxybromide (BiOBr) suspensions under visible light irradiation: A direct hole oxidation pathway. Chemical Engineering Journal. 2015;**274**:290-297. DOI: 10.1016/j.cej.2015.03.077

[50] Zhang T, Chu S, Li J, Wang L, Chen R, Shao Y, Liu X, Ye M. Efficient degradation of aqueous carbamazepine by bismuth Oxybromide-activated peroxide oxidation. Catalysts. 2017;**7**(11):315. DOI: 10.3390/catal7110315

[51] Chu X, Shan G, Chang C, Fu Y, Yue L, Zhu L. Effective degradation of tetracycline by mesoporous Bi_2WO_6 under visible light irradiation. Frontiers of Environmental Science & Engineering. 2016;**10**(2):211-218. DOI: 10.1007/s11783-014-0753-y

[52] Guan D-L, Niu C-G, Wen X-J, Guo H, Deng C-H, Zeng G-M. Enhanced Escherichia coli inactivation and oxytetracycline hydrochloride degradation by a Z-scheme silver iodide decorated bismuth vanadate nanocomposite under visible light irradiation. Journal of Colloid and Interface Science. 2018;**512**:272-281. DOI: 10.1016/j.jcis.2017.10.068

[53] Booshehri AY, Goh SC-K, Hong J, Jiang R, Xu R. Effect of depositing silver nanoparticles on BiVO 4 in enhancing visible light photocatalytic inactivation of bacteria in water. Journal of Materials Chemistry A. 2014;**2**(17):6209-6217. DOI: 10.1039/C3TA15392D

[54] Zhang L-S, Wong K-H, Yip H-Y, Hu C, Yu JC, Chan C-Y, Wong P-K. Effective photocatalytic disinfection of *E. coli* K-12 using AgBr-Ag-Bi_2WO_6 nanojunction system irradiated by visible light: The role of diffusing hydroxyl radicals. Environmental Science & Technology. 2010;**44**(4):1392-1398. DOI: 10.1021/es903087w

[55] Ren A, Liu C, Hong Y, Shi W, Lin S, Li P. Enhanced visible-light-driven photocatalytic activity for antibiotic degradation using magnetic $NiFe_2O_4$/Bi_2O_3 heterostructures. Chemical Engineering Journal. 2014;**258**:301-308. DOI: 10.1016/j.cej.2014.07.071

[56] Zhang Y, Zhu Y, Yu J, Yang D, Ng TW, Wong PK, Jimmy CY. Enhanced photocatalytic water disinfection properties of Bi_2MoO_6–RGO nanocomposites under visible light irradiation. Nanoscale. 2013;**5**(14):6307-6310. DOI: 10.1039/C3NR01338C

[57] Neațu Ș, Maciá-Agulló JA, Garcia H. Solar light photocatalytic CO_2 reduction: General considerations and selected bench-mark photocatalysts. International Journal of Molecular Sciences. 2014;**15**(4):5246-5262. DOI: 10.3390/ijms15045246

[58] Wang W-N, Soulis J, Yang YJ, Biswas P. Comparison of CO_2 photoreduction systems: A review. Aerosol and Air Quality Research. 2014;**14**(2):533-549. DOI: 10.4209/aaqr.2013.09.0283

[59] Kanhere P, Chen Z. A review on visible light active perovskite-based photocatalysts. Molecules. 2014;**19**(12):19995-20022. DOI: 10.3390/molecules191219995

[60] Raja K, Smith Y, Kondamudi N, Manivannan A, Misra M, Subramanian VR. CO_2 photoreduction in the liquid phase over Pd-supported on TiO_2 nanotube and bismuth titanate photocatalysts. Electrochemical and Solid-State Letters. 2011;**14**(5):F5-F8. DOI: 10.1149/1.3543567

[61] Bai Y, Ye L, Chen T, Wang P, Wang L, Shi X, Wong PK. Synthesis of hierarchical bismuth-rich Bi_4O_5Brx I2-x solid solutions for enhanced photocatalytic activities of CO 2 conversion and Cr (VI) reduction under visible light. Applied Catalysis B: Environmental. 2017;**203**:633-640. DOI: 10.1016/j.apcatb.2016.10.066

[62] Chen J, Qin S, Song G, Xiang T, Xin F, Yin X. Shape-controlled solvothermal synthesis of Bi_2S_3 for photocatalytic reduction of CO_2 to methyl formate in methanol. Dalton Transactions. 2013;**42**(42):15133-15138. DOI: 10.1039/C3DT51887F

[63] Palanichamy V, Frites M, Khan S. Conversion of CO_2 to methanol in aqueous medium on visible light active $BiVO_4$, Cu_2BiVO_6 photocatalysts and in CM-n-TiO_2-cu PEC by simultaneous electron and proton transfer reactions. Energy Production and Management in the 21st Century II: The Quest for Sustainable Energy. 2016;**205**:213. DOI: 10.2495/EQ160201

[64] Balat M. Potential importance of hydrogen as a future solution to environmental and transportation problems. International Journal of Hydrogen Energy. 2008;**33**(15):4013-4029. DOI: 10.1016/j.ijhydene.2008.05.047

[65] Hsieh S, Lee G, Davies S, Masten S, Wu J. Synthesis of Cr_2O_3 and Pt doped RuO_2/Bi_2O_3 photocatalysts for hydrogen production from water splitting. American Journal of Environmental Engineering. 2013;**3**(3):115-120. DOI: 10.5923/j.ajee.20130303.01

[66] Adhikari SP, Hood ZD, More KL, Ivanov I, Zhang L, Gross M, Lachgar A. Visible light assisted photocatalytic hydrogen generation by Ta_2O_5/Bi_2O_3, TaON/Bi_2O_3, and Ta_3N_5/Bi_2O_3 composites. RSC Advances. 2015;**5**(68):54998-55005. DOI: 10.1039/C5RA06563A

[67] Hsieh S, Lee G, Chen C, Chen J, Ma S, Horng T, Chen K, Wu J. Synthesis of Pt doped Bi_2O_3/RuO_2 photocatalysts for hydrogen production from water splitting using visible light. Journal of Nanoscience and Nanotechnology. 2012;**12**(7):5930-5936. DOI: 10.1166/jnn.2012.6396

[68] Sharmin R, Ray MB. Application of ultraviolet light-emitting diode photocatalysis to remove volatile organic compounds from indoor air. Journal of the Air & Waste Management Association. 2012;**62**(9):1032-1039. DOI: 10.1080/10962247.2012.695760

[69] Zhao Z, Zhang W, Lv X, Sun Y, Dong F, Zhang Y. Noble metal-free bi nanoparticles supported on TiO 2 with plasmon-enhanced visible light photocatalytic air purification. Environmental Science: Nano. 2016;**3**(6):1306-1317. DOI: 10.1039/C6EN00341A

[70] Ai Z, Ho W, Lee S, Zhang L. Efficient photocatalytic removal of NO in indoor air with hierarchical bismuth oxybromide nanoplate microspheres under visible light. Environmental Science & Technology. 2009;**43**(11):4143-4150. DOI: 10.1021/es9004366

[71] Liu Y, Yu S, Zhao Z, Dong F, Dong X a, Zhou Y. N-doped $Bi_2O_2CO_3$/graphene quantum dot composite photocatalyst: Enhanced visible-light photocatalytic NO oxidation and in situ DRIFTS studies. The Journal of Physical Chemistry C. 2017. DOI: 10.1021/acs.jpcc.7b02285

[72] Feng X, Cui W, Zhong J, Liu X, Dong F, Zhang Y. Enhanced visible light photocatalytic activity of Br-doped bismuth oxide formate nanosheets. Molecules. 2015;**20**(10):19189-19202

[73] Sun J, Li X, Zhao Q, Ke J, Zhang D. Novel V_2O_5/$BiVO_4$/TiO_2 nanocomposites with high visible-light-induced photocatalytic activity for the degradation of toluene. The Journal of Physical Chemistry C. 2014;**118**(19):10113-10121. DOI: 10.1021/jp5013076

[74] Boonprakob N, Chomkitichai W, Ketwaraporn J, Wanaek A, Inceesungvorn B, Phanichphant S. Photocatalytic degradation of phenol over highly visible-light active BiOI/TiO_2 nanocomposite photocatalyst. Engineering Journal. 2017;**21**(1):81-91. DOI: 10.4186/ej.2017.21.1.81

[75] Xu J-J, Chen M-D, Fu D-G. Preparation of bismuth oxide/titania composite particles and their photocatalytic activity to degradation of 4-chlorophenol. Transactions of Nonferrous Metals Society of China. 2011;**21**(2):340-345. DOI: 10.1016/S1003-6326(11)60719-X

Chapter 3

Recent Advances in $BiVO_4$- and Bi_2Te_3-Based Materials for High Efficiency-Energy Applications

Phuoc Huu Le, Nguyen Trung Kien and
Chien Nguyen Van

Additional information is available at the end of the chapter

http://dx.doi.org/10.5772/intechopen.75613

Abstract

This chapter provides recent progress in developments of $BiVO_4$- and Bi_2Te_3-based materials for high efficiency photoelectrodes and thermoelectric applications. The self-assembling nanostructured $BiVO_4$-based materials and their heterostructures (e.g., WO_3/$BiVO_4$) are developed and studied toward high efficiency photoelectrochemical (PEC) water splitting via engineering the crystal and band structures and charge transfer processes across the heteroconjunctions. In addition, crystal and electronic structures, optical properties, and strategies to enhance photoelectrochemical properties of $BiVO_4$ are presented. The nanocrystalline, nanostructured Bi_2Te_3-based thin films with controlled structure, and morphology for enhanced thermoelectric properties are also reported and discussed in details. We demonstrate that $BiVO_4$-based materials and Bi_2Te_3-based thin films play significant roles for the developing renewable energy.

Keywords: $BiVO_4$, bismuth telluride (Bi_2Te_3), photoelectrochemical (PEC) water splitting, thermoelectrics, pulsed laser deposition

1. Bismuth vanadate ($BiVO_4$) material: a highly promising photoanode for use in solar water oxidation

The photoelectrochemical (PEC) water splitting, which uses semiconductors to directly harvest and convert the abundant solar energy into storable and friendly environmental energy in the form of hydrogen and oxygen from water, has been regarded as a promising approach to solve our current energy challenges [1–6]. The PEC cell for energy conversion on a global scale requires the development of devices that are highly efficient, stable, and simple in design. The effective

and economic energy transfer technologies are still under developing stage for more than 40 years. The PEC water splitting becomes more competitive as the cost continues to decrease with the development of nanotechnology, which offers the use of new nano-heterostructure photocatalysts. The current direction along this research field focuses on the development of high efficiency photoelectrodes based on metal oxides due to their high chemical and photostability, low cost, and ease of fabrication. Among these interesting and important photoelectrode materials for PEC, $BiVO_4$ is demonstrated as a promising photocatalyst for PEC water splitting. Originally, the $BiVO_4$ was intensively studied as a ferroelasticity, acoustic-optical, and ionic conductivity materials [7]; however, recently most studies focus on its photocatalytic activity owing to its direct bandgap of ~2.5 eV together with the desirable band edges and good stability [8–11]. Additionally, the theoretical solar-to-hydrogen conversion efficiency of the monoclinic $BiVO_4$ could reach 9.2% with a maximum photocurrent of 7.5 mA cm^{-2} under standard AM 1.5 solar light irradiation, which is significantly higher than those of the common metal oxides, and thus the monoclinic $BiVO_4$ has been recognized as one of the most promising photoanode materials for PEC water splitting [1]. However, its photoactivity performance is limited by its poor electrical conductivity, slow hole transfer kinetics for water oxidation, and poor charge separation [12]. A concise overview of $BiVO_4$ electronic and optical properties as well as the alternative strategies to improve its photocatalytic activities is discussed in this section.

2. Crystal and electronic structures of bismuth vanadate

The synthesis $BiVO_4$ crystallizes in three main crystal structures of tetragonal scheelite, monoclinic phase, and tetragonal zircon structure. The photocatalytic activities of $BiVO_4$ strongly depend on the optical properties of each crystal structure. Among these structures, the monoclinic scheelite $BiVO_4$ was demonstrated to exhibit the highest photocatalytic water oxidation under visible light illumination [13]. The higher photocatalytic activity of the monoclinic scheelite was attributed to its smaller energy band gap and higher crystal distortion, which enhance the optical absorption and the electron-hole separation [14]. The conduction-band minimum of $BiVO_4$ is formed mainly by V 3d, which splits into triplet bands V 3d $x^2–y^2/z^2$, V 3d z^2/zx, and V 3d zy/xy [15]. The valence band (VB) of tetragonal zircon structure $BiVO_4$ is formed by O 2p orbital, but the top region of VB of monoclinic structure is formed by both Bi 6 s and O 2p orbitals. It was demonstrated that Bi 6 s is located above O 2p and the smaller bandgap of monoclinic $BiVO_4$ attributes to the transition from the 6 s electrons of Bi to the 3d orbital of V [14, 16]. Recently, Zou et al. demonstrated that the crystal distortion in monoclinic $BiVO_4$ improves the lone-pair impact of Bi 6 s states which raises up the O 2p states and reduces the bandgap [17]. In addition, the monoclinic scheelite structure possesses the better electron-hole separation owing to its higher degree of structural distortion than that in the tetragonal scheelite structure to result in enhanced photocatalytic activity for the monoclinic structure. In addition, the conduction-band edge of $BiVO_4$ is only slightly below the H+/H2 redox potential, while its valence band is much below the oxidation potential of water resulting in low required external bias [15].

In order to investigate the experimental crystal and electronic structure of monoclinic $BiVO_4$, the single crystal $BiVO_4$, which possesses good crystallinity and eliminates the structural and electronic defects as well as impurity phases, is required. The vacuum deposition such as

sputtering, molecular beam epitaxy, and pulsed laser deposition for the single crystal monoclinic $BiVO_4$ has been developed recently [18–20]. A good lattice match (mismatch less than 1%) of cubic yttrium-stabilized zirconia (YSZ, a = 5.145 Å) was used as substrate for epitaxial growth of high-quality epitaxial monoclinic $BiVO_4$ (a = 5.1935 Å, b = 5.0898 Å, c = 11.6972, γ = 90.3871) films. The X-ray diffraction θ–2θ scan (**Figure 1a**) shows only high intensity and sharp (00 l) reflections of monoclinic $BiVO_4$ phase indicating that growth was *c*-axis oriented: $BiVO_4$ (001) || YSZ (001). The high-resolution TEM image (the inset of **Figure 1**) reveals the

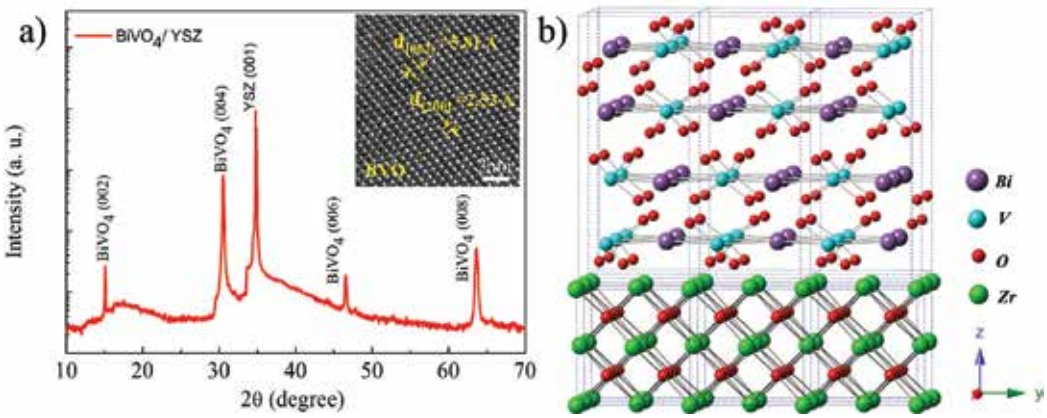

Figure 1. (a) XRD 2θ/θ scans of $BiVO_4$ film grown on YSZ substrate, and the inset shows HR-TEM image of $BiVO_4$; (b) atomic model of $BiVO_4$/ YSZ heteroconjunction.

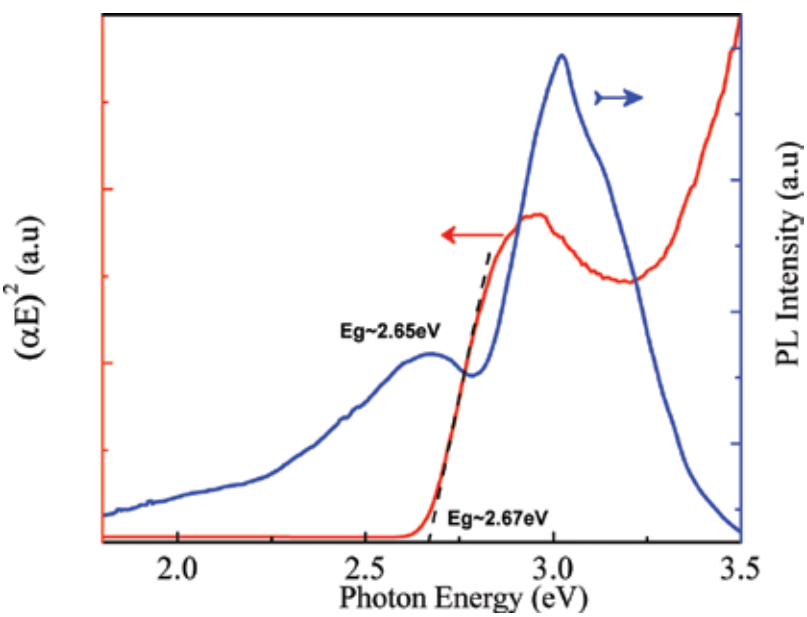

Figure 2. Photoluminescence taken under the irradiation of 325 nm laser at room temperature (green curve) and UV-Vis absorption spectrum (red curve) of $BiVO_4$ epitaxial film.

in-plane and out-of-plane lattice parameters of the $BiVO_4$ with d_{200} = 2.53 Å and d_{002} = 5.81 Å which are in good agreement with the lattice constants of the bulk monoclinic $BiVO_4$. The orientation and growth direction of $BiVO_4$ crystal were identified and constructed in the corresponding atomic model as shown in **Figure 1b**.

The electronic structural properties of single crystal $BiVO_4$ were investigated by the photoluminescence (PL) spectroscopy and UV-Visible spectroscopy. **Figure 2** presents the PL and UV-Vis absorption spectra of a single crystal $BiVO_4$ film. As presented in the UV-Vis absorption spectrum, the observed absorption in the range of 440–480 nm corresponding to the bandgap of ~ 2.67 eV could attribute to the transition from the 6 s electrons of Bi (or the hybrid orbital of Bi 6 s and O 2p) to the empty 3d x^2-y^2/z^2 orbital of V, which is consistent with emission peak of 2.65 eV in the PL spectrum. The second absorption band edge of approximately 3.15 eV and the second PL emission peak at 3.1 eV could be ascribed to the electron transition from O 2p valence band to V 3d z^2/zx and/ or V 3d zy/xy orbitals.

3. Strategies to enhance photoelectrochemical properties of $BiVO_4$

The development of suitable techniques to fabricate high efficiency $BiVO_4$ photoelectrode for PEC water spitting is crucial. To date, there are many methods, which have been developed to prepare $BiVO_4$ photoelectrodes for use in solar water oxidation. The representative synthesis methods are (1) metal organic decomposition (MOD) combining with the spin coating or spray pyrolysis deposition [21–23], (2) electrophoretic deposition (EPD) and chemical bath deposition (CBD) [24–27], and (3) vacuum deposition methods such as sputtering deposition and pulsed laser deposition (PLD) [18–20, 28–29]. The MOD is a facile method to synthesize $BiVO_4$ materials for photoelectrodes. The main advantages of the MOD method are the easy composition tuning and morphology engineering. However, the existence of crystal and surface defect and low adhesion between $BiVO_4$ and conducting substrate could limit its performance. The EPD and CBD methods are simple, have low cost, and are easy to scale up. The vacuum deposition is a powerful method to synthesize good crystalline $BiVO_4$ photoelectrodes. The samples prepared by this method could easily control the doped composition; could facilely tune the crystalline in form of amorphous, polycrystalline, and single crystalline; and possess a good adhesion.

As described above, $BiVO_4$ has many advantages features, however, the actual PEC performance of undoped $BiVO_4$ is still far below its theoretical value, indicating that its advantages have not been fully developed. Many research groups have improved photoelectrochemical water oxidation by the introduction of (1) controlled morphologies, (2) forming nanocomposite structure, (3) doping, and (4) decorating with cocatalysts [30]. A summary of advantages and alternative strategies to enhance photoelectrochemical properties of $BiVO_4$ was depicted in **Figure 3**. The best PEC performance of $BiVO_4$ photoelectrodes that has been demonstrated to date is a combination of several above strategies to take advantages of high surface area, high electron mobility, high water oxidation kinetics, and low charge carrier recombination. Therefore, understanding the benefits and disadvantages of each strategy could provide an effective way to enhance the PEC properties.

http://dx.doi.org/10.5772/intechopen.75613

First, the morphologies of $BiVO_4$ photoelectrode such as shape, size, and particle contact strongly effect on their interfacial energetics, kinetics, and charge transport properties as well as reactive sites. Because the electrochemical reactions only occur at the electrode-electrolyte interfacial area, the photogenerated electron-hole needs to be transferred to the surface for the reactions. Thus, the development of high surface area photoelectrodes is necessary. The porous structure and one-dimensional nanostructure such as nanorod/nanowire arrays reveal high surface areas per electrode volume, which directly improves the PEC efficiency. The high efficient PEC devices based on the $BiVO_4$ porous structure and the one-dimensional nanostructures have been reported by many research groups [31–34]. However, creating more porosity or smaller nanorod/nanowire structures to improve surface area could increase the defect site, increase grain boundaries, and reduce crystallinity leading reduction photocatalytic activity [35]. In addition, with hole diffusion length of ~100 nm and carrier mobility of 0.044 $cm^2\ V^{-2}\ s^{-1}$ [36], the length and thickness of nanostructure should be finely optimized to maximum light absorption and photogenerated charge carrier transport. Furthermore, researchers have recently demonstrated that the charge separation and photoactivity properties are closely related to the exposed crystal facet of $BiVO_4$ photocatalysts [8–9, 37–39]. Therefore, an optimized design and morphological control of crystal facets could improve the PEC performance.

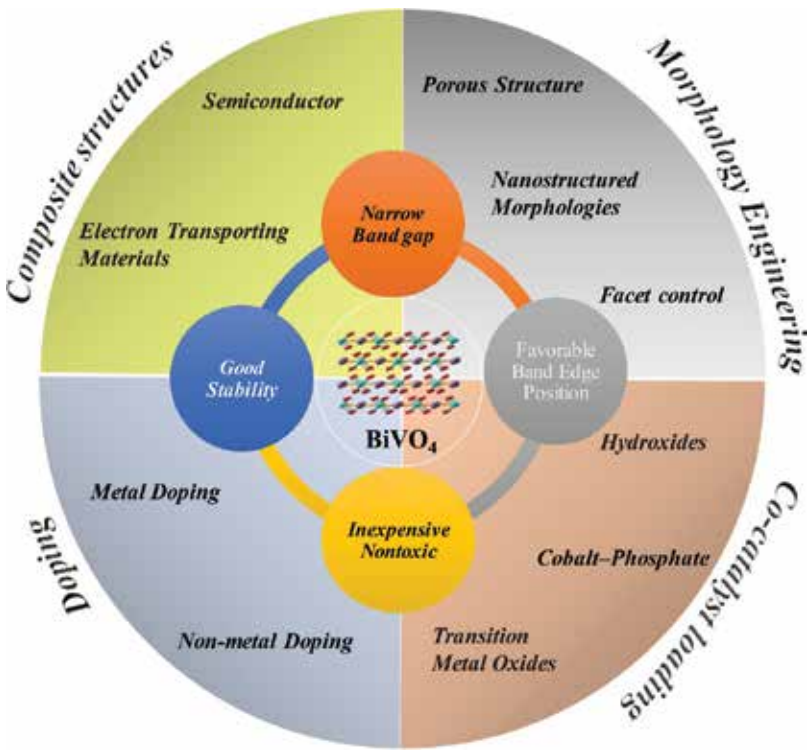

Figure 3. The advantages and strategies to enhance photoelectrochemical properties of $BiVO_4$.

Second, nanocomposites provide a powerful route to overcome limitations in the current studies of single material systems for water splitting, where the photoelectrochemical performance of photoelectrode can be significantly improved by the choice of proper interactions of constituents. The construction of nanocomposite consisting of $BiVO_4$ and addition semiconductor/or conductor can improve the optical absorption, charge carrier separation, and charge transport processes. Combination of $BiVO_4$ with additional metal oxide semiconductors could enhance overall photon absorption and improve electron-hole separation by the rapid photogenerated electron and hole injections at their heterojunctions and extension the optical absorption range. Many $BiVO_4$-based heterostructures have been fabricated successfully such as $TiO_2/BiVO_4$, $Ag_3PO_4/BiVO_4$, $Bi_2S_3/BiVO_4$, g-C3N4/$BiVO_4$, $BiVO_4/SnO_2$, WO_3/$BiVO_4$, BiOCl/$BiVO_4$, $Fe_2O_3/BiVO_4$, $Cu_2O/BiVO_4$, and ZnO/$BiVO_4$ [40–43]. Among them, the WO_3 is a commonly coupled semiconductor with $BiVO_4$ because it is a stable n-type semiconductor with better electron transport properties than the $BiVO_4$ and a suitable conduction-band edge for facile electron injection from conduction band of $BiVO_4$ [29, 44–46].

Recently, we reported a self-assembled nanocomposite photoanode composed of epitaxial $BiVO_4$ matrix embedded with WO_3 mesocrystal for photoelectrochemical application in the visible light regime using PLD [29]. By taking the advantage of the structural feature of this heterostructure, the well-defined crystal facet and interface between WO_3 and $BiVO_4$ phases provide a template for the fundamental understanding of photoactivity in the nanocomposite. The $BiVO_4$-WO_3 crystal structure details were investigated by XRD and TEM as shown in **Figure 4**. The XRD 2θ-θ scans, in-plane Φ-scans, and reciprocal space map results clearly show that $BiVO_4$ and WO_3 spontaneously separated into two single phases during the deposition with an in-plane orientation relationship as $[100]_{BiVO4}$ //$[110]_{WO3}$ //$[001]_{YSZ}$. Both monoclinic $BiVO_4$ and orthorhombic WO_3 phases exhibit two sets of structural domains, which are separated by a 90° rotation around *c*-axis. The microstructure and the epitaxial relationship of $BiVO_4$-WO_3 heterostructure were further investigated as displayed in **Figure 4(b–e)**, which are in an excellent agreement with the XRD analyses. The self-assembled mesocrystal-embedded heterostructure that composed WO_3 and $BiVO_4$ phases is illustrated in **Figure 4g**. The energy band alignment of $BiVO_4$-WO_3 heterojunction illustrated using X-ray photoelectron spectroscopy technique shows that the valence band maxima of WO_3 lies 0.55 eV below that of $BiVO_4$ and the conduction-band minimum of WO_3 lies 0.25 eV below that of $BiVO_4$. This energy band structure could favor the enhancement of photogenerated charge carrier separation, which was further confirmed by photoluminescence and ultrafast transient absorption spectroscopies. **Figure 5** shows Nyquist electrochemical impedance spectroscopy and Mott-Schottky analysis for the $BiVO_4$-WO_3 photoelectrodes. The results demonstrated a much higher electron conductivity of WO_3 with carrier densities of 9.68×10^{18} cm^{-3} under light illumination than $BiVO_4$. Therefore, the $BiVO_4$ matrix serves as the light absorber due to its narrow bandgap, and the WO_3 mesocrystal acts as an electron conductor owing to its high electron conductivity resulting in a significantly enhanced photoelectrochemical performance.

Further example could be observed in the double-deck inverse opal $WO_3/BiVO_4$ structure that could reach a photocurrent density of 3.3 mA/cm^2 at 1.23 V versus RHE and the core-shell WO_3/$BiVO_4$ helix nanostructure, in which $BiVO_4$ was doped with Mo and naturally doped with W from the WO_3 core, exhibits a high photocurrent density of 3.6 mA/cm^2 at 1.23 V versus RHE [34, 47]. More recently, the highest photocurrent density of 6.72 mA/cm^2 at 1.23 V versus RHE for

http://dx.doi.org/10.5772/intechopen.75613

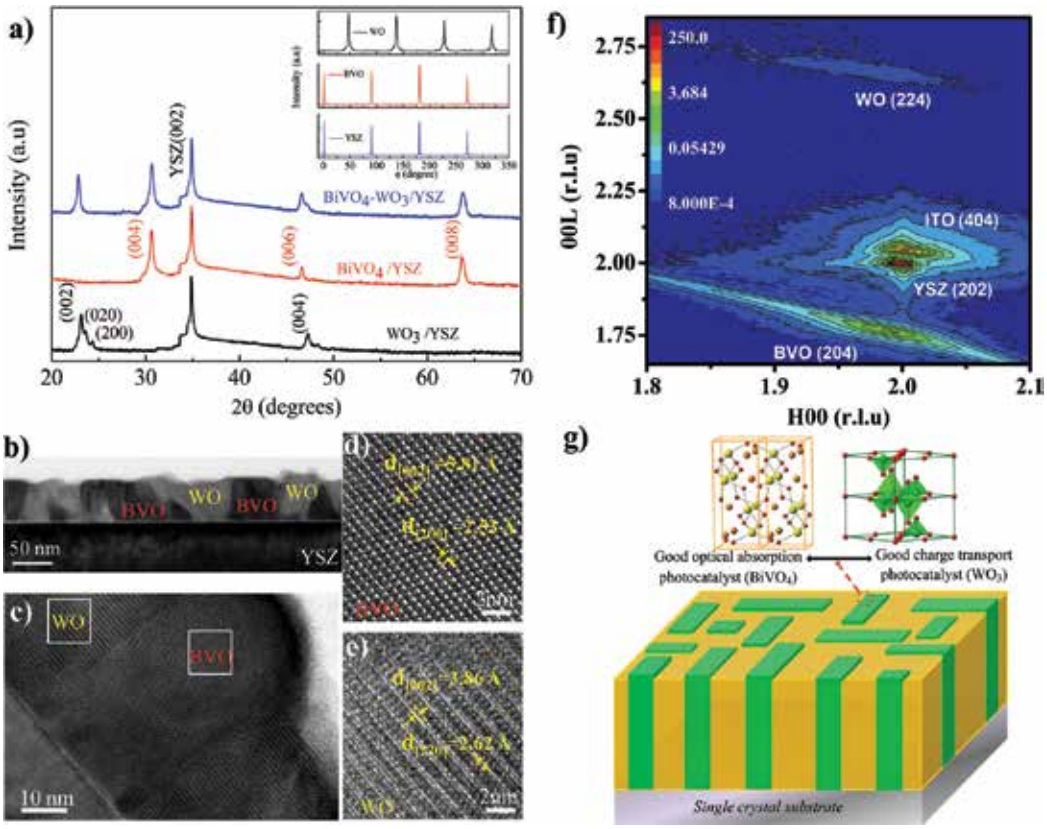

Figure 4. Structure characterization of $BiVO_4$-WO_3 nanocomposite. (a) X-ray diffraction 2θ-θ scans of pure WO_3, $BiVO_4$, and the $BiVO_4$-WO_3 nanocomposite showing only (00 *l*) type peaks of $BiVO_4$ and WO_3. Inset shows XRD φ-scans of YSZ (220), $BiVO_4$ {013}, and WO_3 {022} reflections for $BiVO_4$-WO_3 heterostructure. (b-e) Cross-sectional TEM images of $BiVO_4$-WO_3 (BVO-WO) nanocomposite taken along $[010]_{YSZ}$ zone axis. The enlarged images taken from the marked areas of (d) $BiVO_4$ and (e) WO_3 showing their out-of-plane and in-plane d-spacing parameters. (f) X-ray reciprocal space maps (RSMs) of the composite grown on ITO/YSZ. (g) Illustration of self-assembled $BiVO_4$-WO_3 nanocomposite [29].

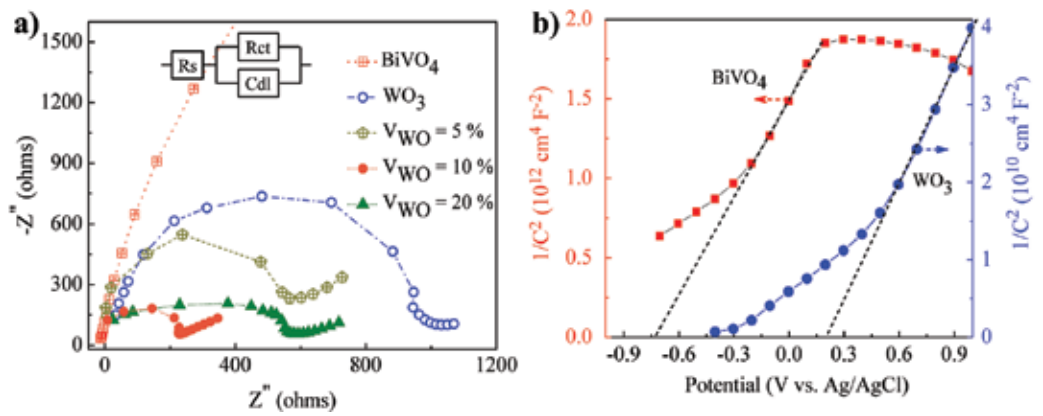

Figure 5. (a) The Nyquist plots and (b) the Mott-Schottky plots for the WO_3, $BiVO_4$, and $BiVO_4$-WO_3 photoelectrodes in 0.5 M Na_2SO_4 solution under AM 1.5 illumination [29].

$BiVO_4$-based photoelectrode was obtained in the CoPi-coated $WO_3/BiVO_4$ core-shell nanorods [21]. The high efficiency photoelectrode was attributed to the superior charge carrier separation and efficient light scattering. In addition, by coupling with a conductor such as reduced graphene oxide and carbon nanotubes, the photocurrent density of the composite electrodes was improved significantly compared to those of the corresponding $BiVO_4$ electrodes which could attribute to the enhancement of charge separation and transport properties [49–57]. However, due to the low crystallinity of $BiVO_4$ as well as the poor $BiVO_4$-conductor and conductor-substrate contact in these nanocomposites, it needs to be further developed to improve the PEC performance.

Third, doping with the metal (such as W, Fe, B, Cu, Zn, Ti, Nb, Sn, Co, Pd, Rb, Ru, Ag, Ga, Sr, and Ir) or nonmetal (such as P and N) materials can change the electrical and optical properties of $BiVO_4$. Among them, only Mo- and W-doped $BiVO_4$ show a significantly enhanced photocurrent and IPCE [21]. The intentional introduction of n-type conductivity W and/or Mo atoms does not change the bandgap energy and band edge positions of doped-$BiVO_4$; however, it can increase the charge carrier density and the electrical conductivity. A suitable doping concentration of Mo and/or W results in significant improvement PEC performance of $BiVO_4$ [54–56]. On the other hand, P doping forms an internal electric field which may improve the photogenerated electron–hole separation. However, it is noted that the doping could induce trap carrier which can enhance charge carrier recombination and reduce the charge transport [35]. Therefore, the optimum doping concentration is a key factor to improve the overall PEC performance of the photoelectrode.

Finally, decoration of $BiVO_4$ with various oxygen evolution catalysts (OECs) such as Co–Pi, Co_3O_4, RhO_2, Pt, CoO, and FeOOH improves the kinetic for oxygen evolution and provides unique active sites for catalytic reactions, thereby strongly enhanced the photocurrent density [3, 27, 40, 57–58]. In addition, it decreases the bias potential and improves the stability of $BiVO_4$ photoanodes. Perhaps the most successful route in the development of high efficient $BiVO_4$ photoelectrode for water oxidation is the modification of the $BiVO_4$-semiconductor nanocomposite surface with OECs. To date, the highest photocurrent density 6.72 mA/cm^2 at 1.23 V versus RHE was obtained for the CoPi-coated $WO_3/BiVO_4$ core-shell nanorods [48].

4. Introduction to thermoelectric bismuth-based materials and applications

Thermoelectric (TE) materials are used in appliances such as heat pumps and power generators [59–63]. TE devices offer unique features of low environmental impact, no moving parts, quiet operation, and high reliability. The performance of TE materials is determined by a dimensionless figure of merit, $ZT = \alpha^2\sigma T/\kappa$, in which α, σ, T, and κ are the Seebeck coefficient, the electrical conductivity, absolute temperature, and the thermal conductivity, respectively. A TE material must exhibit a high power factor ($PF = \alpha^2\sigma$) and low thermal conductivity (κ) to achieve a high ZT value. However, it is challenging for enhancing the ZT value due to the coupling among the TE parameters [62]: the relationship between α and the carrier concentration n (expressed by $|\alpha| \sim n^{-2/3}$ approximately [60]) limits the increase of the PF ($=\alpha^2\sigma$), while the proportional relationship between electrical conductivity and electronic thermal conductivity (the Wiedemann-Franz law) restricts the enhancement of the σ/κ ratio.

Bismuth (Bi)-based chalcogenide narrow-bandgap semiconductors such as Bi_2Te_3, Bi_2Se_3, Sb_2Te_3, $Bi_2(Te_xSe_{1-x})_3$, and $(Bi_xSb_{1-x})_2Te_3$ are of high interest [64–69]. They have been widely exploited for Peltier coolers and thermoelectric generators at low temperature regime (≤150°C) [70, 71]. Thanks to the extensive phonon scattering at grain boundaries, nanocrystalline and nanostructured Bi-based chalcogenide thin films have achieved reduced thermal conductivity [72–77]. However, the lattice imperfections and grain-boundary defects impair the electrical transport properties of the films [72], which call for further investigations to improve PF or the electronic part of ZT. Currently, enhancing the PF of Bi-based thin films is challenging due to not only the coupling among TE material properties [60] but also the tendency of forming nonstoichiometric films at elevated substrate temperatures (T_s) [78]. Numerous charge carriers arising from vacancy defects of volatile elements can constrain the enhancement of $|\alpha|$; however, low carrier concentrations can suppress electrical conductivity if carrier mobility (μ) is poor.

The crystal structures of Bi_2Se_3 and Bi_2Te_3 are usually described by a hexagonal cell that consists of 15 layers of atoms stacking along the c-axis with a sequence shown below [60], as shown in **Figure 6**. ··· $Se^{(1)}$–Bi–$Se^{(2)}$–Bi–$Se^{(1)}$ ··· $Se^{(1)}$–Bi–$Se^{(2)}$–Bi–$Se^{(1)}$ ··· $Se^{(1)}$–Bi–$Se^{(2)}$–Bi–$Se^{(1)}$ ··· and ···$Te^{(1)}$–Bi–$Te^{(2)}$–Bi–$Te^{(1)}$ ··· $Te^{(1)}$–Bi–$Te^{(2)}$–Bi–$Te^{(1)}$···$Te^{(1)}$–Bi–$Te^{(2)}$–Bi–$Te^{(1)}$ ···. The superscripts refer to two different types of bonding for Se or Te atoms. The five-atomic-layer thick lamellae of –($Se^{(1)}$–Bi–$Se^{(2)}$–Bi–$Se^{(1)}$)– or –($Te^{(1)}$–Bi–$Te^{(2)}$–Bi–$Te^{(1)}$)– is called quintuple layers, QLs. The $Se^{(1)}$…$Se^{(1)}$ or $Te^{(1)}$…$Te^{(1)}$ refers to van der Waals force between Se and Te atoms, whereas the $Se^{(1)}$–Bi and Bi–$Se^{(2)}$ or $Te^{(1)}$–Bi and Bi–$Te^{(2)}$ are ionic-covalent bonds. This weak binding between the $Se^{(1)}$ – $Se^{(1)}$ and $Te^{(1)}$…$Te^{(1)}$ accounts for the easy cleavage of these materials perpendicular to the *c*-axis and the anisotropic thermal and electrical transport properties. For example, the thermal conductivity along the *c*-axis direction is ~0.7 $Wm^{-1}K^{-1}$, while it is ~1.5 $Wm^{-1}K^{-1}$ for the plane perpendicular to the *c*-axis [79].

Thin-film technology is advantageous for obtaining nanocrystalline and nanostructured materials by adjusting deposition conditions and subsequent thermal treatments. The extensive phonon scattering at grain boundaries in the nanostructures causes a large reduction in thermal conductivity while maintaining reasonable electrical conductivity, leading to enhanced ZT. Among physical vapor deposition techniques, PLD offers a great versatility in the fabrication of films with multielement stoichiometry and with a variety of structures, from amorphous or nanostructured to polycrystalline or even epitaxial [66–68, 76, 77, 80, 81]. Thin-film TE devices offer some distinctive advantages.

First, a thin-film device has the natural advantage of a small volume (thickness of ≤10 μm, length and width of ~100 μm) as compared to size of millimeters for a bulk TE couple. As a result, thin-film TE cooling can be integrated into microelectronic systems (**Figure 7a**). In principle, the bulk device can be scaled down to micro sizes; however, fabrication processes to do so are difficult.

Second, thin-film devices have a much shorter response time than bulk devices, as shown in **Figure 7c** [59]. The thin-film device achieves the steady state in 15 μs, while the bulk device requires 0.35 s [59]. This is a result of the response time associated with the transport of heat through the thin film (micrometers) rather than through the millimeters associated with bulk devices.

Third, the thin-film device has the ability to handle much larger density of heat pumping power than does the bulk device. Typically, bulk devices are working with pumping power

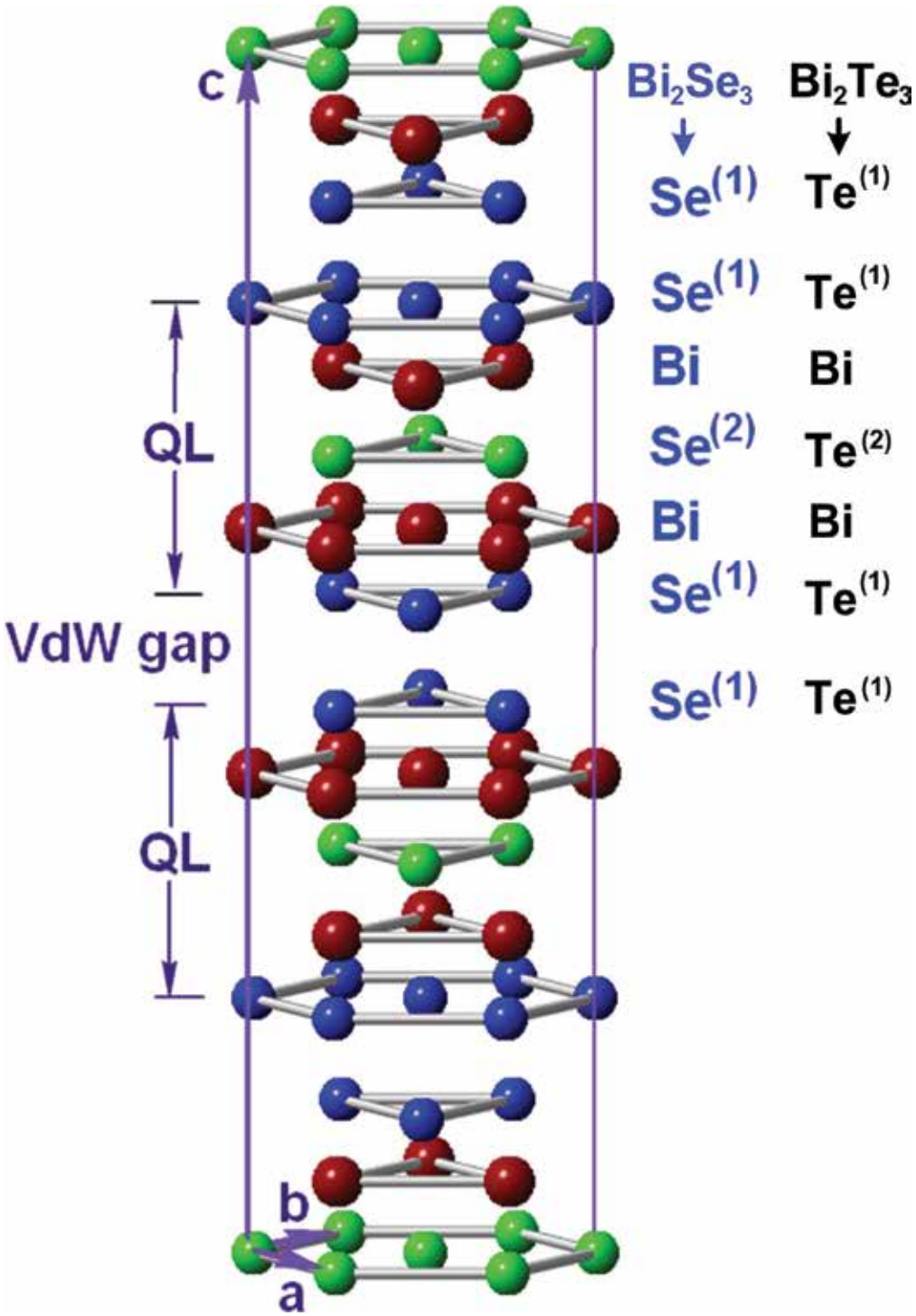

Figure 6. The hexagonal structures of one unit cell of Bi_2Se_3 and Bi_2Te_3.

http://dx.doi.org/10.5772/intechopen.75613

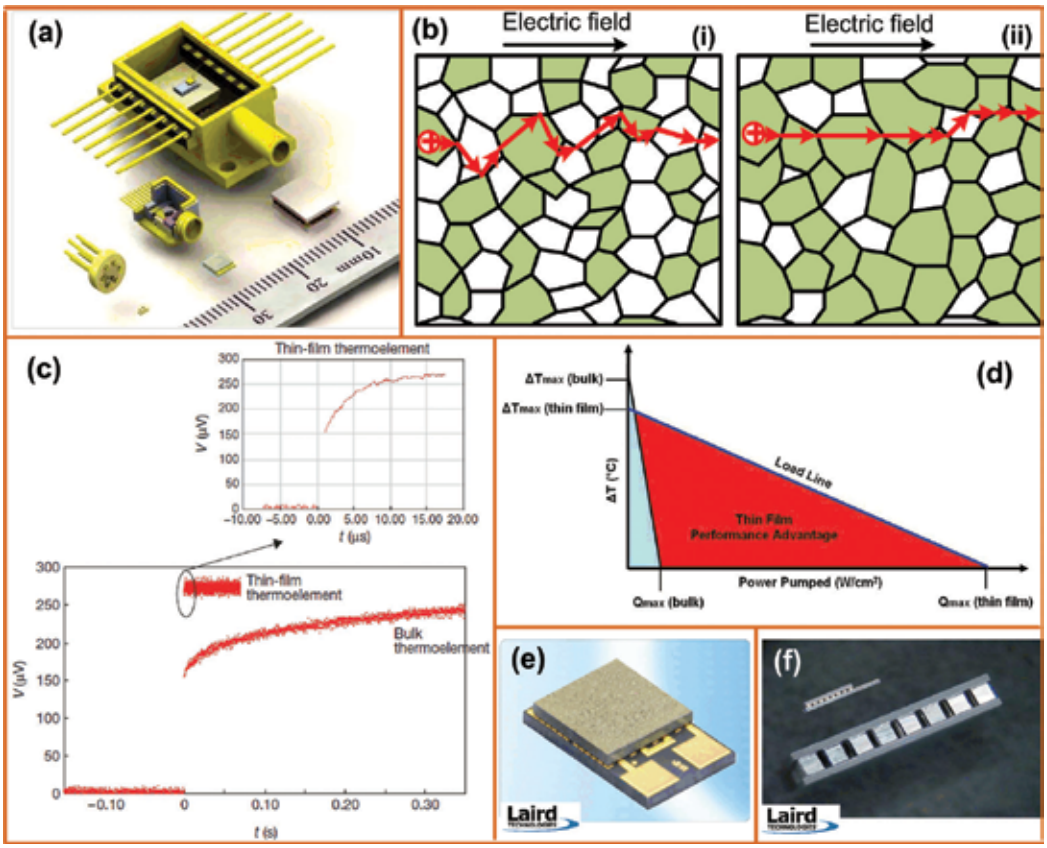

Figure 7. (a) An example for optoelectronics of the continuing reduction in package size. (b) A schematic of grain-boundary scattering for thin-film materials with (i) disoriented-small grains and (ii) highly oriented large grains. (c) The comparison of thermal/cooling time response of thin-film (~5 μm) superlattice device and a bulk device [59]. (d) Thermoelectric module performance chart which presents the temperature drop ΔT versus pumping power [83]. (e) A commercial thin-film TE module. (f) Size comparison between a thin-film TE device and bulk TE device [83].

density lower than 10 W/cm^2; however, the pumping power density in a thin-film device is on the order of hundreds of W/cm^2 [82]. **Figure 7d** illustrates a comparison performance chart between thin-film and bulk TE modules, in which the load line represents the temperature difference (ΔT) between the top and bottom substrate and possible pumping power density (Q) for a given drive current of a TE module [83]. At the maximum drive current for a TE module, the load line is determined by the maximum power density (Q_{max}) and the ΔT_{max}. For a commercial example, under a given drive current, an eTEC™ Series thin-film TE module (Laird technology) possesses a larger pumping power up to ten times (**Figure 7e**) and a comparable maximum temperature difference ΔT_{max} than the conventional bulk TE modules [83].

Fourth, the granular structure-morphology of thin films increases the grain-boundary scattering which is helpful for suppressing κ and enhanced ZT values. **Figure 7b** represents the roles of grain orientation and grain size in carrier mobility. The grains with the same colors illustrate that they have the same/similar orientations. The grain-boundary scattering in

Figure 7b(i) will be greater than that of the **Figure 7b(ii)** case because of its smaller grain size and the greater grain disorientation. The effective mobility is given by [84]

$$\mu_g = \frac{Lq}{\sqrt{2\pi m^* kT}} \exp\left(-\frac{\phi_b}{kT}\right) \quad (1)$$

where q is the carrier charge, m^* is the effective mass, k is the Boltzmann constant, T is the temperature, and ϕ_b is the grain-boundary potential barrier in the depletion region. In polycrystalline silicon, the potential barrier height is approximately twice as high at random boundaries as at low-energy coincidence boundaries.

5. Thermoelectric properties of nanocrystalline and nanostructured Bi_2Te_3-based thin films

Thermoelectric Bi_2Te_3-based materials have played a dominant role in the field of thermoelectrics. The traditional cooling materials are alloys of Bi_2Te_3 with Sb_2Te_3 (such as $Bi_{0.5}Sb_{1.5}Te_3$; p-type) and of Bi_2Te_3 with Bi_2Se_3 (such as $Bi_2Te_{2.7}Se_{0.3}$; n-type), with a ZT at room temperature approximately equal to one [63]. Recently, nanocrystalline and nanostructured Bi_2Te_3-based thin films have recently attracted great interests because of their superior TE performance [72–77, 80, 81, 85, 86]. The PF of Bi_2Te_3 films was 8.8 $\mu Wcm^{-1} K^{-2}$ for an (015)-oriented film with layered-hexagonal morphology [85] and 33.7 $\mu Wcm^{-1} K^{-2}$ for a highly (00l)-oriented layered film [86]. Furthermore, the hexagonal-Bi_2Te_3 film grown using MBE obtained a PF of 27 $\mu Wcm^{-1} K^{-2}$ [87], and the smooth-epitaxial- Bi_2Te_3 film prepared by co-evaporation achieved a PF of 39.9 $\mu Wcm^{-1} K^{-2}$ [88].

Despite fewer studies performed on thermoelectric Bi_2Se_3 as compared to Bi_2Te_3, a considerable amount of recent efforts to enhance TE performance has been devoted to the synthesis of Bi_2Se_3 nanostructures such as hexagonal flakes (PF ≈ 0.28 $\mu Wcm^{-1} K^{-2}$) [89] and nanoflakes (PF ≈ 0.97 $\mu Wcm^{-1} K^{-2}$) [90], using the solvo-thermal method and chemical bath deposition, respectively. Moreover, the Bi_2Se_3 film grown by metal organic-chemical vapor deposition has reached a PF = 5.8 $\mu Wcm^{-1} K^{-2}$ [91]. In PLD, tightly controlling substrate temperatures (T_s)

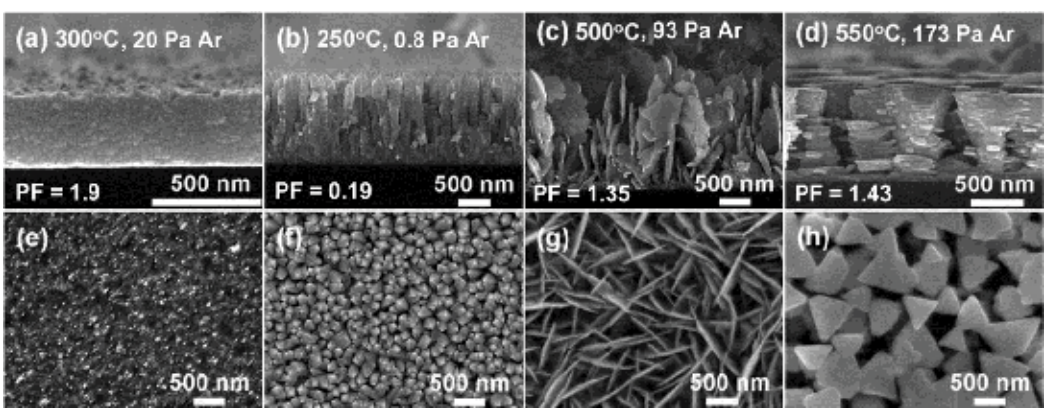

Figure 8. The morphology and power factor (PF, unit $\mu Wcm^{-1} K^{-2}$) of nanostructured Bi_2Te_3 thin films grown by PLD at various substrate temperatures and ambient pressures, reported by Chang and Chen [77].

http://dx.doi.org/10.5772/intechopen.75613

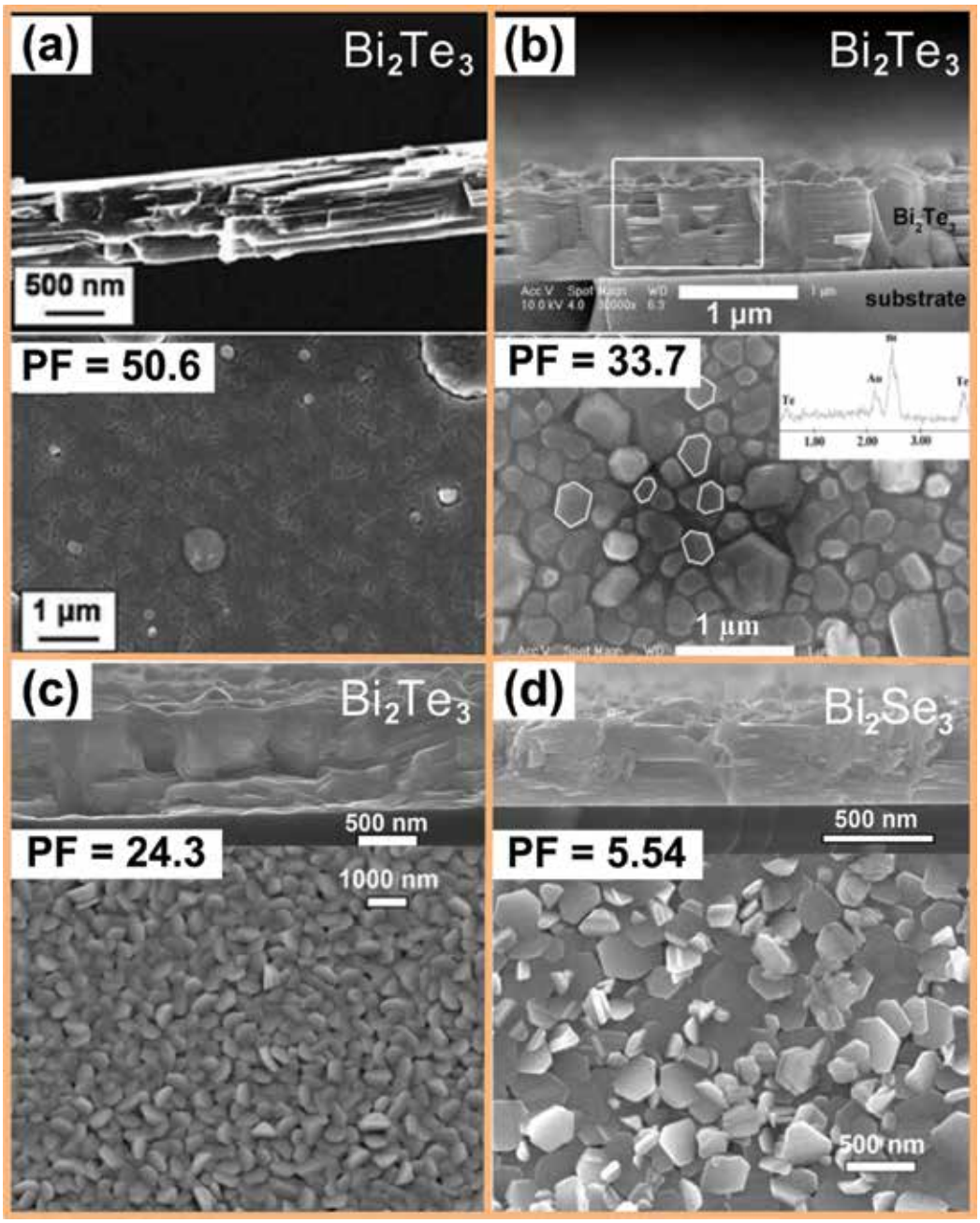

Figure 9. The morphology and power factor (PF, unit $\mu Wcm^{-1} K^{-2}$) of the optimal Bi_2Te_3 and Bi_2Se_3 thin films with layered structures grown by PLD, reported in Refs. [66, 67, 80, 86].

and ambient pressures enable the morphologies and compositions of films to be manipulated extensively, which offer a new method for enhancing the TE properties of films. For example, self-assembled Bi_2Te_3 films featuring well-aligned zero- to three-dimensional nanoblocks have been fabricated (**Figure 8**), but the room temperature PFs of these films remain low (≤ 1.9 $\mu Wcm^{-1} K^{-2}$) due to the low electrical conductivity of the voided structures [77].

By contrast, the Bi_2Te_3-based thin films with compact and/or layered structures possess the high electrical conductivities and relatively high Seebeck values if the films obtain stoichiometry. For example, A. Li Bassi et al. reported a high PF of 50.6 μWcm^{-1} K^{-2} for the layered-smooth Bi_2Te_3 films (**Figure 9a**) [80]. Similarly, the Bi_2Te_3 films with layered-hexagonal grain structure exhibited a high PF of 33.7 μWcm^{-1} K^{-2} (**Figure 9b**) [86]. P.H. Le et al. found that the optimal PF films also present compact-layered structures, namely, PF = 24.3 μWcm^{-1} K^{-2} for the Bi_2Te_3 film (**Figure 9c**) and PF = 5.54 μWcm^{-1} K^{-2} for the hexagonal Bi_2Se_3 film (**Figure 9d**) [66, 67]. Usually, compact or layered structure films obtain high carrier mobility than those with the open/voided nanostructures.

Table 1 summarizes thermal transport properties (at room temperature) of nanocrystalline-nanostructured Bi_2Te_3-based thin films and bulk materials in the literature [62, 72–76, 87, 92].

Sample, fabrication method	Avg. grain size	κ (W/m K)	σ (S/cm)	α (μV/K)	PF = σα² (μW/cmK²)	ZT (300 K)	Ref.
$Bi_2Te_{2.7}Se_{0.3}$ nanocrystalline thin film, flash evaporation	60 nm	0.8 (cross-plane)	540	−186.1(in-plane)	18.7(in-plane)	0.7	[72]
Sintered bulk $Bi_2Te_{3-x}Se_x$ material, hot pressing	30 μm	1.6	930	−177.5	29.3	0.6	
Nanocrystalline bismuth-telluride-based ($Bi_2Te_{3-x}Se_x$) thin film	10 nm	0.61	550	−84.0	3.9	0.19	[73]
	27 nm	0.68	540	−138.1	10.3	0.46	
	60 nm	0.80	540	−186.1	18.7	0.70	
Nanocrystalline Bi-Sb-Te thin film, sputtering	26 nm	0.46	3.3	—	—	—	[75]
	45 nm	0.65	6.7	—	—	—	
	84 nm	0.81	33.3	—	—	—	
Nanocrystalline BiSbTe (8:30:62) thin film, flash evaporation	150 nm	0.6	—	—	—	—	[74]
Single crystal BiSbTe bulk alloys	—	0.75	—	—	—	—	[62]
Bi_2Te_3/Sb_2Te_3 superlattices (period ~5 nm)	—	0.4	—	—	—	—	[93]
$Bi_2Te_{3+0.63}$ bulk	—	2.2	1000	−240	58	0.87	[62]
$Bi_2(Te_{0.95}Se_{0.05})_3$ bulk	—	1.59	901	−223	45	0.85	[62]
$Bi_2Te_3/Bi_2(Te_{0.88}Se_{0.12})_3$ superlattice film, MBE	80 nm	1.25	639	−204	27	0.60	[87]
Bi_2Te_3 films, laser ablation	—	0.2–0.3	—	—	—	—	[92]
$Bi_xSb_{2-x}Te_3$ nanolayer film, PLD	190 nm	1.16	2700	95	25	0.65	[76]
$Bi_xSb_{2-x}Te_3$ nanodisk film, PLD	100 nm	1.00	1100	132	20	0.60	
$Bi_xSb_{2-x}Te_3$ nanocolumn film, PLD	70 nm	0.93	280	207	12	0.39	

Table 1. Room temperature thermal transport properties of nanocrystalline-nanostructured Bi_2Te_3-based thin films and bulk materials in the literature, including sample and fabrication method, average grain size, thermal conductivity κ, electrical conductivity σ, Seebeck coefficient α, power factor PF (= $\alpha^2\sigma$), and ZT (at 300 K).

Generally, the thermal conductivity κ value for polycrystalline films is expected to be smaller than that of bulk alloys because of the contribution of grain-boundary scattering [62, 72, 74]. Moreover, the κ of nanocrystalline Bi_2Te_3-based films will further decrease when the grain size of decreases ($\kappa \leq 0.81$ W/mK) [73, 75]. For Bi_2Te_3/Sb_2Te_3 superlattice films, the coherent backscattering of phonon waves at the superlattice interfaces is outlined for the reduction of lattice thermal conductivity, resulting in the low $\kappa \leq 0.4$ W/mK [93].

For PLD Bi_2Te_3-based films, Walachova et al. [92] estimated κ starting from direct ZT measurement with the Harman method and found a value of about 0.2–0.3 W/mK for films with a thickness comparable to our films (>100 nm). Recently, Chang et al. [76] reported the κ between 0.93 and 1.16 W/mK for granular $Bi_xSb_{2-x}Te_3$ films. The reported κ (at 300 K) of hexagonal flake Bi_2Se_3 was 0.75 W/mK.

6. Conclusion

We report the crystal, electronic structures, optical properties, and PEC activities of $BiVO_4$-based materials. Morphology engineering, cocatalyst loading, and doping with metal and nonmetal composite structures are the approaches to fabricate high efficiency $BiVO_4$ photoelectrode for PEC water spitting. In addition, the Bi_2Te_3-based thin films with nanocrystalline and nanostructured morphologies obtain the reduced thermal conductivity, meanwhile the close stoichiometric films with layered structure morphologies exhibit high thermoelectric power factors. $BiVO_4$-based materials and Bi_2Te_3-based thin films play significant roles for the photoelectrode and thermoelectric applications.

Acknowledgements

Financial support from Vietnam National Foundation for Science and Technology Development (NAFOSTED) under grant numbers 103.99–2015.17, 103.99-2016.75 (PHL), and MOST106-2119-M-009-011-MY3, Taiwan (CNV), is gratefully acknowledged.

Author details

Phuoc Huu Le[1]*, Nguyen Trung Kien[2] and Chien Nguyen Van[3,4]*

*Address all correspondence to: lhuuphuoc@ctump.edu.vn and chienft.u@gmail.com

1 Faculty of Basic Sciences, Can Tho University of Medicine and Pharmacy, Can Tho, Vietnam

2 Faculty of Medicine, Can Tho University of Medicine and Pharmacy, Can Tho, Vietnam

3 Department of Materials Science and Engineering, National Chiao Tung University, Hsinchu, Taiwan

4 Institute of Materials Science, Vietnam Academy of Science and Technology, Ha Noi City, Vietnam

References

[1] Li R, Han H, Zhang F, Wang D, Li C. Highly efficient photocatalysts constructed by rational assembly of dual-cocatalysts separately on different facets of $BiVO_4$. Energy & Environmental Science. 2014;**7**:1369. DOI: 10.1039/c3ee43304h

[2] Zhao X, Luo W, Feng J, Li M, Li Z, Yu T, Zou Z. Quantitative analysis and visualized evidence for high charge separation efficiency in a solid-liquid bulk heterojunction. Advanced Energy Materials. 2014;**4**:1301785. DOI: 10.1002/aenm.201301785

[3] Kim TW, Choi K-S. Nanoporous $BiVO_4$ photoanodes with dual-layer oxygen evolution catalysts for solar water splitting. Science. 2014;**343**:990-995. DOI: 10.1126/science.1246913

[4] Prévot MS, Sivula K. Photoelectrochemical tandem cells for solar water splitting. Journal of Physical Chemistry C. 2013;**117**:17879-17893. DOI: 10.1021/jp405291g

[5] Grätzel M. Photoelectrochemical cells. Nature. 2001;**414**:338-344. DOI: 10.1016/S0140-6736(06)68542-5

[6] Walter MG, Warren EL, James R. McKone JR, Boettcher SW, Mi Q, Santori EA, Lewis NS. Solar water splitting cells. Chemical Reviews. 2010;**110**:6446-6473. DOI: 10.1021/cr1002326

[7] Tan HL, Amal R. Alternative strategies in improving the photocatalytic and photoelectrochemical activities of visible light-driven $BiVO_4$: A review. Journal of Materials Chemistry A. 2017;**5**:16498-16521. DOI: 10.1039/C7TA04441K

[8] Xi G, Ye J. Synthesis of bismuth vanadate nanoplates with exposed {001} facets and enhanced visible-light photocatalytic properties. Chemical Communications. 2010; **46**:1893-1895. DOI: 10.1039/b923435g

[9] Li R, Han H, Zhang F, Wang D, Li C. Highly efficient photocatalysts constructed by rational assembly of dual-cocatalysts separately on different facets of $BiVO_4$. Energy & Environmental Science. 2014;**7**:1369. DOI: 10.1039/c3ee43304h

[10] Yu J, Kudo A. Effects of structural variation on the photocatalytic performance of hydrothermally synthesized $BiVO_4$. Advanced Functional Materials. 2006;**16**:2163-2169. DOI: 10.1002/adfm.200500799

[11] Huang Z-F, Pan L, Zou J-J, Zhang X, Wang L. Nanostructured bismuth vanadate-based materials for solar-energy-driven water oxidation: A review on recent progress. Nanoscale. 2014;(23):14044-14063. DOI: 10.1039/c4nr05245e

[12] Liang Y, Tsubota T, Mooij LPA, Krol R. Highly improved quantum efficiencies for thin film $BiVO_4$ photoanodes. Journal of Physical Chemistry C. 2011;**115**(35):17594-17598. DOI: 10.1021/jp203004v

[13] Tokunaga S, Kato H, Kudo A. Selective preparation of monoclinic and tetragonal $BiVO_4$ with Scheelite structure and their photocatalytic properties. Chemistry of Materials. 2001;**13**:4624-4628. DOI: 10.1021/cm0103390

[14] Kudo A, Omori K, Kato H. A novel aqueous process for preparation of crystal form-controlled and highly crystalline $BiVO_4$ powder from layered vanadates at room temperature and its photocatalytic and photophysical properties. Journal of the American Chemical Society. 1999;**121**:11459-11467. DOI: 10.1021/ja992541y

[15] Cooper JK, Gul S, Toma FM, Chen L, Glans PA, Guo J, Ager JW, Yano J, Sharp ID. Electronic structure of monoclinic $BiVO_4$. Chemistry of Materials. 2014;**26**(18):5365-5373. DOI: 10.1021/cm5025074

[16] Walsh A, Yan Y, Huda MN, Al-Jassim MM, Wei S-H. Band edge electronic structure of $BiVO_4$: Elucidating the role of the Bi s and V d orbitals. Chemistry of Materials. 2009;**21**(3):547-551. DOI: 10.1021/cm802894z

[17] Zhao Z, Li Z, Zou Z. Electronic structure and optical properties of monoclinic clinobisvanite $BiVO_4$. Physical Chemistry Chemical Physics. 2011;**13**:4746-4753. DOI: 10.1039/c0cp01871f

[18] Van CN, Chang WS, Chen J-W, Tsai K-A, Tzeng W-Y, Lin Y-C, Kuo H-H, Liu H-J, Chang K-D, Chou W-C, Wu C-L, Chen Y-C, Luo CW, Hsu Y-J, Chu Y-H. Heteroepitaxial approach to explore charge dynamics across Au/ $BiVO_4$ interface for photoactivity enhancement. Nano Energy. 2015;**15**:625-633. DOI: 10.1016/j.nanoen.2015.05.024

[19] Rettie AJE, Mozaffari S, Mcdaniel MD, Pearson KN, Ekerdt JG, Markert JT, Mullins CB. Pulsed laser deposition of epitaxial and polycrystalline bismuth vanadate thin films. Journal of Physical Chemistry C. 2014;**118**(46):26543-26550. DOI: 10.1021/jp5082824

[20] Stoughton S, Showak M, Mao Q, Koirala P, Hillsberry DA, Sallis S, Kourkoutis LF, Nguyen K, Piper LFJ, Tenne DA, Podraza NJ, Muller DA, Adamo C, Schlom DG. Adsorption-controlled growth of $BiVO_4$ by molecular-beam epitaxy. APL Materials. 2013;**1**:042112. DOI: 10.1063/1.4824041

[21] Luo W, Yang Z, Li Z, Zhang J, Liu J, Zhao Z, Wang Z, Yan S, Yu T, Zou Z. Solar hydrogen generation from seawater with a modified $BiVO_4$ photoanode. Energy & Environmental Science. 2011;**4**:4046-4051. DOI: 10.1039/c1ee01812d

[22] Sayama K, Nomura A, Arai T, Sugita T, Abe R, Yanagida M, Oi T, Iwasaki Y, Abe Y, Sugihara H. Photoelectrochemical decomposition of water into H_2 and O_2 on porous $BiVO_4$ thin-film electrodes under visible light and significant effect of Ag ion treatment. The Journal of Physical Chemistry. B. 2006;**3**:11352-11360. DOI: 10.1021/jp057539+

[23] Su J, Guo L, Bao N, Grimes CA. Nanostructured WO_3/$BiVO_4$ heterojunction films for efficient photoelectrochemical water splitting. Nano Letters. 2011;**11**:1928-1933. DOI: 10.1021/nl2000743

[24] Sui M, Han C, Wang Y, Li J, Gu X. Photoelectrochemical studies on $BiVO_4$ membranes deposition on transparent conductive substrates by a facile electrophoresis route. Journal of Materials Science: Materials in Electronics. 2016;**27**:4290-4296. DOI: 10.1007/s10854-016-4295-x

[25] Zhang Y, Guo Y, Duan H, Li H, Sun C, Liu H. Facile synthesis of $V4^{+}$ self-doped, [010] oriented $BiVO_4$ nanorods with highly efficient visible light- induced photocatalytic activity. Physical Chemistry Chemical Physics. 2014;**16**:24519-24526. DOI: 10.1039/C4CP03795B

[26] Neves MC, Trindade T. Chemical bath deposition of $BiVO_4$. Thin Solid Films. 2002;**406**:93-97. DOI: 10.1016/S0040-6090(01)01787-4

[27] Seabold JA, Choi K. Efficient and stable photo-oxidation of water by a bismuth vanadate photoanode coupled with an iron oxyhydroxide oxygen evolution catalyst. Journal of the American Chemical Society. 2012;**134**:2186-2192. DOI: 10.1021/ja209001d

[28] Song J, Cha J, Lee MG, Jeong HW, Seo S, Yoo JA, Kim TL, Lee J, No H, Kim DH, Jeong SY, An H, Lee BH, Bark CW, Park H, Jang HW, Lee S. Template-engineered epitaxial $BiVO_4$ photoanodes for efficient solar water splitting. Journal of Materials Chemistry A. 2017;**5**:18831-18838. DOI: 10.1039/C7TA04695B

[29] Van CN, Do TH, Chen J-W, Tzeng W-Y, Tsai K-A, Song H, Liu H-J, Lin Y-C, Chen Y-C, Wu C-L, Luo CW, Chou W-C, Huang R, Hsu Y-J, Chu Y-H. WO_3 mesocrystal-assisted photoelectrochemical activity of $BiVO_4$. NPG Asia Materials. 2017;**9**:e357. DOI: 10.1038/am.2017.15

[30] Kim JH, Lee JS. $BiVO_4$-based Heterostructured Photocatalysts for solar water splitting: A review. Energy and Environment Focus. 2014;**3**:339-353. DOI: 10.1166/eef.2014.1121

[31] Qiu Y, Liu W, Chen W, Chen W, Zhou G, Hsu P-C, Zhang R, Liang Z, Fan S, Zhang Y, Cui Y. Efficient solar-driven water splitting by nanocone $BiVO_4$-perovskite tandem cells. Science Advances. 2016;**2**:e1501764. DOI: 10.1126/sciadv.1501764

[32] Zhao J, Guo Y, Cai L, Li H, Wang KX, Cho IS, Lee CH, Fan S, Zheng X. High-performance ultrathin $BiVO_4$ photoanode on textured polydimethylsiloxane substrates for solar water splitting. ACS Energy Letters. 2016;**1**:68-75. DOI: 10.1021/acsenergylett.6b00032

[33] Kim TW, Choi K-S. Nanoporous BiVO4 photoanodes with dual-layer oxygen evolution catalysts for solar water splitting. Science. 2014;**343**:990-995. DOI: 10.1126/science.1246913

[34] Shi X, Choi IY, Zhang K, Kwon J, Kim DY, Lee JK, Oh SH, Kim JK, Park JH. Efficient photoelectrochemical hydrogen production from bismuth vanadate-decorated tungsten trioxide helix nanostructures. Nature Communications. 2014;**5**:4775. DOI: 10.1038/ncomms5775

[35] Park Y, McDonald KJ, Choi K-S. Progress in bismuth vanadate photoanodes for use in solar water oxidation. Chemical Society Reviews. 2013;**42**:2321-2337. DOI: 10.1039/c2cs35260e

[36] Rettie AJE, Lee HC, Marshall LG, Lin J-F, Capan C, Lindemuth J, McCloy JS, Zhou J, Bard AJ, Mullins CB. Combined charge carrier transport and photoelectrochemical characterization of $BiVO_4$ single crystals: Intrinsic behavior of a complex metal oxide. Journal of the American Chemical Society. 2013;**135**(30):11389-11396. DOI: 10.1021/ja405550k

[37] Li R, Zhang F, Wang D, Yang J, Li M, Zhu J, Zhou X, Han H, Li C. Spatial separation of photogenerated electrons and holes among {010} and {110} crystal facets of $BiVO_4$. Nature Communications. 2013;**4**:1432. DOI: 10.1038/ncomms2401

[38] Yang J, Wang D, Zhou X, Li C. A theoretical study on the mechanism of photocatalytic oxygen evolution on $BiVO_4$ in aqueous solution. Chemistry–A European Journal. 2013;(4):1320-1326. DOI: 10.1002/chem.201202365

[39] Li R, Han H, Zhang F, Wang D, Li C. Highly efficient photocatalysts constructed by rational assembly of dual-cocatalysts separately on different facets of $BiVO_4$. Energy & Environmental Science. 2014;**7**:1369-1376. DOI: 10.1039/c3ee43304h

[40] Tolod KR, Hernández S, Russo N. Recent advances in the $BiVO_4$ photocatalyst for sun-driven water oxidation: Top-performing photoanodes and scale-up challenges. Catalysts. 2017;**7**:13. DOI: 10.3390/catal7010013

[41] Li C, Zhang P, Lv R, Lu J, Wang T, Wang S, Wang H, Gong J. Selective deposition of Ag_3PO_4 on monoclinic $BiVO_4$(040) for highly efficient photocatalysis. Small. 2013;(23):3951-3956. DOI: 10.1002/smll.201301276

[42] Balachandran S, Prakash N, Thirumalai K, Muruganandham M, Sillanpa M, Swaminathan M. Facile construction of heterostructured $BiVO_4$–ZnO and its dual application of greater solar photocatalytic activity and self-cleaning property. Industrial and Engineering Chemistry Research. 2014;**53**:8346-8356. DOI: 10.1021/ie404287m

[43] Gao X, Wu HB, Zheng L, Zhong Y, Hu Y, Lou XWD. Formation of mesoporous heterostructured $BiVO_4/Bi_2S_3$ hollow discoids with enhanced photoactivity. Angewandte Chemie, International Edition. 2014;**53**:5917-5921. DOI: 10.1002/anie.201403611

[44] Grigioni I, Stamplecoskie KG, Selli E, Kamat PV. Dynamics of photogenerated charge carriers in $WO_3/BiVO_4$ heterojunction photoanodes. Journal of Physical Chemistry C. 2015;**119**:20792-20800. DOI: 10.1021/acs.jpcc.5b05128

[45] Rao PM, Cai L, Liu C, Cho IS, Lee CH, Weisse JM, Yang P, Zheng X. Simultaneously efficient light absorption and charge separation in $WO_3/BiVO_4$ core/shell nanowire photoanode for photoelectrochemical water oxidation. Nano Letters. 2014;**14**(2):1099-1105. DOI: 10.1021/nl500022z

[46] Hong SJ, Lee S, Jang JS, Lee JS. Heterojunction $BiVO_4/WO_3$ electrodes for enhanced photoactivity of water oxidation. Energy & Environmental Science. 2011;**4**:1781-1787. DOI: 10.1039/c0ee00743a

[47] Ma M, Kim JK, Zhang K, Shi X, Kim SJ, Moon JH, Park J. Double-deck inverse opal photoanodes: Efficient light absorption and charge separation in heterojunction. Chemistry of Materials. 2014;**26**:5592-5597. DOI: 10.1021/cm502073d

[48] Pihosh Y, Turkevych I, Mawatari K, Uemura J, Kazoe Y, Kosar S, Makita K, Sugaya T, Matsui T, Fujita D, Tosa M, Kondo M, Kitamori T. Photocatalytic generation of hydrogen

by core-shell WO_3/ $BiVO_4$ nanorods with ultimate water splitting efficiency. Scientific Reports. 2015;**5**:11141. DOI: 10.1038/srep11141

[49] Fu Y, Sun X, Wang X. $BiVO_4$–graphene catalyst and its high photocatalytic performance under visible light irradiation. Materials Chemistry and Physics. 2011;**131**:325-330. DOI: 10.1016/j.matchemphys.2011.09.049

[50] Ng YH, Iwase A, Kudo A, Amal R. Reducing graphene oxide on a visible-light $BiVO_4$ photocatalyst for an enhanced photoelectrochemical water splitting. Journal of Physical Chemistry Letters. 2010;**1**:2607-2612. DOI: 10.1021/jz100978u

[51] Wu X, Zhao J, Guo S, Wang L, Shi W, Huang H, Liu Y, Kang Z. Carbon dot and $BiVO_4$ quantum dot composites for overall water splitting via a two-electron pathway. Nanoscale. 2016;**8**:17314-17321. DOI: 10.1039/c6nr05864g

[52] Wang Y, Wang W, Mao H, Lu Y, Lu J, Huang J, Ye Z, Lu B. Electrostatic self-assembly of $BiVO_4$–reduced graphene oxide nanocomposites for highly efficient visible light photocatalytic activities. ACS Applied Materials & Interfaces. 2014;**6**:12698-12706. DOI: 10.1021/am502700p

[53] Zhao D, Zong W, Fan Z, Xiong S, Du M, Wu T, Fang Y-W, Ji F, Xu X. Synthesis of carbon-doped BiVO4@multi-walled carbon nanotubes with high visible-light absorption behavior, and evaluation of their photocatalytic properties. CrystEngComm. 2016;**18**:9007-9015. DOI: 10.1039/C6CE01642A

[54] Rao PM, Cai L, Liu C, Cho IS, Lee CH, Weisse JM, Yang P, Zheng X. Simultaneously efficient light absorption and charge separation in WO_3/$BiVO_4$ Core/Shell nanowire photoanode for photoelectrochemical water oxidation. Nano Letters. 2014;**14**(2):1099-1105. DOI: 10.1021/nl500022z

[55] Berglund SP, Rettie AJE, Hoang S, Mullins CB. Incorporation of Mo and W into nanostructured $BiVO_4$ films for efficient photoelectrochemical water oxidation. Physical Chemistry Chemical Physics. 2012;**14**:7065-7075. DOI: 10.1039/c2cp40807d

[56] Park HS, Kweon KE, Ye H, Paek E, Hwang GS, Bard AJ. Factors in the metal doping of $BiVO_4$ for improved photoelectrocatalytic activity as studied by scanning electrochemical microscopy and first-principles density-functional calculation. Journal of Physical Chemistry C. 2011;**115**:17870-17879. DOI: 10.1021/jp204492r

[57] Han L, Abdi FF, Krol RVD, Liu R, Huang Z, Lewerenz H-J, Dam B, Zeman M, Smets AHM. Efficient water-splitting device based on a bismuth vanadate photoanode and thin-film silicon solar cells. ChemSusChem. 2014;**7**:2832-2838. DOI: 10.1002/cssc.201402456

[58] Abdi FF, Han L, Smets AHM, Zeman M, Dam B, Krol RVD. Efficient solar water splitting by enhanced charge separation in a bismuth vanadate-silicon tandem photoelectrode. Nature Communications. 2013;**4**:2195. DOI: 10.1038/ncomms3195

[59] Venkatasubramanian R, Siivola E, Colpitts T, O'Quinn B. Thin-film thermoelectric devices with high room-temperature figures of merit. Nature. 2001;**413**:597-602. DOI: 10.1038/35098012

[60] Snyder GJ, Toberer ES. Complex thermoelectric materials. Nature Materials. 2008;**7**:105-114. DOI: 10.1038/nmat2090

[61] Dongfang Y, editor. Applications of Laser Ablation: Thin Film Deposition, Nanomaterial Synthesis and Surface Modification. Croatia: Intech; 2016. 55-84. doi: dx.doi.org/10.5772/65898

[62] Rowe DM, editor. Thermoelectrics Handbook: Macro to Nano. FL, Boca Raton: CRC/Taylor & Francis; 2006

[63] Nolas GS, Sharp J, Goldsmid HJ. Thermoelectrics: Basic Principles and New Materials Developments. New York: Springer; 2001

[64] Schumacher C, Reinsberg KG, Rostek R, Akinsinde L, Baessler S, Zastrow S, Rampelberg G, Woias P, Detavernier C, Broekaert JAC, Bachmann J, Nielsch K. Optimizations of pulsed plated p and n-type Bi_2Te_3-based ternary compounds by annealing in different ambient atmospheres. Advanced Energy Materials. 2013;**3**:95-104. DOI: 10.1002/aenm.201200417

[65] Soni A, Yanyuan Z, Ligen Y, Aik MKK, Dresselhaus MS. Enhanced thermoelectric properties of solution grown $Bi_2Te_{3-x}Se_x$ nanoplatelet composites. NanoLetters. 2012;**12**:1203-1209. DOI: 10.1021/nl2034859

[66] Le PH, Liao C-N, Luo CW, Lin J-Y, Leu J. Thermoelectric properties of bismuth-selenide films with controlled morphology and texture grown using pulsed laser deposition. Applied Surface Science. 2013;**285P**:657-663. DOI: 10.1016/j.apsusc.2013.08.107

[67] Le PH, Liao C-N, Luo CW, Lin J-Y, Leu J. Thermoelectric properties of nanostructured bismuth–telluride thin films grown using pulsed laser deposition. Journal of Alloys and Compounds. 2014;**615**:546-552. DOI: 10.1016/j.jallcom.2014.07.018

[68] Tuyen LTC, Le PH, Luo CW, Leu J. Thermoelectric properties of nanocrystalline Bi_3Se_2Te thin films grown using pulsed laser deposition. Journal of Alloys and Compounds. 2016;**673**:107-114. DOI: 10.1016/j.jallcom.2016.03.006

[69] Huang B, Lawrence C, Gross A, Hwang G-S, Ghafouri N, Lee S-W, Kim H, Li C-P, Uher C, Najafi K, Kaviany M. Low-temperature characterization and micropatterning of coevaporated Bi_2Te_3 and Sb_2Te_3 films. Journal of Applied Physics. 2008;**104**:113710. DOI: 10.1063/1.3033381

[70] Böttner H, Nurnus J, Gavrikov A, Kühner G, Jägle M, Künzel C, Eberhard D, Plescher G, Schubert A, Schlereth K-H. New thermoelectric components using microsystem technologies. International Journal of Energy & Environment. 2004;**13**:414-420. DOI: 10.1109/JMEMS.2004.828740

[71] Takashiri M, Shirakawa T, Miyazaki K, Tsukamoto H. Fabrication and characterization of bismuth-telluride-based alloy thin film thermoelectric generators by flash evaporation method. Sensors and Actuators A. 2007;**138**:329-334. DOI: 10.1016/j.sna.2007.05.030

[72] Takashiri M, Takiishi M, Tanaka S, Miyazaki K, Tsukamoto H. Thermoelectric properties of n-type nanocrystalline bismuth-telluride-based thin films deposited by flash evaporation. Journal of Applied Physics. 2007;**101**:74301. DOI: 10.1063/1.2717867

[73] Takashiri M, Miyazaki K, Tanaka S, Kurosaki J, Nagai D, Tsukamoto H. Effect of grain size on thermoelectric properties of n-type nanocrystalline bismuth-telluride based thin films. Journal of Applied Physics. 2008;**104**:84302. DOI: 10.1063/1.2990774

[74] Takashiri M, Tanaka S, Miyazaki K, Tsukamoto H. Cross-plane thermal conductivity of highly oriented nanocrystalline bismuth antimony telluride thin films. Journal of Alloys and Compounds. 2010;**490**:L44-L47. DOI: 10.1016/j.jallcom.2009.10.117

[75] Liao C-N, Wang Y-C, Chu H-S. Thermal transport properties of nanocrystalline Bi-Sb-Te thin films prepared by sputter deposition. Journal of Applied Physics. 2008;**104**:104312. DOI: 10.1063/1.3026728

[76] Chang H-C, Chen C-H, Kuo Y-K. Great enhancements in the thermoelectric power factor of BiSbTe nanostructured films with well-ordered interfaces. Nanoscale. 2013;**5**:7017-7025. DOI: 10.1039/c3nr01499a

[77] Chang H-C, Chen C-H. Self-assembled bismuth telluride films with well-aligned zero- to three-dimensional nanoblocks for thermoelectric applications. CrystEngComm. 2011;**13**:5956. DOI: 10.1039/c1ce05350g

[78] Noro H, Sato K, Kagechika H. The thermoelectric properties and crystallography of bi-Sb-Te-se thin films grown by ion beam sputtering. Journal of Applied Physics. 1993; **73**:1252-1260. DOI: 10.1063/1.353266

[79] Tritt TM. Thermoelectric phenomena, materials, and applications. Annual Review of Materials Research. 2011;**41**:433-448. DOI: 10.1146/annurev-matsci-062910-100453

[80] Li Bassi A, Bailini A, Casari CS, Donati F, Mantegazza A, Passoni M, Russo V, Bottani CE. Thermoelectric properties of Bi-Te films with controlled structure and morphology. Journal of Applied Physics. 2009;**105**:124307. DOI: 10.1063/1.3147870

[81] Chang H-C, Chen T-H, Whang W-T, Chen C-H. Superassembling of Bi_2Te_3 hierarchical nanostructures for enhanced thermoelectric performance. Journal of Materials Chemistry A. 2015;**3**:10459-10465. DOI: 10.1039/c5ta00911a

[82] Wang G, Endicott L, Uher C. Recent advances in the growth of Bi-Sb-Te-Se thin films. Science of Advanced Materials. 2011;**3**:539-560. DOI: 10.1166/sam.2011.1182

[83] https://www.lairdtech.com/

[84] Martin J, Wang L, Chen L, Nolas G. Enhanced seebeck coefficient through energy-barrier scattering in PbTe nanocomposites. Physical Review B. 2009;**79**:115311. DOI: 10.1103/PhysRevB.79.115311

[85] Deng Y, Liang H-M, Wang Y, Zhang Z-W, Tan M, Cui JL. Growth and transport properties of oriented bismuth telluride films. Journal of Alloys and Compounds. 2011;**509**:5683-5687. DOI: 10.1016/j.jallcom.2011.02.123

[86] Zhang Z, Wang Y, Deng Y, Xu Y. The effect of (00l) crystal plane orientation on the thermoelectric properties of Bi2Te3 thin film. Solid State Communications. 2011;**151**:1520-1523. DOI: 10.1016/j.ssc.2011.07.036

[87] Peranio N, Eibl O, Nurnus J. Structural and thermoelectric properties of epitaxially grown Bi_2Te_3 thin films and superlattices. Journal of Applied Physics. 2006;**100**:114306. DOI: 10.1063/1.2375016

[88] Zou H, Rowe DM, Min G. Growth of p- and n-type bismuth telluride thin films by co-evaporation. Journal of Crystal Growth. 2001;**222**:82-87. DOI: 10.1016/S0022-0248(00)00922-2

[89] Kadel K, Kumari L, Li WZ, Huang JY, Provencio PP. Synthesis and thermoelectric properties of Bi_2Se_3 nanostructures. Nanoscale Research Letters. 2010;**6**:57. DOI: 10.1007/s11671-010-9795-7

[90] Sun Z, Liufu S, Chen L. Synthesis and characterization of nanostructured bismuth selenide thin films. Dalton Transactions. 2010;**39**:10883-10887. DOI: 10.1039/c0dt00840k

[91] Al Bayaz A, Giani A, Artaud MC, Foucaran A, Delannoy FP, Boyer A. Growth parameters effect on the electric and thermoelectric characteristics of Bi_2Se_3 thin films grown by MOCVD. Journal of Crystal Growth. 2002;**241**:463-470. DOI: 10.1016/S0022-0248(03)01511-2

[92] Walachová J, Zeipl R, Zelinka J, Malina V, Pavelka M, Jelínek M, Studnička V, Lošťák P. High room-temperature figure of merit of thin layers prepared by laser ablation from Bi_2Te_3 target. Applied Physics Letters. 2005;**87**:081902. DOI: 10.1063/1.2001755

[93] Venkatasubramanian R. Lattice thermal conductivity reduction and phonon localization like behavior in superlattice structures. Physical Review B. 2000;**61**:3091-3097. DOI: 10.1103/PhysRevB.61.3091

Section 2

Bismuth Materials for Radiation-Relevant Medical Uses

Chapter 4

Bismuth-Based Nano- and Microparticles in X-Ray Contrast, Radiation Therapy, and Radiation Shielding Applications

Hayden Winter, Anna L. Brown and
Andrea M. Goforth

Additional information is available at the end of the chapter

http://dx.doi.org/10.5772/intechopen.76413

Abstract

Bismuth has gained attention in preclinical research because of its ability to attenuate X-rays and high biocompatibility, which make it an excellent element for use in a biomedical agent or in radiation shielding. Developments in the synthesis of elemental bismuth nano- and microparticles, their X-radiation interactions, and their biological interactions will be reviewed in this chapter. The chapter will pay special focus to emerging medical applications of elemental bismuth nano- and microparticles, including the possibility of targeted molecular X-ray imaging, photo-thermal and X-radiation dose enhancing therapies for cancer treatment, and the construction of flexible radiation shielding materials and X-ray opaque devices.

Keywords: bismuth nanomaterial, contrast agent, therapeutic, X-ray imaging, X-ray shielding

1. Introduction to X-ray attenuating materials for medical applications

Ionizing radiation is used in many minimally invasive surgical techniques and diagnostic tests and is an invaluable tool for both its therapeutic and diagnostic benefit. Therapeutic radiation is used to treat cancers by delivering high doses of ionizing radiation to solid tumors, and diagnostic radiation imaging has been adapted for use in a broad range of medical disciplines including 2D conventional X-ray, 3D Computed Tomography (CT), and real-time

X-ray fluoroscopy imaging. Furthermore, interventional radiology has become its own medical specialty, and in many cases, constitutes an entire department within a modern hospital. Consequently, new materials to be used as X-ray contrast agents (XCAs), X-ray therapeutics, and in radiation shielding garments, have become an intensifying subject of materials research and development.

The X-ray attenuating and shielding properties of a given material are a function of the atomic number, density, and electron configuration of the interacting material. Neglecting K-edge effects, the general equation for the X-ray attenuation coefficient (μ) of an element is described in Eq. (1), where Z is atomic number, A is atomic mass, ρ is density, and E is the incident photon energy [1].

$$\mu = \frac{\rho Z^4}{AE^3} \tag{1}$$

However, X-ray radiation interacts with materials not only through scattering, but also by the photoelectric effect, which occurs at quantized energies characteristic of the atoms present. Thus, a general relationship between atomic number or density and X-ray attenuation is confounded by K-edge effects, where the K-edge is the energy of electrons in the K-shell with principle quantum number equal to 1. When an incident X-ray is at this energy (e.g., 90 keV for bismuth), it has a high probability of being absorbed, which results in a sharp increase in attenuation of incident photons. Furthermore, diagnostic X-ray imaging is typically performed with an X-ray tube voltage between 10 and 150 kVp, dependent on anatomical characteristics such as specimen thickness, and utilizes an energetically broad range of X-ray photons (**Figure 1A**) [2].

Including both scattering and photoelectric effects, plots of the calculated (i.e., theoretical) mass attenuation as a function of X-ray tube voltage are shown in **Figure 1B** for tungsten, lead and bismuth, where it can be seen that lead and bismuth have fairly similar X-ray attenuation per unit density over the majority of the incident photon range. In contrast, tungsten

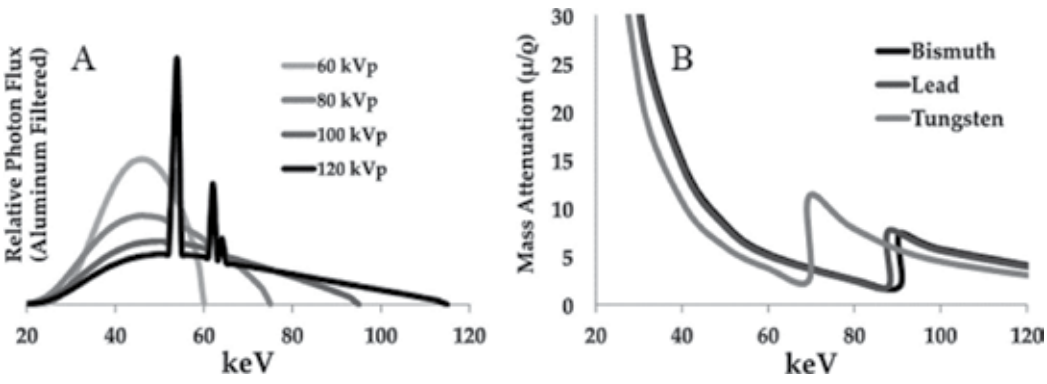

Figure 1. (A) The relative X-ray photon flux produced from a typical medical X-ray tube as a function of the X-ray tube voltage (kVp) after aluminum filtering, which removes lower energy X-rays. (B) The mass attenuation coefficient (μ/ρ) for bismuth, lead, and tungsten is shown as a function of X-ray photon energy (keV).

http://dx.doi.org/10.5772/intechopen.76413

has a lower mass attenuation than lead or bismuth, except in the range of 70–88 keV, where the K-edge effect increases the attenuation. However, keeping in mind that the incident photon flux of a medical X-ray instrument is polychromatic and dependent on the X-ray tube voltage, predicting quantitative contrast for compositionally different attenuating materials used under different instrumental conditions is difficult. Nonetheless, it is generally true that high Z, dense materials will attenuate X-rays to a greater extent relative to low Z, sparse materials, which makes inorganic nanoparticles attractive as X-ray imaging agents and shielding materials. Nanoparticles of elements such as tungsten ($Z = 74$), gold ($Z = 79$), lead ($Z = 82$) and bismuth ($Z = 83$), as well as compounds of these elements, have been considered attractive for this purpose and are the focus of much materials research in this field.

2. Inorganic nanoparticles as biomedical X-ray contrast and therapeutic agents

2.1. Challenges for developing biomedical X-ray-interacting agents

A multitude of challenges must be considered when designing a targeted X-ray-interacting agent for *in vivo* use. This includes how it will selectively and specifically identify its biological target, the dose required to attain X-ray contrast or therapeutic effect, how it will avoid immune response, and possible toxicity.

In terms of the dose required to achieve X-ray contrast, the goal of a targeted XCA for use in CT imaging is to raise the attenuation of a specific biological tissue type (i.e., a solid tumor) by elevating its average atomic number. CT signal strength is measured in Hounsfield Units (HU), where the signal strength of air is designated as −1000 HU and water as 0 HU; the quantitative contrast of an XCA is evaluated in terms of HU per mM (HU/mM) of the agent or attenuating atom. In a 3D reconstructed CT image, each three-dimensional voxel is assigned an HU value indicating its X-ray attenuation. Adjacent tissues can be differentiated by CT when the HU difference between them is at least three times greater than the background noise intensity [3]. Without artificial contrast, bones are clearly visible, but adjacent soft tissues must have substantially different densities to be distinguished.

Clinically available, small molecule XCAs (**Figure 2**), such as iopromide, iohexol, and iobitridol, use iodine ($Z = 53$) to increase the average atomic number of a tissue, and consequentially its HU value. These agents are limited to systemic imaging, as opposed to targeted imaging, since they are hampered by rapid kidney clearance from the bloodstream and a small number (<10) of high Z atoms per molecule. The quick renal clearance means that a radiologist must image a patient with precise timing relative to contrast agent injection. Additionally, long exposure times are commonly required for CT imaging, necessitating that the agent be delivered continuously during the procedure to ensure adequate contrast; this extended administration can result in kidney damage [4]. Furthermore, solutions of these agents are generally highly viscous at concentrations sufficient to give rise to contrast, resulting from the fact that CT imaging is poorly sensitive to contrast agent detection.

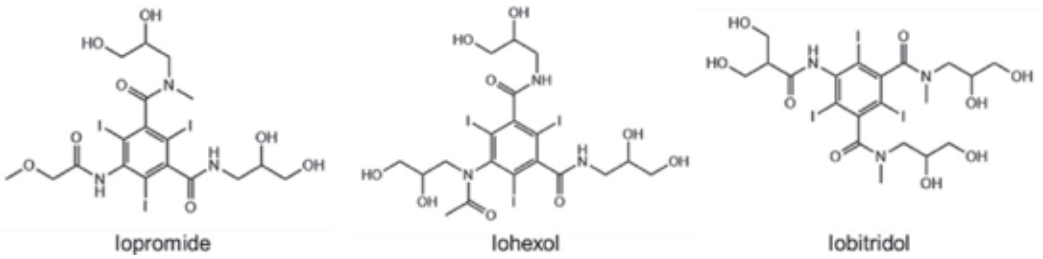

Figure 2. Three examples of iodine-based contrast agents currently in clinical use.

The limitations of current small molecule imaging agents drive the development of new XCAs that can deliver greater per unit contrast to specified biological targets, with longer blood circulation half-lives and less viscous agent doses. Thus, to overcome the high limit of detection of current, small molecule imaging agents and the low sensitivity of CT imaging, nanoparticles carrying thousands or millions of high *Z* atoms (**Figure 3**) may provide the requisite advantage and enable targeted CT imaging. So far, a variety of inorganic nanoparticles have been evaluated as potential X-ray attenuating agents, as further discussed in Section 2.2.

In terms of biological fate and toxicology, the bio-distribution and pharmacokinetics of inorganic nanoparticles is a complex topic. For the last decade, the enhanced permeation and retention effect (EPR) has been cited as a reason for nanoparticle accumulation in tumor tissues, a theory that is supported by multiple observations using a variety of types of nanoparticles. The EPR effect is explained by the large size of fenestrations in tumor vasculature, which are believed to enable uptake of particles as large as 200 nm in diameter. However, the EPR effect has been disputed, since many of the *in vivo* demonstrations of it have been performed in mice with transfected tumors, which are not necessarily reflective of naturally-occurring

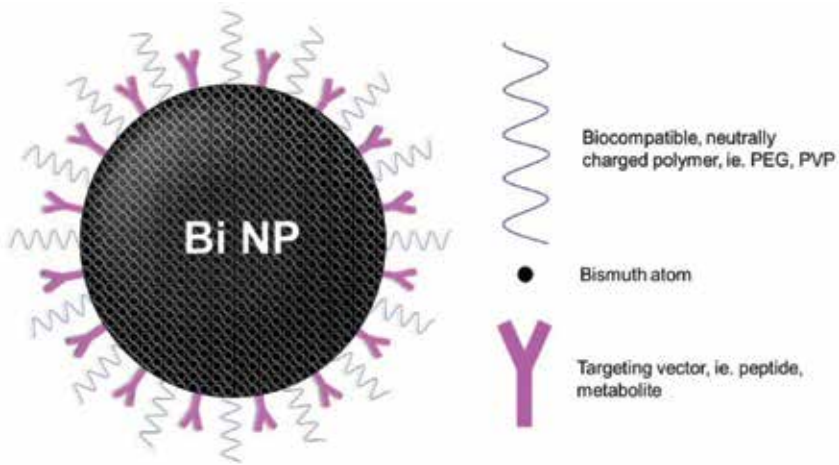

Figure 3. Representation of a targeted Bi NP XCA containing thousands or millions of high-Z bismuth atoms (e.g., a 50 nm Bi NP contains ~1 million Bi atoms). The targeting vector is chosen so that it specifically recognizes a biological receptor, such as a cell surface protein.

human tumors due to their disproportionately large sizes. Further, even in such disproportionately large tumors, low nanoparticle accumulation rates are commonly observed [5, 6].

Despite the absence of well-established principles concerning nanoparticle bio-distribution and fate, several empirically observed trends have been noted and are commonly considered in the design of biomedical agents. When considering the clearance strategy of an intravascularly administered nanoparticle agent, particle size is perhaps the most important variable. It is generally accepted that nanoparticles smaller than 6 nm can be removed by filtration though the kidneys, similar to many small molecules and ions. However, nanoparticles of all sizes can be eliminated by the mononuclear phagocyte system (MPS), a wide-ranging group of cell types that are capable of removing foreign objects from the bloodstream. This occurs due to the accumulation of proteins on the nanoparticle surfaces, which results in identification, uptake, and ultimately clearance by phagocytes. Other factors, including shape, surface charge, and surface chemical functionalities are also important determinants in the identification of nanomaterials by the MPS [7]. To date, a large number of nanoparticles that have been tested in pre-clinical settings have been observed to be sequestered from circulation by the MPS, never reaching their intended target. However, nanoparticles with an electrically neutral surface, and in particular those with polyethylene glycol (PEG) surface coatings, have been shown to accumulate proteins to a lesser extent, which slows MPS recognition and thus enables particles to stay in circulation longer.

2.2. Development of early nanoparticle X-ray contrast agents

The first demonstration of nanoparticles as XCAs was published by Hainfeld et al. [8], where ultra-small gold nanoparticles (Au NPs, ~2 nm) were imaged in an *in vivo* mouse model. The result was the enhancement of X-ray contrast throughout the specimen's entire vasculature 10 min post-injection, followed by eventual renal clearance. Additionally, in mice with transfected tumors, the Au NPs were shown to accumulate preferentially in the tumor, as opposed to healthy tissues, despite the absence of an active targeting molecule on the nanoparticle surfaces. After this study and its follow-up in 2006, Au NPs have been extensively researched as XCAs, as well as for X-ray sensitization (i.e., as agents causing radiation dose enhancement), photo-thermal imaging and therapy, and photo-acoustic imaging [9, 10].

The plethora of biomedical research using Au NPs has been enabled by the development of reliable Au NP synthesis methods, which have resulted in Au NPs with well-defined sizes and low size polydispersity; such Au NP formulations are now readily commercially available. However, while this availability has made Au NPs crucial to the demonstration of nanomaterial-based imaging and therapies, the use of larger Au NPs is limited by poor biological clearance, since elemental gold is quite inert under physiological conditions [11–14]. The oxidative stability of elemental Au presents an apparent advantage in that decomposition products are not expected to interfere with biochemical processes, but also results in the demonstrated disadvantage that Au NPs show high levels of bioaccumulation because they cannot be rapidly degraded into small, molecular species. This has limited several *in vivo* applications, including targeted X-ray imaging, that would benefit from larger (i.e., >6 nm) NPs to achieve detectable radiation interactions.

While many researchers continue to work with Au NPs and look for ways to bypass this issue, there is a widening field of researchers who have focused their work on the development of

bismuth-based nanomaterials as X-ray interactive biomedical agents. A landmark publication demonstrating the use of bismuth-containing XCAs by Rabin et al. illustrated the potential of bismuth(III) sulfide nanoparticles (Bi_2S_3 NPs) in an *in vivo* mouse model [15]. The plate-shaped nanoparticles ranged from 10 to 50 nm on their longest sides, and the surfaces were coated with polyvinylpyrrolidone (PVP), a well-established biocompatible polymer. These PVP-coated Bi_2S_3 NPs showed a superior CT brightness compared to iopromide, a clinically used iodine-based contrast agent, and had a blood circulation half-life of 140 ± 15 min, which is substantially greater than the circulatory half-life of clinical iodinated XCAs. Furthermore, the Bi_2S_3 NP formulation resulted in greater contrast while administered at a lower concentration and as a lower viscosity solution.

Another study of note that utilized Bi_2S_3 NPs as XCAs was performed by Kinsella et al. [16]. In this study, size monodisperse ~10 nm Bi_2S_3 NPs were prepared and surface-coated with the amphiphilic polymer 1,2-distearoyl-*sn*-glycero-3-phosphoethanolamine-N-(amino(polyethylene glycol)) (DSPE-PEG) to produce an uncharged, hydrophilic product. The DSPE-PEG-coated Bi_2S_3 NPs were further conjugated to the LyP-1 peptide, which is a surface antigen for the p32 protein that is over-expressed in several human carcinomas. The accumulation of DSPE-PEG-coated Bi_2S_3 NPs in the tumor was observed to be increased by 70% with the addition of the LyP-1 targeting peptide, although both targeted and untargeted NPs produced adequate contrast to image the tumor. Ultimately, the DSPE-PEG-coated Bi_2S_3 NPs were removed by the hepatic/fecal route, as evidenced by the enhanced contrast of the intestines after a 7-day period. Overall, this publication demonstrated that: (1) even with a fairly small bismuth-based XCA in which the high Z bismuth payload is diluted by sulfur (Z = 16), contrast can be superior to that found in commercial iodinated XCAs, and (2) peptide-mediated active tumor targeting can increase efficacy when designing an intravenous agent.

Despite the successful demonstrations of Au and Bi_2S_3 NPs as XCAs, elemental bismuth nanoparticles (Bi NPs) can be argued to have significant advantages that make them potentially more promising as targeted XCAs. Relative to Au and Bi_2S_3, elemental Bi has a higher overall average atomic number, thus taking greater advantage of the general Z^4 increase in X-ray attenuation. Additionally, elemental Bi is semi-stable with respect to oxidative dissolution, making it more readily biodegradable relative to Bi_2S_3 and Au, and therefore potentially permitting the use of larger particles. Furthermore, the degradation of elemental bismuth into bismuth ions (Bi^{3+}) at physiological pH is expected to occur slowly enough to ensure that the concentration of Bi^{3+} in the blood stays below toxic levels, and the resulting Bi^{3+} complexes are expected to be small and highly biocompatible, thus presenting the opportunity for renal clearance [17, 18]. Finally, similar to many nanoparticles composed of other elements, elemental Bi shares the ability to absorb X-ray, visible, and near-IR radiation, which presents opportunities for additional imaging and treatment modalities that use longer wavelength radiation compared to X-rays.

The remainder of this chapter includes summarizing currently published synthetic strategies for producing aqueous Bi NPs and reviews the biomedical research that has so far explored these materials as XCAs, photo-therapeutic agents, and X-ray shielding materials in biomedical settings. Lastly, we discuss the future of Bi NPs in medical imaging and therapeutic technologies.

http://dx.doi.org/10.5772/intechopen.76413

3. Bi nanoparticles for *in vivo* X-ray applications

3.1. General synthesis considerations for producing medically useful Bi nanoparticles

While Bi NPs are a desirable platform for *in vivo* X-ray contrast and therapeutic applications owing to their dense, un-diluted payload of high *Z* atoms, synthesis of these materials is generally more difficult and less versatile than other high *Z* nanomaterials. This is most notable in contrast to precious metal nanoparticles of gold, silver, and platinum, which have high oxidative stability. The primary difficulty in synthesizing elemental Bi NPs is oxidative decomposition, which has led to a prevalence of anaerobic synthetic strategies to prevent oxidation by O_2. These methods often utilize air-sensitive or pyrophoric reagents in the reduction of a Bi^{3+} precursor in the presence of surface-terminating ligands. Furthermore, apolar solvents and hydrophobic ligands are most frequently used to avoid oxidative dissolution of the reduced Bi NPs by H_2O, which results in products that are not water-dispersible as-prepared. Thus, further ligand coating or polymer wrapping is a common strategy to render stable, aqueous Bi NPs, although such strategies result in less X-ray dense particles with additional pharmacological complexity.

We have recently reviewed Bi NP synthesis methods that produce some of the lowest polydispersity hydrophobic and hydrophilic Bi NP colloids at this time, with their associated size metrics (see Supporting information of reference [19]). However, research by our group and several others, has focused on the synthesis of Bi NPs in aqueous or otherwise polar conditions, as well as scalable production. In general, published aqueous and polar phase syntheses of Bi NPs have rarely approached the colloidal stability, chemical stability, and size monodispersity observed in anaerobic, apolar systems. Nonetheless, a few notable synthetic methods have produced aqueous colloids of Bi NPs that are potentially biomedically useful, which are further discussed in Sections 3.2 and 3.3.

3.2. Syntheses of hydrophilic bismuth nanoparticles and demonstration as CT contrast agents

In a polar phase Bi NP synthesis method developed by our group, Bi^{3+} (from Bi(III) nitrate) was reduced by co-reductants morpholine borane and glucose using 1,2-propanediol as solvent to result in hydrophilic Bi NPs in a single step. The resultant Bi NPs (**Figure 4A**) were observed to have an average diameter of 74 ± 14 nm by transmission electron microscopy (TEM), [20] and it was determined that the presence of the reducing sugar (i.e., glucose) in the formulation enhanced Bi NP oxidative stability in the resulting aqueous colloids. This synthetic method has several attractive features for biomedical usage, including a substantial product yield, reproducibility in the size and size distribution of the products obtained, and use of low cost reagents that are relatively biologically benign. Furthermore, because a polymeric surface stabilizer is not used, the Bi core constitutes the majority of the overall particle volume, representing a dense X-ray opaque payload.

We have shown that the oxidative stability of the Bi NPs prepared in this way is sensitive to pH, with the Bi NPs decomposing into soluble Bi^{3+} species at physiological pH (7.4) within

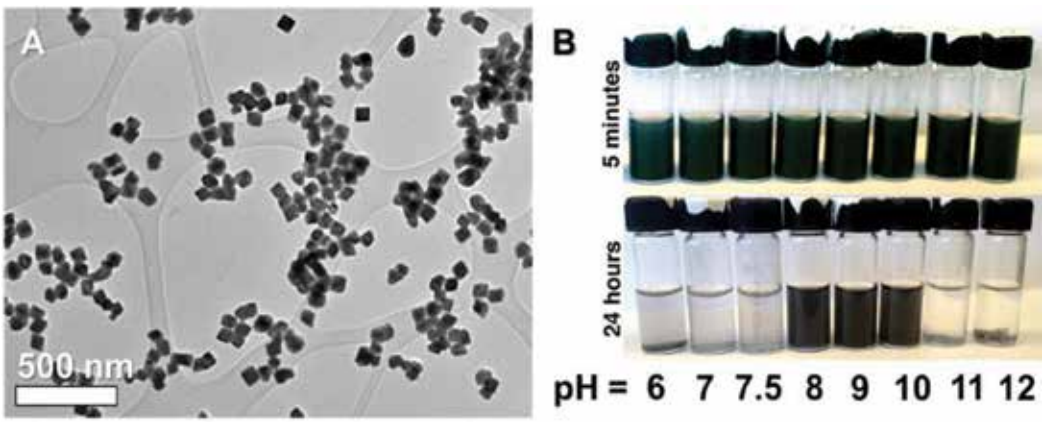

Figure 4. (A) TEM image of Bi NPs synthesized *via* reaction of morpholine borane and glucose with bismuth (III) nitrate in 1,2-propanediol. (B) Photographs showing pH stability of the Bi NPs 5 min (top) and 24 h (bottom) after they are dispersed into aqueous solution (reprinted with permission from reference [21]).

24 h (**Figure 4B**) [21]. This observation suggests a possible mechanism for biological clearance, which has been a substantial clinical translation hurdle for Au NPs. The glucose-stabilized Bi NP colloids were also tested *in vitro*, where no observable cytotoxicity was observed within 1 h in either a cancer or a macrophage cell line at concentrations up to 0.5 mg/mL, suggestive of good biocompatibility. However, at 24 h, the macrophage cell line viability dropped, having an LD50 of 50 μg/mL due to an observed high concentration of internalized Bi NPs.

In a study of quantitative contrast using a clinical CT scanner to image a non-biological phantom (**Figure 5A**), the Bi NPs produced by this method were shown to generate an X-ray contrast of approximately 6 HU/mM Bi (**Figure 5B** and **C**), which is greater at all kVp in comparison to an iodine-based standard, and more than double that of the iodine-based standard at 140 kVp (**Figure 5C**). Additionally, the quantitative X-ray contrast of the Bi NPs was observed to be relatively insensitive to the operating voltage of the CT scanner, performing similarly over the range of 80–140 kVp, while the contrast of an iodinated agent decreased sharply with increasing operating voltage (**Figure 5C**). This synthesis method has since been used and further modified to produce Bi NPs that have been studied *in vivo*. [22, 23]

Li et al. adapted the synthesis method described above to demonstrate X-ray contrast *in vivo* using ~40 nm Bi NPs, which had been additionally PEG-coated to further increase biocompatibility [23]. In non-biological phantom studies, these PEG-coated Bi NPs generated 3.7 times as much contrast as equimolar iopromide, with the measured X-ray attenuation being 60.3 HU/(mg/mL) for the Bi NPs as compared to 16.4 HU/(mg/mL) for the iodinated agent under the same instrumental conditions. *In vitro*, no marked cytotoxicity was observed in either a cancer or an endothelial cell line at concentrations up to 300 μg/mL, although endocytosis was observed, as we also noted. In an *in vivo* study of tumor bearing mice, the PEG-coated Bi NPs were injected intravascularly and were observed to slowly accumulate in tumor tissue over the course of 6 hours, at which time the CT contrast was highest. This degree of non-targeted accumulation in a tumor is higher than that of smaller Bi NPs and was attributed to the EPR effect.

http://dx.doi.org/10.5772/intechopen.76413

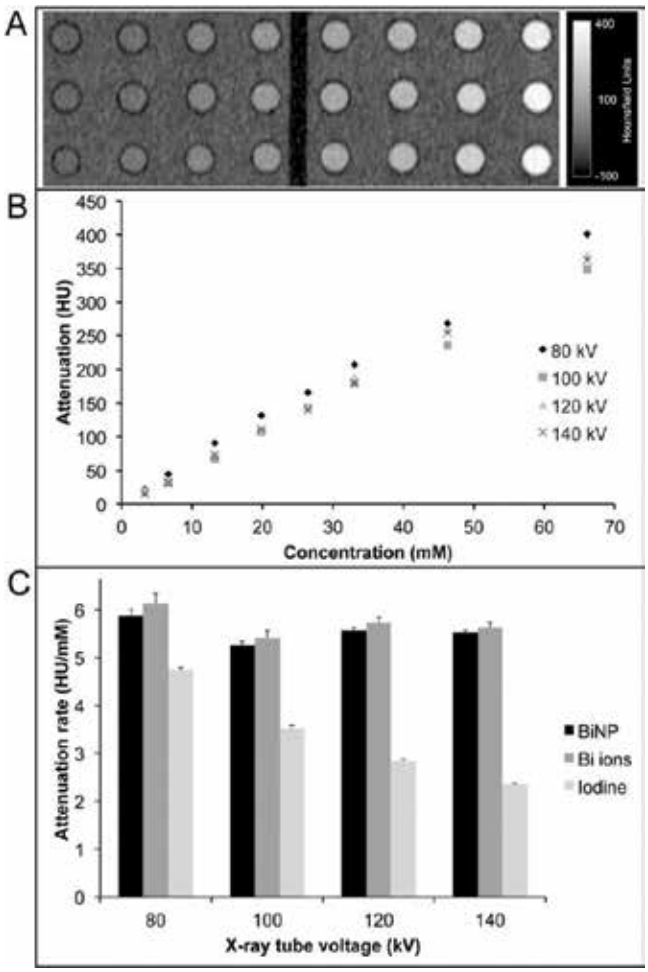

Figure 5. (A) CT image of a concentration gradient of aqueous Bi NP solutions suspended in a non-biological phantom, ranging from 0 to 70 mM Bi in the wells from left to right. (B) The CT attenuation of Bi NP solutions as a function of Bi atom concentration at various operating voltages. (C) Attenuation rates of Bi NPs, ionic bismuth, and ionic iodine in water at various operating voltages. Reprinted from reference [20] with copyright permission from the American Chemical Society. The full text of the article can be found at https://pubs.acs.org/doi/full/10.1021/cm500077z and further permissions related to this material should be directed to the ACS.

However, this observation may in part be due to the large size of the Bi NPs, which are expected to have a long circulation half-life in the bloodstream prior to renal clearance.

Another synthesis method used to make Bi NPs in polar media was developed by Lei et al., which accomplished the reduction of Bi^{3+} using $NaBH_4$ in a glycerol/ethanol solvent mixture and used polyvinylpyrollidone (PVP) to control size [24]. Since the PVP-coated Bi NPs were hydrophilic as-prepared, no further surface modification was required for *in vitro* or *in vivo* work, although the addition of 5 wt% glucose to aqueous solutions of these Bi NPs was also tested. The resultant PVP-coated Bi NPs had an average core diameter of 2.7 ± 1.1 nm by TEM, which is notably substantially smaller compared to the Bi NPs discussed above. However, in non-biological phantoms, dispersions containing the ultra-small, PVP-coated Bi NPs provided approximately 2 times greater contrast than equimolar iobitridol at 120 kVp, with the measured X-ray attenuation

being 7.1 and 3.9 HU/mM for the Bi NP and iobitridol samples, respectively. This study did not observe cytotoxicity in *in vitro* studies using up to 500 μg/mL Bi NP samples.

Lei et al. first assessed the *in vivo* CT contrast of the ultra-small, PVP-coated Bi NPs by intra-tumoral injection, which showed exceptional CT contrast for the tumor. Encouraged by these results, the Bi NPs were administered intravenously and the bio-distribution was monitored. The *in vivo* bio-distribution studies revealed some accumulation in the liver and spleen that had decreased by the 24-h time point, while continued accumulation up to 24 h was observed in the tumor. The HU value of the tumor tissue was observed to increase slowly from 30.3 HU before injection to 53.8 HU at 24 h post-injection, suggesting a slow and passive accumulation of the nanomaterial in the tumor. The Bi NPs were apparently excreted intact within 7 days. Further, using a healthy specimen, a complete blood panel done following an *in vivo* bio-distribution assay revealed that the Bi NP-treated tissues were not significantly different relative to untreated specimens. The further demonstration of a therapeutic application of these ultra-small, PVP-coated Bi NPs is discussed in Section 3.3.

A study by Yu et al. also applied ultra-small Bi NPs as both an XCA and a therapeutic agent [25]. In this study, Bi NPs with an average diameter of 3.6 nm were synthesized by hot injection of a solution containing Bi^{3+} into oleylamine, which acted as solvent, reducing agent, and surfactant. These initially hydrophobic Bi NPs were then made hydrophilic by coating with DSPE-PEG, and further functionalized by covalently attaching LyP-1, a peptide that associates with membrane proteins over-expressed in some cancerous cells. In non-biological phantoms, the Bi NPs generated approximately 3 times greater contrast than equimolar iohexol, with the measured attenuation rates being 13.8 and 4.28 HU/mM for the Bi NPs and iohexol at 80 keV, respectively. Upon intra-tumoral injection, the Bi NP-loaded tumor was clearly visible by CT imaging, having a voxel intensity of >1000 HU, though this result is not extensible to intravenous (IV) administration. However, the bio-distribution and extent of tumor accumulation after IV injection was also examined, which is discussed in Section 3.3 in the context of the use of the LyP-l-DSPE-PEG-coated Bi NPs as a photo-therapeutic agent.

Overall, in the studies noted above, hydrophilic Bi NPs universally outperformed iodinated XCAs by two- to four-fold in terms of contrast at fixed concentrations and had greater blood-circulation half-lives, which demonstrated promise for the use of Bi NPs as lower-dose systemic X-ray contrast agents. Further, the extent of passive tumor accumulation and CT contrast observed in *in vivo* studies demonstrated the possibility of using the Bi NPs to discern diseased tissues, which can be further enhanced by active tumor targeting, i.e., by the addition of pathology-specific recognition groups to the Bi NP surfaces. Additionally, bio-distribution studies of ultra-small (<6 nm) Bi NPs showed that they are cleared largely through the kidneys [24, 25], while larger Bi NPs tend to be cleared hepatically [22, 23]. In addition to their promising application in CT imaging, other biomedical utilities of aqueous Bi NP colloids are further discussed in Section 3.3.

3.3. Applications of Bi nanoparticles in therapeutics

As many nanomaterials have been shown to accumulate in solid tumors, the use of photon therapies that can excite a functional nanomaterial to produce a local and lethal effect on surrounding cells is an active area of cancer research.

http://dx.doi.org/10.5772/intechopen.76413

One example of a photon therapy is photo-thermal therapy, which uses near infrared (NIR) or visible radiation to raise the local temperature of a biological tissue above 48°C, leading to irreversible protein denaturation and aggregation within 4–6 min [26]. NIR radiation is of particular utility in the field of photon therapeutics due to relatively long wavelengths that result in large (~10 mm) tissue penetration depths and low tissue ionization. Bi NPs broadly absorb both visible and NIR radiation, and afterwards vibronically relax to produce heat, which makes Bi NPs a candidate for use as NIR-photo-thermal therapy enhancement agents.

The above referenced study by Lei et al. demonstrated the use of Bi NPs for photo-thermal imaging and therapy [24]. As aqueous colloids, the NIR-to-thermal conversion efficiency of ~3 nm PVP-coated Bi NPs was determined to be as high as 30%, which is higher than for other photo-thermal agents including gold nanoparticles. In a preliminary *in vivo* study using tumor-bearing mice (having both experimental and control specimens), the efficacy of Bi NPs as photo-thermal agents was established by IV administration of 20 mg/kg Bi NPs, which passively accumulated in the tumor of the experimental specimen over the course of 24 h. After 24 h, both control and experimental specimens were subjected to NIR photo-therapy using 808 nm incident light at a power of 1.3 W/cm^2; the temperature of the tumors was monitored using an IR camera. Within 6 minutes, a temperature change of 25°C (to ~65°C) was observed in the tumor tissue of the Bi NP-treated specimen, while the temperature of the control specimen had only increased modestly (<5°C). In further *in vivo* experiments, infrared cameras were used to image the tumor temperature of specimens in four groups, as follows: (1) those not treated with Bi NPs or NIR light, (2) those treated with NIR light only, (3) those treated with Bi NPs (by IV injection) only, and (4) those treated with both NIR light and Bi NPs (by IV injection). The photo-thermal treatment, when applied, delivered 808 nm incident light at a power of 1.3 W/cm^2 and was administered 24 h following the Bi NP injections. For specimens in these groups, the relative tumor volume was monitored over a period of 14 days, and it was observed that in the groups treated with only Bi NPs or only NIR light, the tumor volumes grew at the same rate as the untreated control. However, a significant growth inhibition (~10% the size of the other groups) was observed for the group receiving Bi NPs in combination with NIR therapy, which demonstrated that the local heating correlated with cancer tissue death. Overall, these results showed that ultra-small, passively accumulating Bi NPs could be useful as a photo-thermal therapy agent.

Another possible therapeutic application for Bi NPs is their use in radiation dose enhancement during X- or gamma-ray treatments. Currently in the United States, over half of all cancer patients will receive a form of radiation therapy, typically using extremely high-energy photons in the MeV range. The drawback of this type of treatment is damage incurred to surrounding healthy tissues, which typically limits the radiation doses delivered to patients. Thus, there is a desire to lower the radiation dose delivered to patients while maintaining the efficacy of the radiation therapy for the treatment of cancers. To address this limitation, the development of materials that can enhance the local ionizing effects of radiation could make these treatments substantially more effective. So far, several nanomaterials (e.g., gold nanoparticles and hafnium oxide nanoparticles) have demonstrated an increase in local ionizing damage when used with keV radiation in small animal models, and some are currently in clinical trials [27–32]. However, as outlined above in the context of XCAs, bismuth has

a number of unique advantages for biomedical applications, which should remain true for their application as radiation dose enhancing nanoparticles. Furthermore, not only do Bi NPs attenuate X-rays far more efficiently than soft tissue, they have also been shown to produce photo-generated, ionizing chemical species, which can potentially be leveraged to contribute cellular damage. The mechanisms by which nanoparticles enhance cellular damage from radiation likely involves a multitude of reactions, and is a topic of current investigation [27].

Two groups have recently demonstrated the ability of Bi NPs to multiply local radiation ionization events upon excitation by X-rays in the keV energy range. For example, Yu et al. co-administered 3.6 nm DSPE-PEG-coated Bi NPs with a single dose of 4 Gray (Gy) radiation to tumor-bearing mice. [25] After 14 days, tumor growth rates of the Bi NP/radiation-treated mice-were 33% lower than those treated by radiation alone. In the same study, Yu et al. also found that Bi NPs collected from the urine and feces of mice 24 h after injection had the same size and morphology as when they were initially injected, demonstrating that the 3.6 nm DSPE-PEG-coated Bi NPs can be cleared but not significantly degraded in this timeframe [25]. Another study by Deng et al. showed similar results using 50 nm PVP-coated, untargeted Bi NPs, slowing tumor growth by 43% over a 14 day period. [22] Further modification was performed on these Bi NPs, including conjugation of the biological-targeting group folate and encapsulation within red blood cell membranes. Here, it should be noted that nanoparticles with folate surface ligands have previously shown increased accumulation in multiple cancerous tissues types that overexpress folate receptors. The authors observed that when the RBC-modified, folate-targeted Bi NPs were used, tumor growth rates were reduced by more than 50% compared to radiation alone, and mouse survival rates over 36 days increased from 0 to 60%.

Overall, the studies of Bi NPs as photo-therapuetic agents have shown that a synergistic combination of NIR or X-ray radiation with intravascularly administered Bi NPs can significantly impact tumor growth rates. In addition, several of these recent *in vivo* studies have included monitoring for possible tissue damage or changes in blood serum concentrations after administration of Bi NPs and radiation [22–25]. These studies have revealed that while tumor tissue samples tend to show damage from the co-administration of Bi NPs and radiation, tissues in the heart, lungs, spleen, liver, and kidneys have all been found to remain undamaged. Thus, the use of Bi NPs in NIR and X-ray photo-therapies may prove useful for increasing the efficacy of these procedures in cancer treatments. Finally, while we have discussed the use of Bi NPs as both imaging and therapeutic agents in the former sections, we end this chapter by discussing the use of Bi nano- and microparticles in macroscopic radiation-attenuating tools, such as personal protective equipment and imaging guides.

4. Bi nano- and microparticles for X-ray shielding in medical applications

4.1. Current status of X-ray shielding materials

There is a substantial call from the medical community for improved radiation shielding garments for medical personnel who regularly work in proximity to high-energy radiation [33].

http://dx.doi.org/10.5772/intechopen.76413

Increased awareness of the harmful stochastic effects of radiation exposure, coupled with an increase in the number of medical procedures (primarily X-ray fluoroscopy) and the increased X-ray voltages required for imaging larger patients, have raised concerns about accumulated radiation exposure to medical personnel [34, 35]. Research has shown that medical personnel who regularly work with high-energy radiation are particularly susceptible to, and have increased incidences of, specific types of cancer [36]. Because of the ubiquitous use of ionizing radiation in medicine, specialty garments, tools, and devices have been developed, both for protection against the harmful effects of radiation, as well as for use with radiation imaging.

In radiation imaging, such tools include catheters that contain platinum wires for use with fluoroscopic imaging and gold fiducial markers that are surgically embedded in a patient to provide guides in CT imaging and therapeutic radiation delivery [37]. In personal protective equipment, radiation-interacting (or shielding) materials include specialized rooms with lead-lined walls, leaded glass viewing areas, and lead-based radiation protective garments. More recently, specialized drapes and blankets have become available.

Personal radiation shielding garments have historically been composed of lead salts (e.g., $Pb(II)SO_4$) embedded into a plastic matrix to form a wearable composite material. This design results in a hard, brittle composite containing a large percentage of lead salt (>60%) by weight. This composite is then encased between heavy vinyl sheets to keep the lead from contacting the wearer. The weight burden from lead is roughly 50% of the overall garment weight, with the plastic casing composing the remainder. Recently the isolation of lead dust by this design has caused lead aprons to become a suspected source of lead poisoning in medical settings [38]. Lead aprons are the most commonly encountered garment of this type and by design these are worn as an X-ray shield to protect the torso and upper legs, leaving the head, neck, and arms exposed to radiation. Garments designed to shield additional areas, such as thyroid, gonads and breasts, and less commonly, the head and hands, are also sparingly used in medical environments, but are extremely bulky and cumbersome.

Lead is heavy, toxic, and environmentally damaging, which makes it a good candidate for replacement by alternative elements that can provide good X-ray shielding. Lightweight shielding materials containing lower atomic number elements have been developed and are marketed specifically to address the weight burden issue that lead-based garments suffer from. In these products, the lead salt is replaced with a mixture of salts of lighter elements, including barium, tin, tungsten, and some lanthanoids. These garments are tested and marketed as having a "lead shielding equivalent" at a specific tested X-ray voltage. However, when tested over a range of X-ray voltages (kVp), other than the voltage they were optimized for, they can show an inadequate radiation attenuation. [39] X-ray attenuation is reported in "mm of lead" and as a kVp is not specified for this testing, this has enabled manufacturers to report misleading shielding data and has raised concern for medical personnel who rely on these garments for protection [40].

For high performance X-ray contrast devices, such as catheters or other medical devices that are surgically inserted, tungsten particles or platinum wires are generally utilized. Use of these elements also has drawbacks, including difficulty in manufacturing and processing. Tungsten is extremely hard, requiring specialized equipment to process, while platinum is extremely expensive (>$13,000/lb) and is thus limited to use in small devices, such as catheter tips.

Bismuth is an excellent candidate for lead replacement in garments and platinum and tungsten replacement in surgical devices. Relative to lead, it has a similar or higher X-ray attenuation cross-section, but is non-toxic. Bismuth has a lower melting point relative to tungsten (272 vs. 3422°C) and is much softer (2.2 vs. 7.5 Mohs hardness), making it much easier to machine. The challenge with adapting bismuth for use in shielding garments has historically been the price of raw material. Though much cheaper than platinum and somewhat less expensive than tungsten (approximately $20 per pound), bismuth prices have fluctuated widely over the past decades from $3 to $30 per pound, while lead has historically been roughly $1 per pound. Incorporating bismuth particles into medical devices has been explored by device manufacturers, but the low oxidative stability of bismuth during processing has limited manufacture adaptation. However, we have recently developed a method for the production of surface-stabilized Bi nano- and microparticles that are easily polymer-dispersed for use in medical devices and protective garments, which are described in Section 4.2 [41].

4.2. Fabrication of Bi nano- and micro-composites for X-ray shielding applications

We have recently developed a method to produce microscopic, surface-passivated bismuth particles for the creation of plastic X-ray opaque composites [41]. To produce the surface-passivated, micron-sized bismuth material we utilize high-energy ball milling of bismuth ingot in various organic solvents or other surface coordinating ligands. The organic passivants coat the freshly fractured Bi crystallites, thus minimizing surface oxide formation. Particles produced are of a broad range in size (from a few hundred micrometers, down to the nanometer scale) and can be size selected for a specific application. Excess particles are easily melted on the bench top and the bismuth can be recovered and recycled though the milling and passivating process. Furthermore, the wide choice of organic solvent also permits tuning the particle hydrophilicity and chemical functionality to permit dispersal of the micrometer scale bismuth domains into a variety of plastics. As examples, we have produced hydrophilic bismuth microparticles by milling in the presence of dihydroxyacetone (DHA) and 1,2-propane diol, and hydrophobic bismuth microparticles by milling in the presence of in 1-pentene, or styrene, and toluene. The resulting bismuth microparticles suspended in their milling solvents are generally collected by centrifugation, washed with an appropriate solvent, dried, ground to a fine powder and sieved to collect particles in a narrow size range. Such organic-passivated, size-selected particles can then be mixed into molten or uncured polymers such as silicone, polyurethane, polystyrene, and latex to form X-ray opaque polymer composites **Figure 6**(**A**-**C**). The weight percent of the micron-sized radiopaque filler in these composites can be readily calculated and varied over a wide range. We observed that the bismuth microparticles embedded in these composites do not undergo substantive oxidative decomposition, nor do they aggregate within the polymeric matrix.

We tested one possible application of such composite materials for the fabrication of radiopaque surgical sponge markers, which are commonly used in surgery to avoid retention of foreign objects [21]. In doing so, we prepared polyurethane composites containing 20, 40, 60, and 85 wt% of our bismuth micron material and compared them to a commercial sponge marker. The commercial sponge marker was produced by Medline Industries and is reported to be a polymer-salt composite of polyvinylchloride containing between 60 and 83% $Ba(II)SO_4$ as the radiopaque filler. Our composites were prepared by mixing uncured liquid polyurethane with

http://dx.doi.org/10.5772/intechopen.76413

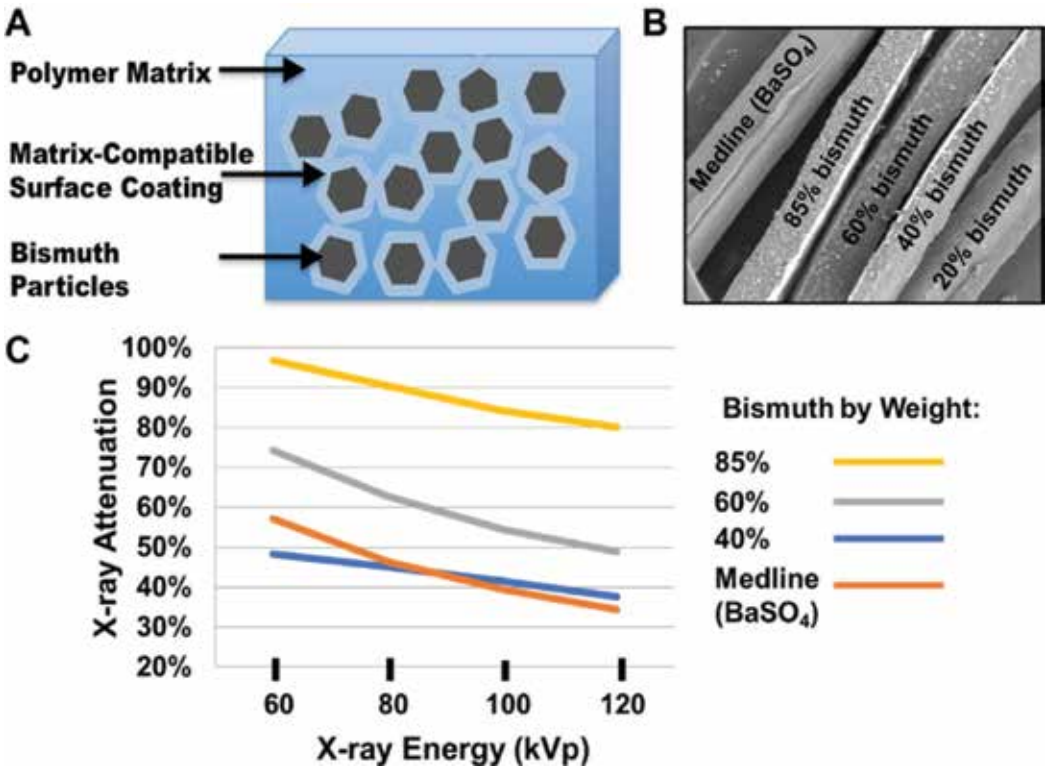

Figure 6. (A) Components of a composite X-ray shielding material. (B) SEM of polymer/filler composite materials with varied mass percent of filler (bismuth microparticles or $BaSO_4$). (C) X-ray attenuation of bismuth microparticle- and $BaSO_4$-containing X-ray shielding materials at various operating voltages (reprinted with permission from reference [21]).

dried, sieved DHA-coated bismuth microparticles, and the resulting mixture was molded using Teflon plates to produce a "ribbon" of similar thickness to the commercial sponge marker.

To compare attenuation of the commercially available surgical sponge marker to the bismuth composite markers, X-ray attenuation measurements were performed by an external analytical laboratory across a range of medically relevant incident photon energies. The composite samples tested were 0.56, 0.55, 0.51 and 0.64 mm thick for the Medline, 40, 60 and 85% by weight bismuth markers, respectively. The attenuation of the commercial composite only exceeded the attenuation of the 20% bismuth composite across all energies, and the 40% bismuth composite at incident photon energies below 80 kVp. However, superior attenuation across all voltages was observed for the 60 and 85% bismuth composites as compared to the commercial composite. For the 85% bismuth composite, the percent X-ray attenuation was nearly 100% at 60 kVp, more than double that of the commercial marker. Further, the 85% bismuth marker was determined to have a lead equivalent X-ray attenuation of 0.21 mm, which would indicate that a 1.2 mm thick sheet of the 85% bismuth composite material would provide similar radiation protection to the lead aprons commonly used in medical facilities (0.5 mm lead equivalent attenuation) [38]. While this is thicker than a sheet of solid lead, the low toxicity of bismuth means that the

shielding material can be placed directly against the skin, and will not require thick protective layers around the functional material. As a substantial portion of the weight burden from lead shielding garments is a result of the vinyl sheeting required to isolate the lead, we estimate that a bismuth particulate shielding garment would be roughly half the weight of a lead garment.

We expect the radiopaque bismuth micromaterial filler we have produced will find use in a variety of thin, flexible plastic composites that can be molded into 3D shapes (such as hats, gloves, or long-sleeved shirts) to provide an improved form factor relative to current technologies. Fabrication of thin, flexible X-ray opaque composite materials should enable better engineering of shielding garments, specifically in regards to the weight burden and flexibility restriction on the wearer.

5. Summary and prospectus for the future of bismuth nano- and microparticles in biomedical X-ray applications

New synthetic methods for producing hydrophilic Bi NPs in the 2–100 nm size range are increasingly reported. As interest in adapting new nanomaterials for biomedical applications continues to grow, it is expected these materials will be further explored and find new niche applications or facilitate development of new technologies in nanomedicine. Bismuth nanoparticles have demonstrated superior X-ray contrast by CT imaging, which exceeds the clinical standard of iodinated X-ray contrast media by 2–4-fold. This may permit the use of systemically administered Bi NPs as lower dose, lower viscosity, and lower toxicity contrast agents. The passive accumulation of untargeted Bi NPs in tumors has demonstrated a high tumor CT signal and has been shown to provide a means of sensitizing cancer tissues to local radiation damage using NIR and X-ray photo-therapies. Additionally, the replacement of lead in personal shielding garments has the potential for development of new and more practical personal protective equipment. The high biocompatibility, low cost, and exceptional X-ray attenuation of bismuth make this unique element a rising star in the application of new technologies in radiation medicine.

The future of hydrophilic Bi NP contrast and therapeutic agents will likely see more active biological targeting studies, with the goal of using Bi NPs to selectively and specifically seek out known biochemical markers of disease. The specific biomarkers of disease that are the target of molecular imaging and therapy are known to be present at low concentrations (10^{-9} to 10^{-10} M), necessitating that the imaging modality used is capable of detecting imaging agents at similarly low concentrations [42]. Since the limit of detection of CT imaging is high, this would necessitate the delivery of a large number of X-ray attenuating atoms to a highly localized area, which may be possible with pathology-targeted, high *Z* nanoparticles. To estimate how many Bi NPs this would require, achieving a 100 mM concentration of Bi in a 1 mm^3 volume would require 10^{-7} mol of Bi, which for uniform 150 nm Bi NPs is approximately 10^9 Bi NPs. Given a reasonable tumor cell density of 10^6–10^7 cells/mm^3, 1–10 Bi NPs per tumor cell would be needed [43]. Further bio-distribution studies of IV injected pathology-targeted Bi NPs would be needed to determine whether this is possible, and to establish the actual limit of detection.

In the majority of the studies reviewed above, favorable *in vitro* and *in vivo* biocompatibility was observed for hydrophilic Bi NPs. However, so far, only ultra-small Bi NPs have a predictable and practical biological clearance mechanism *via* renal filtration, while the larger Bi NPs that could be most useful as targeted imaging agents are unpredictably endocytosed. Endocytosis of larger Bi NPs may be useful if they are selectively uptaken by disease tissue and used in a photo-dynamic therapies, but this would be limiting in a targeted imaging application. Consequently, further research may involve the encapsulation of ultra-small Bi NPs into larger structures, such as blood cells, liposomes, polymeric aggregates and other nano-sized drug-delivery motifs. The goal would be to maximize the overall aggregate signal in a small volume host, while permitting renal clearance of the payload after release from the host. Alternatively, the use of large Bi NPs may be achievable if surface stabilization strategies or appropriate formulations could be designed to control the rate of oxidative dissolution of the Bi NPs.

Acknowledgements

The authors gratefully acknowledge Russell Watt, Matt Dixon, and Joe Janda for intellectual property support, David Cormode and Pratap Naha for CT imaging support, and the Portland State University Center for Electron Microscopy for instrumental support. Further, we acknowledge funding support through the Burroughs Wellcome Fund (Award No. 1007294.01, A.M.G.), the Oregon Nanoscience and Microtechnologies Institute (ONAMI), and Portland State University (A.M.G. start-up funding and the Venture Development Funding program).

Conflict of interest

The authors declare no competing financial or other conflicts of interest.

Author details

Hayden Winter, Anna L. Brown and Andrea M. Goforth*

*Address all correspondence to: agoforth@pdx.edu

Department of Chemistry, Portland State University, Portland, OR, USA

References

[1] Lusic H, Grinstaff MW. X-ray-computed tomography contrast agents. Chemical Reviews. 2013;**113**(3):1641-1666

[2] US Department of Commerce, N. NIST: X-Ray Mass Attenuation Coefficients. http://www.nist.gov/pml/data/xraycoef/index.cfm

[3] Mukundan S, Ghaghada KB, Badea CT, Kao C-Y, Hedlund LW, Provenzale JM, et al. A liposomal nanoscale contrast agent for preclinical CT in mice. American Journal of Roentgenology. 2006;**186**(2):300-307

[4] McCullough PA. Contrast-induced acute kidney injury. Journal of the American College of Cardiology. 2008;**51**(15):1419-1428

[5] Wilhelm S, Tavares AJ, Dai Q, Ohta S, Audet J, Dvorak HF, et al. Analysis of nanoparticle delivery to tumours. Nature Reviews Materials. 2016;**1**(5):16014

[6] Nakamura Y, Mochida A, Choyke PL, Kobayashi H. Nanodrug delivery: Is the enhanced permeability and retention effect sufficient for curing cancer? Bioconjugate Chemistry. 2016;**27**(10):2225-2238

[7] Gustafson HH, Holt-Casper D, Grainger DW, Ghandehari H. Nanoparticle uptake: The phagocyte problem. Nano Today. 2015;**10**(4):487-510

[8] Hainfeld JF, Slatkin DN, Smilowitz HM. The use of gold nanoparticles to enhance radiotherapy in mice. Physics in Medicine and Biology. 2004;**49**(18):N309-N315

[9] Hainfeld JF, Slatkin DN, Focella TM, Smilowitz HM. Gold nanoparticles: A new X-ray contrast agent. The British Journal of Radiology. 2006;**79**(939):248-253

[10] Yang X, Yang M, Pang B, Vara M, Xia Y. Gold nanomaterials at work in biomedicine. Chemical Reviews. 2015;**115**(19):10410-10488

[11] Kennedy LC, Bickford LR, Lewinski NA, Coughlin AJ, Hu Y, Day ES, et al. A new era for cancer treatment: Gold-nanoparticle-mediated thermal therapies. Small. 2011;**7**(2): 169-183

[12] Khlebtsov N, Dykman L. Biodistribution and toxicity of engineered gold nanoparticles: A review of in vitro and in vivo studies. Chemical Society Reviews. 2011;**40**(3):1647-1671

[13] Alkilany AM, Murphy CJ. Toxicity and cellular uptake of gold nanoparticles: What we have learned so far? Journal of Nanoparticle Research. 2010;**12**(7):2313-2333

[14] Kamat PV. Photophysical, photochemical and photocatalytic aspects of metal nanoparticles. The Journal of Physical Chemistry. B. 2002;**106**(32):7729-7744

[15] Rabin O, Manuel Perez J, Grimm J, Wojtkiewicz G, Weissleder R. An X-ray computed tomography imaging agent based on long-circulating bismuth sulphide nanoparticles. Nature Materials. 2006 Feb;**5**(2):118-122

[16] Kinsella JM, Jimenez RE, Karmali PP, Rush AM, Kotamraju VR, Gianneschi NC, et al. X-ray computed tomography imaging of breast cancer by using targeted peptide-labeled bismuth sulfide nanoparticles. Angewandte Chemie International Edition. 2011;**50**(51):12308-12311

[17] Longmire M, Choyke PL, Kobayashi H. Clearance properties of nano-sized particles and molecules as imaging agents: Consideration and caveats. Nanomedicine (London, England). 2008;**3**(5):703-717

[18] Alexis F, Pridgen E, Molnar LK, Farokhzad OC. Factors affecting the clearance and biodistribution of polymeric nanoparticles. Molecular Pharmaceutics. 2008;**5**(4):505-515

[19] Winter H, Christopher-Allison E, Brown A, Goforth A. Aerobic method for the synthesis of nearly size- monodisperse bismuth nanoparticles from a redox non-innocent precursor. Nanotechnology. 2018;**29**(15):155603

[20] Brown AL, Naha PC, Benavides-Montes V, Litt HI, Goforth AM, Cormode DP. Synthesis, X-ray opacity, and biological compatibility of ultra-high payload elemental bismuth nanoparticle X-ray contrast agents. Chemistry of Materials. 2014;**26**(7):2266-2274

[21] Brown A. Bismuth Nanoparticles as Medical X-Ray Contrast Agents: Synthesis, Characterization and Applications. Portland, OR: Portland State University; 2013

[22] Deng J, Xu S, Hu W, Xun X, Zheng L, Su M. Tumor targeted, stealthy and degradable bismuth nanoparticles for enhanced X-ray radiation therapy of breast cancer. Biomaterials. 2018;**154**:24-33

[23] Li Z, Liu J, Hu Y, Li Z, Fan X, Sun Y, et al. Biocompatible PEGylated bismuth nanocrystals: "All-in-one" theranostic agent with triple-modal imaging and efficient in vivo photothermal ablation of tumors. Biomaterials. 2017;**141**:284-295

[24] Lei P, An R, Zhang P, Yao S, Song S, Dong L, et al. Ultrafast synthesis of ultrasmall poly(vinylpyrrolidone)-protected bismuth nanodots as a multifunctional theranostic agent for in vivo dual-modal CT/photothermal-imaging-guided photothermal therapy. Advanced Functional Materials. 2017;**1702018**(35):1702018

[25] Yu X, Li A, Zhao C, Yang K, Chen X, Li W. Ultrasmall semimetal nanoparticles of bismuth for dual-modal computed tomography/photoacoustic imaging and synergistic thermoradiotherapy. ACS Nano. 2017;**11**(4):3990-4001

[26] Jaque D, Martínez Maestro L, del Rosal B, Haro-Gonzalez P, Benayas A, Plaza JL, et al. Nanoparticles for photothermal therapies. Nanoscale. 2014;**6**(16):9494-9530

[27] Her S, Jaffray DA. Gold nanoparticles for applications in cancer radiotherapy: Mechanisms and recent advancements. Advanced Drug Delivery Reviews. 2017;**109**:84-101

[28] Retif P, Pinel S, Toussaint M, Frochot C, Chouikrat R, Bastogne T, et al. Nanoparticles for radiation therapy enhancement: The key parameters. Theranostics. 2015;**5**(9):1030-1044

[29] Schuemann J, Berbeco R, Chithrani DB, Cho SH, Kumar R, McMahon SJ, et al. Roadmap to clinical use of gold nanoparticles for radiation sensitization. International Journal of Radiation Oncology, Biology, Physics. 2016;**94**(1):189-205

[30] Nanoparticles comprising metallic and hafnium oxide materials, preparation and uses thereof. NANOBIOTIX; US20140335015A1, 2012

[31] Inorganic nanoparticles compositions in combination with ionizing radiations for treating cancer. US20150374818A1, 2014

[32] Simon V, Ceccaldi A, Lévy L. Activatable nanoparticles for cancer treatment. Nanobiotix. In: Nanoscience. Berlin, Heidelberg: Springer Berlin Heidelberg; 2009. pp. 1121-1141

[33] Schueler BA. Operator shielding: How and why. Techniques in Vascular and Interventional Radiology. 2010;**13**(3):167-171

[34] Klein LW, Miller DL, Balter S, Laskey W, Haines D, Norbash A, et al. Occupational health hazards in the interventional laboratory: Time for a safer environment. Journal of Radiology Nursing. 2010;**29**(3):75-82

[35] Miller DL, Vañó E, Bartal G, Balter S, Dixon R, Padovani R, et al. Occupational radiation protection in interventional radiology: A joint guideline of the cardiovascular and interventional radiology society of Europe and the society of interventional radiology. Journal of Vascular and Interventional Radiology. 2010;**21**(5):607-615

[36] Hricak H, Brenner DJ, Adelstein SJ, Frush DP, Hall EJ, Howell RW, et al. Managing radiation use in medical imaging: A multifaceted challenge. Radiology. 2011;**258**(3):889-905

[37] National Cancer Institute. NCI Dictionary of Cancer Terms. Vol. 1, National Cancer Institute; 2013. p. 1. https://www.cancer.gov/publications/dictionaries

[38] Burns KM, Shoag JM, Kahlon SS, Parsons PJ, Bijur PE, Taragin BH, et al. Lead aprons are a lead exposure hazard. Journal of the American College of Radiology. 2017;**14**(5):641-647

[39] Peters SMB, Zweers D, de Lange F, Mourik JEM. Lead composite vs. nonlead protective garments: Which are better? A multivendor comparison. Radiation Protection Dosimetry. 2017;**175**(4):460-465

[40] Durán A, Hian SK, Miller DL, Le Heron J, Padovani R, Vano E. Recommendations for occupational radiation protection in interventional cardiology. Catheterization and Cardiovascular Interventions. 2013 Jul;**82**(1):29-42

[41] Goforth A, Brown A. Bismuth Particle X-Ray Contrast Agents. U.S. Patent Application No. 14/124236. 2014

[42] De Leõn-Rodríguez LM, Martins AF, Pinho MC, Rofsky NM, Sherry AD. Basic MR relaxation mechanisms and contrast agent design. Journal of Magnetic Resonance Imaging. 2015;**42**(3):545-565

[43] Swy ER, Schwartz-Duval AS, Shuboni DD, Latourette MT, Mallet CL, Parys M, et al. Dual-modality, fluorescent, PLGA encapsulated bismuth nanoparticles for molecular and cellular fluorescence imaging and computed tomography. Nanoscale. 2014;**6**(21): 13104-13112

Section 3

Bismuth Based Dielectric Materials

Chapter 5

Dielectric Properties of Bismuth Niobate Ceramics

Susana Devesa, Manuel Pedro Fernandes Graça and
Luís Cadillon Costa

Additional information is available at the end of the chapter

http://dx.doi.org/10.5772/intechopen.75100

Abstract

The development of new dielectric materials that allow the reduction of size and weight of electronic components has been in the scope of the researchers. The bismuth-based dielectric ceramics are extensively studied for this purpose, namely, the bismuth niobate ($BiNbO_4$). The first attempt to improve $BiNbO_4$ occurred in 1992 when Kagata reported the microwave dielectric properties of bismuth niobate doped with the addition of oxides. This chapter will present a brief review of the several attempts that have been carried out to enhance the dielectric properties of $BiNbO_4$ by modifying their structure through addition, doping, or atom(s) substitution. This manuscript focuses on a case study that involves bismuth substitution by europium ions. To investigate the inclusion of europium in $BiNbO_4$ ceramics, $(Bi_{1-x}Eu_x)NbO_4$ samples were prepared using the sol-gel method, in particular, the citrate route. The structure of the prepared samples was studied by X-ray diffraction (XRD) and Raman spectroscopy and the morphology by scanning electron microscopy (SEM). The dielectric properties were studied, in the microwave frequency range (MW), using the resonant cavity method, and in the radio frequency range (RF), with the impedance spectroscopy technique.

Keywords: bismuth niobate, europium, sol-gel, dielectric properties

1. Introduction

ABO_4 ternary oxides proved to be attractive materials from the chemical perspective since they have the capacity to combine chemical elements in this basic formula, which lead to an extensive wide array of structures and phases with different properties [1].

They present stibiotantalite structure, where "A" can be bismuth (Bi^{3+}) and "B" niobium (Nb^{5+}) cations, composing the bismuth niobate, $BiNbO_4$ [2, 3].

The bismuth niobate exists in two polymorph structures, an orthorhombic (α) phase and a triclinic (β) phase. According to previous studies, the transition of β-$BiNbO_4$ to α-$BiNbO_4$ occurs at temperatures around 700/750°C, with the opposite, and irreversible transition occurring at 1020/1050°C [3].

The bismuth-containing oxides have large structural diversity and promising physical properties for applications in optics, nanoelectronics and nanophotonics [4].

In the last three decades, the bismuth niobate ceramics have been studied as a dielectric material for applications in radio and microwave frequency range, since the development of the communication systems forced the device miniaturisation, and, for that, new dielectric materials are needed [3, 5].

The general requirements of a ceramic dielectric for radio and microwave applications are high dielectric constant and low losses [5, 6]. However, there are other important parameters that require improvement, such as the density, since dense $BiNbO_4$ (BNO) ceramics are difficult to obtain [7, 8].

Since 1992, when Kagata [9] reported for the first time the microwave dielectric properties of $BiNbO_4$ doped with CuO and V_2O_5, numerous attempts have been carried out to improve the dielectric properties of this ceramic material.

Several authors studied the influence of the preparation process of $BiNbO_4$, the influence of sintering process, the addition of different oxides and also the substitution of bismuth or niobium by other cations.

The relation between the structural characteristics and the dielectric properties should also be considered and that is why the influence of the phase transition on the dielectric properties of the material is normally presented [10].

In the next section, state of the art, specific previous studies will be presented, where the dielectric characterisation of $BiNbO_4$ in the radio and microwave frequency regions is made in BNO samples where the addition of oxides or the substitution of bismuth ion was performed.

The last section of this chapter is devoted to the description of a case study, where the inclusion of europium in $BiNbO_4$ ceramics, $(Bi_{1-x}Eu_x)NbO_4$ samples, prepared using the sol-gel method and then subjected to different heat treatments is analysed. The dielectric properties were studied in the radio and in the microwave frequency range.

2. State of the art

As mentioned, in 1992 Kagata [9] doped $BiNbO_4$ with small amounts of CuO or V_2O_5 with the aim of densifying the ceramic material. In that work, the samples were prepared using the solid-state reaction method, and the dielectric characterisation was performed in the microwave frequency range ($f \approx 4.3$ GHz), using Hakki-Coleman's method. According to the authors, with the addition of these oxides, the samples became dense, even with heat treatments below 1000°C, presenting dielectric constants of about 43 at room temperature.

In 1999, Yang [11] presented the dielectric properties of $BiNbO_4$ ceramics doped with different amounts of CuO, V_2O_5, or CuO-V_2O_5 mixtures. The samples were prepared using the solid-state reaction method, and the dielectric characterisation, in the microwave frequency regime ($f \approx 6.1$ GHz), was performed using Hakki-Coleman's method improved by Courtney and Kobayashi. According to this study, the samples became dense, even with heat treatments below 920°C, and also presented dielectric constants of about 43 at the same environmental conditions.

Tzou and coworkers [6] also used, in 2000, V_2O_5 as a support to lower the sintering temperature of $BiNbO_4$ ceramics. The samples were prepared by the solid-state reaction method, and to study the microwave (5.7~6.2 GHz) dielectric properties and relate them to the amount of V_2O_5, the Hakki-Coleman's method, improved by Courtney and Kobayashi, was used. A bulk density of 98% of the theoretical density was achieved for treatment temperatures of 920, 940 and 960°C. The obtained results suggested that large amount of V_2O_5 is avoidable since the Q values decrease critically.

In 2001 Huang [12] investigated the behaviour and the microwave dielectric properties of $BiNb_{(1-x)}Ta_xO_4$ doped with CuO. The powders were prepared by the solid-state reaction method, and the dielectric measurements, in the frequency range of 6–8 GHz, were performed using the Hakki-Coleman's technique. The dielectric constant of these samples was not significantly influenced by the Ta^{5+} substitution and saturated at a value between 44 and 45, again at room temperature.

Shihua, Xi and Yong [13] sintered, in 2004, $BiNbO_4$ doped with Bi_2O_3, by the solid-state reaction process. Those powders were sintered in air and in N_2 atmosphere. The microwave dielectric properties, at approximately 5 GHz, were measured using the Hakki-Coleman dielectric resonator methods. For low frequencies, the temperature dependence of dielectric properties was measured from 20 to 500°C in a frequency range of 1–100 kHz. This study revealed that the dielectric constant and loss at low frequencies increased rapidly and the microwave dielectric properties deteriorated with increasing of B_2O_3 content when sintered in N_2.

Shihua and coworkers [14] studied, in 2006, the microwave ($f \approx 6$ GHz) dielectric properties of $(Bi_{1-x}R_x)NbO_4$ (R = Ce, Nd, Dy, Er) using CuO and V_2O_5 as sintered aids. In this work, the samples were prepared using the solid-state reaction method, and the dielectric properties were obtained by the Hakki-Coleman resonator method. The mentioned ions were introduced to substitute for Bi^{3+} ions. The dielectric constant varied from approximately 37.5 to 41.58.

In 2008, Zhou et al. [15] designed $Bi(V_xNb_{1-x})O_4$ ceramics by using V^{5+} substituting for Nb^{5+}. The samples were prepared by the solid-state reaction method, and the dielectric behaviour at microwave frequencies (5~6 GHz) was studied by two different processes, Hakki-Coleman's dielectric resonator method improved by Kobayashi and the shielded cavity method. The results obtained by the two methods were similar, with the dielectric constant and the quality factor strongly dependent on the sintering temperature. For values of x between 0.002 and 0.064, the dielectric constant varied between 38 and 46.

The study developed by Zhong and coworkers [16], in 2010, involved two kinds of CuO-V_2O_5 dopants with the aim of reducing the sintering temperature of $BiNbO_4$: one was the mechanical mixture of CuO and V_2O_5, and the other was the compound CuV_2O_6. The samples were

prepared by the solid-state reaction method and sintered in N_2 atmosphere. The dielectric characterisation at microwave frequencies (f = 4.3 GHz) was performed using the Hakki-Coleman dielectric resonator method. The addition of CuV_2O_6 led to uniform and dense microstructures, with higher dielectric constant than those of the samples added with CuO-V_2O_5. The sample with better microwave dielectric properties was sintered at 860°C and was doped with 0.5 wt.% of CuV_2O_6: $\varepsilon' = 47$ and $Q \times f = 11{,}950$ GHz.

In the same year, Butee and coworkers [17] investigated ceramic samples of $BiNbO_4$ and $(Bi_{0.95}Ln_{0.05})NbO_4$ (Ln = Dy^{3+}, Gd^{3+}, Nd^{3+} or La^{3+}) with V_2O_5 addition. The samples were obtained by the solid-state reaction method. The dielectric measurements were made at low frequencies (1 kHz–1 MHz) with a Solartron impedance gain phase analyser and, at microwave frequencies (≈ 4–5 GHz), with the dielectric post resonator technique. The obtained values in the microwave frequency region for the dielectric constant were 46.5 (pure $BiNbO_4$), 40.8 (Ln = Dy^{3+}), 41.7 (Ln = Gd^{3+}), 43.4 (Ln = Nd^{3+}) and 47.5 (Ln = La^{3+}). The dielectric measurements made on the sintered samples at RF frequencies showed dielectric constants between 44.7 and 53.4.

In 2011, Almeida et al. [18] sintered $BiNbO_4$ ceramics with different amounts of PbO and Bi_2O_3, by the solid-state reaction method. The dielectric characterisation was performed with the impedance spectroscopy technique, in the frequency range of 10^2–10^8 Hz. Since the studied samples presented relaxation processes, the activation energies were calculated and varied between 0.55 eV (pure triclinic BNO) and 0.67 (BNO with 10 wt.% of PbO).

Sales and coworkers [3] investigated, in 2012, the dielectric, electrical modulus and impedance properties of $BiNbO_4$ ceramics, doped with different amounts of CuO and prepared by the solid-state reaction method. The frequency range of this study was between 100 Hz and 10 MHz. The highest values of dielectric permittivity occurred at 10 kHz, for the samples of BNO with 3 wt.%, 5 wt.% and 10 wt.% of CuO, with the values of 87.15, 88.63 and 140.73, respectively. The lowest values of the lost tangent occurred for the same samples but at 10 MHz.

In 2014, Czekaj et al. [19] studied the immittance properties of $BiNbO_4$ ceramics fabricated by the solid-state reaction route, with an excess of Bi_2O_3, followed by pressureless sintering. The immittance properties, complex impedance, complex modulus, complex admittance, complex dielectric permittivity and dielectric losses were studied by impedance spectroscopy, in a frequency range of 20 Hz to 1 MHz. Since the investigated samples presented relaxation processes, the Arrhenius relation was applied in order to calculate the activation energies. The values of the activation energy varied between 0.81 and 1.04 when obtained with the impedance formalism and between 0.85 and 1.12 with the modulus formalism.

Devesa and coworkers [7] investigated, in 2015, $(Bi_{1-x}Fe_x)NbO_4$ samples prepared using the sol-gel method. The measurements of the complex permittivity were made in a resonant cavity, using the small perturbation method, at frequencies of 2.7 and 5.0 GHz. With the substitution of bismuth by iron, it was possible to reduce the sintering temperature and simultaneously to decrease the dielectric losses. The dielectric constant of the samples with different percentages of iron was practically independent of the sintering temperature.

In 2016, Butee et al. [20] studied $(Bi_{1-x}Pb_x)NbO_4$ samples, prepared by the solid-state reaction method, with the addition of V_2O_5. The dielectric post (DP) resonator technique was employed for the microwave characterisation of the samples that was performed at room

temperature and at ~4–5 GHz. In this study, dielectric constant values between 42 ($x = 0$) and 71 ($x = 0.2$) were obtained. According to the authors, such increase has never been reported in a BNO system and can be attributed to the formation of the $Pb_2Nb_2O_7$ secondary phase.

Analysing the referenced works, we can see that the solid-state reaction method is the most common preparation process. Furthermore, the dielectric characterisation studies are mainly focused in the microwave frequency regime, which means that the information of the dielectric behaviour of ceramic materials based on bismuth niobate in the RF frequency regime is reduced. Concerning the MW dielectric studies, it is also perceptible that the improved Hakki-Coleman's dielectric resonator method is the most used.

To end this brief state of the art, it is important to note that, for some reason that the authors do not understand, a significant number of microwave dielectric studies of BNO ceramics do not refer the measuring frequency. None of those incomplete works was included in this manuscript.

In **Table 1**, the **key progress of the modified $BiNbO_4$** is presented.

3. Case study

In this work, $(Bi_{1-x}Eu_x)NbO_4$ (x = 0.00, 0.10, 0.20, 0.50) samples were prepared using the sol-gel method and thermally treated at different temperatures, between 650 and 1050°C.

In fact, the solid-state reaction method has been the most applied technique to process ceramic powders; however, more recently the sol-gel method, through citrate route, became considered a promising process and a simple way to obtain stoichiometric fine powders, with high homogeneity, since the formation of citrate complexes allows mixing the component cations in an atomic scale; thus they can immediately react with each other at relatively low temperatures [6].

The structure was studied by X-ray diffraction (XRD) and Raman spectroscopy and the morphology by scanning electron microscopy (SEM).

The measurements of the complex permittivity were performed in a frequency range from 100 Hz to 1 MHz (RF, radio frequency range), using the impedance spectroscopy technique, and at 2.7 GHz (MW, microwave frequency range), using the small perturbation theory.

In the case of the microwave dielectric characterisation, through the small perturbation method, a more detailed study can be consulted in a previous work of Devesa et al. [21], from 2017.

3.1. Sample preparation

The $(Bi_{1-x}Eu_x)NbO_4$ powders were prepared using the sol-gel method, through the citrate route. Bismuth nitrate ($Bi(NO_3)_3{\cdot}5H_2O$), niobium chloride ($NbCl_5$) and europium nitrate ($Eu(NO_3)_3.H_2O$) were used as starting materials and citric acid and ethylene glycol as chelating agent and reaction medium, respectively. All reagents used in the whole procedure were of analytical grade. A suspension containing stoichiometric amounts of starting materials was previously prepared in a minor amount of hydrogen peroxide and dispersed in a mixture of

Reference	Composition of $BiNbO_4$	Preparation method	Frequency	Dielectric measurement method	Dielectric constant	Quality factor	Dielectric loss (tgδ)
[9]	Doped with CuO	Solid-state reaction	4.3 GHz	Hakki-Coleman's	44	2240	_____
	Doped with V_2O_5				44	2750	_____
	Doped with CuO and V_2O_5				43	4260	_____
[11]	Doped with CuO, V_2O_5 and CuO-V_2O_5 mixture	Solid-state reaction	6.1 GHz	Hakki-Coleman's improved by Courtney and Kobayashi	43.2	3310	_____
[6]	Doped with V_2O_5	Solid-state reaction	5.7~6.2 GHz	Hakki-Coleman's improved by Courtney and Kobayashi	43.6	3410	_____
[12]	$BiNb_{(1-x)}Ta_xO_4$ doped with CuO	Solid-state reaction	6–8 GHz	Hakki-Coleman's	44–45	Tem q*f!	_____
[13]	Doped with Bi_2O_3	Solid-state reaction	≈ 5 GHz	Hakki-Coleman's	41.5	4400	_____
			1–100 kHz	_____	1874	_____	_____
[14]	$(Bi_{1-x}R_x)NbO_4$ (R = Ce, Nd, Dy, Er) doped with CuO and V_2O_5	Solid-state reaction	≈ 6 GHz	Hakki-Coleman's	41.58	5000	_____
[15]	$Bi(V_xNb_{1-x})O_4$	Solid-state reaction	5~6 GHz	Hakki-Coleman's improved by Kobayashi and shielded cavity method	38–46	1000–4000	_____
[16]	Doped with CuO and V_2O_5 or CuV_2O_6	Solid-state reaction	4.3 GHz	Hakki-Coleman's	47	2779	_____
[17]	BiNbO4 and $(Bi_{0.95}Ln_{0.05})NbO_4$ (Ln = Dy^{3+}, Gd^{3+}, Nd^{3+} or La^{3+}) doped with V_2O_5	Solid-state reaction	≈ 4–5 GHz	Dielectric post resonator	40.8–47.5	_____	_____
			10^3–10^6 Hz	Solartron impedance gain phase analyser	44.7–53.4	_____	_____
[18]	Doped with PbO and Bi_2O_3	Solid-state reaction	10^2–10^8 Hz	Impedance spectroscopy	78.44	_____	6.26×10^{-2}
[3]	Doped with CuO	Solid-state reaction	10^2–10^7 Hz	Impedance spectroscopy	140.73	_____	1–2

Reference	Composition of $BiNbO_4$	Preparation method	Frequency	Dielectric measurement method	Dielectric constant	Quality factor	Dielectric loss (tgδ)
[19]	With excess of Bi_2O_3	Solid-state reaction	20–10^6 Hz	Impedance spectroscopy	_____	_____	_____
[7]	$(Bi_{1-x}Fe_x)NbO_4$	Sol-gel method	2.7 and 5 GHz	Small perturbation	4.24	_____	2×10^{-2}
[20]	$(Bi_{1-x}Pb_x)NbO_4$ doped with V_2O_5	Solid-state reaction	~4–5 GHz	Dielectric post (DP) resonator	71	_____	_____

Table 1. Summary of the most significant progress of the modified $BiNbO_4$.

http://dx.doi.org/10.5772/intechopen.75100

citric acid and ethylene glycol in a molar ratio 1:3. In order to promote the solubility, the mixture was stirred, during 7 days, until a clear colloidal suspension was obtained. The obtained solution was dried at 400°C for 48 h to evaporate the solvent, and the obtained powders were thermally analysed by differential thermal analysis (DTA), performed in a *Linseis Apparatus L92/095*, in the temperature range of 20–1200°C, with a heating rate of 10°C/min, using Al_2O_3 as reference. Subsequently, the dry powders were pressed into pellets and cylinders and finally heat-treated, according to the differential thermal analysis (DTA) results, at 650, 850 and 1050°C, using a dwell time of 4 h, with a heating rate of 5°C/min.

3.2. Experimental methods

The structural characterisation of the obtained ceramics was performed using XRD. The pattern data were obtained on an Empyrean diffractometer (CuK α radiation, λ = 1.54060 Å) at 45 kV and 40 mA, with a curved graphite monochromator, an automatic divergence slit (irradiated length 20.00 mm), a progressive receiving slit (height 0.05 mm) and a flat plane sample holder in a Bragg-Brentano parafocusing optic configuration. Intensity data were collected by the step counting method (step 0.02° in 1 s) in the 2θ angle range of 10–60°

The Raman spectroscopy measurements were performed at room temperature, in backscattering geometry, with a 442 nm laser line using an HR-800-UV Jobin-Yvon Horiba spectrometer. A microscope objective focused the exciting light onto the sample.

The morphology of the obtained samples was analysed by SEM. The measurements were performed on a TESCAN-Vega III. The samples were covered with carbon before microscopic observation to improve the surface electron conduction.

For the electrical measurements in the frequency range from 100 Hz to 1 MHz, pellets in disc form and with a thickness of about 1 mm and diameter of 10 mm were prepared, and their opposite side surfaces were painted with silver conducting paste. During the electrical measurements, the samples were maintained in a helium atmosphere in order to improve the heat transfer and eliminate the moisture. These measurements were made using a precision impedance analyser (Agilent 4294A) in the Cp-Rp configuration, in the temperature range of 200-400 K. The real part of the complex permittivity, ε', and the imaginary part, ε'', were calculated using Eq. (1) [22]:

$$\varepsilon^* = \varepsilon' - i\,\varepsilon'' = \frac{C_p\, d}{A\,\varepsilon_0} - i\,\frac{d}{\omega\, R_p\, A\,\varepsilon_0} \tag{1}$$

where A and d represent the sample area and thickness, respectively, ε_0 the free space permittivity and ω the angular frequency.

The microwave characterisation was performed using the resonant cavity method, with the cavity operating at 2.7 GHz in the TE105 mode. The measurements were made at room temperature, using a network analyser (HP 8753D) coupled to the cavity.

The insertion of the cylindrical sample at the position where the electric field is maximal causes a perturbation, changing the transmission of the cavity.

Considering only the first-order perturbation in the electric field caused by the sample [7], the shift in the resonant frequency of the cavity, Δf, can be related to the real part of the complex permittivity, ε′, and the change in the inverse of the quality factor of the cavity, Δ(1/Q), can be related to the imaginary part, ε″ [7, 21]:

$$\varepsilon' = K\frac{\Delta f}{f_0}\frac{V}{v} + 1 \tag{2}$$

$$\varepsilon'' = \frac{K}{2}\Delta\left(\frac{1}{Q}\right)\frac{V}{v} \tag{3}$$

where K is a constant related to the depolarization factor, which depends on the geometric parameters; v and V are the volumes of the sample and the cavity, respectively and f_0 is the resonance frequency of the cavity.

$$\Delta f = f_0 - f_l \tag{4}$$

$$\Delta\left(\frac{1}{Q}\right) = \frac{1}{Q_l} - \frac{1}{Q_0} \tag{5}$$

where the indexes *0* and *l* refer to the empty and loaded cavity, respectively.

Using a sample of known dielectric constant, in this study polytetrafluoroethylene (PTFE), the constant K can be calculated.

3.3. Results and discussion

3.3.1. Differential thermal analysis

The DTA data of the obtained powders, shown in **Figure 1**, revealed, for the sample with x = 0.00, three exothermic phenomena centred at 646, 1043 and 1181°C. When x = 0.10, besides the three exothermic phenomena mentioned above, that can clearly be identified although the small displacements, it is visible two new exothermic phenomena centered at 546 and 607°C, and an endothermic peak at 443°C. The powder with x = 0.20 shows an endothermic peak at 443°C, and four exothermic phenomena centred at 530, 667, 1033 and 1189°C. For x = 0.50, there is an endothermic phenomenon centred at 590°C and an exothermic at 978°C.

The heat treatments were made in agreement with these results.

3.3.2. X-ray diffraction pattern analysis

The crystalline phases were identified by X-ray diffraction patterns and are shown in **Figure 2**.

In the host samples, x = 0.00, a combination of orthorhombic and triclinic $BiNbO_4$ was obtained for the heat treatment of 650°C, orthorhombic $BiNbO_4$ for the heat treatment of 850°C and triclinic $BiNbO_4$ for the heat treatment of 1050°C.

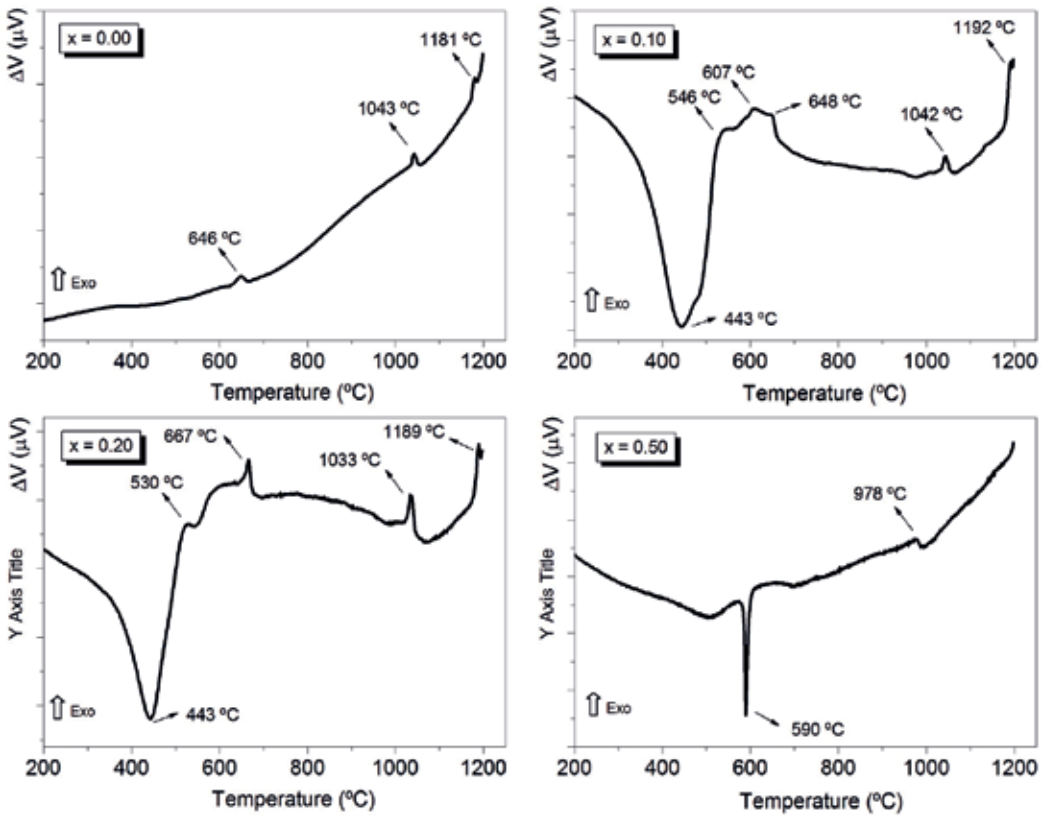

Figure 1. DTA of $(Bi_{1-x}Eu_x)NbO_4$ powders, heated at the rate of 10°C/min.

When x = 0.10, besides the α-$BiNbO_4$ and β-$BiNbO_4$, $EuNbO_4$ and $EuNb_2O_6$, a nonstoichiometric phase of bismuth niobate was formed for the heat treatment of 1050°C. The formation of nonstoichiometric phases of bismuth niobate is associated with the volatile nature of Bi^{3+} ions at high temperature.

With the increase of x to 0.20, besides the α-$BiNbO_4$, β-$BiNbO_4$ and $EuNbO_4$, for the higher treatment temperature, there are two unidentified peaks that should be associated with a different nonstoichiometric phase of bismuth niobate.

For x = 0.50, α-$BiNbO_4$, β-$BiNbO_4$, $Bi_5Nb_3O_{15}$ and $EuNbO_4$ were identified.

The results show that Eu^{3+} ions substituted in $BiNbO_4$ tend to form a separate crystal structure rather simply replacing Bi^{3+} ions.

Analysing the X-ray diffraction data and the DTA results, the consistency of the information is visible.

For x = 0.00, the first peak shows the formation of β-$BiNbO_4$, and the second can be associated with the conversion of α-$BiNbO_4$ in β-$BiNbO_4$.

http://dx.doi.org/10.5772/intechopen.75100

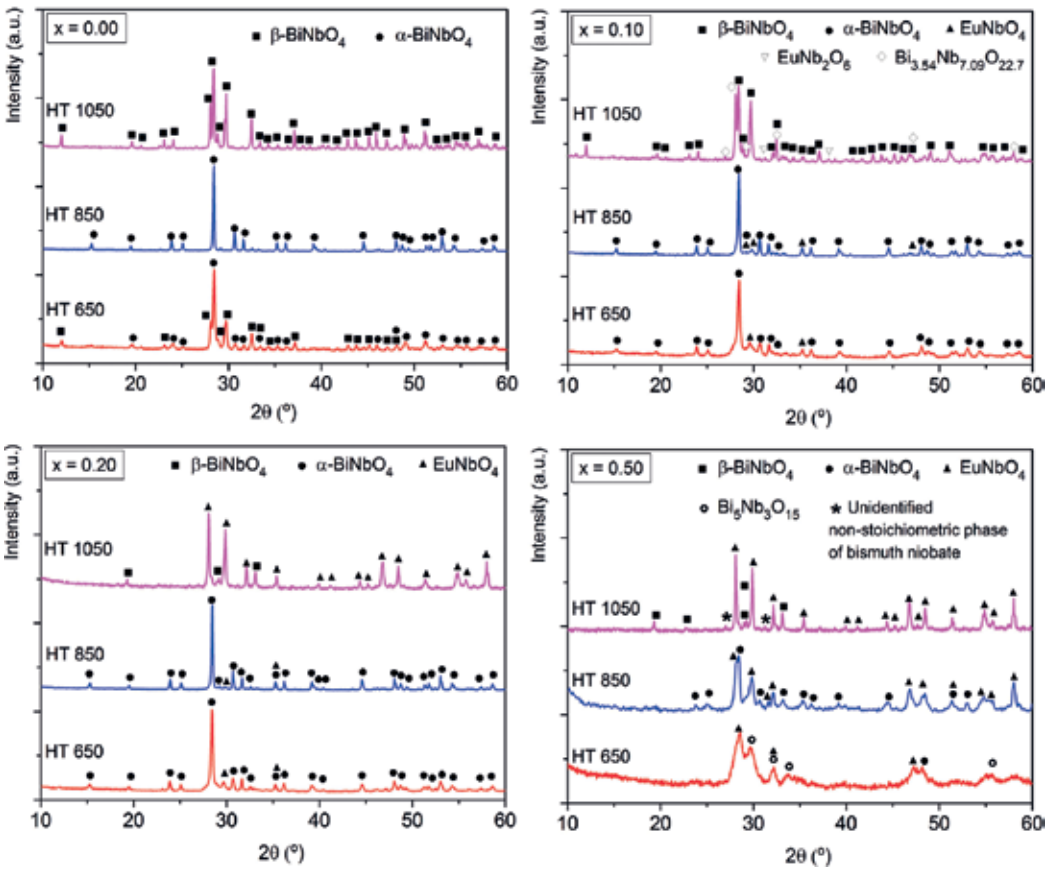

Figure 2. X-ray diffraction patterns of $(Bi_{1-x}Eu_x)NbO_4$ samples heat-treated at 650, 850 and 1050°C.

According to the literature, the formation of α-$BiNbO_4$ is expected for temperatures above 500°C, evidenced by small exothermic peaks between 500 and 600°C [23], which are visible in the DTA of the powders with $x = 0.10$ and 0.20.

As in the reference powders, all of the powders with europium show one peak close to 1000°C that can be related to the transition of β-$BiNbO_4$ to α-$BiNbO_4$. The existence of one endothermic peak in this set of powders can be related to the decomposition of intermediate phases.

The increase of the crystallinity is also perceptible for the heat treatment of 850°C, with the increase of the height and the decrease of the half-high width of the peaks.

The thermal treatment performed at 1200°C caused the fusion of the powders, and therefore there is no information about the exothermic phenomenon that occurs near this temperature.

3.3.3. Raman spectroscopy analysis

The Raman spectra are presented in **Figure 3**.

When x = 0.00, the samples treated at 650 and 1150°C show peaks at 102, 450 and 687 cm^{-1} that are characteristics of the vibration modes of β-$BiNbO_4$. In the case of the sample treated at 850°C, where the single phase α-$BiNbO_4$ was identified, none of these peaks is present. Besides, the peaks at 139 and 199 cm^{-1} are distinctive of the orthorhombic $BiNbO_4$, a fact that justifies their absence in the spectrum of the sample treated at 1050°C, where all are attributed to triclinic $BiNbO_4$ [5, 24]. This means that none of the detected vibrations can be assigned to nonstoichiometric phase $Bi_{3.54}Nb_{7.09}O_{22.7}$.

For x = 0.10 and 0.20, the peaks identified in the samples treated at 650 and 850°C can be attributed to the vibration modes of $BiNbO_4$, with vibrations at 140 and 200 cm^{-1} being characteristic of the orthorhombic $BiNbO_4$. For the sample treated at 1050°C, these two vibrations are absent, though at 690 cm^{-1} it is possible to identify a distinctive peak of the triclinic $BiNbO_4$ [25, 26].

The vibrations present at 120, 133, 175, 290 and 782 cm^{-1} in the sample with x = 0.20 can be attributed to the vibration modes of $EuNbO_4$ [1].

For the samples with x = 0.50, this analysis is still valid, and it is possible to notice that the vibration modes of the nonstoichiometric phase $Bi_5Nb_3O_{15}$ are very similar to the ones obtained for the orthorhombic $BiNbO_4$.

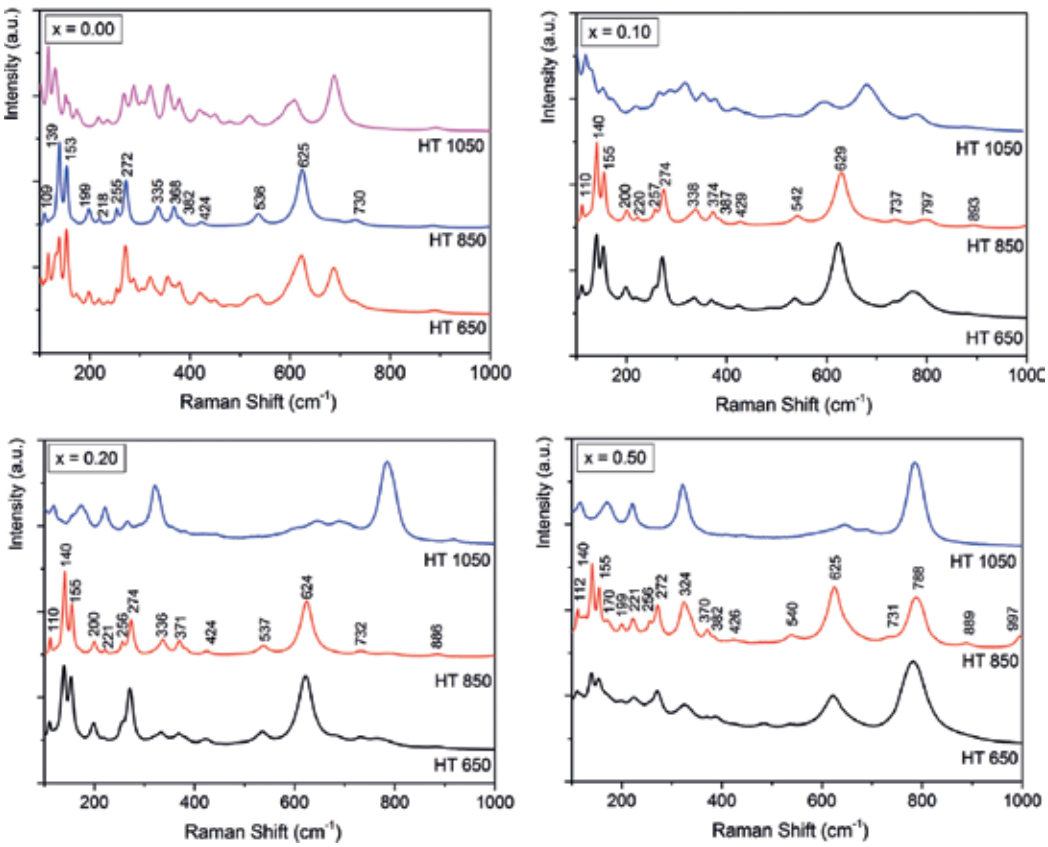

Figure 3. Raman spectra of $(Bi_{1-x}Eu_x)NbO_4$ samples heat-treated at 650, 850 and 1050°C.

3.3.4. Morphological characterisation

SEM micrographs of $(Bi_{1-x}Eu_x)NbO_4$ powders are shown in **Figure 4**. The images for treatment temperature of 650°C revealed that the increase of europium content promotes changes in the morphology of the samples. These changes are more perceptible when x increases from 0.20 to 0.50, with the grain size increasing. For the samples treated at 850°C, one can see that the increase of europium promotes the occurrence of coalescence. The heat treatment of 1050°C promotes the formation of high-temperature triclinic $BiNbO_4$, which leads to a dramatic change in the morphology of the samples, with the grain size showing a very expressive increase.

3.3.5. Dielectric characterisation

Figure 5 shows the real part of the dielectric permittivity as a function of the frequency, at constant temperature T = 300 K, in the RF frequency range, for the prepared samples. It can be verified that it is not significantly influenced by the frequency.

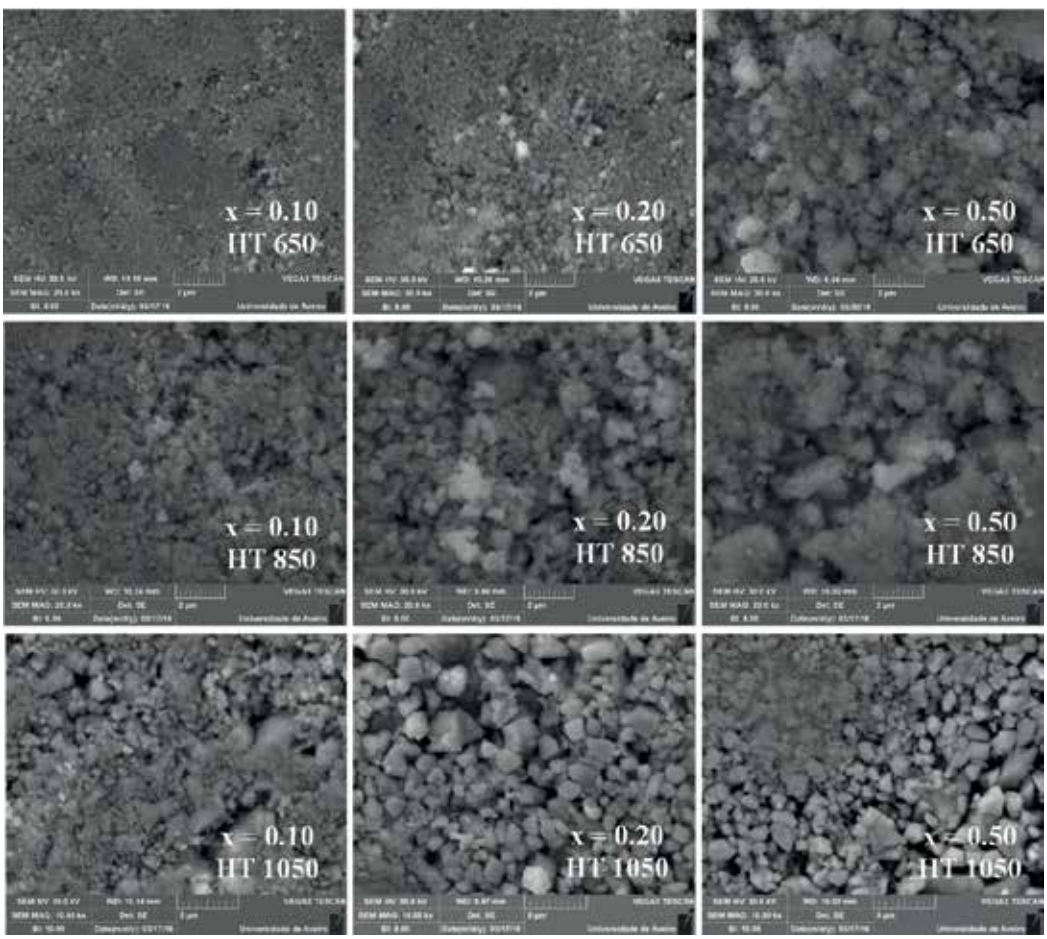

Figure 4. SEM micrographs of $(Bi_{1-x}Eu_x)NbO_4$ samples.

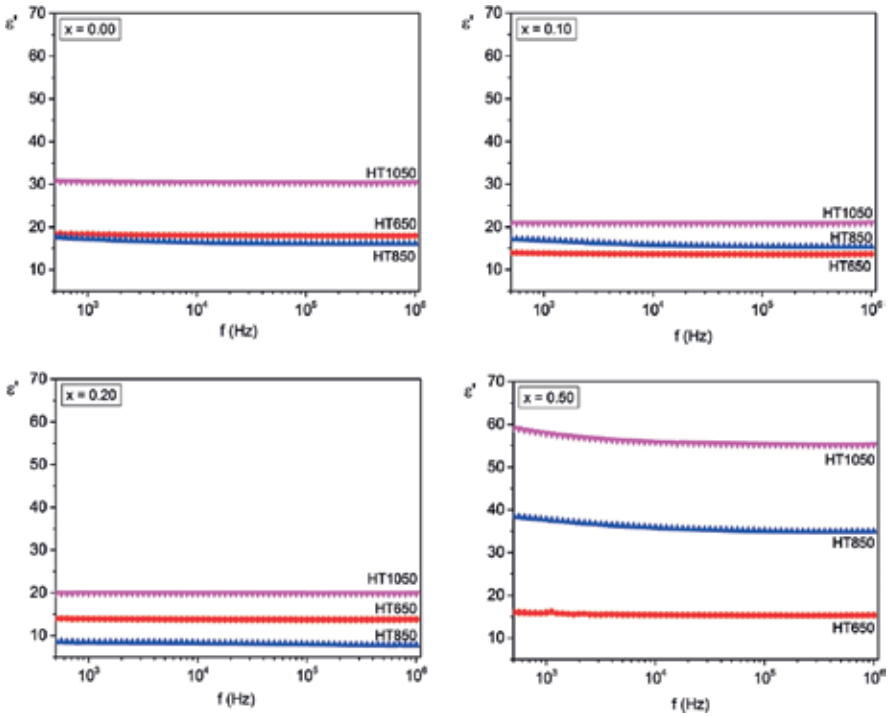

Figure 5. Frequency dependence of the real part of the complex permittivity, ε', at T = 300 K.

For the host samples and for the samples with different amounts of europium, it is perceptible that the presence of triclinic $BiNbO_4$ leads to higher ε′ values.

The highest dielectric constant occurs for the sample with x = 0.50, treated at 1050°C, where besides α-$BiNbO_4$ and $EuNbO_4$, an unidentified nonstoichiometric phase of bismuth niobate was detected.

The variation of the imaginary part of the complex permittivity with frequency, also at constant temperature T = 300 K and in the RF frequency range, is shown in **Figure 6**.

Except in the case of the sample with highest ε′, all the other samples are showing ε″ values lower than 1.

In general, the losses decrease with frequency, except in the sample with x = 0.20, treated at 850°C, where the shape of the curve indicates the occurrence of a relaxation process.

Figure 7 presents the real part of the complex permittivity at 2.7 GHz, at constant temperature T = 300 K, as function of x, for the prepared samples. The samples treated at 1050°C show the highest ε', with the maximum ε', 8.41, occurring for the sample with x = 0.20. The calculated values indicate that the more influent parameter is the treatment temperature since the permittivity does not vary significantly with the amount of europium.

This increase of ε' for the highest treatment temperature can be attributed to the increase of crystallinity, combined with the formation of the high-temperature triclinic $BiNbO_4$.

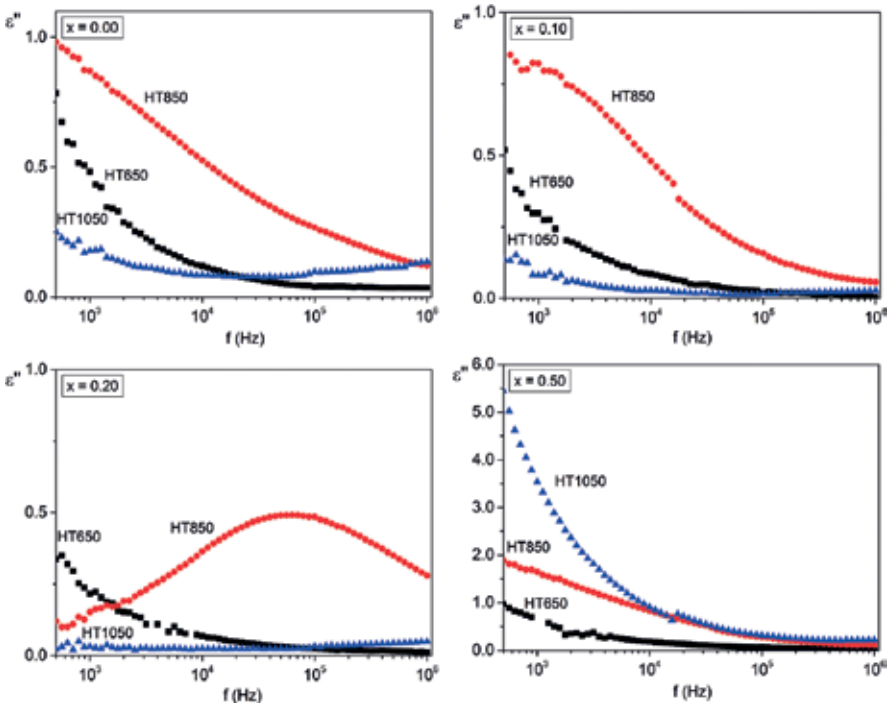

Figure 6. Frequency dependence of the imaginary part of the complex permittivity, ε'', at $T = 300$ K.

In **Figure 8**, the variation of the imaginary part of the complex permittivity with frequency is presented. It can be seen that ε'' values are influenced by the amount of europium and also by the increase of the treatment temperature.

Table 2 resumes ε' and $tg\,\delta = \frac{\varepsilon''}{\varepsilon'}$, for the different samples.

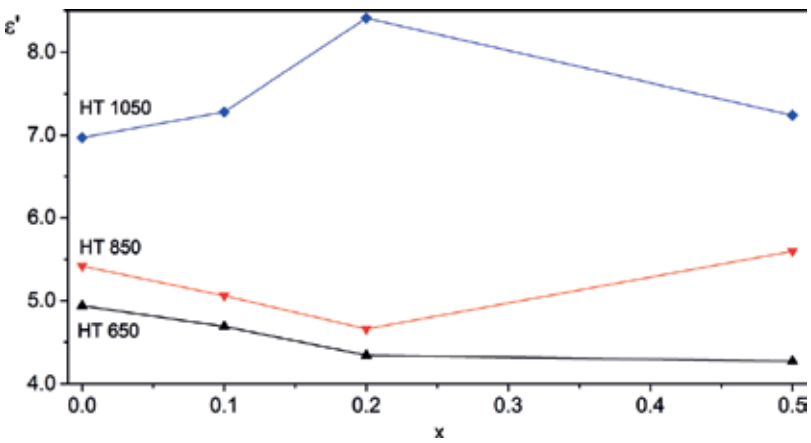

Figure 7. Calculated ε' for all treatment temperatures as a function of x value, at 2.7 GHz and 300 K.

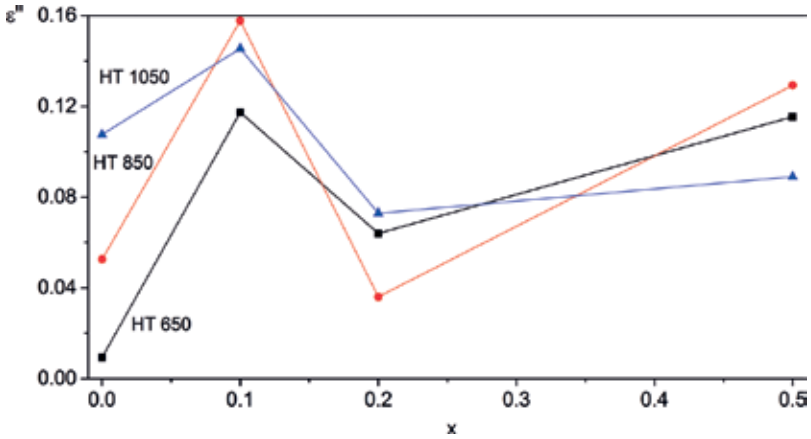

Figure 8. Calculated ε'' for all treatment temperatures as a function of x value, at 2.7 GHz and 300 K.

x	HT (°C)	100 kHz		1 MHz		2.7 GHz	
		ε'	tg δ	ε'	tg δ	ε'	tg δ
0.00	650	17.95	2.2×10^{-3}	17.96	1.9×10^{-3}	4.94	1.9×10^{-3}
	850	16.18	1.6×10^{-2}	16.13	7.5×10^{-3}	5.42	9.7×10^{-3}
	1050	30.39	3.2×10^{-3}	30.48	4.5×10^{-3}	6.97	1.5×10^{-2}
0.10	650	13.56	1.5×10^{-3}	13.64	2.8×10^{-4}	4.69	2.5×10^{-2}
	850	15.42	1.0×10^{-2}	15.36	3.7×10^{-3}	5.06	3.1×10^{-2}
	1050	20.85	8.4×10^{-4}	20.97	1.2×10^{-3}	7.28	2.0×10^{-2}
0.20	650	13.71	1.7×10^{-3}	13.79	8.0×10^{-4}	4.34	1.5×10^{-2}
	850	7.98	6.1×10^{-2}	7.74	3.6×10^{-2}	4.66	7.7×10^{-3}
	1050	19.87	1.6×10^{-3}	19.89	2.5×10^{-3}	8.41	8.7×10^{-3}
0.50	650	15.27	4.3×10^{-3}	15.32	1.7×10^{-3}	4.27	2.7×10^{-2}
	850	35.08	7.8×10^{-3}	34.95	3.2×10^{-3}	5.6	2.3×10^{-2}
	1050	55.32	5.7×10^{-3}	55.25	4.0×10^{-3}	7.24	1.2×10^{-2}

Table 2. Calculated ε' and $tg\ \delta$ for the different samples, at 100 kHz, 1 MHz and 2.7 GHz, at 300 K.

Analysing the presented values, we can see that, for all the presented frequencies, the formation of high-temperature triclinic $BiNbO_4$ contributes to the increase of the permittivity, without the exacerbation of the dielectric losses.

The substitution of bismuth by europium does not contribute to significant changes in the dielectric losses of the samples, being the treatment temperature the most influent parameter.

Considering the samples treated at 650°C, it is visible that the introduction of europium is not advantageous, since the ε′ values decrease and, in general, the losses increase. For this same

temperature, the increase of europium promotes the increase of the grains size, a morphologic alteration which is not reflected in the dielectric properties.

In the samples treated at 850°C, the reflection of the morphology changes in dielectric properties is perceptible mostly in the sample with $x = 0.50$. In these set of samples, the coalescence is noticeable; however, it is in the sample with the higher amount of europium that this phenomenon is more evident, which can explain the increase of the dielectric constant.

The samples treated at 1050°C show the higher dielectric constants, which can be related not only with the formation of the high-temperature triclinic $BiNbO_4$ but also with the growing of the grain size.

For the RF frequency regime, it is also perceptible that, for the samples treated at 1050°C, the increase of the dielectric constant can be related to the amount of europium introduced.

3.4. Conclusion

In this study, we have presented a structural, morphological and dielectric characterisation, in the RF and MW frequency regime, of $(Bi_{1-x}Eu_x)NbO_4$ samples, prepared by the sol-gel method and treated at three different temperatures, between 650 and 1050°C.

For the lowest treatment temperature, one can conclude that the introduction of europium is not an advantage since there is no improvement in the dielectric properties of the samples.

In the case of the intermediate heat treatment, the introduction of europium is advantageous but only for the sample with $x = 0.50$, with the increase of the dielectric constant, without significant increase of the losses.

The samples treated at 1050°C, where the triclinic bismuth niobate was identified, show the highest dielectric constant. In particular, in the case of the RF frequency regime, these sets of samples revealed that the introduction of a higher amount of europium can improve significantly the dielectric constant, without compromising the losses.

Author details

Susana Devesa*, Manuel Pedro Fernandes Graça and Luís Cadillon Costa

*Address all correspondence to: susana_devesa@hotmail.com

I3N and Physics Department, University of Aveiro, Aveiro, Portugal

References

[1] Siqueira KP, Moreira RL, Dias A. Synthesis and crystal structure of lanthanide orthoniobates studied by vibrational spectroscopy. Chemistry of Materials. 2010;**22**(8):2668-2674. DOI: 10.1021/cm100173p

[2] Martinez AL. Síntese e crescimento de cristal da fase $BiNbO_4$ [thesis]. São Paulo: Instituto de Física de São Carlos; 2006. 117 p. Available from: http://www.teses.usp.br/teses/disponiveis/76/76132/tde-14012008-170719/en.php. DOI: 10.11606/T.76.2006.tde-14012008-170719

[3] Sales AJM, Oliveira PWS, Almeida JS, Costa MM, Rodrigues HO, Sombra ASB. Copper concentration effect in the dielectric properties of $BiNbO_4$ for RF applications. Journal of Alloys and Compounds. 2012;**542**:264-270 https://doi.org/10.1016/j.jallcom.2012.07.025

[4] Savina AA, Atuchin VV, Solodovnikov SF, Solodovnikova ZA, Krylov AS, Maximovskiy EA, et al. Synthesis, structural and spectroscopic properties of acentric triple molybdate $Cs_2NaBi(MoO_4)_3$. Journal of solid state chemistry. 2015;**225**:53-58 https://doi.org/10.1016/j.jssc.2014.11.023

[5] Radha R, Gupta UN, Samuel V, Muthurajan H, Kumar HH, Ravi V. A co-precipitation technique to prepare $BiNbO_4$ powders. Ceramics International. 2008;**34**(6):1565-1567 https://doi.org/10.1016/j.ceramint.2007.03.022

[6] Tzou WC, Yang CF, Chen YC, Cheng PS. Improvements in the sintering and microwave properties of $BiNbO_4$ microwave ceramics by V_2O_5 addition. Journal of the European Ceramic Society. 2000;**20**(7):991-996 https://doi.org/10.1016/S0955-2219(99)00228-9

[7] Kagata H, Inoue T, Kato J, Kameyama I. Low-fire bismuth-based dielectric ceramics for microwave use. Japanese Journal of Applied Physics. 1992;**31**(9S):3152 https://doi.org/10.1143/JJAP.31.3152

[8] Devesa S, Graça MP, Henry F, Costa LC. Microwave dielectric properties of $(Bi_{1-x}Fe_x)NbO_4$ ceramics prepared by the sol–gel method. Ceramics International. 2015;**41**(6):8186-8190. DOI: https://doi.org/10.1016/j.ceramint.2015.03.038

[9] Liou YC, Tsai WC, Chen HM. Low-temperature synthesis of $BiNbO_4$ ceramics using reaction-sintering process. Ceramics International. 2003;**35**(6):2119-2212 https://doi.org/10.1016/j.ceramint.2008.11.03

[10] Kim ES, Choi W. Effect of phase transition on the microwave dielectric properties of $BiNbO_4$. Journal of the European Ceramic Society. 2006;**26**(10):1761-1766. DOI: https://doi.org/10.1016/j.jeurceramsoc.2005.09.003

[11] Yang CF. Improvement of the Dielectric Properties of $BiNbO_4$ Ceramics by the Addition of CuO–V2O5 Mixtures. Journal of Materials Science Letters. 1999;**18**(10):805-807 https://doi.org/10.1023/A:1006697318870

[12] Huang CL, Weng MH, Yu CC. Low firable BiNbO4 based microwave dielectric ceramics. Ceramics International. 2001;**27**(3):343-350 https://doi.org/10.1016/S0272-8842(00)00086-9

[13] Shihua D, Xi Y, Yong Y. Dielectric properties of B_2O_3-doped $BiNbO_4$ ceramics. Ceramics International. 2004;**30**(7):1195-1198 https://doi.org/10.1016/j.ceramint.2003.12.030

[14] Shihua D, Xi Y, Yu M, Puling L. Microwave dielectric properties of $(Bi_{1-x}R_x)NbO_4$ ceramics (R= Ce, Nd, Dy, Er). Journal of the European Ceramic Society. 2006;**26**(10):2003-2005 https://doi.org/10.1016/j.jeurceramsoc.2005.09.049

[15] Zhou D, Wang H, Yao X, Liu Y. Microwave dielectric properties of low-firing $BiNbO_4$ ceramics with V_2O_5 substitution. Journal of Electroceramics. 2008;**21**(1-4):469-472 https://doi.org/10.1007/s10832-007-9223-2

[16] Zhong C, Yuan Y, Zhang S, Pang Y, Tang B. Low-fired $BiNbO_4$ microwave dielectric ceramics modified by CuV2O6 addition sintered in N2 atmosphere. Ceramics-Silikaty. 2010;**54**(2):103-107

[17] Butee S, Kulkarni AR, Prakash O, Aiyar RPRC, Sudheendran K, Raju KJ. Effect of lanthanide ion substitution on RF and microwave dielectric properties of $BiNbO_4$ ceramics. Journal of Alloys and Compounds. 2010;**492**(1):351-357 https://doi.org/10.1016/j.jallcom.2009.11.093

[18] Almeida JS, Fernandes TSM, Sales AJM, Silva MAS, Júnior GP, Rodrigues HO, et al. Study of the structural and dielectric properties of Bi_2O_3 and PbO addition on $BiNbO_4$ ceramic matrix for RF applications. Journal of Materials Science: Materials in Electronics. 2011;**22**(8):978-987 https://doi.org/10.1007/s10854-010-0247-z

[19] Czekaj D, Lisińska-Czekaj A, Adamczyk M. Influence of bismuth content on complex Immittance characteristics of Pressureless sintered $BiNbO_4$ ceramics. Archives of Metallurgy and Materials. 2014;**59**(1):225-229 https://doi.org/10.2478/amm-2014-0036

[20] Butee SP, Kambale KR, Upadhyay S. Synthesis and microwave dielectric behavior of $(Bi_{1-x}P_x)NbO_4$ ceramics. Journal of Advanced Dielectrics. 2016;**6**(01):1650006 https://doi.org/10.1142/S2010135X16500065

[21] Devesa S, Graça MPF, Henry F, Costa LC. Structural, morphological and microwave dielectric properties of $(Bi_{1-x}Eu_x)NbO_4$ ceramics prepared by the sol-gel method. International Journal of Materials Engineering Innovation. 2017;**8**(1):12-26 https://doi.org/10.1504/IJMATEI.2017.085808

[22] Devesa S, Graça MP, Henry F, Costa LC. Dielectric properties of $FeNbO_4$ ceramics prepared by the sol-gel method. Solid State Sciences. 2016;**61**:44-50 https://doi.org/10.1016/j.solidstatesciences.2016.09.005

[23] Devesa S, Graça MP, Costa LC. Sol-Gel Synthesis, Structural characterization and microwave dielectric properties of bismuth Niobate modified by iron inclusion. In: Chandra U, editor. Recent Applications in Sol-Gel Synthesis. InTech; 2017. pp. 63-80. DOI: 10.5772/intechopen.68211

[24] Devesa S, Graça MP, Costa LC. Structural, morphological and dielectric properties of $BiNbO_4$ ceramics prepared by the sol-gel method. Materials Research Bulletin. 2016; **78**:128-133 https://doi.org/10.1016/j.materresbull.2016.02.035

[25] Zhai HF, Qian X, Kong JZ, Li AD, Gong YP, Li H, et al. Abnormal phase transition in $BiNbO_4$ powders prepared by a citrate method. Journal of Alloys and Compounds. 2011;**509**(42):1023010233 https://doi.org/10.1016/j.jallcom.2011.08.077

[26] Ayyub P, Multani MS, Palkar VR, Vijayaraghavan R. Vibrational spectroscopic study of ferroelectric $SbNbO_4$, antiferroelectric $BiNbO_4$, and their solid solutions. Physical Review B. 1986;**34**(11):8137. DOI: https://doi.org/10.1103/PhysRevB.34.8137

Section 4

Bismuth Materials for Sensing

Chapter 6

Bismuth Oxide Thin Films for Optoelectronic and Humidity Sensing Applications

Simona Condurache-Bota

Additional information is available at the end of the chapter

http://dx.doi.org/10.5772/intechopen.75107

Abstract

Bismuth oxide thin films still prove attractive to both scientists and engineers due to their semiconducting behavior, large energy bandgap and high refractive index, despite their often complex structure, both polymorphic and polycrystalline. We present here a summary and a comparison of the morpho-structural and optical properties of such films prepared through three physical vapor deposition (PVD) techniques on several types of substrates kept at different temperatures. Thermal vapor deposition, thermal oxidation in air and pulsed laser deposition are discussed as largely used PVD methods. It is proved that the physical properties of the bismuth oxide thin films can be tailored by changing the substrate nature and its temperature during the deposition process in a way even more relevant than even the chosen deposition method. Thus, bismuth oxide thin films with energy bandgaps ranging from the infrared up to near-ultraviolet can be obtained, depending on their structure and morphology. High refractive index of the films can be also attained for specific spectral ranges. When deposited on certain conductive substrates, the films have much lower electrical resistance and even became sensitive to water vapor. Therefore, humidity sensing and optoelectronic applications of the analyzed bismuth oxide thin films can be easily found and used in both science and technology.

Keywords: bismuth oxide, physical vapor deposition, morpho-structural studies, optical analysis, tailored properties, optoelectronics, humidity sensing

1. Introduction

Most high performance electronic and optoelectronic devices are made of crystalline materials. When drastically reducing the size of crystals up till micrometers and nanometers, their properties change dramatically due to quantum size effects, even completely switching their electrical behavior from metallic to semiconducting, as it is also the case with bismuth. Thus,

thin films, nanowires, nanorods, and nanoparticles became really attractive not only to scientists, but also to engineers due to their specific, distinctive properties, but also because of the need of miniaturization and to material saving.

It is considered that a layer of substance deposited on a support (substrate) is a thin film if it has a thickness ranging between nanometer fractions up to 10 micrometers. Thus, a deposited layer is a thin film if it has a thickness in the order of magnitude or less than the average free path of the electric carriers.

Due to the properties induced by the presence of remote order at crystalline semiconductors, studying the methods of obtaining them as thin films and inferring their properties have taken an extraordinary magnitude. Among thin crystalline semiconductor films, the oxides are intensively studied, the presence of oxygen conferring new, special properties, which recommend them for use in Electronics and Optoelectronics, either for coatings or a single component in different circuits and devices.

Bismuth trioxide thin films, Bi_2O_3, which is the most important industrial compound of bismuth, have also captured the interest of researchers because they have large energy bandgap, high refractive index, high photoconductivity, photosensitivity to ultraviolet radiation, etc. [1–6], properties that recommend bismuth trioxide for a wide variety of applications: optical coatings, solar cells, components in electronic circuitry, recording layers in CDs and DVDs and gas and humidity sensors [7–13]. Moreover, complex oxides containing Bi and V, such as $BiVO_4$ have been found as efficient photoelectrochemical (PEC) material for the treatment of polymer-containing wastewater from oilfields, especially when co-doped with W/Mo [14] or Zn [15] or by adding NaCl to the precursor solution when the chemical bath deposition method was employed for $BiVO_4$ photoanodes [16].

The deposition of thin films is subdivided according to the aggregation state of the depositing material in: (1) solution deposition processes, including the sol-gel technique, electrolysis and spray pyrolysis; (2) deposition from the vapor phase, which is subdivided into: (a) chemical vapor deposition (CVD); (b) physical vapor deposition (PVD).

Physical vapor deposition is a technique used for depositing thin films by condensing atomic or molecular vapor phase species on the surface of a certain substrate. The deposition/coating source is a solid or liquid substance. At a PVD deposition, the material to be deposited is vaporized or sprayed, then it is or it is not mixed with a specific gas, and then it condenses from the vapor state as a thin film onto a substrate facing the material source, the substrate having the anterior surface colder than the flow of deposited material. The deposition is carried out in a vacuum enclosure so that the particles of material to be deposited have a maximum average free path. PVD processes can be divided according to the primary vapor formation method into: (i) vaporization (thermal) processes and (ii) spraying (kinetic) processes, respectively. Several techniques of physical vapor deposition are known, such as: cathodic arc deposition (CAD), sputter deposition, evaporative deposition, electron beam physical vapor deposition (EBPVD) and pulsed laser deposition (PLD), respectively.

The deposition and study of the properties of bismuth trioxide films have been and still are difficult because this oxide presents seven polymorphs [17]: α-Bi_2O_3 (primitive, monoclinic,

stable form), β-Bi_2O_3 (tetragonal, metastable form), γ-Bi_2O_3 (cubic centered, metastable form), δ-Bi_2O_3 (cubic centered, stable form), ε-Bi_2O_3 (orthorhombic, metastable), ω-Bi_2O_3 (triclinic, metastable form), and an un-named, metastable form, with cubic primitive structure. Depending on the deposition method and its conditions, on the post-deposition treatment and on the environmental conditions, one or more of bismuth trioxide polymorphs may coexist in the deposited layers. These seven polymorphs have optical and electrical properties that are very different from one another. Thus, the alpha form behaves like a p-type semiconductor at room temperature, passing to n-type conduction around 600°C temperature, depending on the oxygen partial pressure in the surrounding atmosphere [18]. The delta form is among the most efficient ionic conduction oxides, achieved through oxygen vacancies, having a conductivity of about 1 S/cm at 750°C, which is a value with three orders of magnitude larger than the metastable forms of bismuth trioxide, respectively four orders of magnitude greater than the monoclinic alpha form [18, 19].

The deposition of bismuth trioxide can be accomplished by virtually any known method used for thin films: thermal evaporation [11, 20–24]; pulsed laser ablation-PLD [25–30], spray pyrolysis [31–33], electrodeposition [34], sol-gel [35], etc. Depending on the chosen deposition method, on its conditions (nature and temperature of the substrate, the vacuum level, the nature and pressure of the ambient gases, etc.) as well as on the post-deposition thermal treatment, the thin layers of bismuth trioxide deposited up till now have a great variability in terms of structure, morphology and their optical, electrical and other types of physical properties.

Thermal oxidation is a widely used method for the production of oxides of various metals [36–39], including bismuth [9, 21, 22, 40]. Upon thermal oxidation of bismuth, several types of non-stoichiometric oxides (BiO, $Bi_2O_{2.33}$, Bi_4O_7, etc.) can form in addition to Bi_2O_3, whose presence, types of crystalline planes and properties depend on: (i) the properties of the initial bismuth layers; (ii)the oxidation conditions: the maximum attained temperature, the oxidation duration, the heating and cooling rates; (iii) the eventual post-oxidation treatment. There are numerous reports in the scientific literature concerning bismuth oxide thin films obtained by thermal oxidation or by other methods, films exhibiting various structures, morphologies, and optoelectronic properties [1, 9, 21, 40–48]. There are only a few reports on the preparation of bismuth oxide films containing only one type of oxide obtained by thermal oxidation, and these were accomplished at high oxidation temperatures (above 600 K) and/or for long oxidation times of up to a few days, as J. George and collaborators reported [49], along with K. Jayachandran in [22], in both cases the layers consisting of β-Bi_2O_3, while H. A. Zayed obtained polycrystalline δ-Bi_2O_3 thin films [50].

The preparation of bismuth oxide thin films by the PLD (pulsed laser deposition) technique has been rarely used [25–30] because of its relative novelty and of the high cost of the necessary equipment (deposition unit, powerful laser devices, high vacuum, etc.).

The purpose of this chapter is to present three types of physical vapor deposition methods used for the preparation of bismuth oxide thin films with optoelectronic and humidity sensing properties, depending on the set of deposition conditions. A comprehensive methodology for the analysis of the structure, morphology, optical and humidity sensing is also presented together with examples of experimental results and the way the data can and must be interpreted and

further used for practical, scientific and industrial purposes. Thus, this chapter intends to be like a recipe of PVD methods for the preparation of bismuth oxide thin films with tailored properties.

2. Examples of PVD techniques and their corresponding parameters for the preparation of bismuth oxide thin films

As mentioned above, three types of PVD techniques will be discussed here in terms of their most relevant parameters that influence the properties of bismuth oxide thin films. These methods are: (i) thermal vacuum evaporation of bismuth trioxide powder; (ii) thermal oxidation in air of pure bismuth films previously deposited by thermal vacuum evaporation and (iii) pulsed laser deposition of bismuth targets in oxygen atmosphere.

(i) Firstly, classic thermal evaporation in a vacuum can be employed in order to deposit bismuth trioxide thin films, by using high purity Bi_2O_3 (99.999%) as source material, such as the one from Sigma-Aldrich. The depositions have to take place at high vacuum (*e.g.* $8 \cdot 10^{-5}$ *Torr*) onto chemically-cleaned microscope glass substrates (most commonly used, easily available, cheap and resistant to fairly high temperatures) kept at different temperatures, at least 50 degrees apart (*e.g.*27°C = room temperature, RT, 77°C and 127°C, respectively). Such deposition conditions would lead to bismuth trioxide films with a semi-transparent, dark gray appearance [11].

(ii) Alternatively, pure bismuth thin films can be firstly prepared also by thermal evaporation in vacuum (*e.g.* at $5 \cdot 10^{-5}$ *Torr*), onto the same type of microscope glass slides, maintained at different temperatures between room temperature and say 227°C (500 K). After cooling, the bismuth thin films would be submitted to thermal oxidation in air, by means of a home-made device. The oxidation can be performed in two stages of 1 h each, separated by even several days one from the other, such as the properties of the films after the first oxidation stage would not change to air exposure. During the oxidation process, the temperature can be gradually increased up to around 400°C for the first oxidation step and then the temperature should rise at lower temperatures during the second oxidation step (*e.g.* 270°C). The oxidation would be noticed as the films will turn from semi-transparent dark gray as pure bismuth films are, to highly transparent, light yellow-grayish as oxidized layers [23, 24].

(iii) Thirdly, pulsed laser deposition of pure bismuth targets in oxygen atmosphere can also be employed, with and without a radiofrequency discharge of the oxygen inside the high-vacuumed deposition chamber (*e.g.* at $3 \cdot 10^{-5}$ *Torr*). Given the great variability of the types of bismuth oxides that can form and of their properties, depending on the mode and conditions of preparation, it can be chosen to obtain bismuth oxide thin films by the PLD technique by varying: the nature and temperature of the substrate during the depositions, or/and the wavelength (193 or 266 nm) and number of laser pulses (40,000 or 60,000) used for ablation [28–30]. Pure bismuth targets (*e.g.* with 12 mm diameter and 7 mm thickness) can be ablated in a reactive oxygen atmosphere (at *e.g.:* 100 SCCM and 0.6 mbar oxygen partial pressure). An RF source with 13.45 MHz and 150 W can be used for the radio frequency (RF) discharge of the oxygen inside the deposition chamber. Various materials can be employed as substrates at

PLD, from microscope glass slides to silicon, Si (100) or/and Si/Pt, respectively, but the latter proved to give rise to spectacularly different properties of the bismuth oxide films, with electrical resistance up to three orders of magnitude lower than the films deposited on glass and also with a very high sensitivity to humidity as compared to the other prepared films [28]. Substrate heating during the PLD process can also be tried, since this parameter is crucial for the structure, the morphology and the other properties of the deposited films, by controlling the movement, combination, and accumulation of deposing atoms on the substrate. Substrate heating up to even 600°C can be tried and leads to good resulting films.

The thickness of all the deposited and analyzed films can be rather precisely and easily determined by using a Linnik-type of an interference microscope, operated in white light.

The structural analysis of the films can be performed by X-ray Diffractometry (XRD) and/or by transmission electron microscopy (TEM), by means of the SAED (selected area electron diffraction) technique. Thus, typically, an X-ray diffractometer with a Cu Kα (λ = 1.5418 Å) [28, 51] or with a Co Kα target/source (λ = 1.789 Å) [29] can be used. Alternatively, a transmittance electron microscope can be successfully employed for morpho-structural analysis, since it can provide various information about the samples: (i) Bright Field—TEM (BF-TEM) images, (ii) SAED electron diffraction images, with measurements of the radii of the electron diffraction rings through which the interplanar distances can be computed and/or (iii) high-resolution TEM (HRTEM) images from which the interplanar distances can be inferred as well.

The morphology of the films can be analyzed by Scanning Electron Microscopy (SEM) [28, 52, 53] and/or by Atomic Force Microscopy (AFM), the latter with at least 20 nm lateral resolution and 2 nm vertical resolution (*e.g.* a Park XE-100 or a NT-MDT Solver Pro-M AFM [30, 54–57]).

The optical analysis starts by recording the optical transmittance (for the transparent films) and/or reflectance spectra for near-IR, VIS, and near-UV domains, by using a spectrophotometer (*e.g.* type Perkin Elmer Lambda 35), operated at normal incidence, in the air, between at least 200 and 1100 nm. The optical data have to be processed in order to compute the most relevant optical parameters: the refractive index and the absorption coefficient. Then, different models can be applied to these parameters in order to infer new and important figures, such as the energy bandgap and type of electronic transitions within the films [11, 58–61].

Humidity and/or other gas sensing measurements can be performed with a home-made device, made of a closed box kept at room temperature fed with water vapor and a relative humidity meter [28] or a gas and a pressure gauge.

3. Examples of bismuth oxide thin films deposited by the three selected PVD methods: their properties and potential uses

3.1. The structural analysis of bismuth oxide thin films

When thermal vacuum evaporation of Bi_2O_3 powder was employed, most often amorphous films are obtained, independent of the temperature of the glass substrate, as the XRD spectra

proved (see **Figure 1**), by having only one broad maximum instead of individual peaks, like in the case of crystalline samples. The aspect of the XRD spectrum does not change with changing substrate temperature during the depositions.

Instead, when firstly deposing pure Bi thin films onto glass substrates and then thermally oxidize them in open atmosphere, the resulting bismuth oxide films are crystalline, but with very complicated structures. Thus, the oxidized Bi films are most often not only polymorphous but also polycrystalline, and contain not only bismuth trioxide, which is the stoichiometric form of bismuth oxide, but also contain non-stoichiometric bismuth oxides, such as BiO, $Bi_2O_{2.33}$, Bi_4O_7, $Bi_2O_{2.75}$, etc., as they were identified through their specific peaks within the XRD spectrum—see **Figure 2** of such examples. This time, even though the thermal oxidation process is the same for all the pure Bi films, the deposition temperature, t_S of the primary deposited pure Bi films has a decisive influence on the structure of both the primary Bi films, but also on the resulting oxidized films. Thus, as the XRD spectra from **Figure 2** prove, merely

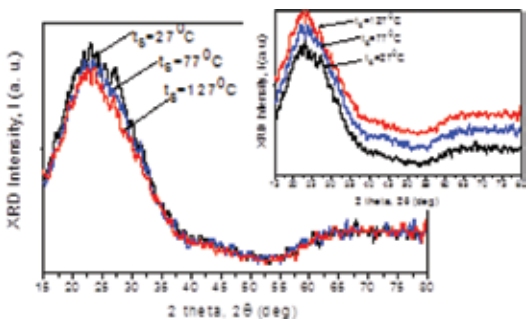

Figure 1. XRD spectrum for a bismuth trioxide thin film [11].

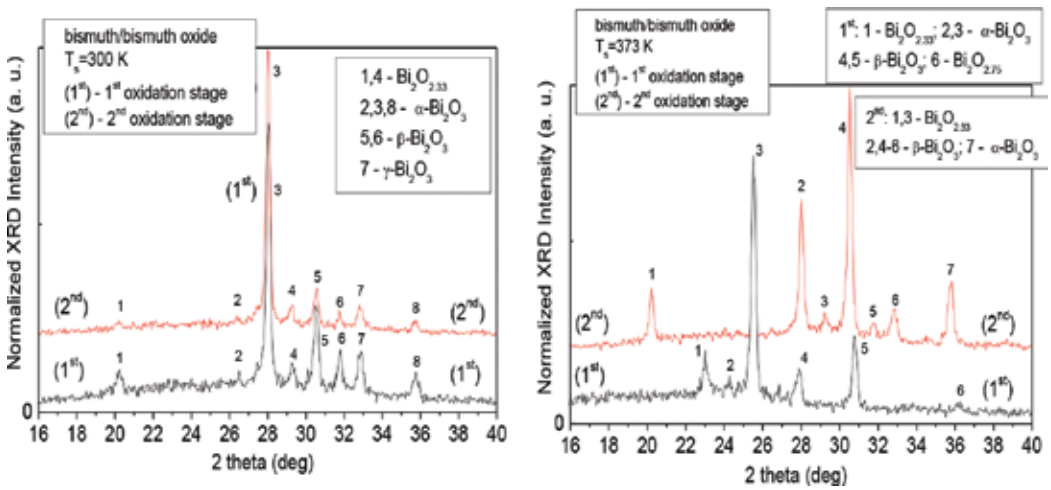

Figure 2. The XRD spectra of two bismuth oxide thin films obtained by two-stage thermal oxidation of pure bismuth films deposited at two different substrate temperatures [62].

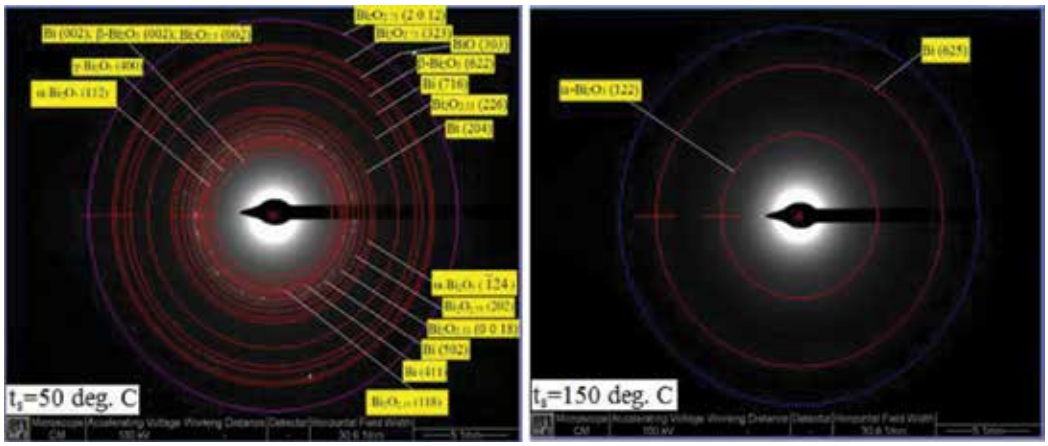

Figure 3. SAED images for two bismuth oxide thin films resulting from the thermal oxidation of pure bi films deposited at different substrate temperatures [63].

changing the substrate temperature with less than 100 degrees makes the thermal oxidation to lead to very different structures. *E.g.* a film deposited at 300 K (27°C) may contain the α, β, γ polymorphs of Bi_2O_3, along with the $Bi_2O_{2.33}$ intermediate oxide, while an oxidized film resulted from a pure Bi layer deposited at 373 K (100°C) may contain only the α and β forms of Bi_2O_3, along with both $Bi_2O_{2.33}$ and $Bi_2O_{2.75}$. The films from **Figure 2** also contain the XRD spectra of the same films after the 2nd oxidation stage (marked with 2nd), showing that further oxidation of the bismuth oxide films changes their structure in a manner and a degree also depending on the substrate temperature during the initial pure bismuth deposition onto the glass. Thus, in the given examples, in the case of a film with T_s = 300 K, the 2nd oxidation stage worsens the crystallinity, as the XRD peaks decreases, while for the films with T_s = 373 K, the 2nd oxidation eliminates some crystalline planes and gives birth to others instead, with a texturizing change [52].

The SAED technique of TEM provides the most detailed structural analysis of low-dimensional structures. This technique allows one to confirm the complicated structures inferred for bismuth oxide films obtained through thermal oxidation in the air as the XRD study shows. As an example of the application of the SAED technique, the images from **Figure 3** confirm the crucial influence of the substrate temperature, t_s (written in the insets of the electron diffraction images) during the initial pure Bi deposition on the resulting oxidized films.

A 100 degrees temperature difference simplifies the structures drastically, the SAED images passing from a multitude of diffraction rings to only a few [63]. Un-oxidized bismuth is generally present as trapped between the formed oxides in all the types of structural analysis of all the deposited bismuth oxide films, and it will also appear even in the morphological studies, when transversal SEM images are obtained, as it will be pointed out later.

Figure 4 presents an example of an HRTEM image of a bismuth oxide film obtained by the thermal oxidation of pure bismuth film deposited at 227°C. The extremely high magnification of the image (over 1,000,000×) allows for the visualization of the families of crystalline planes—two

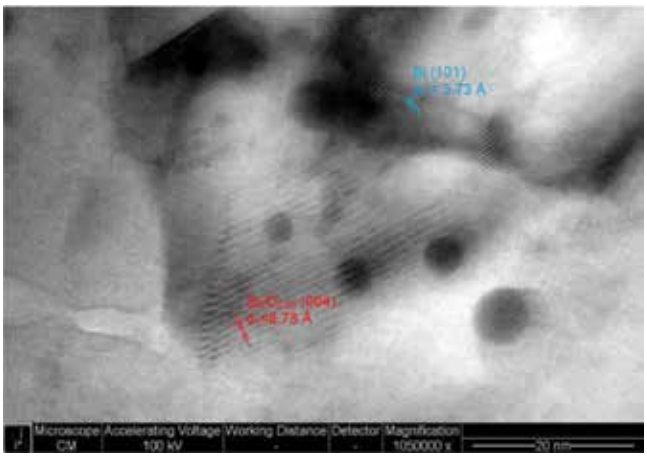

Figure 4. A HRTEM image of a bismuth oxide film with t_S = 227°C.

types in the example: (004) of the non-stoichiometric, seldom found oxide $Bi_2O_{2.33}$, while the others are of the (101) of pure bismuth. The presence of the under-laying and also internally remnant un-oxidized bismuth can be explained by the fact that, as the films are submitted to thermal oxidation, some of the crystalline planes of the forming bismuth oxides block the oxygen access to some bismuth atoms, such the oxidation cannot take place for the entire film.

When using the pulsed laser ablation to prepare bismuth oxide thin films on glass substrates by using pure Bi targets and a reactive oxygen atmosphere (stimulated through a RF discharge), the resulting films still prove to have complicated structures, with remnant un-oxidized bismuth, with intermediate oxides, mixed with different bismuth trioxide polymorphs, as the XRD spectra from **Figure 5** exhibit as examples [29, 56]. Again, the substrate temperature during the deposition process proves critical for the resulting composition and structure of each film, since this parameter controls the mobility of atoms and their mixing and chemical reaction when condensing on the substrates. Moreover, the laser wavelength (namely 266 and 193 nm, respectively) and the number of laser pulses (40,000 or 60,000) used for the ablation of the target also strongly influence the resulting films, as the XRD spectra from **Figure 5** also prove.

Even if the nature of the substrate changes to crystalline silicon, Si (100) or even to Si/Pt, the bismuth oxide thin films prepared by PLD still have complicated structures, as the XRD spectra from **Figure 6** exemplify.

Thus, the films deposited on Si contain both Bi_2O_3 and intermediate oxides [30], along with un-oxidized Bi, while the films deposited on Si/Pt finally reach structural stability, containing merely Bi_2O_3 (*e.g.* β and δ forms) only after thermal treatment (*e.g.* 1-h heating and 1-h cooling) [28]. The substrate temperature, t_S proves important in the case of each type of substrate, even for Si/Pt, the higher t_S (e.g. 600°C as compared to 300°C), the simpler the structure after structural stabilization by post-deposition annealing [28].

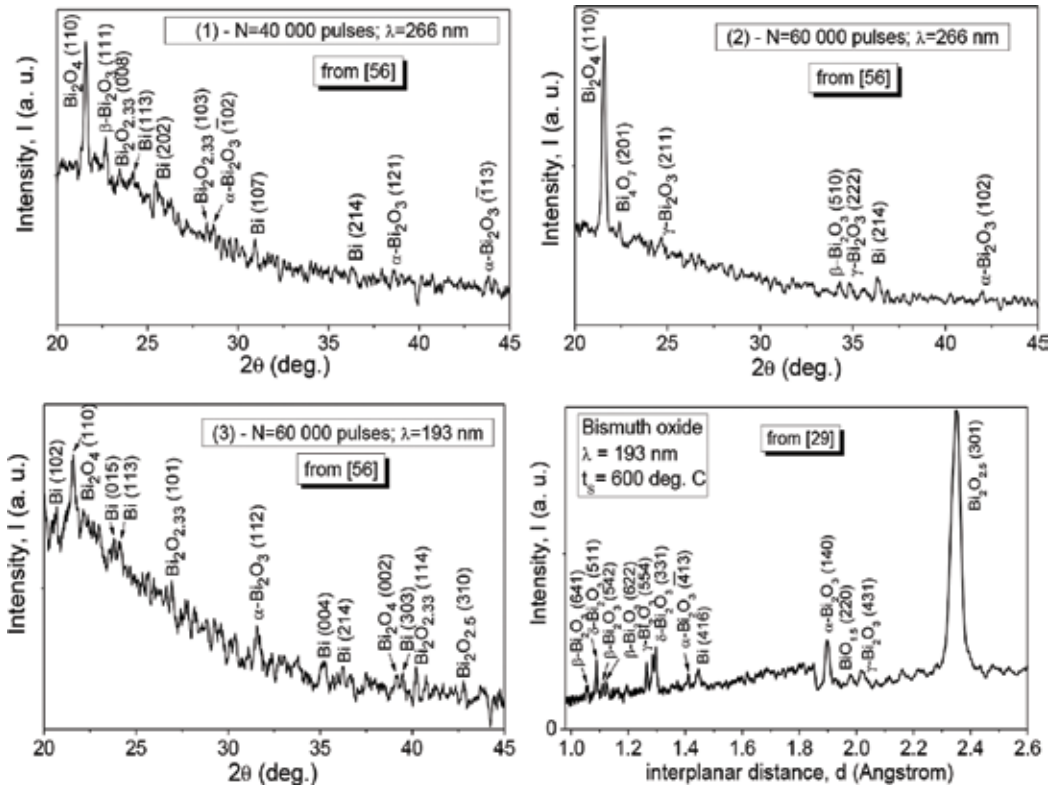

Figure 5. XRD spectra of four bismuth oxide thin films deposited on the glass by RF-PLD, with different deposition conditions [29, 56].

3.2. The morphological analysis of bismuth oxide thin films

Scanning Electron Microscopy can be the choice for the morphological analysis of bismuth oxide thin films. As mentioned above, the remnant bismuth oxide layer underneath the newer formed oxide upon thermal oxidation in air of primary pure Bi films can be also proved by transversal SEM (Scanning Electron Microscopy) images, as the one presented in **Figure 7**.

The normal SEM images as the ones presented in **Figure 8** reveal the morphologies of the bismuth oxide thin films prepared by either method, which are rather uniform when thermal oxidation or PLD are employed on several substrates: glass, Si or Si/Pt.

When using AFM (Atomic Force Microscopy), the aspect of the surface of bismuth oxide thin films is even better revealed as generally having uniformly distributed grains, also sensitive to both the nature of the substrate and to its temperature during the deposition—see **Figures 8** and **9** for such AFM examples. When PLD is used, the grain distribution on the surface of the bismuth oxide film is more uniform, but the grain aspect strongly changes with the wavelength of the UV laser pulses used for the ablation of the bismuth targets, typically 266 and 193 nm.

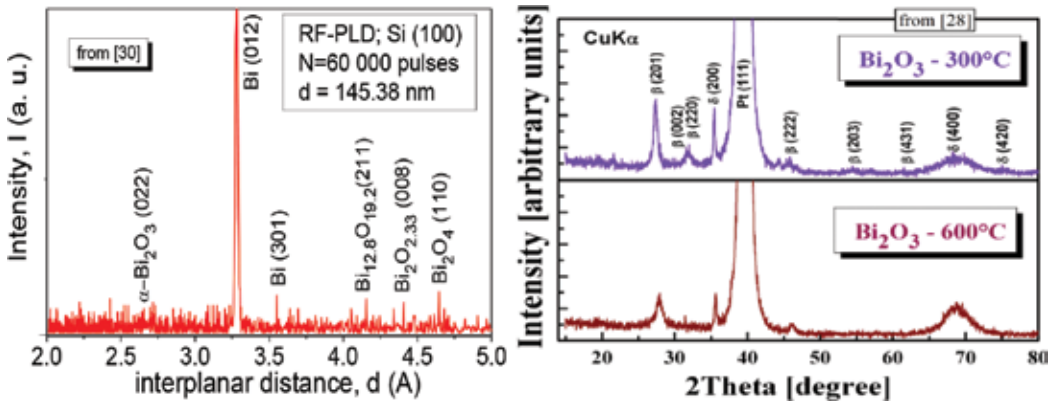

Figure 6. XRD spectra of bismuth oxide thin films deposited by PLD on Si(100) and Si/Pt, respectively [28, 30].

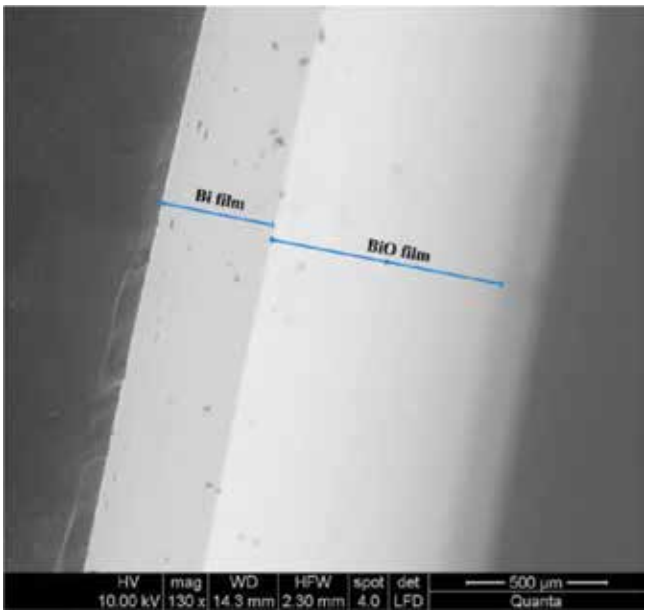

Figure 7. Transversal SEM image of a bismuth oxide thin film prepared by thermal oxidation in air of pure bi films [62].

3.3. Optical analysis of bismuth oxide thin films

The bismuth oxide thin films deposited on glass through each of the three methods described above present high transmittance, either as amorphous or crystalline materials, as the transmittance spectra from **Figure 10** prove. Thus, the transmittance, T of the films surpasses 50% above 400 nm for each of the bismuth oxide film chosen as examples and proofs.

The reflectance of the films presents rather often oscillations with changing wavelength, as **Figure 11** proves.

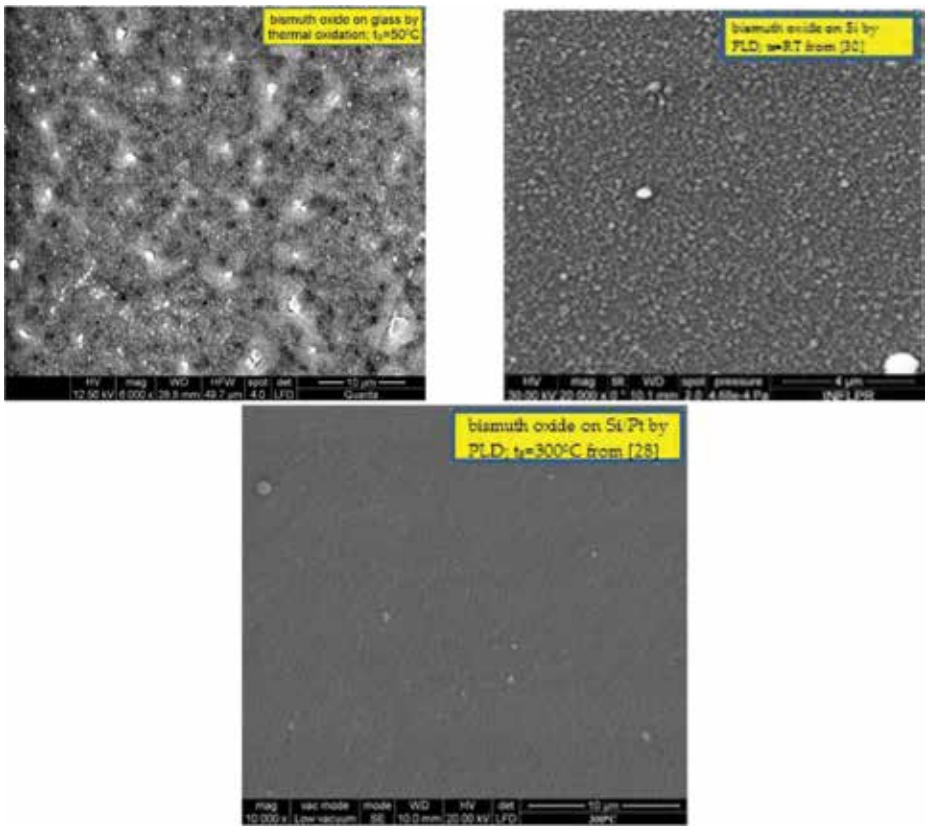

Figure 8. SEM micrographs of bismuth oxide thin films deposited by thermal oxidation (top left image) or by PLD on different substrates (see insets) [28, 30].

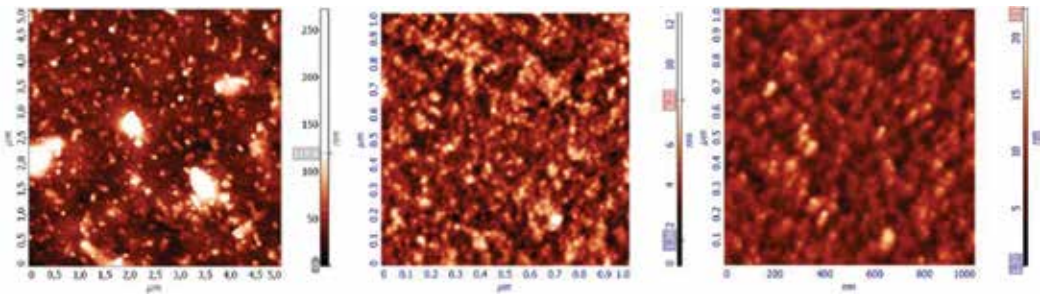

Figure 9. SEM images of bismuth oxide on glass substrates obtained by thermal oxidation (left side image) of by RF-PLD with 266 nm pulses (center image) or with 193 nm pulses (right side image) [55–57].

As the refractive index is concerned, even if its computation is made by taking into account both the reflectance and the transmittance data of the films, its profile or dependence on the wavelength closely follows that of the reflectance data, since it is primarily related to it—see **Figure 12**. Generally, regions with anomalous dispersion can be noticed especially for the

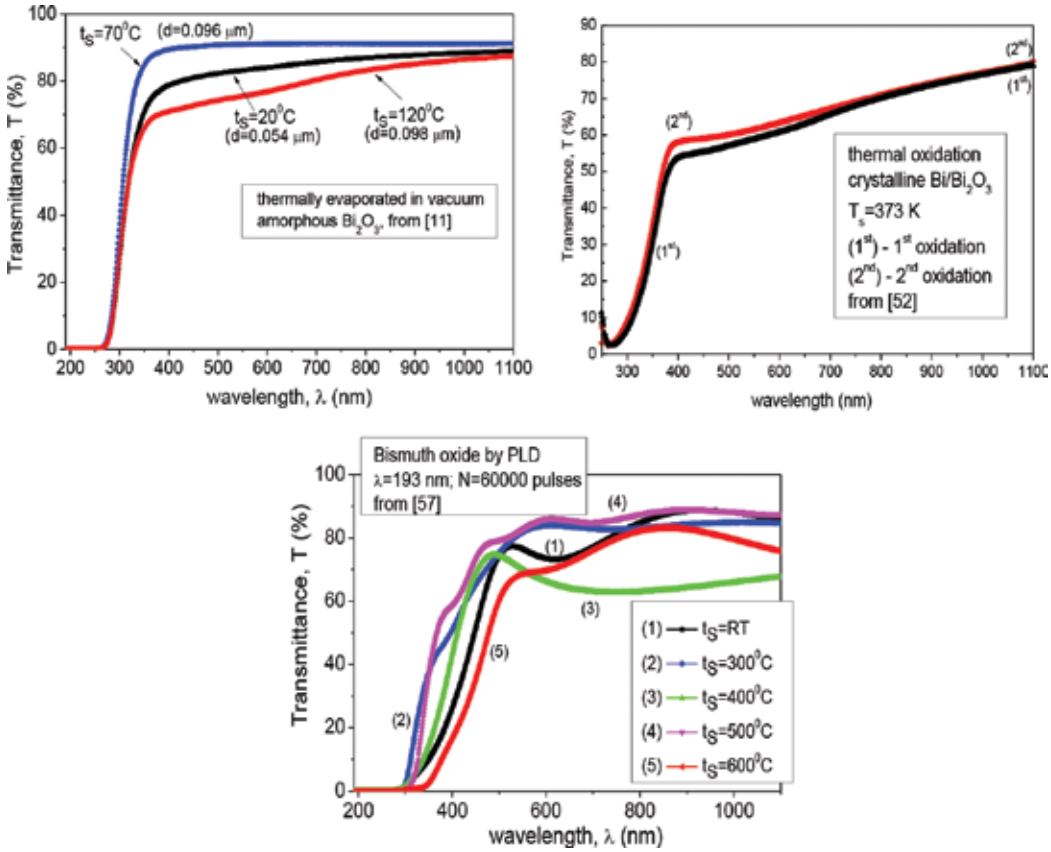

Figure 10. Optical transmission spectra for bismuth oxide thin films prepared by each of the three chosen methods—See insets for details [11, 52, 57].

bismuth oxide films deposited by PLD. Depending on the deposition method and its conditions, the bismuth oxide films can even surpass the value of four for the refractive index.

As for the absorption coefficient, it has to be used for the deduction of the energy bandgap, E_g of the films, according to the model proposed by Tauc [11, 58–61], by plotting $(\alpha \cdot h \cdot \upsilon)^r$ in function of the photon energy, $(h \cdot \upsilon)$ and by extrapolating the graph to zero, as exemplified in **Figure 13** for amorphous bismuth trioxide deposited on glass by thermal evaporation in vacuum. The values of the 'r' coefficient can be 2, 2/3, 1/2 or 1/3, depending on the type of optical transitions most likely to happen within the analyzed semiconducting films. In the case of the structurally complex bismuth oxide films, indirect-type of optical transitions are the most probably allowed, corresponding to r = 1/2.

Such energy bandgap estimation can be performed for each of the bismuth oxide films for whom optical transmittance data can be obtained (i.e. for transparent films deposited onto transparent substrates), but also by applying the Wemple-Didomenico model for refractive index data as a function of wavelength [11]. Examples of values for the energy bandgap of bismuth oxide thin films prepared by different PVD techniques are given in **Table 1**.

http://dx.doi.org/10.5772/intechopen.75107

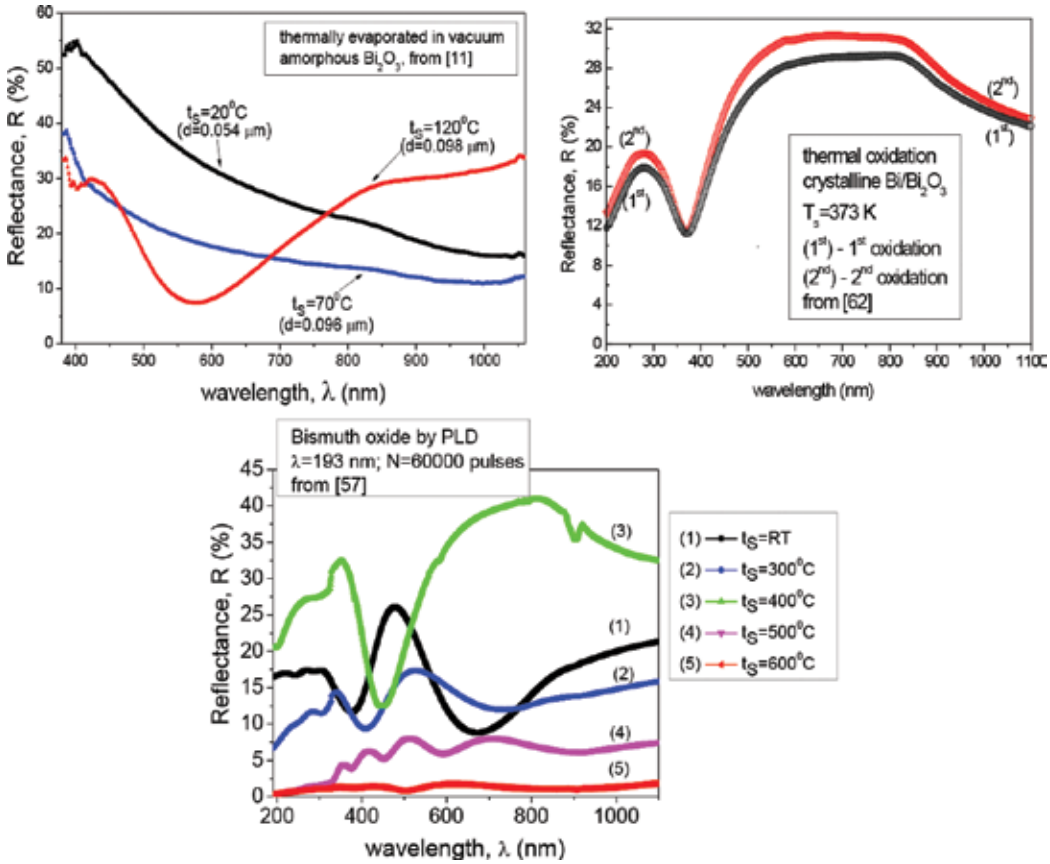

Figure 11. Optical reflectance spectra for bismuth oxide thin films prepared by each of the three chosen methods—See insets for details [11, 51, 62].

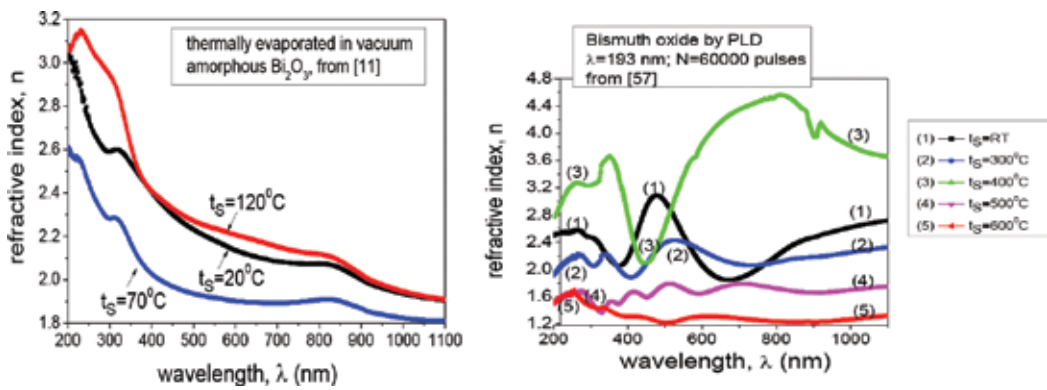

Figure 12. Wavelength dependence of the refractive index for different types of bismuth oxide films [11, 57].

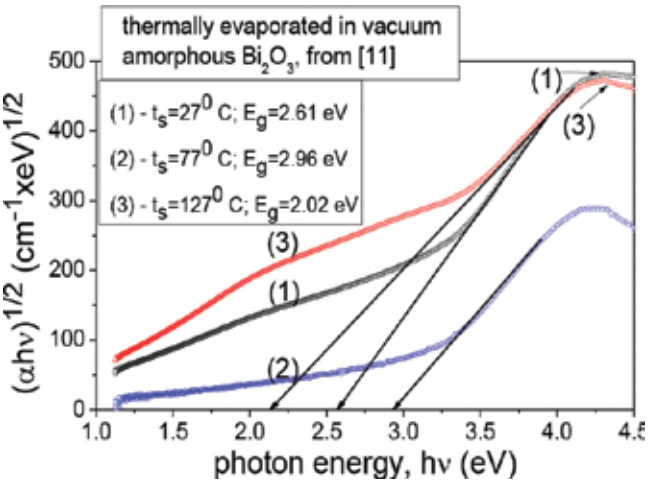

Figure 13. The optical absorption spectra expressed according to Tauc's model, for bismuth trioxide thin films with allowed, indirect transitions and the estimation of their energy bandgaps, E_g [11].

Film preparation method	Substrate temperature, t_S (°C)	Type of optical transition	Optical energy bandgap, E_g (eV)	Reference
Bi thermal oxidation, 1st stage	RT	allowed, indirect $(\alpha \cdot h \cdot \upsilon)^{1/2}$	3.01	[51]
	100		1.53*	[54]
	177		2.90	[51]
	200		1.67*	[54]
	227		2.87	[51]
thermal vacuum deposition of Bi_2O_3	RT		2.61	[11]
	77		2.96	
	127		2.02	
PLD on glass, 193 nm, 60,000 pulses	RT	allowed, direct $(\alpha \cdot h \cdot \upsilon)^2$	4.15 allowed, indirect 3.30	
	300		4.10 3.55	[29]
	400		4.15 3.25	
	500		3.90 3.35	
	600		4.10 2.75	

Table 1. Energy bandgaps and two types of optical transitions within some bismuth oxide thin films deposited by three PVD methods; * E_g inferred through the Wemple-Didomenico model [11, 52, 54, 57].

3.4. Testing the humidity sensitivity of bismuth oxide thin films

Most often, the electrical resistance measurements of bismuth oxide films deposited onto glass and silicon substrates have extremely high resistances, of Gigaohms and more, as in the case of the three PVD methods exemplified here. Still, the films deposited onto conductive substrates, such as Si/Pt exhibit merely Megaohms resistances, which allows for testing their sensitivity to

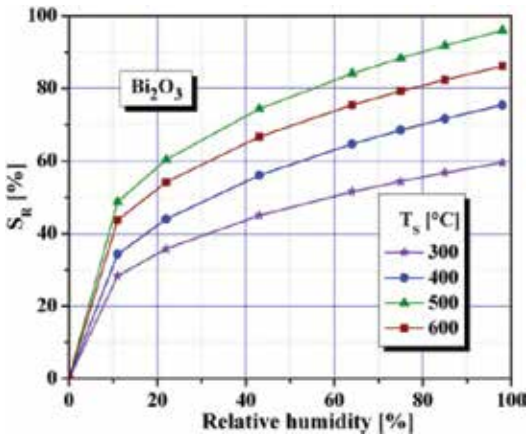

Figure 14. Change of the relative variation of the electrical resistance of bismuth oxide thin films deposited by PLD on Si/Pt substrates, maintained at different temperatures [28].

humidity and/or other gases. As **Figure 14** exemplifies, bismuth oxide thin films deposited by PLD on Si/Pt present excellent sensitivity to increasing humidity, which recommends them for atmospheric sensors [28]. Thus, as the relative humidity increases, the electrical resistance of such films strongly increases, up to 100% relative variation. This behavior is given by the oxygen affinity of metal oxides thin films which can uptake oxygen atoms from the atmosphere in the pores of the structures, linking to the free metal atoms and also because, generally, metal oxide films are oxygen defectives and, thus, need oxygen for stoichiometry. Again, the substrate temperature during the depositions has a relevant influence even on the humidity sensitivity of the films. In the case of the examples from **Figure 14**, the film deposited at 500°C has the highest sensitivity to relative humidity.

4. Conclusions

Bismuth oxide thin films represent both an attraction and a challenge for scientists in terms of their properties depending on their often complicated structure. Different PVD methods can be used to prepare such films, each method having its specific advantages and disadvantages related to the technique itself, but also to the implied costs of needed devices.

This chapter presented a comparison between the structures, morphologies, optical and humidity sensing properties of bismuth oxide thin films prepared by three PVD methods: thermal vacuum evaporation of bismuth trioxide powder, thermal oxidation in air of pure bismuth films previously prepared by thermal evaporation in vacuum, and pulse laser deposition of pure bismuth targets in oxygen atmosphere.

Generally, polymorphic and polycrystalline bismuth oxide films are obtained by using pure bismuth as starting material and then thermal oxidation or PLD in oxygen atmosphere are employed. Thus, mixtures of Bi_2O_3 polymorphs (α, β, γ and δ - most often) along with several

non-stoichiometric oxides ($Bi_2O_{2.33}$—most encountered) are more likely to be obtained. The structure, morphology, optical properties and humidity sensing properties of the bismuth oxide films depend on the nature and temperature of the substrate during the primary deposition much stronger than on the chosen deposition method. Thus, the films deposited onto conductive substrates, such as Si/Pt present much lower electrical resistance than those deposited onto typical substrates such as glass or silicon. Humidity or even other gas sensing cannot be tested for films with high electrical resistance since the resistance variation with gas concentration would not be significant or even measurable.

Generally, bismuth oxide thin films prove to have high optical transmittance and rather high refractive index, along with a semiconducting behavior and a large energy bandgap, properties recommending them to Optoelectronics, especially since these properties can be tailored by properly changing the deposition method and especially the nature and temperature of the substrate.

Acknowledgements

Professors G. I. Rusu, N. Tigau, and C. Gheorghies, as well as physicists C. Constantinescu, R. Gavrila, V. Tiron, G. Prodan, A. P. Rambu, F. Tudorache, L. Leontie and I. Petrila are acknowledged for their collaboration in the preparation and analysis of the films, as well as for their support and advice. The Sectoral Operational Programme Human Resources Development 2007-2013, Project POSDRU/159/1.5/S/132397 is acknowledged for a partial financial support.

Author details

Simona Condurache-Bota

Address all correspondence to: scondurache@ugal.ro

Chemistry, Physics and Environment Department, Faculty of Sciences and Environment, Dunarea de Jos University of Galati, Romania

References

[1] Patil RB, Puri RK, Puri V. Oxidation temperature dependent optical properties of bismuth oxide thin films: Effect of vapor chopping and air exposure. Applied Surface Science. 2007;**253**:8682-8688

[2] Leontie L, Caraman M, Delibas M, Rusu GI. Optical properties of bismuth trioxide thin films. Materials Research Bulletin. 2001;**36**(9):1629-1637

[3] Leontie L. Optical properties of bismuth oxide thin films prepared by reactive magnetron sputtering. Journal of Optoelectronics and Advanced Materials. 2006;**8**:1221-1224

[4] Leontie L, Rusu GI. On the electronic transport properties of bismuth oxide thin films. Journal of Non-Crystalline Solids. 2006;**352**:1475

[5] Leontie L, Caraman M, Rusu GI. On the photoconductivity of Bi_2O_3 in thin films. Journal of Optoelectronics and Advanced Materials. 2000;**2**:385-389

[6] Takeyama T, Takahashi N, Nakamura T, Ito S. Growth of the high reflectivity Bi_2O_3 glass films by atmospheric pressure halide CVD. Optical Materials. 2004;**26**:413-415

[7] Hwang GH, Han WK, Kim SJ, Hong SJ, Park JS, Park HJ, Kang SG. An electrochemical preparation of bismuth nanoparticles by reduction of bismuth oxide nanoparticles and their application as an environmental sensor. Journal of Ceramic Processing Research. 2009;**10**(2):190

[8] Leontie L, Caraman M, Alexe M, Harnagea C. Structural and optical characteristics of bismuth oxide thin films. Surface Science. 2002;**507-510**:480-485

[9] Bhande SS, Mane RS, Ghule AV, Han S-H. A bismuth oxide nanoplate-based carbon dioxide gas sensor. Scripta Materialia. 2011;**65**:1081-1084

[10] Jitianu M, Fruth V. Structural aspects of antimony doped Bi_2O_3. Revue Roumaine de Chimie. 2002;**47**:1171-1176

[11] Condurache-Bota S, Rusu GI, Tigau N, Leontie L. Important physical parameters of Bi_2O_3 thin films found by applying several models for optical data. Crystal Research and Technology. 2010;**45**(5):503-511

[12] Gou X, Li R, Wang G, Chen Z, Wexler D. Room-temperature solution synthesis of Bi_2O_3 nanowires for gas sensing application. Nanotechnology. 2009;**20**:495501

[13] Jiang Z, Geng Y, Gu D. Write-once medium with BiOx thin films for blue laser recording. Chinese Optics Letters. 2008;**6**:294-296

[14] Zhou Y, Li W, Wan W, Zhang R, Lin Y. W/Mo co-doped $BiVO_4$ for photocatalytic treatment of polymer-containing wastewater in oilfield. Superlattices and Microstructures. 2015;**82**:67-74

[15] Su J, Liu C, Liu D, Li M, Zhou J. Enhanced Photoelectrochemical performance of the $BiVO_4$/Zn:$BiVO_4$ homojunction for water oxidation. ChemCatChem. 2016;**8**:1-9

[16] Xia L, Li J, Bai J, Li L, Chen S, Zhou B. $BiVO_4$ photoanode with exposed (040) facets for enhanced photoelectrochemical performance. Nano-Micro Letters. 2018;**10:11**:1-10

[17] JCPDS data files nos. 41–1449, 71–0465, 71–2274, 72–0398, 76–1730, 27–50, 29–236, 18–244, 74–2351, 74–1374, 78–1793, 77–0374, 71–0466, 74–1633, 77–2008, 16–654, 27–52, 45–1344, 71–0467, 74–1375, 74–1373

[18] http://www.nanum.com.br/interna.php?area=produto&idIdioma=2&escolha=39

[19] Mehring M. From molecules to bismuth oxide-based materials: Potential homo- and heterometallic precursors and model compounds. Coordination Chemistry Reviews. 2007; **251**:974-1006

[20] Condurache-Bota S, Rusu GI, Tigau N, Nica V, Drasovean R. Structural and optical analysis of superimposed bismuth and antimony oxides. Journal of Optoelectronics and Advanced Materials. 2009;**11**:2159

[21] Ismail RA. Characteristics of bismuth trioxide film prepared by rapid thermal oxidation. e-Journal of Surface Science and Nanotechnology. 2006;**4**:563-565

[22] Jayachandran K. Electrical, Optical and Structural Studies in Bismuth, Antimony, Bismuth Oxide and Antimony Oxide. Ph. D. Thesis, Mahatma Gandhi University, India. 1997. http://shodhganga.inflibnet.ac.in/bitstream/10603/113/15/10_chapter3.pdf

[23] Condurache-Bota S, Rusu GI, Tigau N. Detailed computation of optical features for vacuum-deposited thin films of bismuth trioxide. Annals of the "Dunarea de Jos" University of Galati, Mathematics, Physics, Theoretical Mechanics, Fascicle II. 2009;**XXVI** (XXXII):72-79

[24] Murariu G, Condurache-Bota S, Tigau N. Polynomial fitting approach for the Kramers–Kronig method for optical properties computing for Bi_2O_3 fabric. International Journal of Modern Physics B. 2012;**26**(7):1250049-12500458

[25] Leontie L, Caraman M, Visinoiu A, Rusu GI. On the optical properties of bismuth oxide thin films prepared by pulsed laser deposition. Thin Solid Films. 2005;**473**:230-235

[26] Zhu BL, Zhao XZ. Study on structure and optical properties of Bi_2O_3 thin films prepared by reactive pulsed laser deposition. Optical Materials. 2006;**29**:192-198

[27] Al Waisy ET, Al Wazny MS. Structural, surface morphology and optical properties of Bi_2O_3 thin film prepared by reactive pulse laser deposition. Journal of University of Anbar for Pure Science. 2013;**7**(2)

[28] Tudorache F, Petrila I, Condurache-Bota S, Constantinescu C, Praisler M. Humidity sensors applicative characteristics of granularized and porous Bi_2O_3 thin films prepared by oxygen plasma-assisted pulsed laser deposition. Superlattices and Microstructures. 2015;**77**:276-285

[29] Condurache-Bota S, Constantinescu C, Praisler M, Tigau N. The influence of the substrate temperature on the structure and on the optical energy bandgap of bismuth oxide thin films prepared by pulsed laser deposition. Digest Journal of Nanomaterials and Biostructures. 2015;**10**(3):1025-1032

[30] Condurache-Bota S, Constantinescu C, Tigau N, Praisler M. Bismuth oxide thin films deposited on silicon through pulsed laser ablation, for infrared detectors. Surface Review Letters. 2016;**23**(2):1550104 (9 pages)

[31] Gujar TP, Shinde VR, Lokhande CD. Spray pyrolysed bismuth oxide thin films and their characterization. Materials Research Bulletin. 2006;**41**(8):1558-1564

[32] Madler L, Pratsinis SE. Bismuth oxide nanoparticles by flame spray pyrolysis. Journal of the American Chemical Society. 2002;**85**(7):1713-1718

[33] Rico-Fuentes O, Sanchez-Aguilera E, Velasquez C, Ortega-Alvarado R, Alonso JC, Ortiz A. Characterization of spray deposited bismuth oxide thin films and their thermal conversion to bismuth silicate. Thin Solid Films. 2005;**478**:96-102

[34] Takeuchi M, Takeyama T, Takahashi N, Nakamura T. Preparation of amorphous bismuth oxide films by electrodeposition. Electrochemistry. 2005;**73**(12):1030-1034

[35] Mallahi M, Shokuhfar A, Vaezi MR, Esmaeilirad A, Mazinani V. Synthesis and characterization of bismuth oxide nanoparticles via sol-gel method. American Journal of Engineering Research. 2014;**3**:162-165

[36] Sreemany M, Bose A, Sen S. A study on structural, optical, electrical and microstructural properties of thin TiOx films upon thermal oxidation: Effect of substrate temperature and oxidation temperature. Physica B. 2010;**405**:85-93

[37] Dantus C, Rusu GB, Rusu GG, Gorley P. On the structural characteristics of thermally oxidized CdO thin films. Journal of Optoelectronics and Advanced Materials. 2008;**10**(11): 2988-2992

[38] Rusu DI, Rusu GG, Luca D. Structural characteristics and optical properties of thermally oxidized zinc films. Acta Physica Polonica A. 2011;**119**(6):850-856

[39] Rambu AP, Sirbu D, Rusu GI. Influence of the oxidation conditions on the structural characteristics and optical properties of zinc oxide thin films. Journal of Vacuum Science and Technology A. 2010;**28**:1344

[40] Salazar-Perez AJ, Camacho-Lopez MA, Morales-Luckie RA, Sanchez-Mendieta V, Urena Nunez F, Arenas Alatorre J. Structural evolution of Bi_2O_3 prepared by thermal oxidation of bismuth nano-particles. Superficies y Vacío. 2005;**18**(3):4-8

[41] Ismail RA. Fabrication and characteristics study of n-Bi_2O_3/n-Si heterojunction. Journal of Semiconductor Technology and Science. 2006;**6**(2):119-123

[42] Leontie L. Optical properties of Bi_2O_3 in thin films. The Scientific Annals of the Alexandru Ioan Cuza University of Iasi, Romania, **XLV - XLVI**, Condensed Matter Physics Series. 1999-2000:98-103

[43] Leontie L, Caraman M. On the photovoltaic effect in bismuth oxide thin films. The Scientific Annals of the Alexandru Ioan Cuza University of Iasi, Romania, **XLV-XLVI**, Condensed Matter Physics Series. 1999-2000:91-97

[44] Tahboub RM, Guindy M, Merchant HD. Oxidation kinetics of bismuth and its dilute alloys. Oxidation of Metals. 1979;**13**(6):545-556

[45] Patil RB, Puri RK, Puri V. Effect of chopping on the properties of bismuth oxide thin films. Materials Letters. 2008;**62**:198-201

[46] Gujar TP, Shinde VR, Lokhande CD. The influence of oxidation temperature on structural, optical and electrical properties of thermally oxidized bismuth oxide films. Applied Surface Science. 2008;**254**:4186-4490

[47] Patil S, Kulkarni D, Puri V. Microwave studies of thermally oxidized vacuum evaporated bismuth thin films on alumina. Journal of Physics: Conference Series. 2008;**114**:012040–1-6

[48] Yang B, Mo M, Hu H, Li C, Yang X, Li Q, Qian Y. A rational self-sacrificing template route to β-Bi_2O_3 nanotube arrays. European Journal of Inorganic Chemistry. 2004;**2004**(9):1785-1787

[49] George J, Pradeep B, Joseph KS. Oxidation of bismuth films in air and superheated steam. Thin Solid Films. 1986;**144**:255-264

[50] Zayed HA. Physical properties of δ–Bi_2O_3 thin films. Fizika A. 1995;**4**:45-53

[51] Condurache-Bota S, Tigau N, Rambu AP, Rusu GG, Rusu GI. Optical and electrical properties of thermally-oxidized bismuth thin films. Applied Surface Science. 2011;**257**: 10545-10550

[52] Condurache-Bota S, Rusu GI, Tigau N, Drasovean R, Gheorghies C. Structural and optical characterization of thermally oxidized bismuth films. Revue Roumaine de Chimie. 2009; **54**(3):205-211

[53] Condurache-Bota S, Constantinescu C, Rusu GI, Tigau N, Cantaragiu AM. Oxidized bismuth films deposited by PLD with and without RF. Annals of Dunarea de Jos University of Galati, Mathematics, Physics, Theoretical Mechanics, Fascicle II. 2010;**II (XXXIII)** (2):206-211

[54] Condurache-Bota S, Tigau N, Praisler M, Prodan G, Gavrila R. Near-infrared energy bandgap bismuth oxide thin films and their in-depth morpho-structural and optical analysis. Romanian Reports in Physics. 2017;**69**(3):1-10

[55] Condurache-Bota S, Constantinescu C, Praisler M, Gavrila R, Tigau N, Gheorghies C. Influence of the Preparation Method on the Morpho-Structural and Optical Properties of Bismuth Oxide Thin FilmsCAS 2014 Proceedings, IEEE Catalog Number: CFP14CAS-PRT; ISBN: 978–1–4799-3916-9; ISSN: 1545-827X. 2014:69-72

[56] Condurache-Bota S, Constantinescu C, Praisler M, Tiron V, Tigau N, Gheorghies C. The influence of laser wavelength and pulses number on the structure and the optical properties of pulsed laser-deposited bismuth oxide thin films. CAS 2014 Proceedings, IEEE Catalog Number: CFP14CAS-PRT; ISBN: 978-1-4799-3916-9; ISSN: 1545-827X. 2014:87-90

[57] Condurache-Bota S, Tiron V, Praisler M. Highly transparent bismuth oxide thin films deposition: Morphology - optical properties correlation studies. Journal of Optoelectronics and Advanced Materials. 2015;**17**(9–10):1296-1301

[58] Dongol M. Effect of composition and annealing on some of the optical parameters of Ge_x Te_{100-x} thin films. Egyptian Journal of Solids. 2000;**23**:297-306

[59] Tigau N. Structural characterization and optical properties of annealed Sb_2S_3 thin films. Romanian Journal of Physics. 2008;**53**(1–2):209-215

[60] Yakuphanoglu F, Durmus M, Okutan M, Köysal O, Ahsen V. The refractive index dispersion and the optical constants of liquid crystal metal-free and nickel(II) phthalocyanines. Physica B: Condensed Matter. 2006;**373**(2):262-266

[61] Chongjun H, Feng X, Jiming W, Youwen L. Refractive index dispersion of relaxor ferroelectric $0.9Pb(Zn_{1/3}Nb_{2/3})O_3$-$0.1PbTiO_3$ single crystal. Crystal Research and Technology. 2009;**44**:211

[62] Condurache-Bota S, Drasovean R, Tigau N, Rambu AP. The influence of substrate temperature on the structure and on the optical reflection spectrum of bismuth thin films. Revue Roumaine de Chimie. 2011;**56**(12):1097-1102

[63] Condurache-Bota S, Tigau N. The influence of the oxidation degree of bismuth oxide thin films on their optical properties. Revue Roumaine de Chimie. 2017;**62**(10):757-762

Chapter 7

Multifunctional Bismuth-Based Materials for Heavy Metal Detection and Antibiosis

Yiyan Song and Jin Chen

Additional information is available at the end of the chapter

http://dx.doi.org/10.5772/intechopen.75809

Abstract

The increasing complexity of environmental contamination has boosted the search of multifunctional nanomaterials that are produced in a green and economical manner. The bismuth-based materials have been long regarded as safe materials used in cosmetics as well as biomedical aspects. Particularly, as one of the most important bismuth oxyhalides, bismuth oxychloride (BiOCl), due to its intrinsic properties including high surface area, superior photocatalytic/electrochemical performance, and good biocompatibility, possesses enormous potential for environmental applications. In this chapter, we mainly introduced bismuth-based materials as typified by BiOCl as ecofriendly multifunctional materials for the purposes of heavy metal detection as well as antibiosis.

Keywords: bismuth, heavy metal detection, electrochemical stripping analysis, antibiosis

1. Introduction

As one of the heavy metal elements in the periodic table, bismuth has attracted considerable interests for industrial and biotechnological applications. Cosmetic and pharmaceutical uses of bismuth compounds can be dated back over two centuries ago. Bismuth materials including metal bismuth as well as its compounds have been long regarded as green materials due to their eco-friendliness. Owing to their biocompatibility, extensive research of bismuth has been conducted in diverse fields. For example, the layered structure of bismuth oxychloride (BiOCl) enabling it to give pearl-like coloring was used in cosmetics. Electrodes decorated with bismuth-based materials such as $Bi(NO_3)_3$ and Bi_2O_3 have been used for the electrochemical stripping analysis of heavy metals as an alternative method to replace toxic mercury-based ones [1–3].

In particular, owing to its large surface area, extraordinary electronic transport properties and high electrocatalytic activities, BiOCl has been extensively studied especially for industrial purpose such as photocatalytic/electrochemical materials [4, 5]. Notably, it was reported that bismuth subsalicylate (BSS), the active ingredient of an antacid drug with the trademark of Pepto-Bismol that was approved for sale over a century in North America, is hydrolyzed into BiOCl in the stomach [6–9], suggesting its organism safety for clinical practice. Meanwhile, because of their therapeutic efficacy to deal with gastrointestinal disorders and microbial infections, bismuth-based conjugates such as colloidal bismuth subcitrate have been explored in the pharmaceutical industry.

2. The morphology of bismuth-based materials

Despite the extraordinary photo/electro-chemical properties, the layer structure of bismuth-related material typified by BiOCl may limit its practical applications. Therefore, in an effort to obtain BiOCl-based material of defined morphology, mesoporous silica materials including Korea Advanced Institute of Science and Technology-6 (KIT-6) have been tested as structural support to produce BiOCl-KIT-6 composites. As shown in **Figure 1A**, scanning electron microscopic image (SEM) of BiOCl has revealed its layer assembly, which was composed of microspheres with a diameter of about 3 μm. By comparison, BiOCl-KIT-6 composites exhibited a relatively large form distributing in a size range of tens of micrometers (**Figure 1B**) with a raspberry-like display of bunched balls. It was found that both BiOCl and BiOCl-KIT-6 composites were composed of nanoplates of several nanometers in thickness, aligning radically and tightly to form hierarchical microspheres. X-ray diffraction (XRD) analysis was performed to study the crystallographic structure of the BiOCl-KIT-6 composites. As shown in **Figure 2**, the well-crystallized phase of BiOCl-KIT-6 composite agreed well with that of the tetragonal BiOCl (JCPDS Card No.06-0249). The peaks located at 24.0°, 34.8°, and 36.5° correspond to (002), (012), and (003) crystalline planes of the BiOCl structure, respectively, representing the characteristics of lamellar structures. The crystallite size (average size of the

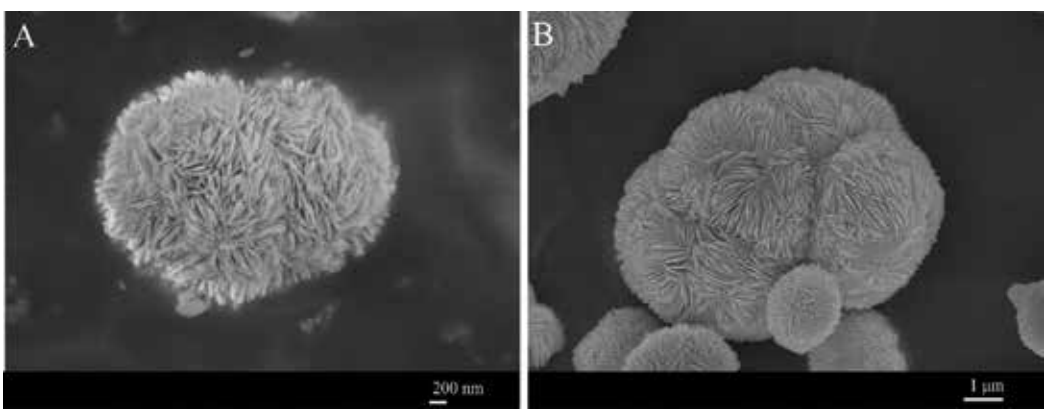

Figure 1. SEM images of (A) BiOCl (Adapted from Ref. [10]) and (B) BiOCl-KIT-6.

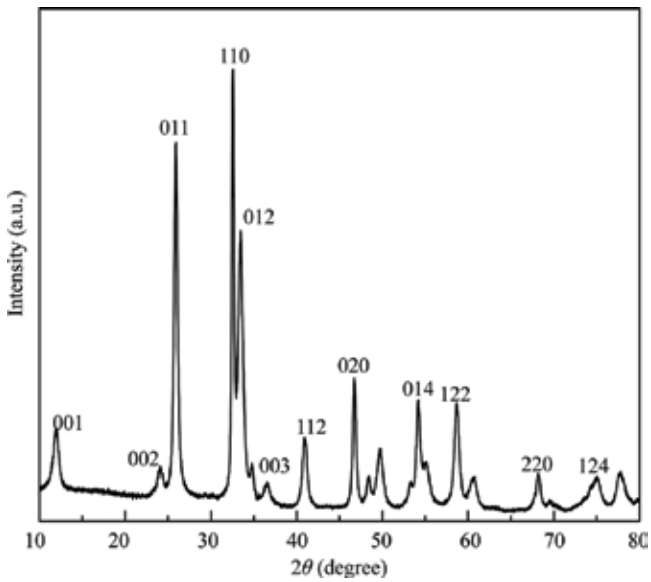

Figure 2. XRD pattern of BiOCl-KIT-6 composite (adapted from Ref. [10]).

coherent scattering region) for the BiOCl component was found to be 17.8 nm, calculated according to the Scherrer formula [10].

3. Bismuth-based sensor for the determination of heavy metals

The method to achieve bismuth-based electrode mainly included in situ plating and ex situ plating. The in situ plating involves the addition of Bi^{3+} into the sample solution. The bismuth film was formed on the surface of the electrode through the deposition during analyzing process. This method is limited as the assay pH of the sample solution has to be kept acidic. The ex situ plating includes plating the bismuth film on the electrode prior to the analysis of the sample solution. As such, preforming bismuth film on the electrode surface is not influenced by the assay conditions, ex situ method is relatively versatile for the real analysis though additional cautions and preparations are needed compared with in situ one. It is worth mentioning that bismuth-based electrode prepared by ex situ method can be reused. After the measurement, the bismuth-based electrode can be reactivated by holding the electrode at an adequate potential, which is more negative than the oxidation potential of bismuth while more positive than the oxidation stripping potential of analyzed metal ions. Therefore, after the reactivation, the bismuth-based electrode can be regenerated without any possible interference of deposited metals.

The application of bismuth-based electrode for heavy metal detection dated back to 2000 when Wang and coauthors tried to plate thin bismuth films on the carbon electrode as an alternative to mercury-based electrode [1]. The main advantage of bismuth-based material modified electrode is its nontoxicity to the environment as well as the biosafety for the operational

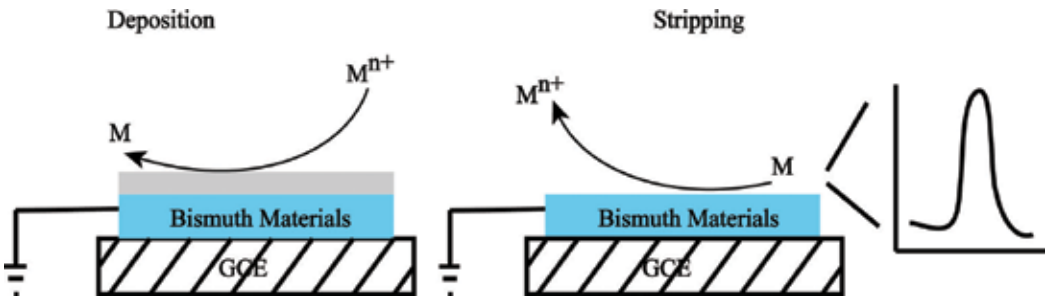

Figure 3. A schematic diagram of measurement of heavy metal ions using anodic stripping voltammetry.

personnel. Meanwhile, the bismuth-based sensors provide detection sensitivity and accuracy comparable to that of mercury-based ones [11], which are attractive for practical applications. Recently, bismuth-based sensors, exhibiting improved separation ability of intermetallic compounds, compared with mercury-based ones, have been used to evaluate heavy metals such as Cd^{2+} and Pb^{2+}. These toxic heavy metals originating from severe environmental conditions including mining area, smelting works, and sewage plant [12] are harmful for the public health.

Nowadays, electrochemical methods owing to their portability, ultrasensitivity, readiness, and low cost have become useful and efficient for the trace determination of heavy metals [13–17]. Among them, anodic stripping voltammetry (ASV), which involves an effective preconcentration step to form metals on the electrode surface by reducing metal ions in the assay solution, followed by a sensitive stripping analysis where metals were reoxidized contributing to a remarkable signal-to-noise ratio, has been intensively employed in this aspect during the past decade (**Figure 3**). The amplified stripping signal resulting from bismuth-based electrodes reflects the ability of bismuth to form "fused" multicomponent alloys with targeted heavy metals [18]. Bismuth-based sensors thus hold potentials for the assays of heavy metal with applications ranging from continuous remote sensing to disposable chips. Since the bismuth-based electrode was applied for the determination of heavy metals in 2000 [1], many reports related to various bismuth-based material modified electrodes have been devoted to this area. In 2008, Xu and coworkers used a Nafion-coated bismuth electrode to achieve the simultaneous determination of three heavy metals including Pb^{2+}, Cd^{2+}, and Zn^{2+} in vegetables using differential pulse anodic stripping voltammetry [19]. In 2014, Sosa and coworkers analyzed Cd^{2+} and Pb^{2+} in groundwater based on sputtered bismuth screen-printed electrode [20]. In 2015, Cerovac and coworkers used the bismuth-oxychloride particle-multiwalled carbon nanotube composite-modified glassy carbon electrode to detect trace-level lead and cadmium in sediment pore water [21]. And it is also readily possible to evaluate the heavy metal amounts of human blood sample. For example, Song and coworkers determined Cd^{2+} in blood samples based on BiOCl-KIT-6 modified glassy carbon electrode [11]. During the past decade, many studies have introduced a number of trace heavy metal detection methods based on bismuth-based electrode. Some typical bismuth-based sensors as well as the resulting analytical performance are summarized in **Table 1**.

Nevertheless, in comparison with mercury-based electrode, bismuth-based one often works well in a relatively narrow potential window, particularly being in a more negative anodic range due to the fact that bismuth is more easily oxidized than mercury. Meanwhile, the

Sensor	Method	Deposit. potent. (v)	Deposit. time (s)	Linear range (μg/L)		LOD(μg/L)		Ref.
				Pb	Cd	Pb	Cd	
Bi-CNT SPE	SWASV	−1.4	300	2–100	2–100	1.3	0.7	[27]
NCBFE	DPASV	−1.4	180	4–36	4–36	0.17	0.17	[19]
Bi/GCE	SWASV	−1.2	600	5–60	5–60	0.8	0.4	[28]
Bi_{sp}SPE	DPASV	−1.3	360	0.5–20	0.3–12	0.16	0.10	[20]
BiOCl/MWCNT-GCE	SWASV	−1.2	120	5–50	5–50	0.57	1.2	[21]
BiOCl-KIT-6/GCE	SWASV	−1.3	120	0.2–300	0.2–300	0.05	0.06	[12]

Bi-CNT SPE, bismuth-modified carbon nanotube modified screen-printed electrode; NCBFE, Nafion-coated bismuth film electrode; Bi/GCE: bismuth nanoparticles modified GCE; Bi_{sp}SPE, sputtered bismuth screen-printed electrode; MWCNT, multiwalled carbon nanotube; SWASV, square wave anodic stripping voltammetry; DPASV, differential pulse anodic stripping voltammetry.

Table 1. Bismuth-based electrodes for determination of Pb (II) and Cd (II) using anodic stripping voltammetry.

cathodic limit of bismuth-based electrode posed by hydrogen reduction is close to that of mercury-based one. Therefore, the accessible potential window of bismuth-based electrode is narrower than that made of mercury. Additionally, it was found that the potential window of bismuth-based electrode was strongly affected by the pH values of the sample solution. The relationship of operational potential windows of bismuth-based electrode and assay pH is shown in **Table 2** [22]. Moreover, it was observed that the constructed BiOCl-KIT-6/GCE possessed a wide potential window ranging from −1.22 to −0.25 V versus SCE by recording the CV spectra of electrode in 0.1 M acetate buffer (pH 4.5) (**Figure 4**). The wide potential window of BiOCl-KIT-6/GCE may permit the simultaneous determination of Zn^{2+} (stripped at −1.15 V), Pb^{2+} (stripped at −0.58 V) and Cd^{2+} (stripped at −0.83 V). It should be noted that the stripping analysis of heavy metals is limited if oxidation potentials of analyzed metals are close to or more positive than that of bismuth such as Cu, Sn, and Sb.

In the aspect of heavy metal measurement, many earlier studies have focused on the design of bismuth-based sensors as well as the detection principle. However, their applications to environmental, food, and clinical samples have just started. For example, by the use of anodic stripping voltammetry, cadmium and lead at trace levels in environmental samples [23, 24], food products [25, 26] and biological fluids [11] have been determined. Using square-wave

Medium	pH	Anodic limit (V)	Cathodic limit (V)	Potential window (V)
0.1 M $HClO_4$	1.00	−0.05	−1.05	1.10
0.2 M HAc-NaAc	4.24	−0.25	−1.25	1.00
0.1 M NaOH	12.17	−0.55	−1.55	1.00

Table 2. Operational potential of bismuth-based materials plated on carbon-paste electrodes at different pH (Data taken from Ref. [22]).

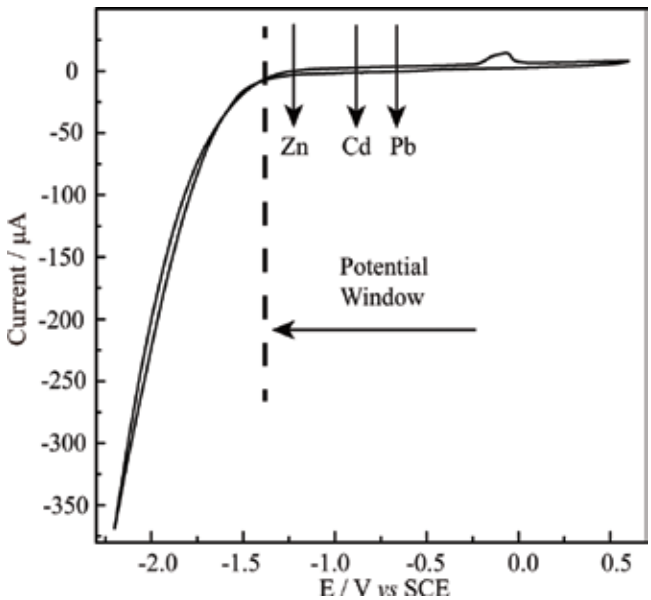

Figure 4. Cyclic voltammetry (CV) analysis of BiOCl-KIT-6/GCE in acetate buffer solution (0.1 M, pH 4.5) (adapted from Ref. [10]).

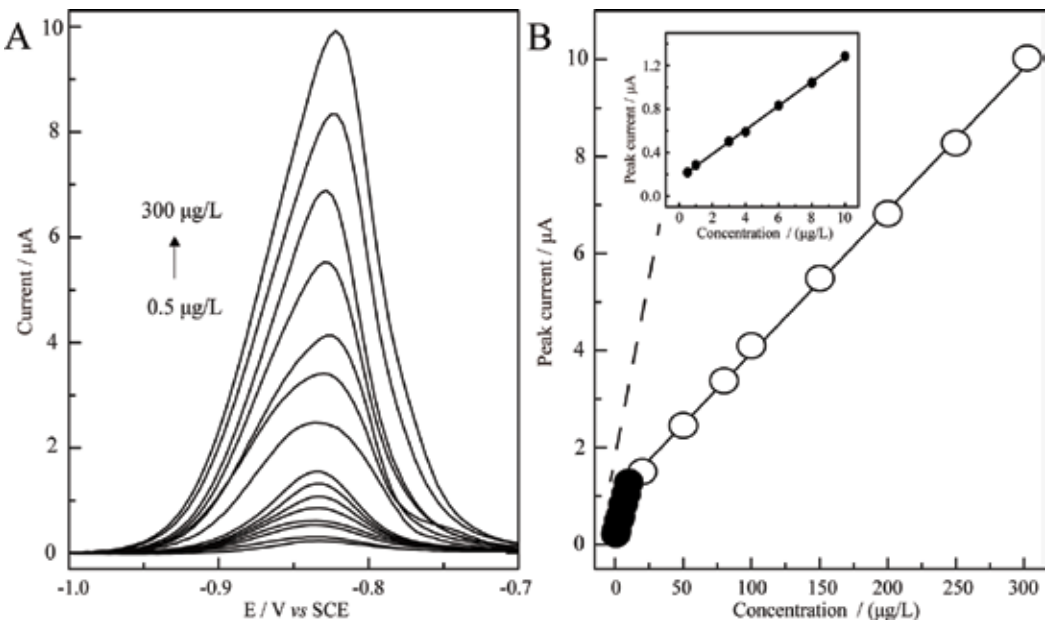

Figure 5. (A) Square-wave anodic stripping voltammetric (SWASV) responses of peak current on the concentration of Cd^{2+} using BiOCl-KIT-6/GCE in acetate buffer solution (pH 4.5) at the deposition potential of −1.3 V and deposition time of 120 s. (B) Calibration curves of Cd^{2+} over a concentration range of 0.5–300 μg/L (adapted from Ref. [10]).

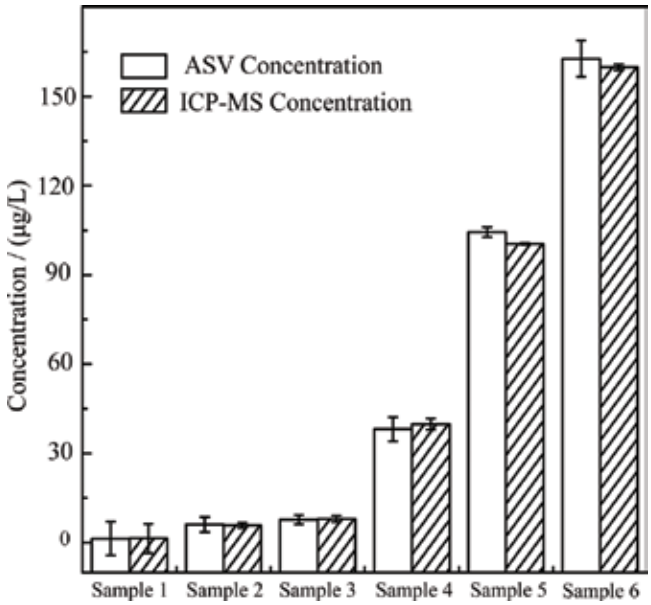

Figure 6. The determination results of blood cadmium concentration by anodic stripping voltammetry (ASV) using BiOCl-KIT-6/GCE in comparison with ICP-MS assay (adapted from Ref. [11]).

anodic stripping voltammetry (SWASV), the constructed BiOCl-KIT-6/GCE applied to the determination of cadmium-spiked human blood samples resulted in a calibration curve of Cd^{2+} with 2 linear ranges from 0.5 to 10 and from 10 to 300 μg/L (**Figure 5**), respectively, and a detection limit of 65 ng/L. As shown in **Figure 6**, a good agreement between the detection methods of SWASV and inductively coupled plasma mass spectrometry (ICP-MS) was observed [11]. Moreover, the BiOCl-KIT-6/GCE could be repeatedly used for at least 30 continuous times in one day and at least 10 continuous days with a marginal reduction of stripping peak current of 6.8 and 3.6%, respectively.

Despite considerable progress achieved during the past decade, most of the earlier studies have mainly explored various bismuth-based materials towards the sensor fabrication. Therefore, practical concerns still remain to be addressed to fulfill the demands of environmental protection and so on. Further works to utilize the constructed sensor under harsh operational conditions and to simply the assay procedures are still needed in the future.

4. Bismuth-based materials for biomedical use

Bismuth is a heavy metal element located close to lead and tin elements in the periodic table of elements, and thus shares similar physicochemical properties with these elements. But different from lead and tin, bismuth is usually regarded as nontoxic and biologically safe. Therefore, bismuth as well as its derivate has been extensively explored in biomedical applications. For example, bismuth salts are valuable for synthesis of various bismuth-based complexes as the

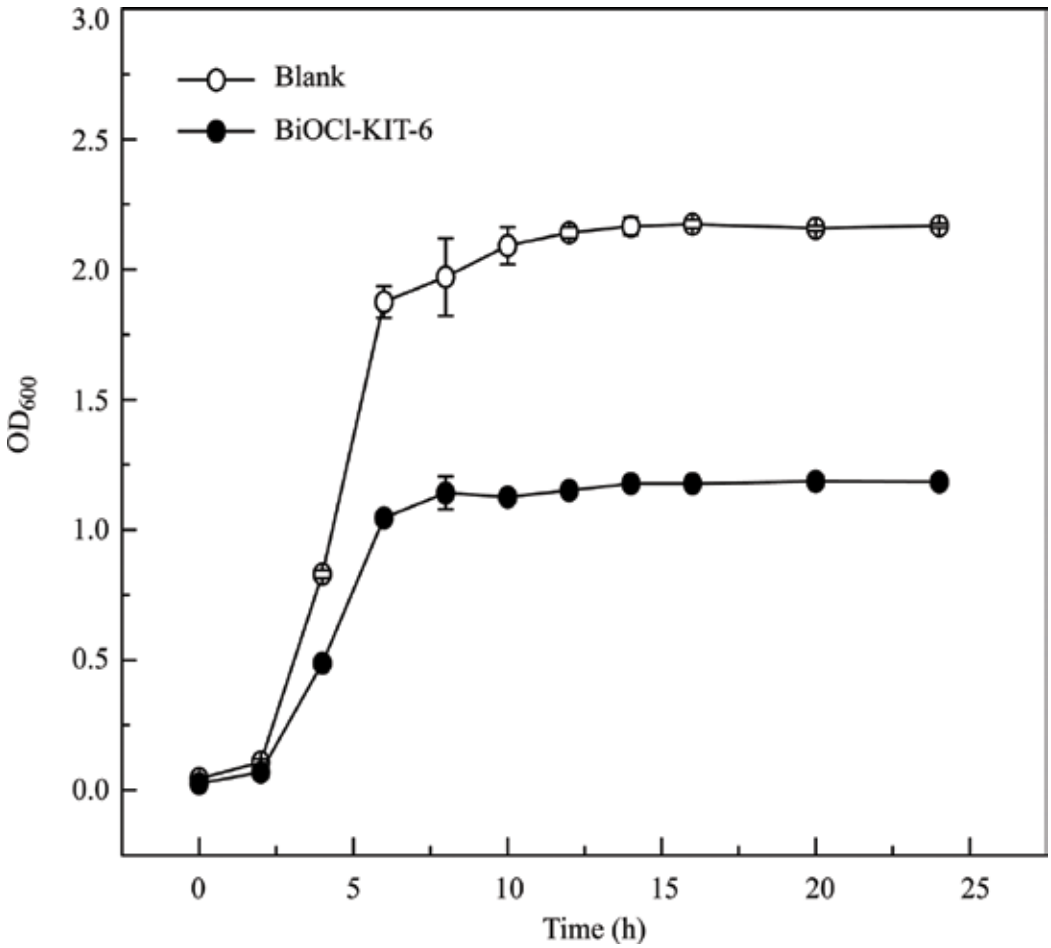

Figure 7. Growth curves of *S. aureus* cultured in LB media containing 20 μg/mL BiOCl-KIT-6 composite suspension. Each data point is the average of three independent assays with standard error of the mean (adapted from Ref. [12]).

active ingredients for pharmaceutical uses. The first report on bismuth-containing medicine in 1786 revealed its efficacy in the treatment of dyspepsia. And since then, there is a growing number of bismuth complexes which were explored to deal with gastrointestinal disorders and microbial infections including syphilis, diarrhea, gastritis, and colitis, which point out desirable therapeutic effects yet low toxicity after the intake of drug molecules.

In the laboratory, the antimicrobial activities of bismuth-based materials can be evaluated by recording the growth curve of model bacteria such as Gram-positive *Staphylococcus aureus* and Gram-negative *Escherichia coli* in the presence of materials. As shown in **Figure 7**, the growth curves of *S. aureus* cells in the presence and absence of 20 μg/mL BiOCl-KIT-6 were observed. There was an apparent decrease in the growth curve when adding BiOCl-KIT-6 composite, suggesting that BiOCl-KIT-6 composite can be used as an antimicrobial agent against *S. aureus*. The underlying antimicrobial mechanism of bismuth-based materials can be further studied using radical-sensitive fluorescent dyes. The generation of free radicals has been considered

http://dx.doi.org/10.5772/intechopen.75809

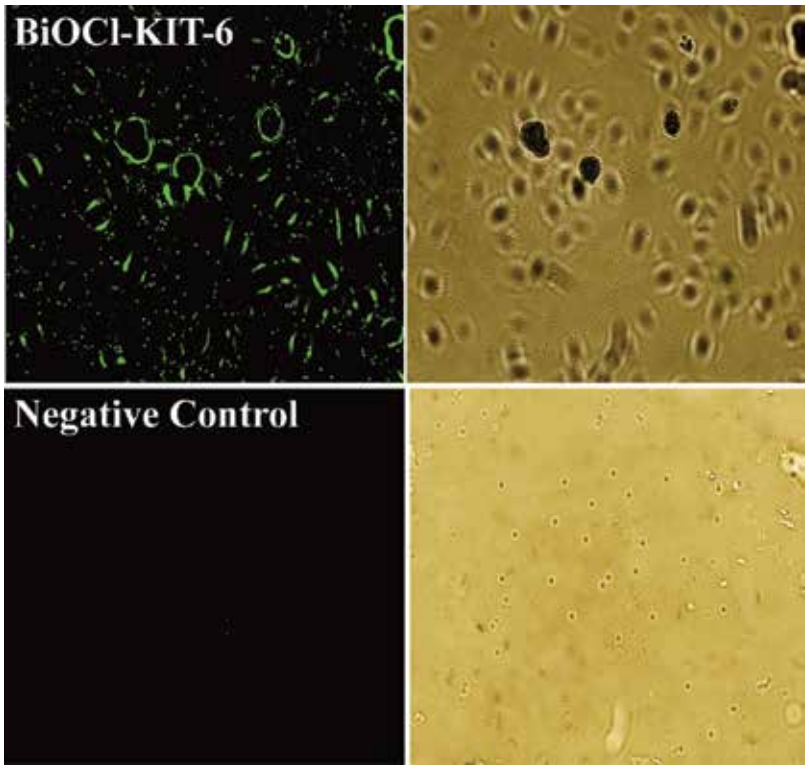

Figure 8. In the presence and absence of BiOCl-KIT-6 suspension (200 μg/mL), *S. aureus* were stained with 10 μM ROS-dependent fluorescent probe (DCFDA) in the dark field (left) and bright field (right) under a fluorescence microscope (adapted from Ref. [12]).

as one of the causes of metal particle-induced cytotoxicity in bacteria [29]. Therefore, the cytotoxicity of BiOCl-KIT-6 composite may be linked to the formation of reactive oxygen species (ROS). Cellular accumulation of ROS can be detected using the fluorogenic dye DCFDA based on the oxidation of the non-fluorescent 2′,7′-dichlorodihydrofluorescein (DCFH) that reacts with H_2O_2, O^{2-}, and $ONOO^-$ into the green fluorescent dichlorofluorescein (DCF), which provides a general indication of ROS levels. As shown in **Figure 8**, *S. aureus* incubated with BiOCl-KIT-6 showed more green fluorescence compared with the untreated group (negative control), indicating the formation of ROS detrimental to the cell growth (**Figure 7**).

H. pylori has been considered to play a role in the development of chronic gastritis, peptic ulcers, and even gastric cancer, and thus bismuth-based drugs are usually prescribed once *H. pylori* infection is diagnosed. Based on the clinical survey, *H. pylori* is susceptible to several antibiotics such as clarithromycin, amoxicillin, metronidazole, tetracycline, and rifabutin and exhibits resistance to many other antibiotics like bacitracin, vancomycin, trimethoprim, polymyxins, and nalidixic acid. Therefore, it remains challenging to cure *H. pylori* infection. In an effort to minimize the antibiotic resistance, bismuth complex has been utilized to treat gastrointestinal disorders and ulcers with pronounced inhibition activity against *H. pylori* [9]. Some commercial medicines with bismuth-containing ingredients are summarized in **Table 3**.

Bismuth complex	Name of pharmaceuticals
Bismuth potassium citrate	Livzon Dele, Bielomatik
Bismuth subcitrate	De-nol, Tripotassium dicitratobismuthate
Bismuth citrate	Ranitidine
Colloidal bismuth pectin	Colloidal bismuth pectin capsules
Bismuth aluminate	Debitai, Compound bismuth aluminate tablets

Table 3. Bismuth-containing drugs for the treatment of gastrointestinal diseases.

Basically, the bismuth-containing pharmaceuticals have two functions—antiulcer and antibacterial. The antiulcer activity of bismuth complex is explained by the precipitation of bismuth around the ulcer point to form a glycoprotein-bismuth complex as a protective coating promoting the healing of the lesion. The underlying molecular mechanisms of bismuth compounds to deal with *H. pylori* are not fully elucidated. Some preliminary reports have indicated that the biological targets of bismuth compounds are closely related to several *H. pylori*-related proteins [8].

Over the years, to produce a number of bismuth complexes for biomedical uses, the synthesis methods have also historically evolved, which mainly include hydrothermal, solvothermal, and microwave synthesis. Hydrothermal synthesis is a method to synthesize single crystals from high temperature aqueous solutions at high vapor pressures. Chen et al. synthesized bismuth-amino acid coordination polymers (BACPs) with different sizes by heating the aqueous reacting solution of $Bi(NO_3)_3{\cdot}5H_2O$ and asparagine at different temperatures [30]. The prepared BACPs synthesized in a facile green hydrothermal method exhibited unique biological activities and potential applications in biomedicine. He et al. prepared low-toxicity bismuth asparagine coordination polymer spheres (BACP-2) with sphere-like microstructures of an average 800 nm in diameter through a hydrothermal reaction at 80°C overnight [31]. Solvothermal synthesis is usually carried out in organic media to produce chemicals of refined crystallinity and morphology through a combination of sol-gel and hydrothermal routes. Andrews and coworkers have developed two new bis-carboxylate Bi(III) complexes including PhBi(o-$MeOC_6H_4CO_2)_2$(bipy)·0.5 EtOH and $PhBi(C_9H_{11}N_2O_3CO_2)_2{\cdot}6H_2O$, for anti-Leishmanial through a refluxing reaction in ethanol for 10-12 h [32]. Li et al. reported a nine-coordinate Bi(III) complex, $(Bi(H_2L)(NO_3)_2)NO_3$ (**Figure 9**) that was prepared in methanol [33]. Microwave synthesis is an efficient and environment-friendly method to accomplish various inorganic syntheses to achieve products in high yields within shorter reaction times. The coordination behaviors of bismuth (III) compounds with benzothiazoline were investigated by Mahajan et al. and the reaction takes few minutes under 700 W inside a microwave oven [34].

Several bismuth derivates have revealed antibacterial and antifungal activities. For example, $(Bi(H_2L)(NO_3)_2)NO_3$ shows higher antibacterial properties with the minimum inhibitory concentration (MIC) of 10.66 μM against Gram-positive bacteria *B. cereus* and Gram-negative bacteria *S. typhimurium* than the control of antibiotics chloramphenicol (MIC of 96.71 μM against *B. cereus* and *S. typhimurium*) and kanamycin sulfate (MIC of 107.3 μM against *B. cereus*,

http://dx.doi.org/10.5772/intechopen.75809

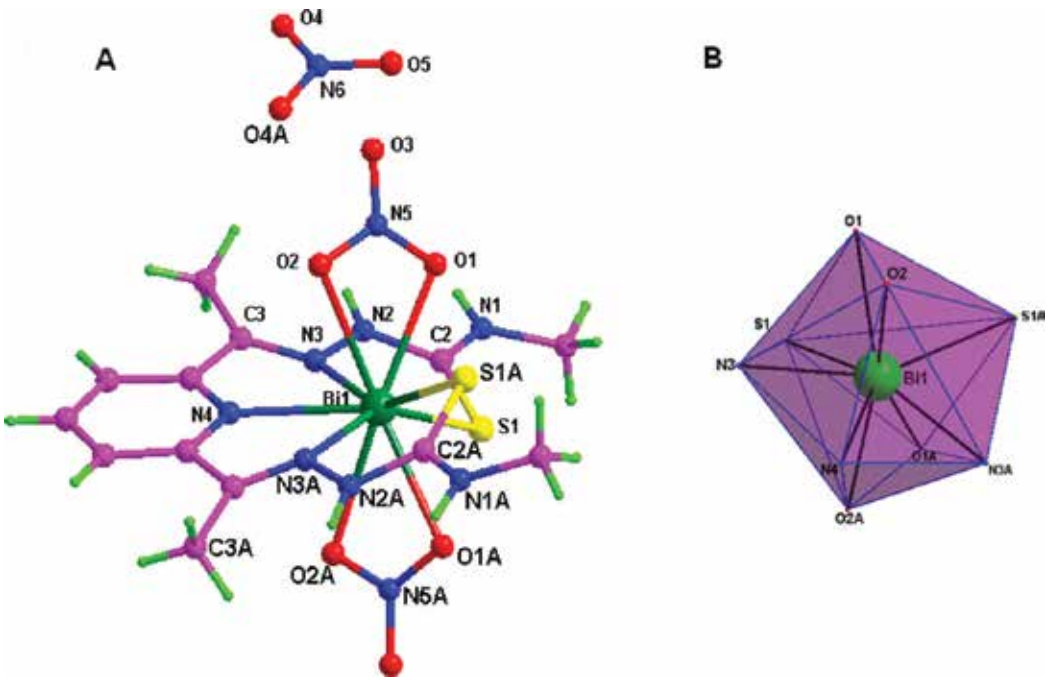

Figure 9. (A) Structure of $(Bi(H_2L)(NO_3)_2)NO_3$ with atomic numbering scheme. (B) Polyhedra showing distorted geometry around the bismuth atom. H_2L, 2,6-diacetylpyridine bis(^{4}*N*-methylthiosemicarbazone) (adapted from Ref. [33]).

53.64 μM against *S. typhimurium*), respectively [33]. Aqueous colloidal bismuth oxide nanoparticles (Bi_2O_3 NP) with fungicidal activity against *Candida albicans* and antibiofilm capabilities were synthesized by Rene and coworkers [35]. Colloidal Bi_2O_3 NP displayed better antifungal activity against *C. albicans* growth (colony size is reduced by 85%) and more complete inhibition of biofilm formation than those obtained by chlorhexidine, nystatin, and terbinafine, demonstrating the candidate role of Bi_2O_3 NP as a fungicidal component of oral antiseptic. Several bis-carboxylate phenylbismuth (III) and *tris*-carboxylate bismuth (III) complexes reported by Andrews and coworkers showed significant antimicrobial activity against the promastigotes of *Leishmania major* [32].

It should be noted that although bismuth complexes have been widely applied for medical practice against *H. pylori* infection in peptic ulcer, some side effects have been reported including disturbances of taste, dizziness, abdominal pain, and mild diarrhea in some patients, and a few cases of parageusia and glossitis. But so far no statistically identified difference in the incidences of side effects was found among the standard triple therapy, bismuth pectin quadruple and sequential therapies, demonstrating the biosafety of bismuth complexes [36, 37]. According to the statistical analysis, 99% of ingested bismuth is in essence not absorbed by human body but is excreted in the feces. The bismuth encephalopathy may therefore result from the long-term ingestion of overdosed bismuth complexes, attributed to the chronically neurologic dysfunction of bismuth. Although bismuth toxicity is usually difficult to occur, it is necessary to control the dosage of bismuth compounds.

5. Conclusion and outlook

Because of the nontoxicity of bismuth (III) salts, there is growing interest to explore various bismuth (III) salts for diverse applications including stripping analysis of heavy metals as well as antimicrobial agents. The bismuth-based sensors for the heavy metals are extensively studied in an effort to replace the mercury-based methods. The precise control of morphology and surface properties of bismuth-based materials on the modified electrode will greatly determine the sensitivity and accuracy of the constructed sensors. On the other hand, bismuth-based compounds as the inorganic pharmaceutical molecules may offer advantages over organic ones for biomedical use. As the dosage is the major cause of neurotoxicity of bismuth compounds, it is of importance to monitor the in vivo efficacy of bismuth-based pharmaceuticals. Along this direction, some cargo molecules of ordered structure such as metal-organic frameworks (MOFs) for the controlled release of bismuth hold potentials to improve the curative effect.

Acknowledgements

The work was supported by National Natural Science Foundation of China (U1703118), a project funded by the Priority Academic Program Development of Jiangsu Higher Education Institutions (PAPD), Jiangsu Shuangchuang Program, Open Funds of the State Key Laboratory for Chemo/Biosensing and Chemometrics (2016015) and the National Laboratory of Biomacromolecules (2017kf05) and Jiangsu Specially-Appointed Professor project, China.

Author details

Yiyan Song[1] and Jin Chen[1,2]*

*Address all correspondence to: okachen30@gmail.com

1 School of Public Health, Nanjing Medical University, Nanjing, China

2 The Key Laboratory of Modern Toxicology, Ministry of Education, School of Public Health, Nanjing Medical University, Nanjing, China

References

[1] Wang J, Lu JM, Hocevar SB, Farias PAM, Ogorevc B. Bismuth-coated carbon electrodes for anodic stripping voltammetry. Analytical Chemistry. 2000;**72**:3218-3222. DOI: 10.1021/ac000108x

[2] Hocevar SB, Ogorevc B, Wang J, Pihlar BA. Study on operational parameters for advanced use of bismuth film electrode in anodic stripping voltammetry. Electroanalysis. 2002;**14**:1707-1712. DOI: 10.1002/elan.200290014

[3] Kadara RO, Tothill IE. Development of disposable bulk-modified screen-printed electrode based on bismuth oxide for stripping chronopotentiometric analysis of lead (II) and cadmium (II) in soil and water samples. Analytica Chimica Acta. 2008;**623**:76-81. DOI: 10.1016/j.aca.2008.06.010

[4] Peng HL, Chan CK, Meister S, Zhang XF, Cui Y. Shape evolution of layer-structured bismuth oxychloride nanostructures via low-temperature chemical vapor transport. Chemistry of Materials. 2009;**21**:247-252. DOI: 10.1021/cm802041g

[5] Myung Y, Wu F, Banerjee S, Park J, Banerjee P. Electrical conductivity of p-type BiOCl nanosheets. Chemical Communications. 2015;**51**:2629-2632. DOI: 10.1039/c4cc09295c

[6] Yang D et al. NIR-driven water splitting by layered bismuth oxyhalide sheets for effective photodynamic therapy. Journal of Materials Chemistry B. 2017;**5**:4152-4161. DOI: 10.1039/c7tb00688h

[7] Rivera EJ et al. Bismuth@US-tubes as a potential contrast agent for X-ray imaging applications. Journal of Materials Chemistry B: Materials for Biology and Medicine. 2013;**1**:4792-4800. DOI: 10.1039/c3tb20742k

[8] Bierer DW. Bismuth subsalicylate: History, chemistry, and safety. Reviews of Infectious Diseases. 1990;**12**(Suppl 1):S3-S8

[9] Gorbach SL. Bismuth therapy in gastrointestinal diseases. Gastroenterology. 1990;**99**:863-875

[10] Borchert H et al. Determination of nanocrystal sizes: A comparison of TEM, SAXS, and XRD studies of highly monodisperse COPt3 particles. Langmuir. 2005;**21**:1931-1936. DOI: 10.1021/la0477183

[11] Song Y et al. Raspberry-like bismuth oxychloride on mesoporous siliceous support for sensitive electrochemical stripping analysis of cadmium. Molecules. 2017;**22**:797. DOI: 10.3390/molecules22050797 Basel, Switzerland

[12] Song Y, Jiang H, Bi H, Zhong G, Chen J, Wu Y, Wei W. Multifunctional bismuth oxychloride/mesoporous silica composites for photocatalysis, anti-bacterial test and simultaneous stripping analysis of heavy metals. ACS Omega. 2018;**3**:973-981. DOI: 10.1021/acsomega.7b01590

[13] Petovar B, Xhanari K, Finsgar MA. Detailed electrochemical impedance spectroscopy study of a bismuth-film glassy carbon electrode for trace metal analysis. Analytica Chimica Acta. 2018;**1004**:10-21. DOI: 10.1016/j.aca.2017.12.020

[14] Li J, Guo S, Zhai Y, Wang E. High-sensitivity determination of lead and cadmium based on the Nafion-graphene composite film. Analytica Chimica Acta. 2009;**649**:196-201. DOI: 10.1016/j.aca.2009.07.030

[15] Hutton EA, Ogorevc B, Hocevar SB, Smyth MR. Bismuth film microelectrode for direct voltammetric measurement of trace cobalt and nickel in some simulated and real body fluid samples. Analytica Chimica Acta. 2006;**557**:57-63. DOI: 10.1016/j.aca.2005.10.003

[16] Xu H et al. Highly ordered platinum-nanotube arrays for oxidative determination of trace arsenic (III). Electrochemistry Communications. 2008;**10**:1893-1896. DOI: 10.1016/j.elecom.2008.09.037

[17] Bagheri H et al. Simultaneous electrochemical sensing of thallium, lead and mercury using a novel ionic liquid/graphene modified electrode. Analytica Chimica Acta. 2015;**870**:56-66. DOI: 10.1016/j.aca.2015.03.004

[18] Wang J. Stripping analysis at bismuth electrodes: A review. Electroanalysis. 2005;**17**:1341-1346. DOI: 10.1002/elan.200403270

[19] Xu H, Zeng LP, Huang DK, Man YZ, Jin LT. A Nafion-coated bismuth film electrode for the determination of heavy metals in vegetable using differential pulse anodic stripping voltammetry: An alternative to mercury-based electrodes. Food Chemistry. 2008;**109**:834-839. DOI: 10.1016/j.foodchem.2007.12.065

[20] Sosa V, Serrano N, Arino C, Diaz-Cruz JM, Esteban M. Sputtered bismuth screen-printed electrode: A promising alternative to other bismuth modifications in the voltammetric determination of Cd(II) and Pb(II) ions in groundwater. Talanta. 2014;**119**:348-352. DOI: 10.1016/j.talanta.2013.11.032

[21] Cerovac S et al. Trace level voltammetric determination of lead and cadmium in sediment pore water by a bismuth-oxychloride particle-multiwalled carbon nanotube composite modified glassy carbon electrode. Talanta. 2015;**134**:640-649. DOI: 10.3016/j.talanta.2014.12.002

[22] Economou A. Bismuth-film electrodes: Recent developments and potentialities for electroanalysis. Trac-Trends in Analytical Chemistry. 2005;**24**:334-340. DOI: 10.1016/j.trac.2004.11.006

[23] Kadara RO, Tothill IE. Stripping chronopotentiometric measurements of lead(II) and cadmium(II) in soils extracts and wastewaters using a bismuth film screen-printed electrode assembly. Analytical and Bioanalytical Chemistry. 2004;**378**:770-775. DOI: 10.1007/s00216-003-2351-x

[24] Yang D, Wang L, Chen Z, Megharaj M, Naidu R. Determination of trace lead and cadmium in water samples by anodic stripping voltammetry with a nafionionic liquid-coated bismuth film electrode. Electroanalysis. 2014;**26**:639-647. DOI: 10.1002/elan.201300622

[25] Baldo MA, Daniele S. Anodic stripping voltammetry at bismuth-coated and uncoated carbon microdisk electrodes: Application to trace metals analysis in food samples. Analytical Letters. 2004;**37**:995-1011. DOI: 10.1081/al-120030293

[26] Keawkim K, Chuanuwatanakul S, Chailapakul O, Motomizu S. Determination of lead and cadmium in rice samples by sequential injection/anodic stripping voltammetry using a bismuth film/crown ether/Nafion modified screen-printed carbon electrode. Food Control. 2013;**31**:14-21. DOI: 10.1016/j.foodcont.2012.09.025

[27] Hwang GH, Han WK, Park JS, Kang SG. Determination of trace metals by anodic stripping voltammetry using a bismuth-modified carbon nanotube electrode. Talanta. 2008;**76**:301-308. DOI: 10.1016/j.talanta.2008.02.039

[28] Yang D, Wang L, Chen Z, Megharaj M, Naidu R. Anodic stripping voltammetric determination of traces of Pb(II) and Cd(II) using a glassy carbon electrode modified with bismuth nanoparticles. Microchimica Acta. 2014;**181**:1199-1206. DOI: 10.1007/s00604-014-1235-4

[29] Song Y, Jiang H, Wang B, Kong Y, Chen J. Silver-incorporated mussel-inspired polydopamine coatings on mesoporous silica as an efficient nanocatalyst and antimicrobial agent. ACS Applied Materials & Interfaces. 2018;**10**:1792-1801. DOI: 10.1021/acsami.7b18136

[30] Chen R et al. Facile synthesis of functional bismuth-amino acid coordination polymer nano-structures. Chemical Communications. 2011;**47**:8136-8138. DOI: 10.1039/c1cc11837d

[31] He NN et al. Exploring the toxicity of a bismuth-asparagine coordination polymer on the early development of Zebrafish Embryos. Chemical Research in Toxicology. 2013;**26**:89-95. DOI: 10.1021/tx3004032

[32] Andrews PC et al. Anti-Leishmanial activity of homo- and heteroleptic bismuth(III) carboxylates. Journal of Inorganic Biochemistry. 2011;**105**:454-461. DOI: 10.1016/j.jinorgbio.2010.08.007

[33] Li MX, Yang M, Niu JY, Zhang LZ, Xie SQ. A nine-coordinated bismuth(III) complex derived from pentadentate 2,6-diacetylpyridine bis((4)N-methylthiosemicarbazone): Crystal structure and both in vitro and in vivo biological evaluation. Inorganic Chemistry. 2012;**51**:12521-12526. DOI: 10.1021/ic301959z

[34] Mahajan K, Swami M, Singh RV. Microwave synthesis, spectral studies, antimicrobial approach, and coordination behavior of antimony(III) and bismuth(III) compounds with benzothiazoline. Russian Journal of Coordination Chemistry. 2009;**35**:179-185. DOI: 10.1134/s1070328409030038

[35] Hernandez-Delgadillo R et al. Bismuth oxide aqueous colloidal nanoparticles inhibit Candida albicans growth and biofilm formation. International Journal of Nanomedicine. 2013;**8**:1645-1652. DOI: 10.2147/IJN.S38708

[36] Mesquita MA et al. One-week dual therapy with ranitidine bismuth citrate and clarithromycin for the treatment of *Helicobacter pylori* infection in Brazilian patients with peptic ulcer. World Journal of Gastroenterology. 2005;**11**:3566-3569. DOI: 10.3748/wjg.v11.i23.3566

[37] Gao XZ, Qiao XL, Song WC, Wang XF, Liu F. Standard triple, bismuth pectin quadruple and sequential therapies for *Helicobacter pylori* eradication. World Journal of Gastroenterology. 2010;**16**:4357-4362. DOI: 10.3748/wjg.v16.i34.4357

Section 5

Bismuth Materials for Optical Application

Chapter 8

Effects of Post Treatments on Bismuth-Doped and Bismuth/Erbium Co-doped Optical Fibres

Shuen Wei, Mingjie Ding, Desheng Fan,
Yanhua Luo, Jianxiang Wen and Gang-Ding Peng

Additional information is available at the end of the chapter

http://dx.doi.org/10.5772/intechopen.75106

Abstract

Bismuth-doped and bismuth/erbium co-doped optical fibres have attracted much attention for their great potential in the photonic applications at ultrawide O, E, S, C and L bands. The effects of post treatments, including various heating, high energy ray radiation, laser radiation and H_2 loading processes, on these fibres' performance, functionality and stability have been experimentally studied. Experimental results demonstrate that these post treatments could allow us to get insights regarding the formation and the structure of bismuth active centre (BAC) and be used to control and regulate the formation of BAC.

Keywords: bismuth-doped fibre (BDF), bismuth and erbium co-doped optical fibre (BEDF), bismuth active centre (BAC), broadband, post treatments, thermal treatment, gamma radiation, photo-bleaching, H_2 loading

1. Introduction

Since the first demonstration of the broadband near infrared (NIR) luminescence in the bismuth-doped silicate glass [1], bismuth-doped materials, including crystal, glass, fibre, and so on, have been developed and studied for photonic applications at the extended band [2–7]. Especially, bismuth-doped optical fibres (BDFs) have been developed for fibre amplifiers and lasers from 1250 to 1500nm and 1600 to 1800nm [8–13]. Later on, Bi/Er co-doped silicate optical fibres (BEDFs), due to their great potential in photonic applications from 1150 to 1700nm covering both the used bandwidth (C band) and the huge unused bandwidth, have been proposed and developed [14–16].

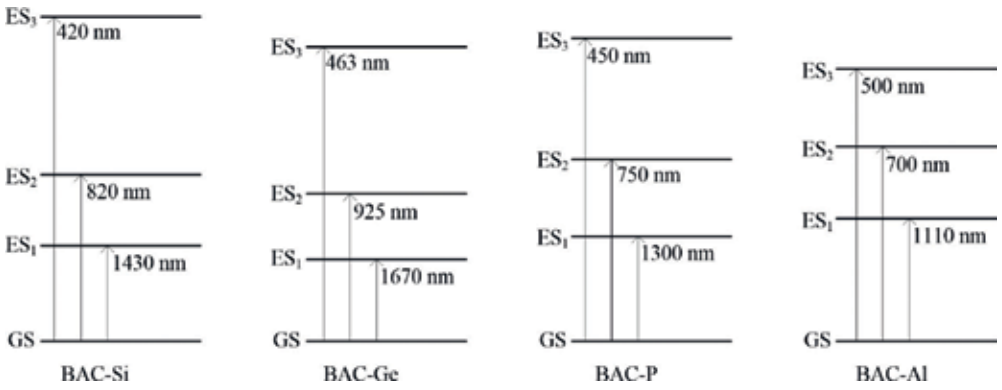

Figure 1. Energy level diagrams of different BACs in BDFs.

Although there have been a lot of breakthroughs in the unused spectral range, there remain many prominent scientific and technological challenges [17, 18]. The fundamental understanding of NIR emitting BAC is one key challenge. Unlike the well-shielded *f-f* transitions of Er^{3+}, the electronic transition of the unshielded Bi centre(s) is closely linked to the microenvironment. According to the type of the local environment, there are four types of BACs in BDFs, which are BAC-Si, BAC-Ge, BAC-P and BAC-Al, linked to SiO_2, GeO_2, P_2O_5:SiO_2 and Al_2O_3:SiO_2, respectively [18]. Their energy diagrams are shown in **Figure 1**.

Previous reports have demonstrated that the formation of BAC greatly depends upon the processing conditions. More specifically, BAC can be activated by high-intensity femtosecond laser [19], high-temperature melting [20, 21], γ-radiation [22, 23], and so on. Here, effects of post treatments on BDF and BEDF by thermal treatment, high energy ray radiation, laser radiation and H_2 loading have briefly been reviewed. It is generally believed that these post treatments will greatly change the spectroscopic properties of these fibres via the variation of the BAC. Further research into reasons of variations will help to understand BAC. With further understanding of the BAC, it is also hopeful to find an appropriate way to control and regulate the BAC for the performance improvement of BDF and BEDF.

2. Thermal treatment

It is known that the unshielded outer electron shell of bismuth makes the energy structure of Bi more complex and closely related to the microstructure of the host material [18]. In addition, Bi itself, as a polyvalent element, often undergoes oxidation-reduction (redox) reaction in molten glass, which is significantly influenced by the melting temperature, atmosphere and composition [12, 20, 21, 24–26]. In general, this redox reaction moves toward the reduction side with increasing melting temperature, and the variation of the valence state of Bi can be represented as follows [12, 24]:

$$Bi^{3+} \rightarrow Bi^{2+} \rightarrow Bi^{+} \rightarrow Bi \rightarrow Bi\ \text{clusters}\ (\text{e.g., } Bi_2,\ Bi_2^{-},\ Bi_3) \rightarrow (Bi)_n\ \text{colloids} \qquad (1)$$

http://dx.doi.org/10.5772/intechopen.75106

These facts make it difficult to determine the exact nature of BACs in BDF and BEDF as the redox reaction mentioned above often occurs during the preform fabrication and fibre drawing processes. In spite of that, the reduction processes have hinted that BACs most likely consist of Bi with low valence state [27], although it is still controversial. The latest experimental data has already confirmed that BACs are the clusters consisting of Bi ions and oxygen deficiency centres instead of Bi ions themselves [12].

Since valence states of Bi as well as the deficiency [28] can be altered at high temperature, post thermal treatment has become a common method to modify the properties of Bi-doped glasses/fibres, and thus to further investigate the origin of BACs [25, 29]. Therefore, in this section, the effects of the thermal treatment upon BDFs and BEDFs, summarized and listed in **Table 1**, are presented and discussed.

2.1. Bismuth-doped fibres

2.1.1. BAC emission at high temperature

In terms of BDFs, the emission of BACs at high temperature of aluminosilicate fibres have been reported as early as 2008 [30]. However, their interpretations are not convincible owing to the limited data. Later on, thermal effects on emission of BAC-Si at 830 nm and 1420 nm under 808 nm pumping have been studied in bismuth-doped silicate fibres (SBi) [31, 32], bismuth-doped germanosilicate fibre (GSBi) [31] as well as bismuth-doped silicate tube (SBi*) [33] (**Table 1**). It is observed that the emission of BAC-Si at ~1420 nm shows an increasing trend when treating at a specific high temperature, along with the reduction of emission at 830 nm. It is believed that the increase of NIR emission is associated with the increase of the non-radiative transition rate between ES_2 and ES_1 of BAC-Si (**Figure 1**) at high temperature, which is confirmed by the lifetime results in GSBi [31] and SBi* [33]. Taking GSBi [31] for example, the lifetime at ES_2 of BAC-Si drops directly from 30 μs to <3 μs, whereas the lifetime of 1400nm luminescence decreases by 25% when heating from room temperature to 900°C, as shown in **Figure 2**.

2.1.2. Formation of BACs

The preform of SBiO (**Table 1**) shows luminescence and absorption in both visible and NIR region before drawing, whereas SBiO drawn with oxygen in holes has no luminescence but low background loss. However, when SBiO listed in **Table 1** is annealed with argon in holes at 1100°C for 30 minutes, absorption bands of BAC-Si at 830 nm and 1420 nm appear, accompanied by the increment of the background loss [29]. The appearance of absorption at 830 and 1420 nm indicates the formation of BAC-Si, which is further confirmed by the observation of luminescence after annealing [29]. On the contrary, when SBiO is annealed with oxygen in holes, no obvious change can be detected [29]. These results demonstrate that Bi ions in BAC-Si can be oxidized into the high valence state in an oxidizing atmosphere, resulting in the decrease of both luminescence and background loss, vice versa, annealing bismuth-doped silicate glasses in argon can lead to the high background loss and possible formation of BAC-Si. These facts indicate not only the formation of BAC-Si, but also the association of BAC-Si with the low valence state of bismuth ions.

Fibre	Fabrication techniques	Core composition	λ_{ex} (nm)	λ_{em} (nm)	FWHM (nm)@ λ_{em} (nm)	Lifetime (μs)@ λ_{em} (nm)	Treatment conditions	Reference
Emission at high temperature								
SBi-P	PIT	100SiO_2-Bi(<0.02 at%)	808	830; 1400	72@1400	—	23–700°C in air	[31]
SBi* (quartz glass)	SPCVD	100SiO_2-Bi(<10^{19} cm^{-3})		825; 1420	14@825; 120@1420	60@825; 658@1420	23–600 °C in air	[33]
SBi	SPCVD	100SiO_2-Bi(<0.02 at%)		830; 1420	30@830; 117@1420	—	23–600 °C in air	[32]
SBi-LF	SPCVD	100SiO_2-Bi(<0.02 at%)-low flourine doping in core			36@830; 117@1420	—	23–500°C in air	
SBi-HF	SPCVD	100SiO_2-Bi(<0.02 at%)-high flourine doping in core			36@830; 107@1420	—	23–500°C in air	
SBi-H (holey fibre)	FCVD	100SiO_2-Bi(<0.02 at%)		830; 1400	87@1400	—	23–500°C in air	[31]
GSBi	MCVD	95SiO_2–5GeO_2-Bi(<0.02 at%)			94@1400	600@1400	23–400°C in air	
Thermal annealing								
SBiO (holey fibre)	FCVD	100SiO_2–Bi_2O_3(~0.03 at%)	337; 454-676; 975; 1064	Absence	—	—	1100°C in argon 1100°C in oxygen	[29]
ASBiY	MCVD	SiO_2-Al_2O_3-P_2O_5-Y_2O_3	750	1120	177@1120	10@820; 800@1150	≥550°C in air	[34]
ASBi	MCVD	SiO_2-Al_2O_3-Bi_2O_3	532	700; 1100	136@700; 171@1100	—	1200°C in air	[35]
SBi-H (holey fibre)	FCVD	100SiO_2-Bi(<0.02 at%)	808	830; 1400	87@1400	—	1200°C in air	[31]
GSBi	MCVD	95SiO_2–5GeO_2–Bi_2O_3(<0.02 at%)			94@1400	30@830; 600@1400	>400°C in air	
SBi-HF	SPCVD	100SiO_2-Bi(<0.02 at%)-high flourine doping in core			87@1400	—	600 °C in air	[32]
BEDF	MCVD	SiO_2-Al_2O_3-GeO_2-P_2O_5-Er_2O_3-Bi_2O_3	830	1420	98@1420	—	800°C in air 100°C/200°C/ in air	[36] [37]

Note: PIT—powder in tube, SPCVD—surface plasma chemical vapour deposition, FCVD—furnace chemical vapour deposition, MCVD—modified chemical vapour deposition.

Table 1. Summary of designations, fabrication techniques, core compositions, the excitation and emission peak wavelengths, full-width at half maximum (FWHM) of luminescence bands, and lifetime of Bi luminescence and thermal treatment conditions of BDFs.

http://dx.doi.org/10.5772/intechopen.75106

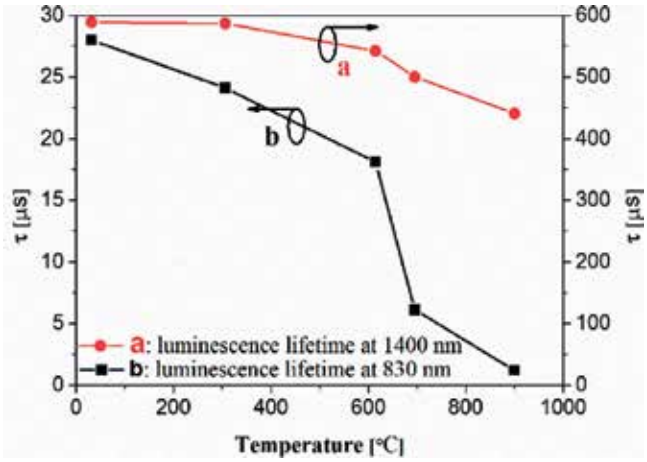

Figure 2. Luminescence lifetime at the wavelength of 830 and 1400 nm as a function of temperature excited at 808 nm [31].

Similar effects have been observed when ASBiY [34] is annealed at ≥550°C and ASBi at 1200°C [35] as listed in **Table 1**. After annealing, absorption peaks of BAC-Al at 500, 750 and 1000 nm increase, and the NIR emission at 1150 nm is enhanced. These changes obviously indicate the formation of BAC-Al. Hence, it is believed that the extra "generation" (formation of BAC-Si or BAC-Al) is associated with the reduction of $Bi^{3+} \rightarrow Bi^{2+} \rightarrow Bi^{+} \rightarrow Bi^{0}$ at high temperature [34].

2.1.3. Degradation of BACs

However, in some cases, luminescence at 1420 nm of BAC-Si starts to decrease when fibre is annealed at the high temperature in air. Such phenomenon is very prominent in BEDF [37], fabricated by conventional MCVD combined with in situ solution doping technique. When one BEDF is annealed at each prescribed temperature for 1 hour and slowly cooled down to the room temperature, without significant variation of background loss, the luminescence

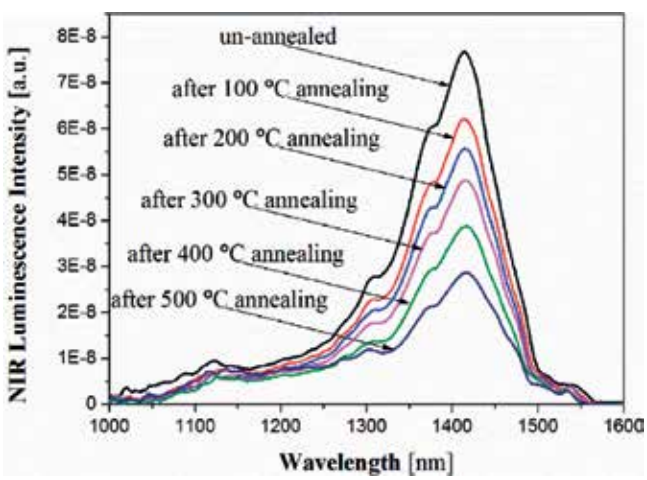

Figure 3. NIR emission spectra of BEDF after annealing at different temperatures under 830 nm excitation [37].

at 1420 nm excited at 830 nm starts to decrease after 100°C annealing, as shown in **Figure 3**, showing the degradation of BAC-Si. The degradation is attributed to the redistribution of point defect in annealed BEDF [37].

In addition, the reduction of emission of BAC-Si has also been observed in SBi-H, SBi-HF and GSBi after annealing at high temperature, as listed in **Table 1** [31, 32]. The features, behaviours and causes of these phenomena vary case by case. In SBi-H, the dissociation of BAC-Si is due to the oxygen diffusion (oxygen with high temperature tends to form an oxidation atmosphere). Another possibility is the reconfiguration of clusters in a greater porosity in SBi-HF [32], resulting in an irreversible reduction of their luminescence. In addition, the dissociation of BAC-Si due to the oxidation by GeO_2 is also observed in GSBi [31], although it is a reversible process.

2.1.4. Thermal darkening

A strong and irreversible thermal darkening effect has also been found in both BEDF and SBiO annealed at high temperature as listed in **Table 1**. When a section of BEDF is heated from room temperature to 800°C and slowly cooled down, the background losses irreversibly increase in both visible and NIR regions, which make NIR luminescence almost undetectable after annealing. Such darkening effect is obvious when comparing the radial profile of visible light intensity in the unannealed and 800°C annealed BEDF from an optical microscope, as shown in **Figure 4**.

A similar increase in background loss is observed in the annealed SBiO, of which the background loss starts to increase significantly from 600°C and up [29]. Such growths of the background loss observed in both BEDF and SBiO are consistent with Mie theory's hyperbolic dependence: $(A/\lambda) + B$, where A is assumed to be mainly determined by the average value of the product of the concentration and the volume of particles at different temperatures, B is correction constant, and λ is the wavelength of incident light. So the increment of the background loss is attributed to the formation of the metallic bismuth nanoparticles $(Bi)_n$ [29, 36, 38, 39].

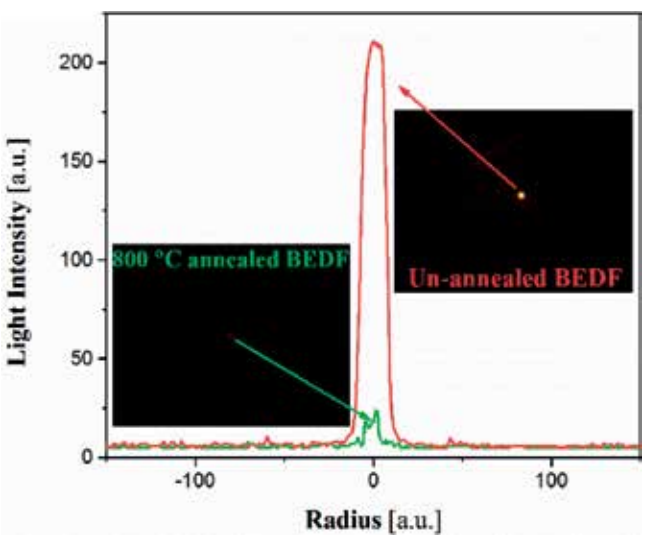

Figure 4. Radial profile of visible light intensity in the un-annealed and 800°C annealed BEDF (~2 cm) [36].

The origin of the growth of background loss is further linked to the excessive reduction of bismuth ions in Bi-doped silicate fibres [29, 36].

3. High energy ray treatment

Radiation technologies with high-energy rays, already established in materials processing, have properties uniquely suited for the creation of new advanced materials. When fibres are exposed to radiation, a darkening process occurs due to the formation of colour centres (or defects), in which radiation-induced-absorption (RIA) is observed. Extensive studies on radiation-induced darkening on pure silica and rare-earth-doped fibres have been carried out for assessing the radiation effects on fibres and understanding the possible underlying mechanisms as well as the possible use in space-borne applications [40–46].

For BDFs, radiation by high-energy rays has resulted in variations (decrease or increase) of the characteristic absorption and luminescence of corresponding BACs, thus further providing information on their properties. Moreover, it has been reported that gamma-ray irradiation can increase the density of BAC leading to an enhancement of fluorescence [47, 48]. The activation of BAC by radiation is ascribed to the reduction of Bi^{3+} to low valence state, which contributes to the NIR fluorescence by capturing radiation-released free electrons [23].

3.1. Gamma-radiation effect

Gamma radiation seems to favour the formation of new BACs in BDF, BEDF and Bi/Er/Yb co-doped fibres (BEYDFs). Wen et al. observe the radiation-induced increase of Bi ion absorption peaks as well as enhancement of photoluminescence in BDF fabricated by MCVD and atomic layer deposition technique [47]. Apart from the radiation-induced increase of Bi ion absorption, a new peak at ~580 nm arises, increasing with the increment of the dosage, which is related to the formation of aluminium oxygen hole centres (Al-OHCs). This radiation-induced defect, together with radiation-induced background increase, causes a slight decrease of NIR fluorescence excited at 532 nm. However, when pumped by 980 nm excitation, the fibres exhibit an enhancement of emission at 1410 nm of BAC-Si and at 1150 nm of BAC-Al. Besides that, their result also indicates that BAC-Al is less sensitive to radiation than BAC-Si. The enhanced fluorescence may originate from the valence state conversion as follows:

$$Bi^{5+} + 2e \xrightarrow{h\nu} Bi^{3+} \tag{2}$$

$$Bi^{5+} + 4e \xrightarrow{h\nu} Bi^{+} \tag{3}$$

$$Bi^{5+} + 5e \xrightarrow{h\nu} Bi^{0} \tag{4}$$

$$Bi^{3+} + 2e \xrightarrow{h\nu} Bi^{+} \tag{5}$$

$$Bi^{3+} + 3e \xrightarrow{h\nu} Bi^{0} \tag{6}$$

With the γ irradiation of BEDF from 1.0 to 50 kGy, the absorption at 830 nm is increased significantly while the absorption at a longer wavelength is reduced and emission is restrained [48–50]. The results show that BAC can be activated by gamma irradiation. A comparative study of gamma radiation effect upon BEDF and BEYDF indicates that Yb co-doping to BEDF will enhance the activation of BAC. The enhancement might be due to Compton electron capture of Yb^{3+}: $Yb^{3+} + e^{-} \rightarrow Yb^{2+}$ [42], confirmed by the reduction of the Yb^{3+} characteristic absorption at ~980 nm [48]. Moreover, the report by Sporea et al. has suggested that gamma irradiation can be used for tailoring the luminescence properties of BEDF [50]. Investigation on RIA of irradiated BEDF also suggests that BEDFs have good radiation resistance to low and moderate gamma irradiation.

Gamma-radiation effect on bismuth-doped germanosilicate fibres has recently been reported by Firstov et al. through measurement of absorption and emission after post irradiation annealing [51]. A series of BDFs with various bismuth and GeO_2 are subjected to ^{60}Co-source to different total doses of 1–8 kGy. No significant changes in the absorption and emission bands of BACs by gamma irradiation are observed. From the RIA analysis, it demonstrates that RIA is dependent upon fibre composition, where higher germanium and bismuth concentrations lead to higher radiation sensitivity.

3.2. Electron-radiation effect

Besides of gamma radiation, electron irradiation is another alternative method to change the valence state of Bi, similar to that of gamma irradiation in Bi: α-BaB_2O_4 single crystal [23]. Kir'yanov et al. studied the effect of electron irradiation in bismuth-doped germane- and alumina-silicate fibres and observed two opposite effects (decrement/increment) [52, 53]. Both fibres fabricated by MCVD and solution-doping methods are exposed to electrons of high energy (6 MeV) at room temperature to different total doses of 2×10^{12}, 1×10^{13} and 5×10^{13} cm^{-2}, respectively. Different from general behaviour of background loss increase with increasing doses, the resonant absorption peaks of Bi centres decrease with higher radiation doses, indicating a radiation-induced bleaching effect for Bi centres by electron irradiation. Deeper comparative study on fluorescence spectra of pristine and irradiated fibres reveals that the fluorescence emission spectra and lifetimes are slightly influenced by electron irradiation and the absorption changes are ascribed to the concentration change of Bi centres. Different from bismuth-doped germane-silicate optical fibre, bismuth-doped alumina-silicate fibre exhibits an increase of BAC-Al due to the electron irradiation.

4. Laser radiation

Femtosecond laser irradiation at 800 nm is reported to facilitate the activation of emission centres in bismuth-doped glass [19, 54]. UV laser radiation at 193 nm and 244 nm can also enhance the fluorescence of Bi/Al co-doped optical fibres after H_2 loading, ascribed to the increase of BACs [55, 56]. In addition, laser-induced attenuation change in active optical fibre is another common effect. This change can be photo-bleaching or photo-darkening. Photo-bleaching refers to the decrease of the absorption after the radiation, and photo-darkening is the reverse effect. Photo-darkening is severe in Al-silicate Yb-doped fibres with high Yb^{3+} doping [57]. The

http://dx.doi.org/10.5772/intechopen.75106

absorption coefficient of Yb^{3+} can be photo-bleached by 977 nm laser radiation [58]. The similar photo-bleaching effect has been observed in thulium-doped fibre [59] as well as BDF [60]. To improve the performance of BDF lasers and amplifiers, the photo-bleaching effect induced by the pump radiation has drawn attention [60]. In this section, the behaviour and mechanism of photo-bleaching of BAC-Si and BAC-Ge in BDF and BEDF have been described in detail.

4.1. Photo-bleaching of BAC-Si

The photo-bleaching of BAC-Si in BEDF under 830 nm pumping has been reported [61]. By pumping the fibre with the power of 0.12 MW/cm^2, the luminescence of BAC-Si at 1420 nm decreases by ~15% after 40 minutes as plotted in **Figure 5(a)**. This decrease of the luminescence is proved to be the bleaching of BAC-Si under the resonant pump radiation. In addition, the self-reversible effect is observed according to the recovery of the absorption of 816 nm, as shown in **Figure 5(b)**. After 2 days at room temperature, both absorption and emission recover to the pristine condition.

Through the investigation of the dependence of bleaching effect upon the pump power, wavelength and temperature, the photo-bleaching mechanism of BAC-Si has further been illuminated [62]. To quantify the bleaching behaviour, the stretched exponential function (SEF) is employed to describe the bleaching process. The SEF is expressed as:

$$I_A(t) = I_{A,\infty}(P) + I_{B,\infty}(P)\, e^{-\left(\frac{t}{\tau(P)}\right)^{\beta(P)}}, \tag{7}$$

where $I_A(t)$ and $I_{A,\infty}$ are the luminescence intensity at time t and at the time when the bleaching effect is saturated under the radiation power P. $I_{B,\infty}$ stands for the bleachable part of the luminescence, τ is the time constant and β is the stretched parameter. Especially, the bleaching ratio is defined as $r_B = \frac{I_{B,\infty}}{I_{A,\infty} + I_{B,\infty}}$. By fitting the decay curve of luminescence of BAC-Si at 1420 nm, it is found that the pump power dependence of r_B and τ shows a high similarity with that of the luminescence intensity as plotted in **Figure 6(a)**, indicating the involvement of the excitation of BAC-Si in the photo-bleaching process. This idea is further proved by the photo-bleaching dependence of BAC-Si on the pump radiation wavelength, as shown in **Figure 6(b)**.

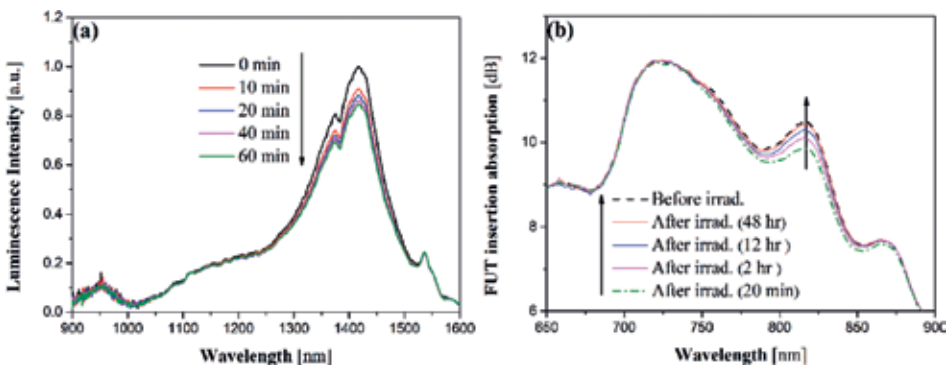

Figure 5. (a) Luminescence spectra of the BEDF under 830 nm pumping measured as a function of time. (b) BEDF insertion absorption spectra obtained before and after irradiation (20 min, 2, 12, and 48 hrs) [61].

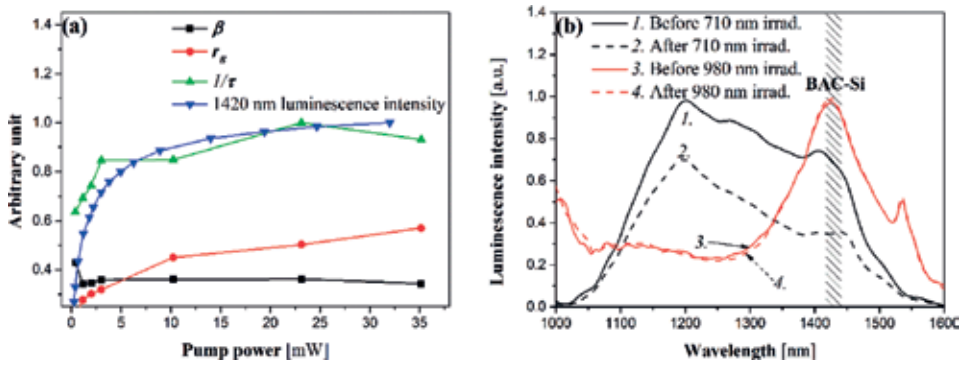

Figure 6. (a) 1420 nm luminescence intensity, the inverse of time constant ($1/\tau$), bleaching ratio (r_B) and stretched parameter (β) vs. pump power. (b) The 710 nm excited luminescence before-*1* and after-*2* 710 nm irradiation and the 830 nm (0.2 mW) excited luminescence before-*3* and after-*4* 980 nm irradiation [62].

In the case of 710 nm irradiation, luminescence of BAC-Si is significantly bleached, while the 830 nm excited luminescence has no change after 30 minutes irradiation of 980 nm pump with 35 mW. The reason for using 830 nm to excite the luminescence is that 980 nm light cannot excite luminescence of BAC-Si. Thereby, it is suggested that the pump laser-induced bleaching effect of BAC-Si is the electron escape from an excited Bi site, expressed as:

$$Bi^{+x}_{BAC-Si} \xrightarrow{h\nu} {}^{*}Bi^{+x}_{BAC-Si} \xrightarrow{kT} Bi^{+(x+1)}_{BAC-Si} + e^{-}, \tag{8}$$

where Bi^{+x}_{BAC-Si} is the bismuth ion in BAC-Si with valance state of $+x$, * symbolizes the excited state and kT stands for the thermal energy. First, Bi^{+x}_{BAC-Si} absorbs photon $h\nu$ and is excited to the second excited level corresponding to 816 nm. Second, some of ${}^{*}Bi^{+x}_{BAC-Si}$ fall to the lower excited states via non-radiative transition, while some release the electron e^{-} to the acceptor site (a nearby material defect) with the aid of thermal vibrational energy kT and thus induce the decay of luminescence and ground-state absorption. Furthermore, the bleaching ratio of the BAC-Si luminescence can be suppressed by half when lowering the temperature to the liquid nitrogen temperature.

4.2. Photo-bleaching of BAC-Ge

Photo-bleaching of BAC-Ge in BDF has also been observed in bismuth-doped silicate fibre and bismuth-doped germanosilicate fibre [60, 63]. Under the irradiation of 244 nm UV light, the luminescence at 1700 nm of BAC-Ge is totally bleached, as shown in **Figure 7**. Besides, this effect can be activated by 532 nm radiation as well. Further study shows that this photo-bleaching can be reversed by thermal treatment after the irradiation stops and this bleaching-recovery process can be repeated showing a memory effect [64, 65].

It is noted that the structure of BAC-Si/Ge is composed of a Bi ion and SiODC(II)/GeODC(II) [66]. The bleaching of GeODC(II) would deactivate BAC-Ge leading to the decrease of luminescence and absorption when GeODC(II) is photoionized into E′ centre by 244 nm irradiation [67]. So the photo-bleaching of BAC-Ge is caused by the bleaching of the GeODC(II).

http://dx.doi.org/10.5772/intechopen.75106

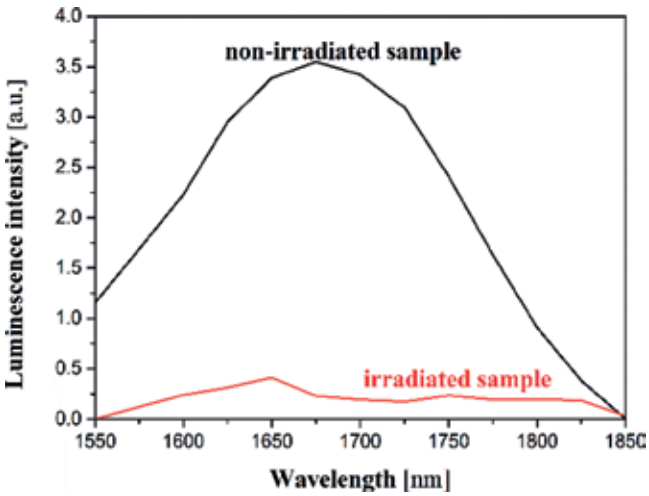

Figure 7. BAC-Ge luminescence spectra at 1700 nm band before and after 1 kJ/cm^2 244 nm irradiation excited at 1460 nm [60, 63].

The destruction of GeODC(II) by UV light leads to the bleaching of BAC-Ge. Such photo-bleaching process can be expressed as [65]:

$$Bi^{+n} + ODC \xrightarrow{h\upsilon} Bi^{+n} + e^{-} + E' \, center \tag{9}$$

which is confirmed by two evidences: 1) the dependence of bleaching speed upon the irradiation power is close to 2 indicating a two-photon process [68]; 2) the thermal dynamic behaviours of BAC-Ge and GeODC are similar [64]. The photo-bleaching effect of BAC-Si in BDF can be explained with a similar mechanism [60]. Therefore, more than one reason possibly induces the photo-bleaching effect dependent upon the material environment.

5. H_2 treatment

Both H_2 and D_2 are the popular reducing agents in the chemical processing of optical fibre. For example, the fabrication of photosensitive optical fibre through H_2 loading, photo-chemical interaction of dissolved H_2 with UV laser-induced electronic excitations significantly quickens grating formation in Ge-doped silica-core fibres. In addition, they can reduce the Bi from the higher valence state to the lower valence state. As a result, H_2 loading will change the absorption and luminescence properties of BDFs. In addition, dissolved H_2 molecules can deactivate excited defects. So, the presence of H_2 molecules leads to the decrease of lifetime and steady-state intensity of triplet luminescence associated with oxygen-deficient centres in fibres, which has been confirmed as one of the key element for the formation of BAC [12]. Hence, in this section, different Bi-doped materials, including crystal, glass and fibre will be treated by H_2 or D_2 under different temperature/pressure. Their spectroscopic properties (e.g., absorption and emission) and photosensitivity before and after H_2 treatment will be described and compared in detail.

5.1. Effect upon spectroscopic properties

5.1.1. Bismuth-doped single crystals annealed in H_2 atmosphere

In Bi: α-BaB_2O_4 crystal, Bi^{3+} will partially substitute Ba^{2+} in the crystal lattice. When the crystal sample is annealed up to 800°C in H_2 atmosphere, a broadband NIR luminescence will appear at 985 nm with FWHM of 187 nm excited at ~808 nm, as shown in **Figure 8** [23]. The lifetime of the emission at 985 nm is about 408 μs. Further investigation of the absorption, excitation and emission spectra indicates that the NIR luminescent centres in the crystal are basically consistent with the multiplets of free Bi^+ for the transition of $^3P_0 \rightarrow {}^1D_2$. Such experimental results demonstrate that thermal annealing of crystal in H_2 atmosphere will produce free electrons in crystal lattice to reduce Bi^{3+} to low-valence Bi^+, accompanied with the creation of O^{2-} vacancies [23].

5.1.2. Bismuth-doped glasses annealed in H_2 atmosphere

However, the heat treatment of bismuth borate glass ($75B_2O_3$–$25Bi_2O_3$) at 450°C under H_2 atmosphere will weaken the luminescence in both the NIR band (1000–1300 nm) and the visible band (650 nm) [69]. The reduction of NIR fluorescence after annealing in oxidation and reduction atmosphere indicates that the valence of the active centres might be a middle state, not the highest Bi^{5+} or the Bi atoms [69]. Similar negative effect of hydrogen annealing of bismuth-doped sodium aluminosilicate glasses at 498°C has been found, which also gives rise to a decrease of the NIR emission and, at the same time, formation of metallic bismuth particles in the surface region. Furthermore, surface tinting as well as the decrease of visible luminescence follow Arrhenius kinetics, suggesting that hydrogen permeation is the rate-governing process [70].

5.1.3. Bismuth-doped fibre after H_2 loading

The presence of H_2 in glass network provides an additional way for non-radiative transitions of activators from excited states to ground states, which therefore negatively affects pump efficiency of fibre lasers and amplifiers. Bi luminescence of hydrogen-impregnated silicate

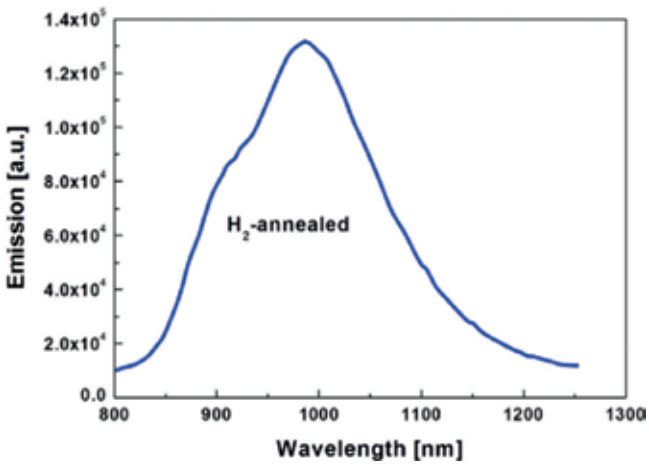

Figure 8. NIR emission spectra of H_2-annealed Bi: α-BaB_2O_4 crystals under excitation at 808 nm [23].

optical fibres will be quenched by deactivation of activators' excited states via collisions with H_2 migrating inside the glass network [71].

In bismuth and fluorine-doped-core silicate fibres, H_2 and D_2 loading at pressures of up to 125 bar leads to a decrease of the steady-state luminescence intensity and lifetime [32]. It is attributed to the appearance of an energy transfer bridge from bismuth clusters to vibrational degrees of freedom of diatomic molecules. In the presence of H_2 or D_2 experiencing random walking in silica, luminescence decay kinetics stops following a single exponential function even in fluorine-free silica-core fibre, especially at higher temperatures. The induced quenching rate increases with the increase of temperature as well and is greater for H_2 molecules than that for D_2. At temperatures below ~250 K, the presence of dissolved molecules has no effect, indicating the primary importance of having rotational degrees of freedom of migrating interstitial diatomic molecules in an excited state for effective quenching of bismuth electronic excitations. Especially, the influence of dissolved D_2 is weaker than that of H_2, due to a greater angular momentum of the D_2 and correspondingly smaller energy of the molecule's rotational quantum. In addition, such experimental results provide additional evidence for a cluster rather than a point defect model for bismuth defects in silica being responsible for NIR luminescence [32].

5.1.4. Bismuth-doped fibre after H_2 loading and thermal annealing

After H_2 loading (100°C, 140 bars, 5 days) and annealing (few seconds at 1000°C) of BDF (SiAlGeP), it is impossible to detect any emission band [72]. Such quenching is due to a similar reason for the degradation of Bi active ions into BiO molecules, Bi metals, and/or Bi_2/Bi_4 clusters. For H_2-loaded BDF, such degradation more probably happens due to the thermochemical reaction between glass network and H_2 molecules, resulting in a partial or complete reduction of the Bi-O linkages. This reaction results in the reduction of Bi ions into Bi metal or Bi atomic clusters and then a complete disappearance of the Bi-related luminescent centres, confirmed by the absence of visible and NIR photoluminescence, as well as the disappearance of all absorption bands in the accessible wavelength range [72].

5.1.5. Bismuth-doped fibre after H_2 loading and UV irradiation

After the irradiation by 193 nm pulsed laser, the H_2-loaded Bi-Al-doped silicate fibre shows huge increase of 1130 and 1390 nm luminescence intensity under 1053 and 1357 nm pumping. This luminescence enhancement seems to be attributed to an increase of the BAC concentration [55], where one evidence is the increase of the absorption peaks of BAC, as shown in **Figure 9**. In addition, the increase of luminescence for H_2-loaded Bi/Al doped optical fibres is also obtained by CW 244 nm laser irradiation. The luminescence increase depends upon accumulated laser fluence [56]. Especially, the luminescence scales with the power of the accumulated dose, where the power exponent m is 0.12 and 0.18 for the CW 244 nm laser and the pulsed 193 nm laser, respectively [56].

5.1.6. Bismuth/erbium co-doped fibre after H_2 loading

Similarly, after H_2 loading (27 hours, 194 bars, 180°C), the absorption of BEDF increases, as shown in **Figure 10(a)**. Meanwhile, the emission is evidently quenched by H_2 loading, as shown in **Figure 10(b)**. The additional appearance of peak at ~1240 nm indicates the diffusion of H_2 molecules in BEDF as in the previous report [32], which is verified by the disappearance of

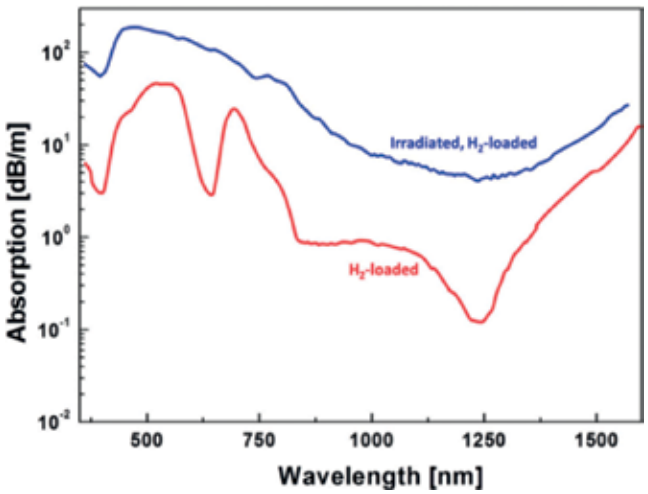

Figure 9. Absorption spectra of H_2-loaded, and irradiated H_2-loaded Bi-Al-doped silicate fibre [55].

the peak after 7 days exposure in air after the loading. The background loss has also increased compared with an unloaded sample. Especially, the emission of BAC-Si at >1380 nm is stronger than that at <1380 nm for the pristine, while after H_2 loading, the emission at >1380 nm becomes weaker than that at <1380 nm. It may due to the increase of the absorption at 1380 nm, which might possibly link with the formation of BAC-Si at 1420 nm [55] or the induced OH absorption at 1380 nm by the reduction of H_2.

5.2. Effect upon photosensitivity

Besides the variation of spectroscopic properties, with H_2 loading (pre-sensitization), the photosensitivity of BDF and BEDF can be changed as well as their stability of the gratings. **Table 2** summarizes the photosensitivity of BDF and BEDF with and without H_2 loading reported so far. The photosensitivity is evidently enhanced by H_2 loading, often leading to higher refractive index changes [73]. The enhanced photosensitivity in H_2-loaded BDF might be attributed

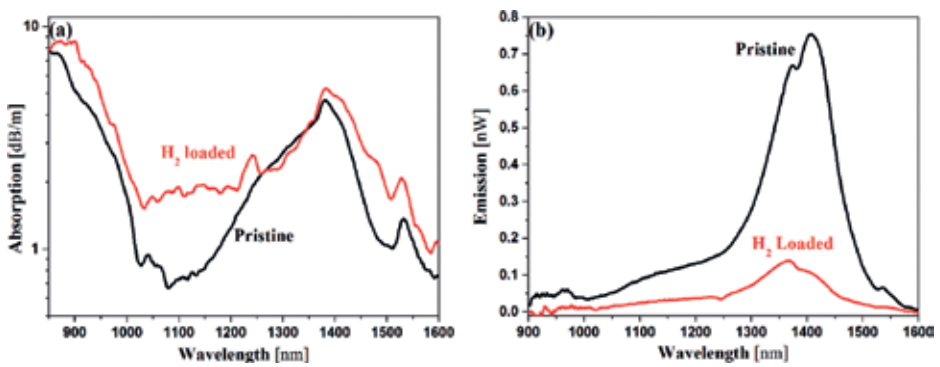

Figure 10. Absorption (a) and emission (b) spectra of BEDF before and after H_2 loaded (27 hours, 194 bars, 180°C) excited by 830 nm.

to Bi-H species (BiH, BiOH, …) [74]. The index changes are sufficient to directly inscribe high-reflective fibre Bragg gratings (FBG) into BDF for laser mirrors. Inscription of FBG directly into the active fibre would reduce the loss caused by splicing and mode field mismatch, leading to higher laser efficiency [74]. Moreover, the thermal stability of these gratings is very important for future applications [75].

5.2.1. Photosensitivity of BDF

The first investigation on the photosensitivity of BDF is performed in 2008 [55]. From fibre grating inscription of the Bi/Al-doped fibre, the induced index change is estimated to be 1×10^{-4} and 1.2×10^{-3} in the H_2 unloaded and H_2-loaded BDFs, respectively [55], showing the enhancement of photosensitivity by H_2 loading. Further investigation demonstrates that a mean index change up to 2.2×10^{-3} can be achieved in H_2-loaded Ge free Bi/Al doped fibre by irradiation of 193 nm pulsed ArF excimer laser, while 2.0×10^{-4} in H_2 unloaded fibres [74, 76]. In addition, the index change greatly depends upon the bismuth dopant concentration, and the higher doping concentration, the higher index change is achieved overall [74, 76]. That is, to say, the high Bi concentration optical fibre exhibits larger index changes for the same amount of irradiation dose [78].

A CW 244 nm Ar^+ laser is also used to fabricate Bragg gratings in pristine and H_2-loaded Bi/Al-doped fibres with index changes as high as 3.6×10^{-4} and 19.3×10^{-4}, respectively [75, 77]. Thermal annealing reveals peaks in the energy distribution at 1.2 and 2.3 eV [75]. Continuous isochronal thermal annealing reveals that although SMF-28e fibres, with and without hydrogen, are more stable than Bi/Al-doped fibres, higher thermal stability for the H_2-loaded Bi/Al-doped fibres is achieved, compared with the pristine one [77]. Moreover, thermal annealing results indicate that the grating in such H_2-loaded BDF has good thermal stability up to 678°C [75].

So far, the maximum index changes as high as $+2.5 \times 10^{-3}$ by 508 W/cm^2 244 nm laser has been achieved in high Bi doping BDF with H_2 loading, giving a maximum reflectivity >93% [78]. In addition, in Bi-doped microstructured optical fibre (BMOF) without H_2 loading, average refractive index changes of 2.7×10^{-4} is induced by a 5.3 kJ/cm^2 193 nm ArF excimer laser [73].

Through the stress study, it is shown in that H_2 loading also leads to a colour centre–based refractive index change. Tensile stress changes indicate a contribution of compaction to the total refractive index change related to volume changes [74, 76]. Especially, the comparison of the measured core stress changes before and after UV irradiation further indicates a compaction contribution to the total refractive index change depends on Bi-concentration [78]. In addition, the irradiation with the higher energy photons for Bi/Al fibre gives rise to a new band that appears at 3.4 eV. This could be an indication that the higher 193 nm photon excites a state that was previously inaccessible with 244 nm photon [82].

5.2.2. Photosensitivity of BEDF

The photosensitivity of BEDF has been studied by Bragg gratings inscription with 193 nm ArF pulsed laser [80] and 244 nm Ar^+ laser [81]. With 193 nm inscription, the average index n_{av} in the Bi-containing fibre with H_2 loading (P = 180 bars, T = 80°C, t = 2 days) grows faster than that in standard highly photosensitive fibre (GF1) and achieves a maximum average index change of 4.5×10^{-4}. Despite the large effective index changes, the index modulation n_{mod} is

Fibre	Key elements	Bi content	H_2 loading	Radiation conditions	Δn	Reference
BDF	Al, Si	0.15–0.3 at%	150 bars for 2 weeks at room temperature	160 mJ/cm^2 193 nm pulsed ArF excimer laser	2.2×10^{-3}	[74, 76]
BDF	Al, Si	0.02 at%	×	500 W/cm^2 CW Ar^+ laser	3.6×10^{-4}	[75]
BDF	Al, Si	0.02 at%	~150 bars for 2 weeks at room temperature	500 W/cm^2 CW Ar^+ laser	1.9×10^{-3}	[77]
BDF	Al, Si	0.15–0.3 at%	~150 bars for 2 weeks at room temperature	508 W/cm^2 CW Ar^+ laser	2.5×10^{-3}	[78]
BDF	Al, Si	0.02 at%	~150 bars for 2 weeks at room temperature	508 W/cm^2 CW Ar^+ laser	1.8×10^{-3}	[78]
BMOF	Si	0.03 at%	×	5.3 kJ/cm^2 193 nm ArF excimer laser	2.7×10^{-4}	[73, 79]
BDF	Al, Si	0.02 at%	×	5.3 kJ/cm^2 193 nm ArF excimer laser	1.0×10^{-4}	[73, 79]
BEDF	Er, Al, P, Ge, Si	0.16 mol% Bi_2O_3	180 bars for 2 days at 80 °C	9.66 J/cm^2 193 nm ArF excimer laser	4.5×10^{-4}	[80]
BEDF	Er, Al, P, Ge, Si	0.16 mol% Bi_2O_3	×	190 mW CW Ar^+ laser	1.1×10^{-4}	[81]

Note: BMPOF-microstructured optical fibre.

Table 2. Summary of photosensitivity in BDFs.

generally found to be quite low in BEDF compared to single-mode germanosilicate fibres. n_{mod} of the grating in pristine fibre decreases rapidly with the increasing temperature. However, the FBG in H_2-loaded BEDF appears more stable when the temperature is under 750°C [80].

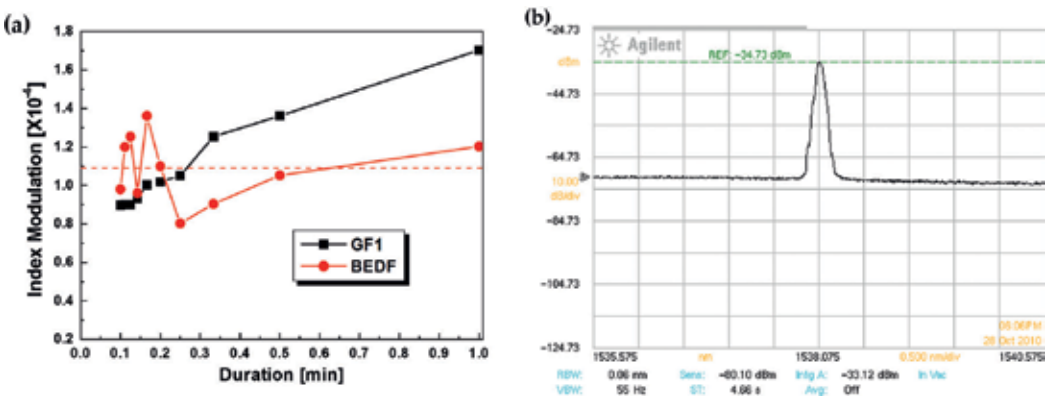

Figure 11. (a) Change in index modulation, n_{mod}, and average index n_{av}, in the BEDF and GF1 fibres vs inscription time with 244 nm laser. (b) Laser spectrum of the DFB fibre laser in 5 nm scanning range. (Fibre length: 20 cm; grating length: 4 cm; pump: 980 nm 70 mW).

Without H_2 loading, BEDF has shown good photosensitivity @ 244 nm [81], comparable to GF1 as expected given similar GeO_2 concentrations, as shown in **Figure 11(a)**. Different from the monotonous increase of GF1 vs the inscription duration, the index modulation of BEDF fluctuates, due to the non-uniformity of the BEDF, with an average index modulation of 1.1×10^{-4}. Especially, based on the phase-shifted gratings fabricated in BEDF, a distributed feedback (DFB) fibre laser operated at ~1538 nm has further been achieved, as shown in **Figure 11(b)**.

6. Summary and outlook

Significant progress has been made in research, development and application of BDF and BEDF since the first demonstration of NIR luminescence in bismuth-doped glass. Many studies have been carried out and demonstrated that the performance, functionality as well as stability, BDF and BEDF of these fibres can be changed by post treatments such as heating, high energy ray radiation, laser exposure and H_2 loading. For example, NIR emission of BAC-Si in BDF excited at 808 nm can be enhanced at high temperature. The thermal treatment could make Bi ions transfer from higher valence to lower valence, even precipitate to Bi_n colloids, which would result in irreversible thermal darkening effect. In addition, the degradation of BAC could occur by implementing thermal treatment in air, while new BAC could form in reduction atmosphere. However, the radiation treatment by gamma ray or electron produces more complicated effects. The radiation can activate the BACs, increase the absorption and enhance the NIR luminescence, dependent upon fibre compositions. Photo-bleaching effect has been observed in both BDF and BEDF by laser radiation. Some photo-bleaching is reversible after undergoing thermal treatment. In addition, the photo-bleaching is found to depend upon radiation wavelength, laser radiation power, temperature as well as material environment. Post treatment by H_2 will not only enhance the photosensitivity of the BDF and BEDF, but also change their spectroscopic properties. As a reducing agent, H_2 will enhance the reduction of Bi from higher valence to lower valence. It could result in the formation of new BAC, but may not increase luminescence due to the deactivation of excited defects or over-reduction. Through the investigations of these post-treatment effects, more understanding of BACs has been obtained and alternative ways to control and regulate the BACs in BDF and BEDF for better performance could be found.

Acknowledgements

Authors are thankful for the support of National Natural Science Foundation of China (61520106014, 61405014 and 61377096), Key Laboratory of In-fibre Integrated Optics, Ministry Education of China, State Key Laboratory of Information Photonics and Optical Communications (Beijing University of Posts and Telecommunications) (IPOC2016ZT07), Key Laboratory of Optical Fibre Sensing and Communications (Education Ministry of China), Key Laboratory of Optoelectronic Devices and Systems of Ministry of Education and Guangdong Province (GD201702) and Science and Technology Commission of Shanghai Municipality, China (SKLSFO2015-01 and 15220721500). The authors also thank Shanghai University for providing them with Fibre Index Profiler for index profiling analysis for the fibre samples.

Author details

Shuen Wei[1], Mingjie Ding[1], Desheng Fan[1], Yanhua Luo[1]*, Jianxiang Wen[2] and Gang-Ding Peng[1]

*Address all correspondence to: yanhua.luo1@unsw.edu.au

1 Photonics and Optical Communications, School of Electrical Engineering and Telecommunications, UNSW Sydney, NSW, Australia

2 Key Laboratory of Specialty Fibre Optics and Optical Access Networks, Shanghai University, Shanghai, China

References

[1] Murata K, Fujimoto Y, Kanabe T, Fujita H, Nakatsuka M. Bi-doped SiO_2 as a new laser material for an intense laser. Fusion Engineering and Design. 1999;**44**(1-4):437-439

[2] Fujimoto Y, Nakatsuka M. Infrared luminescence from bismuth-doped silica glass. Japanese Journal of Applied Physics. 2001;**40**(3B):L279-L281

[3] Ohkura T, Fujimoto Y, Nakatsuka M, Young-Seok S. Local structures of bismuth ion in bismuth-doped silica glasses analyzed using Bi L_{III} X-ray absorption fine structure. Journal of the American Ceramic Society. 2007;**90**(11):3596-3600

[4] Fujimoto Y. New infrared luminescence from Bi-doped glasses. In: Advances in Solid State Lasers Development and Applications. InTech; 2010

[5] Sokolov VO, Plotnichenko VG, Koltashev VV, Dianov EM. Centres of broadband near-IR luminescence in bismuth-doped glasses. Journal of Physics D: Applied Physics. 2009;**42**(9):0954101-0954107

[6] Meng X, Qui J, Peng M, Chen D, Zhao Q, Jiang X, Zhu C. Near infrared broadband emission of bismuth-doped aluminophosphate glass. Optics Express. 2005;**13**(5):1628-1634

[7] Sun H-T, Zhou J, Qiu J. Recent advances in bismuth activated photonic materials. Progress in Materials Science. 2014;**4**:1-72

[8] Dvoyrin VV, Mashinsky M, Dianov EM, Umnikov AA, Yashkov MV, Guranov AN. Absorption, fluorescence and optical amplification in MCVD bismuth-doped silica glass optical fibres. In: 31st European Conference on Optical Communication. 2005. ECOC 2005, Vol. 4; IET. 2005. pp. 949-950

[9] Dianov EM. Amplification in extended transmission bands using bismuth-doped optical fibers. Journal of Lightwave Technology. 2013;**31**(4):681-688

[10] Dianov EM. Bismuth-doped optical fibres: A new breakthrough in near-IR lasing media. Quantum Electronics. 2012;**42**(9):754-761

[11] Riumkin KE, Melkumov MA, Bufetov IA, Shubin AV, Firstov SV, Khopin VF, Guryanov AN, Dianov EM. Superfluorescent 1.44 μm bismuth-doped fiber source. Optics Letters. 2012;**37**(23):4817-4819

[12] Dianov EM. Nature of Bi-related near IR active centers in glasses: State of the art and first reliable results. Laser Physics Letters. 2015;**12**(9):095106 1-6

[13] Dianov EM. Fiber for fiber lasers: Bismuth-doped optical fibers: advances in an active laser media. Laser Focus World. 2015;**51**(9):16

[14] Luo Y, Wen J, Zhang J, Canning J, Peng G-D. Bismuth and erbium codoped optical fiber with ultrabroadband luminescence across O-, E-, S-, C-, and L-bands. Optics Letters. 2012;**37**(16):3447-3449

[15] Sathi ZM, Zhang J, Luo Y, Canning J, Peng G-D. Improving broadband emission within Bi/Er doped silicate fibres with Yb co-doping. Optical Materials Express. 2015;**5**(10):2096-2105

[16] Luo Y, Yan B, Zhang J, Wen J, Peng G-D. Development of Bi/Er co-doped optical fibre (BEDF) for ultra-broadband photonic applications. Frontiers of Optoelectronics. 2017:1-16

[17] Peng G-D, Luo Y, Zhang J, Wen J, Yan B, Canning J. Recent development of new active optical fibres for broadband photonic applications. In: 2013 IEEE 4th International Conference on Photonics (ICP); IEEE. 2013. pp. 5-9

[18] Bufetov IA, Melkumov MA, Firstov SV, Riumkin KE, Shubin AV, Khopin VF, Guryanov AN, Dianov EM. Bi-doped optical fibers and fiber lasers. IEEE Journal of Selected Topics in Quantum Electronics. 2014;**20**(5):111-125

[19] Kononenkoa V, Pashinina V, Galagana B, Sverchkova S, Denkera B, Konova V, Dianov EM. Activation of color centers in bismuth glass by femtosecond laser radiation. Laser Physics. 2011;**21**(9):1585-1592

[20] Sanz O, Haro-Poniatowski E, Gonzalo J, Navarro JF. Influence of the melting conditions of heavy metal oxide glasses containing bismuth oxide on their optical absorption. Journal of Non-Crystalline Solids. 2006;**352**(8):761-768

[21] Khonthon S, Morimoto S, Arai Y, Ohishi Y. Redox equilibrium and NIR luminescence of Bi_2O_3-containing glasses. Optical Materials. 2009;**31**(8):1262-1268

[22] Denker BI, Galagan BI, Musalitin AM, Shulman IL, Sverchkov SE, Dianov EM. Alternative ways to form IR luminescence centers in Bi-doped glass. Laser Physics. 2011;**21**(4):746-749

[23] Xu J, Zhao H, Su L, Yu J, Zhou P, Tang H, Zheng L, Li H. Study on the effect of heat-annealing and irradiation on spectroscopic properties of Bi: α-BaB_2O_4 single crystal. Optics Express. 2010;**18**(4):3385-3391

[24] Dianov EM. Bismuth-doped optical fibers: A challenging active medium for near-IR lasers and optical amplifiers. Light: Science & Applications. 2012;**1**(5):e12 1-7

[25] Xu B, Zhou S, Guan M, Tan D, Teng Y, Zhou J, Ma Z, Hong Z, Qiu J. Unusual luminescence quenching and reviving behavior of Bi-doped germanate glasses. Optics Express. 2011;**19**(23):23436-23443

[26] Peng M, Zollfrank C, Wondraczek L. Origin of broad NIR photoluminescence in bismuthate glass and Bi-doped glasses at room temperature. Journal of Physics: Condensed Matter. 2009;**21**(28):285106 1-6

[27] Peng M, Dong G, Wondraczek L, Zhang L, Zhang N, Qiu J. Discussion on the origin of NIR emission from Bi-doped materials. Journal of Non-Crystalline Solids. 2011;**357**(11):11-13

[28] Hanafusa H, Hibino Y, Yamamoto F. Formation mechanism of drawing-induced E' centers in silica optical fibers. Journal of Applied Physics. 1985;**58**(3):1356-1361

[29] Zlenko AS, Mashinsky VM, Iskhakova LD, Semjonov SL, Koltashev VV, Karatun NM, Dianov EM. Mechanisms of optical losses in Bi: SiO_2 glass fibers. Optics Express. 2012;**20**(21): 23186-23200

[30] Bulatov LI, Mashinsky VM, Dvoirin VV, Kustov EF, Dianov EM, Sukhorukov AP. Structure of absorption and luminescence bands in aluminosilicate optical fibers doped with bismuth. Bulletin of the Russian Academy of Sciences: Physics. 2008;**72**(12):1655-1660

[31] Dvoretskii DA, Bufetov IA, Velmiskin VV, Zlenko AS, Khopin VF, Semjonov VF, Guryanov AN, Denisov LK, Dianov EM. Optical properties of bismuth-doped silica fibres in the temperature range 300-1500 KJ. Journal of Quantum Electronics. 2012;**42**(9):762-769

[32] Bazakutsa AP, Golant KM. Near-infrared luminescence of bismuth in fluorine-doped-core silica fibres. Optics Express. 2015;**23**(3):3818-3830

[33] Bazakutsa AP, Butov OV, Savel'ev EA, Golant KM. Specific features of IR photoluminescence of bismuth-doped silicon dioxide synthesized by plasmachemical method. Journal of Communications Technology and Electronics. 2012;**57**(7):743-750

[34] Granados DR, Kir'yanov AV, Barmenkov YO, Halder A, Das S, Dhar A, Paul MC, Bhadra SK, Didenko SI, Koltashev VV, Plotnichenko VG. Effects of elevating temperature and high-temperature annealing upon state-of-the-art of yttia-alumino-silicate fibers doped with Bismuth. Optical Materials Express. 2016;**6**(2):486-508

[35] Dvoretsky DA, Bufetov IA, Khopin VF, Guryanov AN, Denisov LK, Dianov EM. Optical properties of the bismuth-doped aluminosilicate fiber within the temperature range 300-1500 K. In: Proc. ICONO/LAT; Moscow, Russia. 2013. pp. 18-22

[36] Wei S, Luo Y, Ding M, Cai F, Xiao G, Fan D, Zhao Q, Peng G-D. Thermal effect on attenuation and luminescence of Bi/Er co-doped fiber. IEEE Photonics Technology Letters. 2017;**29**(1): 43-46

[37] Wei S, Luo Y, Ding M, Cai F, Zhao Q, Peng G-D. Annealing effects on bismuth active centers in Bi/Er co-doped fiber. In: 2016 Conference on Lasers and Electro-Optics (CLEO); IEEE. 2016. pp. 1-2

[38] Park SY, Weeks RA, Zuhr RA. Optical absorption by colloidal precipitates in bismuth-implanted fused silica: Annealing behaviour. Journal of Applied Physics. 1995;**77**(12): 6100-6107

[39] Pan Z, Morgan SH, Henderson DO, Park SY, Weeks RA, Magruder RH III, Zuhr RA. Linear and nonlinear optical response of bismuth and antimony implanted fused silica: Annealing effects. Optical Materials. 1995;**4**(6):675-684

[40] Vivona M, Girard S, Marcandella C, Robin T, Cadier B, Cannas M, Boukenter A, Ouerdane Y. Influence of Ce codoping and H_2 pre-loading on Er/Yb-doped fiber: Radiation response characterized by confocal micro-luminescence. Journal of Non-Crystalline Solids. 2011;**357**(8):1963-1965

[41] Girard S, Vivona M, Laurent A, Cadier B, Marcandella C, Robin T, Pinsard E, Boukenter A, Ouerdane Y. Radiation hardening techniques for Er/Yb doped optical fibers and amplifiers for space application. Optics Express. 2012;**20**(8):8457-8465

[42] Sheng Y, Yang L, Luan H, Liu Z, Yu Y, Li J, Dai N. Improvement of radiation resistance by introducing CeO_2 in Yb-doped silicate glasses. Journal of Nuclear Materials. 2012;**427**(1):58-61

[43] Peng T-S, Huang Y-W, Wang LA, Liu R-Y, Chou F-I. Photo-annealing effects on gamma radiation induced attenuation in Erbium doped fibers and the sources using 532-nm and 976-nm lasers. IEEE Transactions on Nuclear Science. 2010;**57**(4):2327-2331

[44] Chang SH, Liu R-Y, Lin C-E, Chou F-I, Tai C-Y, Chen C-C. Photo-annealing effect of gamma-irradiated erbium-doped fibre by femtosecond pulsed laser. Journal of Physics D: Applied Physics. 2013;**46**(49):1-6

[45] Lezius M, Predehl K, Stower W, Turler A, Greiter M, Hoeschen C, Thirolf P, Assmann W, Habs D, Prokofiev A, Ekstrom C, Hansch TW, Holzwarth R. Radiation induced absorption in rare earth doped optical fibers. IEEE Transactions on Nuclear Science. 2012;**59**(2):425-433

[46] Fox BP, Simmons-Potter K, Moore SW, Fisher JH, Meister DC. Gamma-radiation-induced photodarkening in actively pumped Yb^{3+}-doped optical fiber and investigation of post-irradiation transmittance recovery. No. SAND2009-4532C. Albuquerque, NM (United States): Sandia National Laboratories (SNL-NM); 2009

[47] Wen J, Liu W, Dong Y, Luo Y, Peng GD, Chen N, Pang F, Chen Z, Wang T. Radiation-induced photoluminescence enhancement of Bi/Al-codoped silica optical fibers via atomic layer deposition. Optics Express. 2015;**23**(22):29004-29013

[48] Yan B, Luo Y, Sporea D, Mihai L, Negut D, Ding M, Wang C, Wen J, Sang X, Peng G-D. Enhanced gamma radiation effect in Bi/Er co-doped optical fibre by co-doping Yb. Asia Communications and Photonics Conference. Optical Society of America. 2016: AF2A, p. 135

[49] Yan B, Luo Y, Sporea D, Mihai L, Negut D, Sang X, Wen J, Xiao G, Peng G-D. Gamma radiation-induced formation of bismuth related active centre in Bi/Er/Yb co-doped fibre. Asia Communications and Photonics Conference. Optical Society of America; 2015: ASu2A-56

[50] Sporea D, Mihai L, Negut D, Luo Y, Yan B, Ding M, Wei S, Peng G-D. γ irradiation induced effects on bismuth active centres and related photoluminescence properties of Bi/Er co-doped optical fibres. Scientific Reports. 2016;**6**:29827 1-11

[51] Firstov SV, Khopin VF, Alyshev SV, Firstova EG, Riumkin KE, Melkumov MA, Khegai AM, Kashaykin PF, Guryanov AN, Dianov EM. Effect of gamma-irradiation on the optical properties of bismuth-doped germanosilicate fibers. Optical Materials Express. 2016;**6**(10):3303-3308

[52] Kir'yanov AV, Dvoyrin AV, Mashinsky VM, Il'ichev NN, Kozlova NS, Dianov EM. Influence of electron irradiation on optical properties of bismuth doped silica fibers. Optics Express. 2011;**19**(7):6599-6608

[53] Kir'yanov AV. Effects of electron irradiation upon absorptive and fluorescent properties of some doped optical fibers. In: Radiation Effects in Materials. InTech; 2016

[54] Peng M, Zhao Q, Qiu J, Wondraczek L. Generation of emission centers for broadband NIR luminescence in bismuthate glass by femtosecond laser irradiation. Journal of the American Ceramic Society. 2009;**92**(2):542-544

[55] Ban C, Bulatov LI, Dvoyrin VV, Mashinsky VM, Limberger HG, Dianov EM. Infrared luminescence enhancement by UV-irradiation of H_2-loaded Bi-Al-doped fiber. In: 35th European Conference on Optical Communication, 2009. ECOC'09. IEEE. 2009. pp. 1-2

[56] Violakis G, Limberger HG, Mashinsky VM, Dianov EM. Dose dependence of luminescence increase in H_2-loaded Bi-Al co-doped optical fibers by cw 244-nm and pulsed 193-nm laser irradiation. Optical Fiber Communication Conference. Optical Society of America; 2013. OTh4C-2

[57] Piccoli R, Robin T, Brand T, Klotzbach U, Taccheo S. Effective photodarkening suppression in Yb-doped fiber lasers by visible light injection. Optics Express. 2014;**22**(7):7638-7643

[58] Guzman Chávez AD, Kir'yanov AV, Barmenkov YO, Il'ichev NN. Reversible photodarkening and resonant photobleaching of ytterbium-doped silica fiber at in-core 977-nm and 543-nm irradiation. Applied Physics Letters. 2007;**4**(10):734-739

[59] Laperle P, Chandonnet A, Vallée R. Photobleaching of thulium-doped ZBLAN fibers with visible light. Optics Letters. 1997;**22**(3):178-180

[60] Firstov S, Alyshev S, Melkumov M, Riumkin K, Shubin A, Dianov EM. Bismuth-doped optical fibers and fiber lasers for a spectral region of 1600-1800 nm. Optics Letters. 2014;**39**(24):6927-6930

[61] Ding M, Wei S, Luo Y, Peng G-D. Reversible photo-bleaching effect in a bismuth/erbium co-doped optical fiber under 830 nm irradiation. Optics Letters. 2016;**41**(20):4688-4691

[62] Ding M, Fang J, Luo Y, Wang W, Peng G-D. Photo-bleaching mechanism of the BAC-Si in bismuth/erbium co-doped optical fibers. Optics Letters. 2017;**42**(24):5222-5225

[63] Firstov S, Alyshev S, Khopin V, Melkumov M, Guryanov A, Dianov EM. Photobleaching effect in bismuth-doped germanosilicate fibers. Optics Express. 2015;**23**(15):19226-19233

[64] Firstov SV, Firstova EG, Alyshev SV, Khopin VF, Riumkin KE, Melkumov MA, Guryanov AN, Dianov EM. Recovery of IR luminescence in photobleached bismuth-doped fibers by thermal annealing. Laser Physics. 2016;**26**(8):084007

[65] Firstov SV, Alyshev SV, Kharakhordin AV, Riumkin KE, Dianov EM. Laser-induced bleaching and thermo-stimulated recovery of luminescent centers in bismuth-doped optical fibers. Optical Materials Express. 2017;**7**(9):3422-3432

[66] Dianov EM. On the nature of near-IR emitting Bi centres in glass. Journal of Quantum Electronics. 2010;**40**(4):283

[67] Skuja L. Optically active oxygen-deficiency-related centers in amorphous silicon dioxide. Journal of Non-Crystalline Solids. 1998;**239**(1):16-48

[68] Firstov SV, Alyshev SV, Firstova EG, Melkumov MA, Khegay AM, Khopin VF, Guryanov AN, Dianov EM. Dependence of the photobleaching on laser radiation wavelength in bismuth-doped germanosilicate fibers. Journal of Luminescence. 2017;**182**:87-90

[69] Qiu YQ, Kang J, Li CX, Dong XY, Zhao C-L. Broadband near-infrared luminescence in bismuth borate glasses. Laser Physics. 2010;**20**(2):487-492

[70] Nielsen KH, Smedskjaer MM, Peng M, Yue Y, Wondraczek L. Surface-luminescence from thermally reduced bismuth-doped sodium aluminosilicate glasses. Journal of Non-Crystalline Solids. 2012;**358**(23):3193-3199

[71] Bazakutsa AP, Butov OV, Golant KM. Influence of hydrogen loading on active fibers. Optical Fiber Communication Conference and Exposition and the National Fiber Optic Engineers Conference (OFC/NFOEC); IEEE. 2013. pp. 1-3

[72] Truong VG, Bigot L, Lerouge A, Douay M, Razdobreev I. Study of thermal stability and luminescence quenching properties of bismuth-doped silicate glasses for fiber laser applications. Applied Physics Letters. 2008;**92**(4):1-3

[73] Violakis G, Limberger HG, Zlenko AS, Semjonov SL, Bufetov IA, Mashinsky VM, Vel'miskin VV, Dianov EM. Fabrication of Bragg gratings in microstructured and step index Bi-SiO_2 optical fibers using an ArF laser. Optics Express. 2012;**20**(26):B118-B123

[74] Ban C, Limberger HG, Mashinsky V, Dvoyrin V, Dianov EM. UV-Photosensitivity of Germanium-Free Bi-Al Silica Fibers. Bragg Gratings, Photosensitivity, and Poling in Glass Waveguides. Optical Society of America. Karlsruhe, Germany. 2010. BWD3

[75] Violakis G, Limberger HG, Mashinsky V, Dianov EM. Fabrication and thermal decay of fiber Bragg gratings in Bi-Al co-doped optical fibers. In: 2011 37th European Conference and Exhibition on Optical Communication (ECOC). IEEE; 2011. pp. 1-4

[76] Ban C, Limberger HG, Mashinsky V, Dianov EM. Photosensitivity and stress changes of Ge-free Bi-Al doped silica optical fibers under ArF excimer laser irradiation. Optics Express. 2011;**19**(27):26859-26865

[77] Violakis G, Limberger HG, Mashinsky VM, Dianov EM. Fabrication and thermal decay of fiber Bragg gratings in pristine and H_2-loaded Bi-Al co-doped optical fibers. Optics Express. 2011;**19**(26):B350-B356

[78] Violakis G, Limberger HG, Mashinsky V, Dianov EM. Strong fiber Bragg gratings in Bi-Al co-doped H_2-loaded optical fibers using CW-Ar^+ laser. Optical Fiber Communication Conference and Exposition (OFC/NFOEC), 2011 and the National Fiber Optic Engineers Conference; IEEE. 2011. pp. 1-3

[79] Violakis G, Limberger HG, Zlenko AS, Semjonov SL, Mashinsky VM, Dianov EM. Fabrication of Bragg gratings in microstructured Bi: SiO_2 optical fiber using an ArF laser. European Conference and Exhibition on Optical Communication. Optical Society of America; 2012. We. 1. F. 3

[80] Cook K, Shao L-Y, Canning J, Wang T, Luo Y, Peng G-D. Bragg gratings in few-mode Er/Al/Bi/P Co-doped germanosilicate ring-core fibre. OFS2012 22nd International Conference on Optical Fiber Sensors, Vol. 8421. International Society for Optics and Photonics; 2012. 842155 1-4

[81] Qi H, Luo Y, Yang H, Zhang J, Canning J, Peng G-D. Photosensitivity, phase shifted grating and DFB fibre laser in bismuth/erbium co-doped germanosilicate optical fibre. 19th Optoelectronics and Communications Conference (OECC) and the 39th Australian Conference on Optical Fibre Technology (ACOFT); Engineers Australia. 2014. pp. 495-497

[82] Violakis G, Saffari P, Limberger HG, Mashinsky VM, Dianov EM. Thermal decay of UV Ar+ and ArF excimer laser fabricated Bragg gratings in SMF-28e and Bi-Al-doped optical fiber. Bragg Gratings, Photosensitivity, and Poling in Glass Waveguides. Optical Society of America; 2012. BM4D-6

Section 6

Bismuth Materials for Industrial Catalysis

Chapter 9

Bismuth Molybdate-Based Catalysts for Selective Oxidation of Hydrocarbons

Minh Thang Le

Additional information is available at the end of the chapter

http://dx.doi.org/10.5772/intechopen.75105

Abstract

Bismuth molybdate materials (α-$Bi_2Mo_3O_{12}$, β-$Bi_2Mo_2O_9$, and γ-Bi_2MoO_6) are well-known in the field of catalysis due to their excellent activity for one of the most important industrial processes: the oxidation/ammoxidation of lower olefins. These processes play an important role in society since the production of one quarter of the most important industrial organic chemicals and intermediates (such as acrolein, acrylic acid, propylene oxide, etc.) used in the manufacture of industrial products and consumer goods is based on these reactions. Although the materials were developed since the 1960s, the topic still attracts many attentions; new catalysts with different additive elements to enhance catalytic activity are still explored. Advanced researches on bismuth molybdate-based catalysts have been performed not only with the change in composition but also in the synthesis methods. This book chapter summarizes recent researches on the development of bismuth molybdate-based catalysts with new achievements in catalysis field.

Keywords: selective oxidation, hydrocarbons, catalysts, bismuth molybdates, reaction mechanism

1. Introduction

Since they were developed by SOHIO company in 1959, bismuth molybdates have received a large attention owing to their high selectivity and activity for partial oxidation and ammoxidation of lower olefins to essential intermediate products for industrial applications. Aspects of these compounds such as structure, catalytic property, conductivity, etc. have been thoroughly investigated. Most studies are concentrated on the catalytic property of bismuth molybdates. Here, the reactions, the mechanism, and all related aspects have been explored

although there are still a lot of controversies. Among many other selective oxidation catalysts, bismuth molybdates are the most extensively studied and serve as the basis for today's many highly active and selective commercial catalyst systems [1]. There are many kinds of bismuth molybdates with different Bi/Mo atomic ratios, but those which have been quite thoroughly investigated and exhibit good catalytic properties are in the range of composition Bi/Mo = 2/1–2/3.

Three phases of bismuth molybdates, α, β, and γ, exhibit good catalytic properties for oxidation of propylene. Their catalytic activities decrease in the following generally accepted order, $Bi_2Mo_2O_9$ (β) ≥ $Bi_2Mo_3O_{12}$ (α) > Bi_2MoO_6 (γ), which is reported by many authors [1–5]. However, there are some authors who reported the opposite trend: $\gamma \geq \beta > \alpha$ [6, 7], $\beta > (\alpha = \gamma)$ [8], $\alpha > \beta > \gamma$ [9].

Catalysts based on bismuth molybdates can be divided into the following components:

Primary bismuth molybdate system: These catalysts are mixed oxide constituted from Bi_2O_3 and MoO_3 at specified ratios as mentioned above.

Multicomponent bismuth molybdate system: These catalysts were developed by the modification of primary bismuth molybdates by replacing or adding other metal elements. The first replacement of half of the amount of the bismuth molybdate by iron in $Bi_9P_1Mo_{12}O_{52}$ increased the catalytic activity for the ammoxidation of propylene noticeably. The Bi-Fe-Mo-O system consists of several different composite oxides including bismuth molybdate, iron molybdate, and $Bi_3FeMo_2O_{12}$. Following this improvement, divalent transition metal cations such as Co^{2+} and Ni^{2+} were also found to enhance the catalytic activity and selectivity significantly [4].

The catalyst $Bi_{1-x/3}\phi_{x/3}V_{1-x}Mo_xO_4$, which form a solid solution with composition limits of bismuth vanadate, x = 0, and the α phase of bismuth molybdate, x = 1, attracted many attentions [10, 11] since it is a good system to investigate the diffusion of lattice oxide. The participation of the lattice oxide ion into the reaction is quite prominent in this catalyst system, but the degree of the participation depends on the catalyst composition.

2. Phase diagram of bismuth molybdates

To understand on the bismuth molybdate catalysts, it is necessary to explore the phase diagram of this system since three catalytic active phases of bismuth molybdates exhibit some unique properties. The phase diagram established by Egashira et al. (**Figure 1**) [12] is the most well known in literature. In this phase diagram, three main phases of bismuth molybdates can be found.

2.1. The Scheelite (α) phase

This phase has the nominal composition $Bi_2Mo_3O_{12}$ (written in short as the 2/3 phase). The α phase forms a eutectic with MoO_3 at 615°C and at 71 atom% Mo:

$$\text{liq.} \rightarrow Bi_2Mo_3O_{12} + MoO_3 \quad (1)$$

http://dx.doi.org/10.5772/intechopen.75105

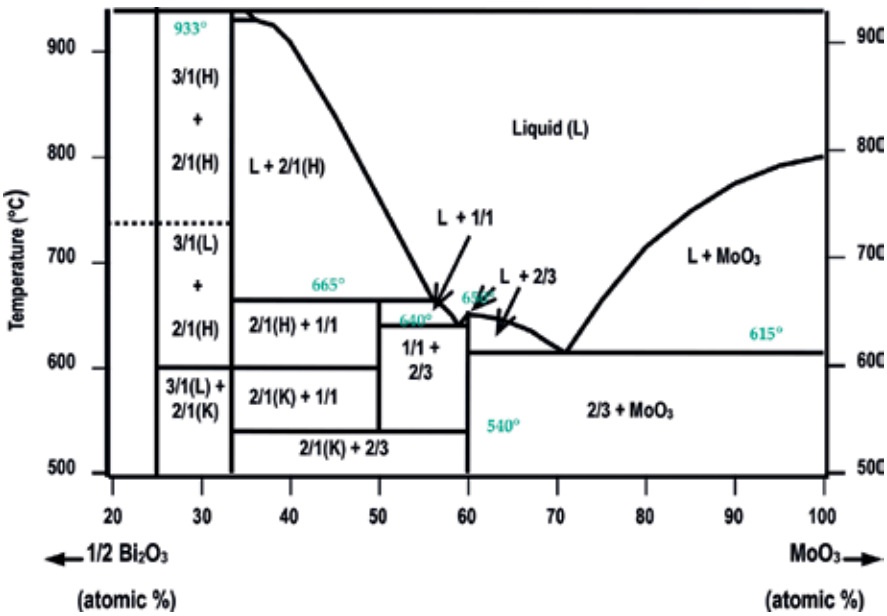

Figure 1. Phase diagram for the bismuth molybdate system by Egashira [12].

The α phase also forms a eutectic with 1/1 at 640°C and at 59 atom% Mo:

$$\text{liq.} \rightarrow \ Bi_2Mo_3O_{12} + Bi_2Mo_2O_9 \tag{2}$$

The α phase has been reported to be stable in a large temperature range between room temperature and 650°C [13]. The α phase congruently melts at 650°C.

The α phase has a monoclinic structure (a = 0.789 nm, b = 1.170 nm, c = 1.224 nm, β = 116°20′) which was related to the Scheelite-type structure with space group P21/c.

2.2. The Erman (β) phase

This phase has the nominal composition $Bi_2Mo_2O_9$ (written in short as the 1/1 phase). The β phase is only stable in the relatively narrow temperature range of 665–540°C. The β phase is formed by the peritectic reaction of liquid MoO_3 with the high-temperature form of the γ phase at 665°C:

$$MoO_3\,(\text{liq.}) + Bi_2MoO_6\,(\text{H}) \ \rightarrow \ Bi_2Mo_2O_9 \tag{3}$$

but disproportionates into 2/1 (K) and 2/3 below 540°C:

$$2\,Bi_2Mo_2O_9 \ \rightarrow \ Bi_2MoO_6\,(\text{K}) + Bi_2Mo_3O_{12} \tag{4}$$

However, since the rate of reaction (Eq. 4) is very low, $Bi_2Mo_2O_9$ can exist even at room temperature as a metastable phase. There are two metastable modifications: β' and β'' [14].

The β phase of bismuth molybdate which was first identified by Erman et al. [14] has an orthorhombic crystal structure with lattice parameters: a = 1.079 nm, b = 1.189 nm, c = 1.186 nm, and space group Pnmm or Pnm21.

2.3. The Koechlinite (γ) phase

This phase has the nominal composition Bi_2MoO_6 (written in short as the 2/1(K) phase). The high-temperature modification of this phase is indicated by γ′ - Bi_2MoO_6 (2/1(H)). The intermediate metastable polyform between γ and γ′ is γ″ (or 2/1(I)). The formation of Bi_2MoO_6 (H) from liquid is also due to a peritectic reaction as in the case of the β phase. The solid which takes part in this reaction is indicated to be the high-temperature form of $3Bi_2O_3.\ 2MoO_3$ (3/1):

$$MoO_3\,(liq.) + 3Bi_2O_3.2MoO_3\,(H) \rightarrow 3\,[Bi_2O_3\,.\,MoO_3(H)] \quad (5)$$

The high-temperature phase Bi_2MoO_6 (H) is transformed into Bi_2MoO_6 (K) at 600°C, but the rate of this transition is low so that Bi_2MoO_6 (H) can exist even at room temperature [12, 15].

Earlier reports by Zemann and Aykan [16, 17] showed that the crystal structure of natural koechlinite, Bi_2MoO_6, was orthorhombic, a = 0.550 nm, b = 1.624 nm, c = 0.549 nm, and space

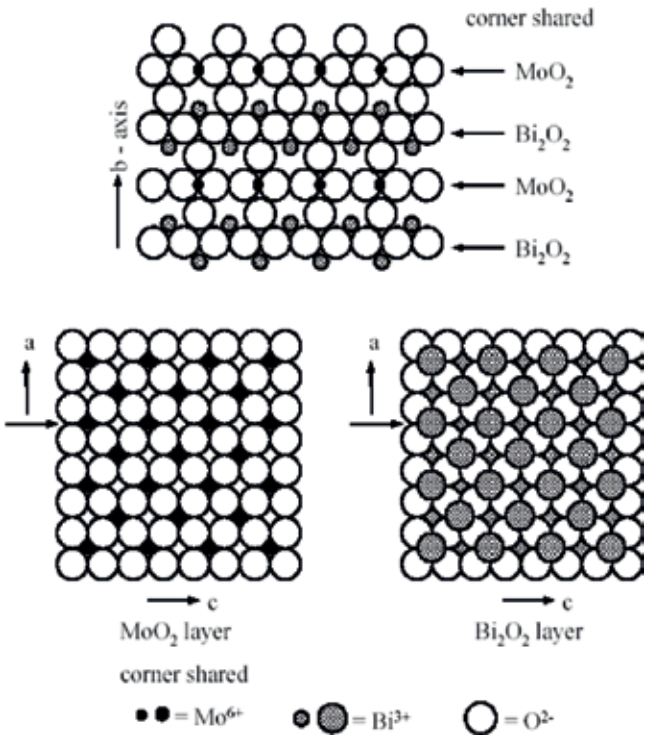

Figure 2. Layered structure of Bi_2MoO_6 [19].

group Cmca (D2h18); Van den Elzen and Rieck [18] reported the same lattice parameters but different space groups: Pca21.

The structure was described as alternate layers of $(BiO^{+})_{2n}$ and $(MoO_4^{2-})_n$ perpendicular to the y direction. The $(MoO_4^{2-})_n$ layer consists of deformed oxo-molybdenum octahedra, sharing four corners with neighboring oxo-molybdenum octahedra in the same layer perpendicular to the y direction. The molybdenum-oxygen bond distances in such a layer can be divided in two classes, the first with bond lengths of approximately 0.224 nm. The two other apical ions of the oxo-molybdenum octahedra point toward a $(BiO^{+})_{2n}$ layer, one below and one above.

Thus, if a $Bi_2O_2^{2+}$ = B layer and a MoO_2^{2+} = A layer, in crystals they will be connected via layers of oxygen anions denoted by O. Schematically, therefore, the schemata of three bismuth molybdate phases can be written as the following [8]:

- α phase=(BOAOAOAO)m.
- β phase=(BOAOAO)m.
- γ phase=(BOAO)m.

The structure of the γ phase can be seen in **Figure 2** [19]. The position of bismuth and molybdenum atoms in the unit cell is shown together with their bonds to oxygen.

3. Synthesis of bismuth molybdates

Bismuth molybdates can be obtained via different methods, for example, co-precipitation [9, 20], solid-state reaction [21], spray drying [22–24], hydrothermal [25, 26], solution combustion [27], and solgel route [28].

3.1. Co-precipitation

The most popular method to prepare bismuth molybdates is co-precipitation. Almost all authors [7, 29, 30] follow this method although there are some modifications. The starting reactants are typically a solution of $Bi(NO_3)_3.5H_2O$ in water, a suitable quantity of HNO_3, and a solution of $(NH_4)_6Mo_7O_{24}.4H_2O$ in water. The solution of bismuth nitrate is added to ammonium molybdate or vice versa. pH is adjusted in the range of about 1–9 by adding NH_3 or HNO_3, depending on each author. The precipitate is filtered and dried or the liquid is directly evaporated. Some other modifications of precipitation synthesis use $Bi(NO_3)_3.5H_2O$ and H_2MoO_4 or $BiONO_3.H_2O$ and $(NH_4)_6Mo_7O_{24}.4H_2O$ as starting materials [7, 31]. Precipitates are calcined at some given temperature, normally from 450 to 580°C.

3.2. Solid-state reaction

Another conventional method to prepare bismuth molybdate is a solid-state reaction from mixtures of bismuth oxide and molybdenum oxide powders [12, 29, 32] or a mixture of $Bi(NO_3)_3.5H_2O$ and $(NH_4)_6Mo_7O_{24}.4H_2O$ powders [33] at the temperature range of 500–650°C.

3.3. Solgel

This method is used by a few authors. Godard et al. [28] prepared bismuth molybdates by a citrate-based method from aqueous solutions of Bi^{3+} and Mo^{6+} and citric acid in equivalent amounts. Wildberger et al. [34] used an alkoxide method to prepare bismuth molybdates supported by titania. The gelation occurs at low temperatures and results in amorphous materials with unique morphology and extraordinary dispersion of the active compound. Bismuth molybdates are obtained by calcining these materials at about 500°C.

Solgel method was considered as an effective pathway to afford pure phases of these catalysts. However, it requires acidic conditions in general, which is harsh and less suitable for practical applications [28]. A solgel synthesis of bismuth molybdates as thin film has been reported at quite neutral pH conditions [35], but the synthesis proved to be effective at different pH values. However, at neutral and basic pH conditions, it turns difficult to obtain pure phases of bismuth molybdates. The gelation process is considered to be entirely different at pH 1 and 5. With increasing content of bismuth, the formation of the impure Bi_2O_3 phases turns more difficult to be avoided. Among different catalysts, sample $Bi_2Mo_3O_{12}$ synthesized at pH 5 displayed high conversion and selectivity. Additionally, it can be synthesized in more convenient manner, making it suitable for the applications in practical technical processes [36].

3.4. Hydrothermal method

The hydrothermal method has been applied to prepare bismuth molybdates by Beale and Sanka [37, 38]. Stoichiometric amounts of acidified bismuth nitrate solutions were mixed with ammonium heptamolybdate dissolved in ammonium hydroxide. The pH of this mixture was adjusted to a specific range (2–6) before introducing this mother liquor into a Teflon-lined autoclave. The autoclave was placed in a preheated furnace (140°C) for several hours. After a specific period (20 h), the contents were washed and dried. Thus, this method requires very low temperatures (except the β phase which needs to be calcined further at 560°C) and results in high surface area (9–10 m^2/g).

3.5. Spray drying

As known, bismuth molybdates can be prepared by conventional methods such as precipitation and solid-state reaction, which have been used for long and are widely applied for laboratory scale and industrial processes. However, pure bismuth molybdates prepared by conventional methods are not often obtained, and all commercial oxidation catalysts are multiphase [39].

Spray drying was applied to synthesize many multi-metal oxides, which exhibit good characteristics [40]. Homogeneity, stoichiometry, uniformity of product size, hardness, and abrasiveness are advantages of spray drying. Spray drying can be applied to replace conventional synthesis methods, which opens interesting industrial applications. To synthesize bismuth molybdates, the precursor solution for spray drying was prepared from a solution of $(NH_4)_6Mo_7O_{24}$ and a solution of $Bi(NO_3)_3$ with the addition of few milliliters of concentrated

http://dx.doi.org/10.5772/intechopen.75105

HNO_3 in order to keep the Bi-salt dissolved. This precursor solution was spray dried using a laboratory spray dryer with a reasonable nozzle and feeding rate at a suitable temperature (about 200°C). Spray drying is one of the best methods to prepare pure phases of bismuth molybdates. It is a versatile method which is able to prepare mixtures of bismuth molybdates with desired Bi/Mo ratio in accordance with the phase diagram, which is very useful for preparing mixed catalysts with higher activity than the pure one owing to the synergy effect. Spray drying confirmed its reputation as a reliable method for the synthesis of pure catalysts [41]. Therefore, the XRD patterns of the spray drying bismuth molybdate samples with different Bi/Mo ratios (**Figure 3** [42]) are considered as the standard to determine the phase composition of these compounds.

3.6. Solution combustion

The solution combustion synthesis is a quite simple method and presents several advantages. It is based on highly exothermic redox chemical reactions between metallic compounds and nonmetallic ones. The first step of the solution combustion synthesis is the preparation of an aqueous solution of suitable metal salts, e.g., nitrates (bismuth nitrate, ammonium molybdate), because of their high solubility in water and the oxidizing potential of NO_3^- groups. An organic molecule such as urea, glycine, hydrazine, or precursors containing a carboxylate anion is then added to form complexes with the metal ions. The organic molecule works as a fuel as its combustion enables to release a huge amount of heat in a short period of time. The

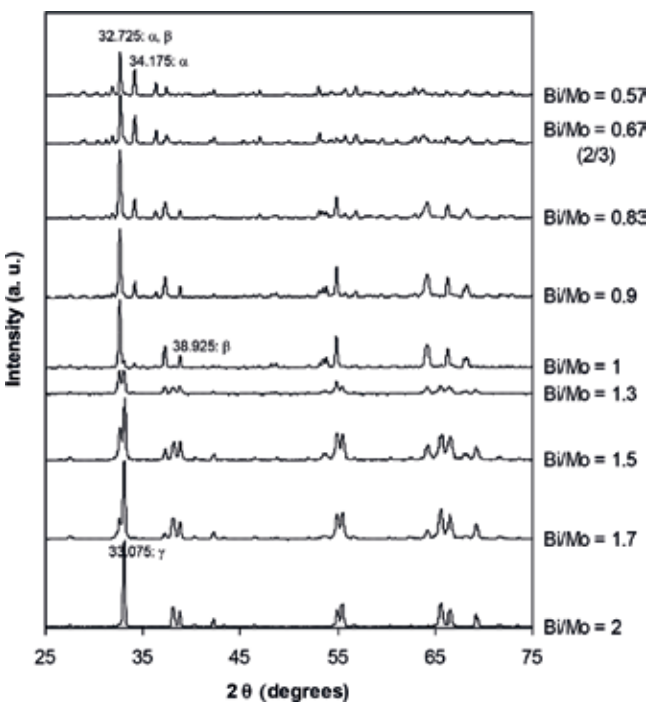

Figure 3. XRD patterns of bismuth molybdate samples with 0.57 < Bi/Mo < 2 [42].

final solution is then heated until reaching temperatures in the range of 300–450°C for a very short residence time to avoid sintering, which brings the solution to ebullition. The resulting mixture then becomes dry and in a matter of minutes ignites that sets off highly exothermic, self-sustaining, and fast redox reactions that generate a dry, usually crystalline, fine powder. The obtained powders can be calcined or not since the uncalcined powders are crystallized well already. The products possess a relatively high specific surface area. The rapidity of the method may also allow the formation of metastable phases [27, 43–46].

4. Selective oxidation of light hydrocarbons on catalysts

Selective oxidation and ammoxidation of hydrocarbons play an important role in society since the production of one quarter of the most important industrial organic chemicals and intermediates used in the manufacture of industrial products and consumer goods is based on these reactions [55]. Hence, they contribute significantly to the gross national products of industrial countries and afford future opportunities for developing countries. They also present opportunities for significant fundamental research.

The selective oxidation of light hydrocarbons, especially propylene, is the most significant and well-studied process. Its products include important intermediates such as acrolein, acrylic acid, propylene oxide, etc. The catalytic process was first discovered in 1948 by Hearne and Adams [47] with the use of cuprous oxide catalysts. In 1959 and in 1962, Idol [48] and Callahan [49], respectively, improved the yield of the reaction with the discovery of bismuth molybdate catalysts. Shortly after that, this process was industrialized by SOHIO company and has then been developed and improved year by year by this company [3]. Drastic and empirical changes have been introduced to the catalyst composition and preparation as well as to the reaction process. As a result, the reaction yield has been increased over the past 40 years from 50% to over 80% [50].

4.1. Reaction and products

Since selective oxidation of propylene is the most popular process among those of other light hydrocarbons, it is chosen to be described here as an example. The product of the reaction, acrolein, is formed from propylene in a two-step process through the allylic alcohol intermediate (**Figure 4**). The second step is more exothermic ($\Delta H = -195.5$ kJ, mol^{-1}) than the first one

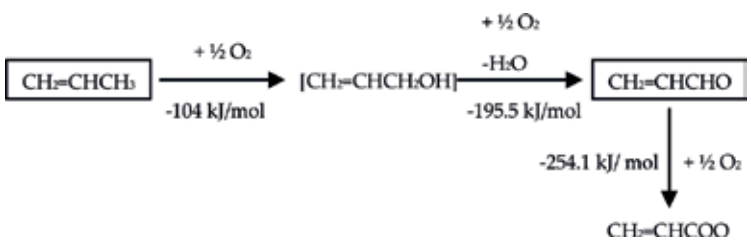

Figure 4. Reaction pathway of the selective oxidation of propylene.

($\Delta H = -104$ kJ mol^{-1}), probably due to the stabilization energy of the conjugated electronic system of acrolein [4].

By-products of this reaction are acrylic acid and carbon oxides in addition to minor products such as acetaldehyde, acetic acid, formaldehyde, and polyacrolein. The yield of acrylic acid is only 10% mol, while the yield of acrolein is more than 70%. If acrylic acid is to be obtained, it must be synthesized from the oxidation of acrolein in a second-stage reactor with a different catalyst [51]. Carbon oxides are the products of the complete oxidation of acrolein or acrylic acid as well as parallel complete oxidation of propylene [52]. Acetaldehyde and formaldehyde formation during the reaction is due to the oxidative breaking of the propylene C = C bond:

$$CH_3CH = CH_2 + O_2 \rightarrow CH_3CHO + CH_2O \quad (6)$$

Acetaldehyde and formaldehyde can also be oxidized further [4].

In the industry, the reaction is carried out in a fluidized bed reactor to facilitate the heat transfer and allow good temperature control, which is important for maintenance of selectivity. The silica support provides mechanical stability for the catalyst in the abrasive environment of the fluidized bed. Pressures are low (about atmospheric) and temperatures are in the range 400–500°C [5].

4.2. Catalysts

Catalysts which exhibit above properties for selective oxidation are usually mixed systems in which transition metal oxides of group B (most often Mo or V) are combined with oxides of groups IVA, VA, and VIA (Bi, Sb, Sn, P, Te) or group VIIIB (Fe, Co, Ni). Favored structures are scheelites, fluorites, rutiles, trirutiles, pyrochlores, and perovskites. Industrial catalysts contain as a rule small amounts of promoters: alkali or alkaline earth metals are commonly reported in the catalyst formula, and several other elements of variable valency and rare earth metals can be also found therein.

These catalysts can be divided into following system:

- Antimonate system included (i) the uranium antimonate system based on USb_3O_{10} (UO_3 + Sb_2O_4) catalyst which was developed in 1966; (ii) the iron antimonate system, $Fe_{10}Sb_{25}Si_{50}$, consisting of the active components $FeSbO_4$, Sb_2O_4, and SiO_2; and (iii) the tin antimonate systems based on SbSnO which were studied since 1969 [53] and attracted attention during the 1980s [54]. Although the in-tank acrylonitrile yields of the above antimonate catalyst compositions are respectable, they do not measure up to the productivities of the best molybdate catalysts. In addition, the antimonate-based catalysts are much more fragile than the molybdate-based systems under commercial operation. Therefore, it is imperative to operate the antimonate systems under rigidly controlled operating conditions, in order to prevent possible plant upsets and irreversible reduction which leads to the destruction of the antimonate catalysts. In contrast, the later-generation molybdate-based catalysts are almost indestructible and can easily withstand inadvertently plant upsets, including severe reductions. It is for these reasons that the complex mixed metal molybdates are currently the industrially preferred catalysts for the ammoxidation of propylene to acrylonitrile [55].

- The cuprous oxide system: Cu_2O powder is obtained by CuO reduction at about 400°C. This system is more accurately defined as a multiphase (Cu-Cu_2O-CuO) system. Consequently, it has proven to be very difficult to characterize. The catalyst undergoes changes in its bulk chemical composition, activity, and selectivity during oxidation of propylene; therefore, its activity is less stable than the other catalyst system. Anyway, the simple oxide Cu_2O is reported to exhibit significant activity and selectivity and has been often chosen as a model catalyst for the determination of the involved reaction mechanism [4]. It was reported that catalytic activity of Cu_2O catalyst system is lower than that of bismuth molybdate catalysts; therefore, the Cu_2O catalyst is less popular [56].
- Bismuth molybdate system: Catalysts based on bismuth molybdates are the most efficient class of catalyst for oxidation and ammoxidation of propylene and olefin. They are also most thoroughly investigated. This system will be described more detailed in the next section.

4.3. Mechanism of the reaction

Mechanism of selective oxidation of propylene to acrolein over bismuth molybdate catalyst was proposed by Burrington et al. [54, 57] (**Figure 5**). Details about active sites are shown in **Figure 6**.

According to Burrington [57] and Grasselli [58], initial chemisorption of propylene occurs on molybdenum dioxo groups bridged to bismuth-oxygen group 1, followed by allylic abstraction by Bi oxygens to form a π-allyl complex 2, which then undergoes C–O bond formation resulting

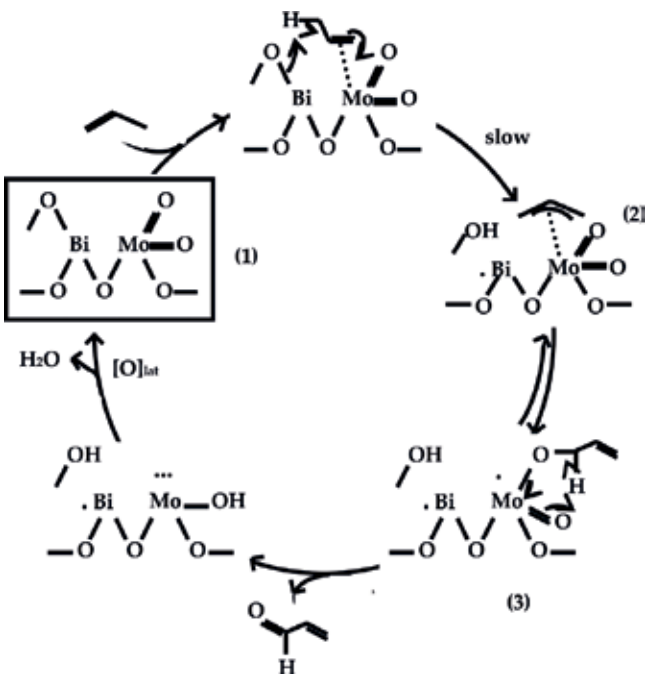

Figure 5. Mechanism of selective oxidation of propylene to acrolein over bismuth molybdate catalyst by Burrington et al. [57].

http://dx.doi.org/10.5772/intechopen.75105

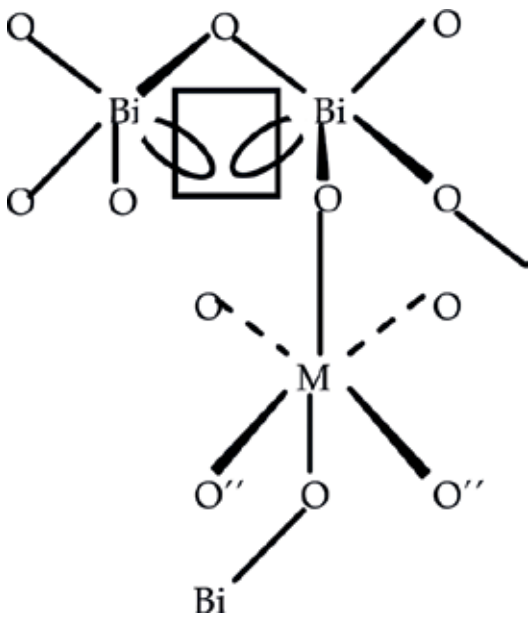

Figure 6. Schematic representation of the catalytic site for partial oxidation of propylene on Bi_2MoO_6 [58]. The oxygen designated O′ is believed to be responsible for the α-hydrogen abstraction; that designated O″, associated with Mo, is believed to be responsible for oxygen insertion into the allylic intermediate to give acrolein. Square (two lone pairs of electron associated with Bi–O–Bi surface groups) designates the center for O_2 reduction and dissociative chemisorption.

in a σ-O-allyl molybdate 3, the acrolein precursor, and Mo(V) analog to Mo(VI) esters formed from allyl alcohol and $Bi_2O_3.MoO_3$. Lattice oxygen removed from the catalyst during the surface oxidation of propylene to form acrolein must be replenished by gaseous oxygen in order to reconstitute the active site 1 and complete the redox cycle. Thus, the reaction occurs via a Mars and Van Krevelen mechanism in which propylene adsorbs reversibly and then reacts with an oxygen atom of the catalyst. This rate-limiting step leads to cleavage of one of the C–H bonds of the methyl group of the adsorbed propylene and results in the formation of an adsorbed OH group and a loosely adsorbed allyl radical that is rapidly stabilized as an adsorbed vinylalkoxide [59]. The sites for chemisorption and dissociation of gaseous oxygen molecule are spatially and structurally distinct from the active sites, at which adsorption and oxidation of propylene take places. These sites are singly coordinated unsaturated metal cations on the surface. These sites may reduce molybdenum cations because molybdenum is known to form various multivalent coordinate compounds containing oxygen and molybdenum is also stable in its lower valence states [60]. Therefore, the partially reduced catalysts are good catalysts (rule of "site isolation" [61]).

This mechanism can be applied to explain the difference in activity noted in the three phases of bismuth molybdates. The γ phase and Bi_2O_3 have too few chemisorption sites, while MoO_3 has no α-hydrogen abstracting sites, and, thus, these catalysts are the least active ones. The α and β phases have a favorable balance of these two sites necessary to effect the rate-determining first hydrogen abstraction. The multicomponent system possesses the greatest number of active surface sites having the proper structure and composition and a solid-state structure with the ability to rapidly reconstitute these surface sites with bulk lattice oxygen [1].

However, experiments using gaseous O^{18} showed that 16% of the lattice oxygen in the α phase and 100% of lattice oxygen in the γ phase were involved in the formation of both acrolein and carbon dioxide at 430°C [6]. On the other hand, the layer structure of γ phase results in low-energy pathways than the more closed parked structure of α phase so that oxygen anions can diffuse easier [1]; for example, in the reoxidation cycle, γ phase can be more active than the others. These may support for the opposite observation of some authors about the order of catalytic activity of three phases.

5. Catalytic properties of bismuth molybdate system

The most popular industrial catalysts for selective oxidation of propylene are based on multicomponent metal oxides containing mainly Bi/Mo(W)-O phases modified by various metal elements such as Fe, Co, and Ni. Commercial catalysts introduced by SOHIO for the ammoxidation of propylene to acrylonitrile are summarized in **Table 1** [50].

These commercial catalysts, however, were developed based on the fundamental researches on basic types of bismuth molybdate catalysts.

5.1. Catalytic activity of different primary bismuth molybdate phases

Three phases of bismuth molybdates, α, β, and γ, exhibit good catalytic properties for oxidation of propylene. Their catalytic activities decrease in the following generally accepted order: $Bi_2Mo_2O_9$ (β) ≥ $Bi_2Mo_3O_{12}$ (α) > Bi_2MoO_6 (γ). Although this order is reported by many authors [1, 2, 28, 60, 62], there are some papers in which the opposite trend is stated: γ ≥ β > α [6, 7] or β > (α = γ) [8] or α > β > γ [9], β > α > γ [41], γ > α [63]. These reports, however, are not exhaustive, but it shows the large divergence of opinion. All these catalysts were not prepared in the same manner nor were the reaction conditions equivalent. In addition, some of the early results were reported on a per-gram basis and not per unit surface area. Some authors explain the higher activity of α and β phases compared to γ phase that α and β phases possess more molybdenum dioxo groups than γ phase does; for example, they possess more active sites for propylene chemisorption [41]. The higher activity γ phase compared to α phases was assigned for the facile oxygen mobility of γ [63]. Especially, the conflicting results on the activity of Bi_2MoO_6 found in the literature were explained by a surface enrichment with bismuth during prolonged calcination or reaction, resulting in a deactivation of the catalyst.

Year	Catalysts	Acrylonitrile yield (%)
1960–1963	$Bi_9PMo_{12}O_{52}/SiO_2$	55
1963–1965	$Bi_{4.5}Fe_{4.5}PMo_{12}O_{52}/SiO_2$	65
1969–1970	$K_{0.1}(Ni,Co)_9Fe_3BiPMo_{12}O_x/SiO_2$	75
1975–1991	$(K,Cs)_a(Ni,Co,Mn)_{9.5}(Fe,Cr)_{2.5}Bi/Mo_{12}O_x/SiO_2$	78–80
1992–1995	$(K,Cs)_a(Ni,Mg,Mn)_{7.5}(Fe,Cr)_{2.3}Bi_{0.5}Mo_{12}O_x/SiO_2$	>80

Table 1. Commercial catalysts introduced by SOHIO [50].

It was found that the activity and selectivity of Bi_2MoO_6 catalysts, in the selective oxidation of propylene to acrolein, are very sensitive to the presence of small amounts of excess bismuth. This excess leads to a surface enrichment with bismuth and thereby to a low-active and low-selective catalyst. However, such catalysts with a Bi/Mo slightly above 2 do show reasonable activities and selectivities after calcination at moderate temperatures and/or for a short period of time. These catalysts loose their activity after calcination at a higher temperature or for a longer period of time. This makes that the activity and selectivity of these catalysts are strongly dependent on the calcination time and temperature. The reasonable initial activities of catalysts with a Bi/Mo slightly above 2 are ascribed to relative low Bi/Mo ratios at parts of the surface after calcination for a short period of time. The excess bismuth merges with the active parts of the surface during calcination, leading to the deactivation of the catalyst. The sublimation of molybdenum from the catalyst may play a minor role in the deactivation process. The deactivated samples can be reactivated by reduction, while the activity of the active samples is hardly affected by reduction. This reactivation is a result of the formation of bismuth particles leading to a decrease in the Bi/Mo ratio at other parts of the surface. The deactivation during calcination and after reduction occurs at similar rates indicating that these deactivation processes are similar [64].

5.2. Synergy effect in the mixtures of bismuth molybdates

The synergy effect is expressed as the enhancement of the catalytic activity when two or three phases are present in the catalysts. One of the best-known examples of the synergy effect is the cooperation between α and γ phases obtained by chemical decomposition at about 540°C of the β phase [9, 65, 66]. However, types of cooperation and explanations offered are different among authors (**Table 2**).

In general, due to the presence of the synergy effect in the mixtures of bismuth molybdates, the catalytic activity of these catalysts may be influenced strongly if the samples are not pure bismuth molybdate phases (alpha, beta, or gamma, corresponding to Bi/Mo ratios of 2/3, 1/1, and 2/1, respectively). Samples with other Bi/Mo ratios (Bi/Mo ratios of 1.5, 1.3, etc.) even exhibited higher activity since they are mixtures of these bismuth molybdate phases. Thus, the catalytic activity of bismuth molybdate samples depends significantly on the Bi/Mo ratio of the samples. Catalytic activity of bismuth molybdate samples with different Bi/Mo ratio is presented in **Figure 7** [42].

The synthesis method also influences on the catalytic activity of bismuth molybdate catalysts since different synthesis methods may result in different purities of the catalysts and different surface areas. Samples synthesized by solid-state reaction and precipitation sometimes exhibit unexpected catalytic activity due to the formation of other unexpected bismuth molybdate phases and even MoO_3 or Bi_2O_3. Due to the presence of unexpected bismuth molybdate phases, the samples may possess the synergy effect which increase catalytic activity [68].

5.3. Multicomponent bismuth molybdate catalysts

Synergy effect in the mixtures of bismuth molybdate phases may be one of the reasons for the plentiful researches on multicomponent bismuth molybdates. Many different metals have been added to bismuth molybdate to increase their activities such as Fe, V, Ni, Sn, Zr, etc.

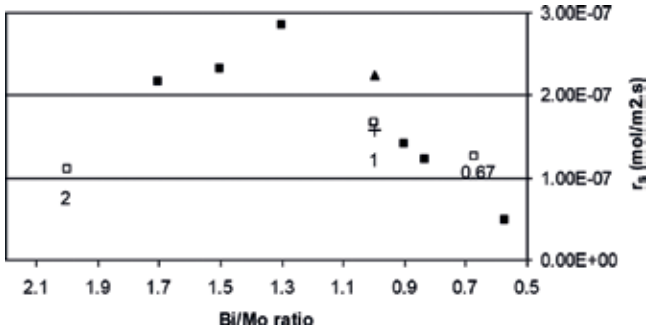

Figure 7. Reaction rate for acrolein formation of bismuth molybdates with Bi/Mo ratio from 0.57 to 2 (synthesized by spray drying): □, pure samples; ▲, Bi/Mo = 1 (47% γ, 47% α, 6% β); +, Bi/Mo = 1 (29% γ, 29% α, 42% β).

Multicomponent $Ni_xFe_3Bi_1Mo_{12}O_{42+x}$ catalysts were applied to the oxidative dehydrogenation of C_4 raffinate-3 to 1,3-butadiene. Conversion of n-butene, selectivity for 1,3-butadiene, and yield for 1,3-butadiene over $Ni_xFe_3Bi_1Mo_{12}O_{42+x}$ catalysts showed volcano-shaped curves with respect to nickel content. Among the catalysts tested, $Ni_9Fe_3Bi_1Mo_{12}O_{51}$ showed the best catalytic performance. The conversion of n-butene was increased with increasing surface acidity of the catalyst. The largest surface acidity of the $Ni_9Fe_3Bi_1Mo_{12}O_{51}$ catalyst was responsible for its enhanced catalytic performance in the oxidative dehydrogenation of C_4 raffinate-3. The facile oxygen mobility of the Bi_2MoO_6 phase in the $Ni_9Fe_3Bi_1Mo_{12}O_{51}$ catalyst also played an important role in enhancing the catalytic performance of the $Ni_9Fe_3Bi_1Mo_{12}O_{51}$ catalyst [69].

Bismuth molybdenum titanium oxides containing 14 or 25 wt% of bismuth molybdate were prepared in a highly dispersed state by the solgel method. Their catalytic performance in propene oxidation to acrolein was studied. The increase in activity of BiMoTi oxides in propene

Authors	Type of cooperation	Explanation
Matsuura et al. [62]	α + γ in n-C4 = ODH	Formation of a phase similar to β
Carson et al. [9]	α + γ in n-C3 = Ox	Decomposition of α or γ
Weng et al. [67]	α + various oxides in n-C4 = Ox	Action of spillover oxygen
Godard et al. [28]	α + γ in n-C4 = ODH	Dual role
Soares et al. [20]	β + γ in selective catalytic oxidation of 1-butene	The high oxygen mobility in the lattice of the γ phase that allows the migration of oxygen species from the γ to the β phase
Le et al. [42]	α/β + γ in the selective oxidation of propylene to acrolein	High conductivity of γ + α/β possesses more active sites to absorb α-hydrogen atoms of propylene
Jung et al. [63]	α + γ in the oxidative dehydrogenation of C4 raffinate-3 to 1,3-butadiene	A combination of the facile oxygen mobility of γ and the abundant adsorption sites of α for n-butene

Table 2. Explanation given in the literature for the cooperative effects between bismuth molybdates.

oxidation as compared to that of bulk bismuth molybdate can be tentatively related to the stabilization of small aggregates of Bi- and Mo-containing phases due to the beneficial presence of the titania matrix. The catalytic performance of the samples is significantly depended on the crystal size of bismuth molybdate phase; an optimum size (23 nm) should exist to enhance the catalytic performance [70].

Several investigations have shown that the apparent activation energy for propylene oxidation to acrolein can be reduced by the replacement of Mo by V for catalysts maintaining a scheelite structure with the composition $Bi_{1-x/3}V_{1-x}Mo_xO_4$ (x = 0–1), which was first reported by Sleight et al. in the 1970s [71]. Cesari and coworkers also obtained this compound, which forms a solid solution with composition limits of bismuth vanadate (x = 0) and the α phase of bismuth molybdate (x = 1) [72]. The authors found that the V^{5+} ion in $BiVO_4$ can be replaced by Mo^{6+} until x = 1, forming cationic vacancies without changing its original structure. Catalytic activity for the reactions producing both acrolein and acrylonitrile in the oxidation or ammoxidation of propylene increases drastically with increasing concentration of cationic vacancies of $Bi_{1-x/3}V_{1-x}Mo_xO_4$. The lattice parameter changed regularly with x, and it was concluded that the replacement of vanadium by molybdenum atoms resulted in random vacancies of the bismuth cations in order to balance the difference in negative charges between the tetrahedral anion groups VO_4^{3-} and MoO_4^{2-}. The selectivity of the reaction is also improved with the degree of substitution to some extent [73]. It was also reported that the activation barrier for the rate-limiting step is well described by the band-gap of such catalysts, the activation energy decreases with the band gap [3]. Among the multicomponent metal oxide system $Bi_{1-x/3}V_{1-x}Mo_xO_4$, $Bi_{0.85}V_{0.55}Mo_{0.45}O_4$ exhibited the highest catalytic activity due to combining a high ability to adsorb propylene and abstract α-hydrogen to convert propylene to incomplete oxidized organic compounds while having a high conductivity to allow mobility of lattice oxygen [74].

Recently, an investigation of propylene oxidation was conducted over Bi, Mo, and V oxides having the aurivillius structure with the composition $Bi_4V_{2-x}Mo_xO_{11+x/2}$(x = 0–1). The activity of the aurivillius structure was compared with oxides having the scheelite structure. The aurivillius-phase catalysts again show a correlation between the apparent activation energy and the band gap of the oxide, and the only difference being that for a given band gap is that the apparent activation energy for the aurivillius-phase catalysts is 1.5 kcal/mol higher than that of the scheelite-phase catalysts. This difference is attributed to the lower heat of propene adsorption on the aurivillius-phase catalysts. A further finding is that for catalysts with band gaps greater than 2.1 eV, the acrolein selectivity is 75% for the conditions used and independent of the propylene conversion. When the band gap falls below 2.1 eV, the intrinsic selectivity to acrolein decreases rapidly and then decreases further with increasing propylene conversion. This pattern shows that when the activity of oxygen atoms at the catalyst surface becomes very high, two processes become more rapid—the oxidation of the intermediate from which acrolein is formed and the sequential combustion of acrolein to CO_2 [59].

In the most recent work on multicomponent bismuth molybdate catalysts, other components including conductive materials (SnO_2, ZrO_2) and nonconductive materials (MgO) were added to beta-bismuth molybdates (β-$Bi_2Mo_2O_9$). Comparison of the catalytic activities of these samples showed that the addition of a suitable amount (10% mol) of SnO_2 improved

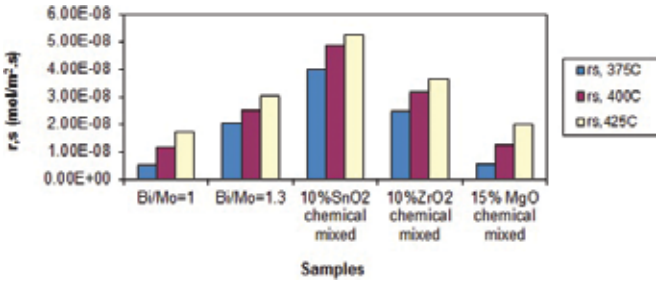

Figure 8. Comparison of the catalytic activities (reaction rates for acrolein formation based on catalyst surface area, r_s, mol/m²s) of different catalysts based on beta-bismuth molybdate with other oxides.

significantly the catalytic activity of beta-bismuth molybdate to an unprecedented high level for any known single bismuth molybdate catalyst phase or other highly active bismuth molybdate mixtures (bismuth molybdate with Bi/Mo ratio of 1.3). When adding ZrO_2 to beta-bismuth molybdate, the catalytic activity of the sample increases slightly. In contrast, adding MgO to beta-bismuth molybdate does not increase the catalytic activity of the samples (**Figure 8**). SnO_2 was found to exhibit much higher conductivity than ZrO_2, leading to bismuth tin molybdate catalyst also exhibiting high conductivity, while MgO is a nonconductive material. This is evidenced that the increase of the conductivity of the bismuth tin molybdate could be one of the reasons for the increase of their catalytic activity resulting in a synergy effect in its catalytic activity [75].

6. Conclusions

Although bismuth molybdate catalysts have been studied and developed for many years, nowadays, they still attract many research interests worldwide not only due to the importance of the chemical processes that they catalyze in industry but also due to the interesting aspects raised during the researches such as the involvement of lattice oxygen during the catalytic processes or the synergy effects occurring in the mixtures of bismuth molybdate phases. There are many factors influenced on the catalytic properties of these materials including synthesis methods and addition of other elements on the multicomponent systems. The recent studies show that the addition of Sn or V in the basic bismuth molybdate catalysts increase significantly or the mobility of lattice oxygen or the ability to adsorb α-hydrogen in reacted hydrocarbons and, thus, increase their catalytic activity. The increase of surface area of bismuth molybdate catalysts using advanced synthesis methods such as hydrothermal, solgel, and solution combustion also contributes on the increase of catalytic activity. Catalytic performance of the recently developed bismuth molybdate-based catalysts generally reaches to more than 80% conversion of hydrocarbons and 75% selectivity of the desired products. However, the wish to increase selectivity and yield of desired products in these popular chemical processes will still continue to attract worldwide researchers to study to improve catalytic performances of these popular catalyst compounds.

Acknowledgements

The author thanks the following organizations, which supported for her long years of researches on bismuth molybdate materials: VLIR, Ghent University (Belgium), DANIDA, Technical University of Denmark (Denmark), NAFOSTED, and Ministry of Education and Training (Vietnam).

Author details

Minh Thang Le

Address all correspondence to: thang.leminh@hust.edu.vn

Hanoi University of Science and Technology, Hanoi, Vietnam

References

[1] Grasselli RK, Burrington JM. Selective oxidation and ammoxidation of propylene by heterogeneous catalysis. Advances in Catalysis. 1981;**30**:133

[2] Keulks GW, Krenzke LD. Selective oxidation of propylene. Notermann TM. Advances in Catalysis. 1978;**27**:183

[3] Moro-oka Y, Ueda W. Multicomponent bismuth molybdate catalyst: A highly functionalized catalyst system for the selective oxidation of olefin. Advances in Catalysis. 1994;**40**:233-273

[4] Bettahar MM. On the partial oxidation of propane and propylene on mixed metal oxide catalysts. Applied Catalysis A: General. 1996;**145**:1

[5] Gates BC. Catalytic Chemistry. 1992. pp. 403

[6] Krenzke LD, Keulks GW. The catalytic oxidation of propylene: VI. Mechanistic studies utilizing isotopic tracers. Journal of Catalysis. 1980;**61**:316

[7] Batist PA, Bouwens JFH, Schuit GCA. Bismuth molybdate catalysts. preparation, characterization and activity of different compounds in the Bi- Mo- O system. Journal of Catalysis. 1972;**25**:1

[8] Batist PA, Der Kinderen AHWM, Leeuwenburgh Y, Metz FAMG, Schuit GCA. The catalytic oxidation of 1-butene over bismuth molybdate catalysts: IV. Dependence of activity on the structures of the catalysts. Journal of Catalysis. 1968;**12**:45

[9] Carson D, Coudurier G, Forissier M, Vedrine JC. Synergy effects in the catalytic properties of bismuth molybdates. Journal of Chemical Society, Faraday Transactions. 1983; **I**(79):1921

[10] Ueda W, Asakawa K, Chen CL, Moro-Oka Y, Ikawa T. Catalytic properties of tricomponent metal oxides having the scheelite structure: I. Role of bulk diffusion of lattice oxide ions in the oxidation of propylene. Journal of Catalysis. 1986;**101**:360

[11] Porta P, Jacono ML, Valigi M, Minelli G, Anichini A, De Rossi S, Gazzoli D. Structural, surface, and catalytic properties of bismuth molybdovanadates containing foreign atoms: I. X-ray characterization of iron-containing bismuth molybdovanadate catalyst. Journal of Catalysis. 1986;**100**:86

[12] Egashira M, Matsuo K, Kagawa S, Seiyama T. Phase diagram of the system Bi_2O_3. MoO_3. Journal of Catalysis. 1979;**58**:409

[13] Gates BC, Katzer JR, Schuit GCA. Chemistry of Catalytic Processes. 1st ed. New York: McGraw-Hill; 1979

[14] Erman LY, Gal'perin EL, Kolchin IK, Dobrzhanskii GF, Chernyshev KS. Russian Journal of Inorganic Chemistry. 1964;**9**:1174

[15] Snyder TP, Hill CG Jr. Stability of bismuth molybdate catalysts at elevated temperatures in air and under reaction conditions. Journal of Catalysis. 1991;**132**:536

[16] Zemann Journal of Structure Reports. 1948;**11**:305

[17] Aykan K. Reduction of Bi_2O_3. MoO_3 catalyst during the ammoxidation of propylene in the absence of gaseous oxygen. Journal of Catalysis. 1968;**12**:281

[18] Van den Elzen AF, Rieck GD. Redetermination of the structure of Bi_2MoO_6. Koechlinite-Acta Crystallographia, Section B. 1973;**29**:2436

[19] Van den Elzen AF, Rieck GD. The crystal structure of $Bi_2(MoO_4)_3$ Acta Crystallographia, Section B. 1973;**29**:2433

[20] Soares APV, Dimitrov LD, de Oliveira MC-RA, Hilaire L, Portela MF, Grasselli RK. Synergy effects between β and γ phases of bismuth molybdates in the selective catalytic oxidation of 1-butene. Applied Catalysis, A: General. 2003;**253**(1):191-200

[21] Rastogi RP, Singh AK, Shukla CS. Kinetics and mechanism of solid-state reaction between bismuth (III) oxide and molybdenum (VI) oxide. Journal of Solid State Chemistry. 1982;**42**(2):136-148

[22] Le MT, Van Well WJM, Van Driessche I, Hoste S. Influence of organic species on surface area of bismuth molybdate catalysts in complexation and spray drying methods. Applied Catalysis, A: General. 2004;**267**(1-2):227-234

[23] Schuh K, Kleist W, Høj M, Trouillet V, Jensenc AD, Grunwaldt J-D. One-step synthesis of bismuth molybdate catalysts via flame spray pyrolysis for the selective oxidation of propylene to acrolein. Chemical Communications. 2014;**50**(97):15404-15406

[24] Le MT, Van Well WJM, Van Driessche I, Hoste S. Spray drying, a versatile synthetic method to control purity in single phases and mixed phases of bismuth molybdates. Canadian Journal of Chemical Engineering. 2005;**83**(2):336-343

[25] Schuh K, Kleist W, Høj M, Trouillet V, Jensenc AD, Beato P, Jensen AD, Grunwaldt J-D. Bismuth molybdate catalysts prepared by mild hydrothermal synthesis: Influence of pH on the selective oxidation of propylene. Catalysts. 2015;**5**(3):1554

[26] Schuh K, Kleist W, Høj M, Trouillet V, Beato P, Jensen AD, Patzke GR, Grunwaldt J-D. Selective oxidation of propylene to acrolein by hydrothermally synthesized bismuth molybdates. Applied Catalysis A. 2014;**482**:145-156

[27] Farin B, Alessandro HA, Videla M, Specchia S, Gaigneaux EM. Bismuth molybdates prepared by solution combustion synthesis for the partial oxidation of propene. Catalysis Today. 2015;**257**(Part 1):11-17

[28] Godard E, Gaigneaux EM, Ruiz P, Delmon B. New insights in the understanding of the behaviour and performances of bismuth molybdate catalysts in the oxygen-assisted dehydration of 2-butanol. Catalysis Today. 2000;**61**(1-4):279-285

[29] Trifiro F, Hoser H, Scarle RD. Relationship between structure and activity of mixed oxides as oxidation catalysts: I. Preparation and solid state reactions of Bi-molybdates. Journal of Catalysis. 1972;**25**:12

[30] Grzybowska B, Haber J, Komorek J. The chemistry of Bi-Mo oxide catalysts: I. Phase composition of catalysts and its relation to the structure of precursors. Journal of Catalysis. 1972;**25**:25

[31] Boon L, Metselaar R. Electrical transport properties of beta-bismuth molybdate $Bi_2Mo_2O_9$. Journal of Solid State Inorganic Chemistry. 1990;**27**:381

[32] Buttrey DJ, Vogt T, White BD. High-temperature incommensurate-to-commensurate phase transition in the Bi_2MoO_6 catalyst. Journal of Solid State Chemistry. 2000;**155**:206

[33] Wragg RD, Ashmore PG, Hockey JA. Heterogeneous selective ammoxidation over bismuth molybdate catalysts. Journal of Catalysis. 1973;**31**:293

[34] Wildberger MD, Grunwaldt JD, Maciejewski M, Mallat T, Baiker A. Sol–gel bismuth–molybdenum–titanium mixed oxides I. Preparation and structural properties. Applied Catalysis A: General. 1998;**175**:11

[35] Le MT, Kovanda M, Myslik V, Vrnata M, Van Driessche I, Hoste S. Pulsed laser deposition and dip-coating techniques in the fabrication of bismuth molybdate gas sensors. Thin Solid Films. 2006;**497**(1-2):284-291

[36] Le MT, Do VH, Truong DD, Pham NN. Sol–Gel Synthesis of Bismuth molybdate catalysts for the selective oxidation of propylene to acrolein: Influence of pH value and theoretical molar atomic ratio. Journal of the Chinese Chemical Society. 2017;**64**:1326-1332

[37] Beale AM, Sanka G. In situ study of the formation of crystalline bismuth molybdate materials under hydrothermal conditions. Chemistry of Materials. 2003;**15**:146

[38] Beale AM, Sanka G. In situ characterization of iron phosphate and bismuth molybdate catalysts prepared by hydrothermal methods: An EDXRD and combined XRD/XAS study. Nuclear Instruments and Methods in Physics Research, Section B. 2003;**199**:504

[39] Grasselli RK. Comments on the papers on selective oxidation catalysis. Catalysis Today. 1987;**1**:337

[40] Van Driessche I, Mouton R, Hoste S. Rapid formation of the Bi_2-xPbx$Sr_2Ca_2Cu_3Oy$ high Tc-phase, using spray-dried nitrate precursor powders. Materials Research Bulletin. 1996;**31**:979

[41] Le MT, Van Craenenbroeck J, Van Driessche I, Hoste S. Bismuth molybdate catalysts synthesized using spray drying for the selective oxidation of propylene. Applied Catalysis A: General. 2003;**249**:355-364

[42] Le MT, Van Well WJM, Stoltze P, Van Driessche I, Hoste S. Synergy effects between bismuth molybdate catalyst phases (Bi/Mo from 0.57 to 2) for the selective oxidation of propylene to arcrolein. Applied Catalysis A: General. 2005;**282**:189-194

[43] Specchia S, Galletti C, Specchia V. Solution combustion synthesis as intriguing technique to quickly produce performing catalysts for specific applications. Studies in Surface Science and Catalysis. 2010;**175**:59-67

[44] Specchia S, Finocchio E, Busca G, Specchia V. Combustion synthesis. In: Lackner M, Winter F, Agarwal AK, editors. Handbook of Combustion. Weinheim: Wiley-VCH Verlag GmbH & Co. KGaA; 2010. pp. 439-472

[45] Moore JJ, Feng HJ. Combustion synthesis of advanced materials: Part II. Classification, applications and modelling. Progress in Materials Science. 1995;**39**:243-273

[46] Moore JJ, Feng HJ. Combustion synthesis of advanced materials: Part II. Classification, applications and modelling. Progress in Materials Science. 1995;**39**:275-316

[47] Hearne GW, Adams ML. U.S. Patent 2451485; 1948

[48] Idol Jr JD. U.S. Patent 2904508; 1959

[49] Callahan JL, Gertisser B. Mixed antimony oxide-uranium oxide oxidation catalyst. U.S. Patent 3,198,750; 1965

[50] Grasselli RK. Fundamental principles of selective heterogeneous oxidation catalysis. Topics in Catalysis. 2002;**21**:79

[51] Ullmann's Encyclopedia of Industrial Chemistry. Vol. A1. 1985. p. 149

[52] Grzybowska B. Thirty years in selective oxidation on oxides: What have we learned? Topics in Catalysis. 2000;**11**(/12):23

[53] Godin GW, Mac Cain CC, Porter EA. On the partial oxidation of propane and propylene on mixed metal oxide catalysts. In: Hightower JW, editor. Proceedings of the 4th International Congress on Catalysis. Vol. 1. Moscow; 1968; Elsevier. 1969. p. 347

[54] Burrington JD, Kartisek CT, Grasselli RK. Surface intermediates in selective propylene oxidation and ammoxidation over heterogeneous molybdate and antimonate catalyst. Journal of Catalysis. 1984;**87**:363

[55] Grasselli RK. Advances and future trends in selective oxidation and ammoxidation catalysis. Catalysis Today. 1999;**49**:141

[56] Song W, Ferrandez DMP, van Haandel L, Liu P, Nijhuis TA, Hensen EJM. Selective propylene oxidation to acrolein by gold dispersed on $MgCuCr_2O_4$ spinel. ACS Catalysis. 2015;**5**:1100-1111

[57] Burrington JD, Kartisek CT, Grasselli RK. Mechanism of nitrogen insertion in ammoxidation catalysis. Journal of Catalysis. 1983;**81**:489

[58] Glaeser LC, Brazdil JF, Hazel MAS, Mehecic M, Grasselli RK. Identification of active oxide ions in a bismuth molybdate selective oxidation catalyst. Journal of the Chemical Society, Faraday Transactions. 1985;**1**(81):2903

[59] Zhai Z, Wütschert M, Licht RB, Bell AT. Effects of catalyst crystal structure on the oxidation of propene to acrolein. Catalysis Today. March 2016;**261**(1):146-153

[60] Brazdil JM, Suresh DD, Grasselli RK. Redox kinetics of bismuth molybdate ammoxidation catalysts. Journal of Catalysis. 1980;**66**:347

[61] Grasselli RK. Genesis of site isolation and phase cooperation in selective oxidation catalysis. Topics in Catalysis. 2001;**15**:93

[62] Matsuura I, Shut R, Hirakawa K. The surface structure of the active bismuth molybdate catalyst. Journal of Catalysis. 1980;**63**:152

[63] Jung JC, Kim H, Kim YS, Chung Y-M, Kim TJ, Lee SJ, Oh S-H, Song IK. Catalytic performance of bismuth molybdate catalysts in the oxidative dehydrogenation of C4 raffinate-3 to 1, 3-butadiene. Applied Catalysis A: General. 2007;**317**:244-249

[64] van Well WJM, Le MT, Schiodt NC, Hoste S, Stoltze P. The influence of the calcination conditions on the catalytic activity of Bi_2MoO_6 in the selective oxidation of propylene to acrolein. Journal of Molecular Catalysis A: Chemical. 2006;**256**:1-8

[65] Carson D, Forissier M, Vedrine JC. Kinetic study of the partial oxidation of propene and 2-methylpropene on different phases of bismuth molybdate and on a bismuth iron molybdate phase. Journal of the Chemical Society, Faraday Transactions. 1980;**1**(84):1017

[66] Bing Z, Pei S, Shishan S, Xiexian G. Cooperation between the α and γ phases of bismuth molybdate in the selective oxidation of propene. Journal of the Chemical Society, Faraday Transactions. 1990;**86**:3145

[67] Weng LT, Sham E, Doumain N, Ruiz P, Delmon B. In: Centi G, Trifiro F, editors. New developments in selective oxidation. Amsterdam: Elsevier; 1990. p. 757

[68] Le MT. Synthesis and application of bismuth molybdate. [PhD thesis]. Ghent University; 2005

[69] Jung JC, Lee H, Kim H, Chung Y-M, Kim TJ, Lee SJ, Oh S-H, Kim YS, Song IK. Catalytic performance of multicomponent bismuth molybdates ($NiXFe_3Bi_1Mo_{12}O_{42}$+X) in the oxidative dehydrogenation of C4 raffinate-3 to 1,3-butadiene: Effect of nickel content and acid property. Catalysis Communications. 2008;**9**:447-452

[70] Carrazán SRG, Martín C, Mateos R, Rives V. Influence of the active phase structure Bi-Mo-Ti-O in the selective oxidation of propene. Catalysis Today. 2006;**112**:121-125

[71] Sleight AW, Aykan K, Rogers DB. New nonstoichiometric molybdate, tungstate, and vanadate catalysts with the scheelite-type structure. Journal of Solid State Chemistry. 1975;**13**:231

[72] Cesari M, Perego G, Zazzetta A, Manara G, Notari B. The crystal structures of the bismuth molybdovanadates and of the α-phase bismuth molybdate. Journal of Inorganic and Nuclear Chemistry. 1971;**10**:3595

[73] Kim YC, Ueda W, Moro-oka Y. Selective oxidation of propane to acrolein and ammoxidation to acrylonitrile over Ag-doped bismuth vanadomolybdate catalysts. Studies in Surface Science and Catalysis. 1990;**55**:491

[74] Nguyen TT, Le TM, Truong DD, Fehrmann R, Riisager A, Van Driessche I. Synergy effects in mixed Bi_2O_3, MoO_3 and V_2O_5 catalysts for selective oxidation of propylene. Research on Chemical Intermediates. 2012;**38**(3):829-846

[75] Le MT, Do VH, Truong DD, Bruneel E, Van Driessche I, Riisager A, Fehrmann R, Trinh QT. Synergy effects of the mixture of bismuth molybdate catalysts with SnO_2/ZrO_2/MgO in selective propene oxidation and the connection between conductivity and catalytic activity. Industrial and Engineering Chemistry Research. April 12, 2016;**2016, 55**(17):4846-4855

Section 7

Specialized Characterization of Defects in Bismuth

Chapter 10

Application of Positron Annihilation Spectroscopy Studies of Bismuth and Subsurface Zone Induced by Sliding

Jerzy Dryzek

Additional information is available at the end of the chapter

http://dx.doi.org/10.5772/intechopen.75269

Abstract

The positron annihilation, experimental and theoretical results obtained for bismuth are presented, mainly concerning the open volume defects created during compression and dry sliding. Positron lifetime in vacancy clusters increases with the size of the cluster; however, it saturates at the value of about 0.42 ns already for six vacancies in a cluster. Similar values were resolved in the positron lifetime spectra of bismuth samples exposed to dry sliding. Detection of the subsurface zone in bismuth exposed to dry sliding reveals exponential decay of vacancy clusters concentration with the depth increase from the worn surface. The high strain of about 70% was evaluated in the layer adjoined the worn surface The temperature of recrystallization obtained from the isochronal measurements of annihilation line shape parameter was equal about 90°C, and the activation energy for grain migration is about 0.84 ± 0.11 eV.

Keywords: bismuth, positron annihilation, defects, subsurface zone

1. Introduction

The technological processes like machining, polishing, sandblasting, and sliding or more sophisticated, i.e., laser treatments or ion implantations not only affect the surface of the material but also modify the subsurface region below it changing its physical properties. This is due to the elastic and plastic deformation, which expands into the interior. In the literature, a zone adjoining the surface which properties are changed due to sliding or friction is called work hardening zone because an increase in hardness is apparent [1]. Nevertheless,

some changes expand deeper and the whole region affected we called the subsurface zone [2]. Generation of the subsurface zone is inherent in any surface treatment.

When two bodies are in a sliding contact, a load at their surfaces is supported by asperities of the rough solid surfaces [3]. The asperities deform through elastic and plastic modes, increasing the contact area between the two surfaces until the contact area is sufficient to support the load. High-stress concentration in these regions can lead to a damage and thus also the crack initiation [4]. The asperity region is the source of dislocations that are driven introducing the stress concentration in the subsurface zone [5]. It is not excluded that a great number of small impacts on the worn surface force propagate deformation at large distances into the interior [6] and is the deformation is observed at depth of hundreds of micrometers from the surface [7].

One can indicate several layers in the subsurface zone, **Figure 1**. Directly on top is a layer of contamination, then an adsorption layer and a deeper reaction layer with oxides and other compounds [1]. These layers are present at the depth of about 10 nm from the surface. Much deeper in the damage zone, with deformed grains, band shears, and other defects is extended. This zone has the thickness more than a hundred micrometers, and it seems that this is the main layer, which carries the stress induced by the load on the surface. Below, undamaged and unaffected bulk region is located. The strain and accompanied crystalline defects are distributed in the subsurface zone and they are linked with surface treatments. The most important is the friction and wear which are always present during manufacturing.

The subsurface zone is a subject of tribology; however, its existence can affect for instance electrical properties of conductors as well. Due to the skin effect, alternating electric current (AC) flows within a conductor near the surface at the depth of about 100 μm depending on the frequency and electrical properties of a conductor. This depth coincides with the subsurface

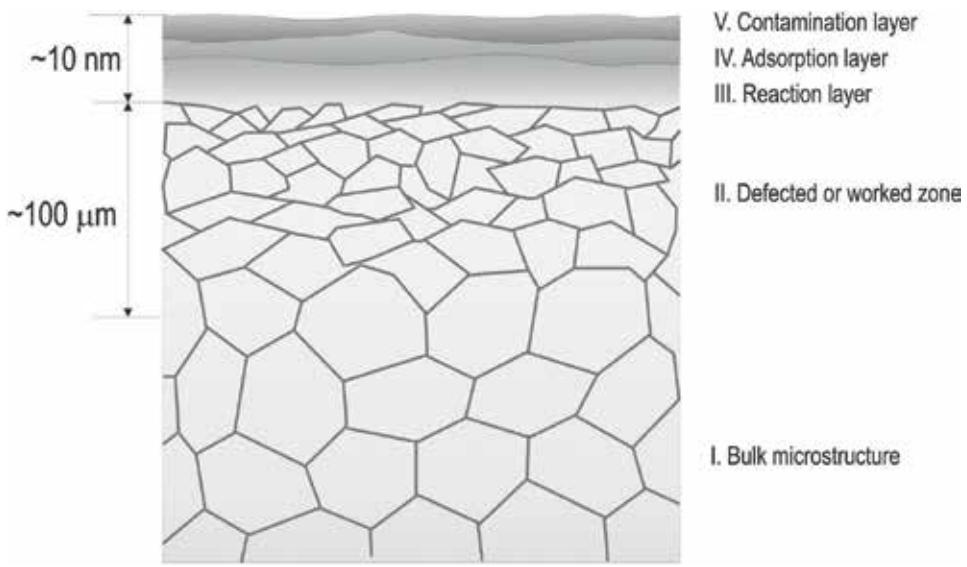

Figure 1. The schema of the subsurface region located below the worn surface (on the top).

zone depth generated during, e.g. machining or sandblasting, in copper it is about 140–800 μm as it was reported, see Ref [8]. The skin effect causes that electrons flow mainly near the surface of the conductor, but in this region, they can scatter at crystalline defects which were created during manufacturing of wires or other devices. Therefore, recently, we focused our interest on the subsurface zone in metals and alloys, which are used for the construction of the electronic devices in radio frequency techniques [9].

The experimental study of the subsurface zone is not an easy task. Measuring the depth profile of microhardness in a sample cross section is one of the methods. However, this is not a suitable method of detecting defects at the atomic level. Commonly used methods such as XRD, SEM and TEM also fail in the case of point defects, which occur in large amounts during a plastic deformation under sliding condition. Positron annihilation methods, due to the several reasons, complete the gap. Extremely sensitivity and selectivity to the open volume defects at atomic level, large positron implantation depth, they are only one of them [10]. Experiments have shown the usefulness of these methods for studies of defects and their distribution in subsurface zones.

Bismuth is a plastic semimetal, and it is not the material in tribo junctions; however, it is used as a component of several alloys, for instance, solid lubricants or recently in low friction aluminum alloy DHT-3 [11]. Low melting point of this metal, i.e., 270.8°C, allows us to suppose that this can affect the subsurface zone generation under dry sliding condition. Other positron annihilation studies of bismuth samples are also presented.

2. Outline of positron annihilation spectroscopy

After thermalization, the positron implanted into matter annihilates with an electron, emitting two photons of energy about 511 keV in almost opposite direction. Positron annihilation spectroscopy utilizes the detection of those photons. This allows us to measure the Doppler broadening of annihilation line or the positron lifetime, i.e., how long it exists in the matter. Both reflect the matter properties at the atomic level. This is because the time prior to annihilation, which an implanted positron spends in the matter depends on the local electron density [10]. Briefly, the following correlation was established theoretically and experimentally: the higher electron density in the site where a positron annihilates the lower value of its lifetime. The electron density is highest in the core region of an atom; however, a positively charged nucleus repels the positron into interstitial sites occupied by valence and conduction electrons. Electronic density is much lower in these sites, and therefore the annihilation with these electrons contributes to the positron lifetime.

The real crystalline lattice can be locally disturbed by defects, for instance, open volume defects, like vacancies or its clusters and/or dislocations. In such defects the electronic density is lower than in interstitial sites. Positrons can be localized at these defects and this causes an increase in the positron lifetime value depending on the type of defect. For instance, the lifetime of a positron trapped at monovacancy is about four-thirds of that in bulk. These values are fingerprints which can be used for defect identification as it is reported in numerous papers [12]. The positron lifetime spectroscopy application to study the matter is based on this fact.

Additionally, the measurements of the broadening of the annihilation line allow us to trace the momentum of electrons undergoing the annihilation. The momentum of the annihilating positron electron pair depends on the local electronic density too. Then any disturbance can be reflected in the broadening, and/or shape of the annihilation line. This can happen in the open volume defects, where electronic density is suppressed. Positron annihilation with such electrons causes the annihilation line is narrower than in the case of the annihilation with interstitial valence electrons in bulk. For characterization of the annihilation line shape, the value of the S-parameter is commonly used. The S parameter is defined as the ratio of the central area to the total area under the annihilation line. This parameter is extremely sensitive to the presence of open volume defects, like monovacancies or its clusters and jogs at dislocation lines, where due to their positive charge, positrons are localized. Usually, the measurements are performed using high purity germanium detector with the good energy resolution. These both experimental techniques are widely applied to study many aspects of condensed matter problems. One should also add that temperature itself does not affect the positron lifetime or S-parameter. The main reasons of the observed altering in their values are induced by structural changes: like vacancy generation, its migration or reaction with other defects, phase transition or other structural processes.

Using conventional positron sources, i.e., beta plus isotopes like ^{22}Na one has to take into account the positron implantation range. The fraction of positrons, which are implanted into the matter, decreases exponentially with the depth increase from the entrance surface. In the case of bismuth linear absorption coefficient for positrons emitted from ^{22}Na is about 569 cm $^{-1}$, it means about 63% positrons annihilates in the layer of the depth of about 17 μm from the entrance surface [13]. This allows to probe large region in a sample by positrons and reflects its bulk properties at the atomic scale.

3. Positron lifetime in bismuth

In our studies, all measurements were performed for the samples of pure bismuth (99.997% purity). They had a disc shape of 3 mm height and 10 mm in diameter. For removing defects that occurred during manufacturing and preparation of virgin samples all discs were annealed in the flow of N_2 gas at the temperature of 200°C for 1 h, and then slowly cooled to room temperature. Additionally, they were etched in the 25% solution of nitride acid in distilled water to reduce their thickness by 50 μm and clean their surface. Only one component equal to 0.241 ± 0.001 ns was detected in the measured positron lifetime spectrum for such virgin sample. This value corresponds well with the experimental value reported, i.e. 0.240 ± 0.001 ns. However, for positrons trapped at monovacancy, this lifetime increases to the value of 0.325 ns [12]. The positron lifetime for vacancy cluster one can calculate theoretically.

The results of *ab inition* calculations were carried out using the PAW formalism as implemented in ABINIT code [14, 15]. The positron lifetime computations were performed on 64 atoms of bismuth supercell. A specific supercell was constructed to introduce vacancy around the central atom. The obtained values are depicted in **Figure 2**. For bulk value, the obtained positron lifetime is equal to 0.255 ns and it is slightly higher than the measured value. However, the theoretical value obtained by other authors was about 0.202 ns [12]. The almost linear increase

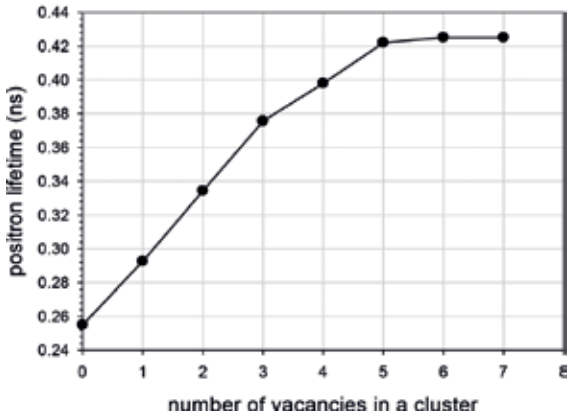

Figure 2. The theoretical values of positron lifetime as a function of the number of vacancies in a cluster of bismuth. The calculation was performed using ABINIT code [15].

of the positron lifetime with the increase of the size of the vacancy cluster is clearly visible, **Figure 2**. However, for the number of vacancies in the cluster larger than five or six this dependency saturates. The obtained results can be helpful in identification of vacancy clusters in the bismuth host.

4. Temperature measurements in bismuth

4.1. Thermally activated monovacancy

For metals, the increase of temperature induces the creation of thermally activated monovacancy. Their concentration increases with the temperature increase. This is reflected also in the temperature increase of the mean positron lifetime (defined below) or values of the S-parameter and hence it can be used for determination of the monovacancy creation enthalpy [16]. The important condition is that the monovacancy must localize positrons. Nevertheless, in the case of bismuth, no increase of the S-parameter with the increasing temperature in the range of 25–200°C is observed, **Figure 3**. The value of the S-parameter remains almost constant indicating lack of positron trapping at thermally activated monovacancy. Similar results were observed not only for bismuth but also for gallium [17] and tin [18]. Thus, the monovacancies in these metals are very weak positron traps because the trapping efficiency rate for such defect must be low. Although $Bi_{40}Sn_{60}$ alloy does not exhibit positron trapping at monovacancies positron trapping at grain boundaries has been observed [19]. The grain boundaries consist of many imperfections including vacancy clusters. Positron trapping at such defects will be shown in the results of the next measurements presented.

4.2. Defects after plastic deformation

In these measurements, bismuth samples were compressed in a flat geometry between two martensitic steel plates using a press with the pressure equal to 3 MPa and the engineering strain

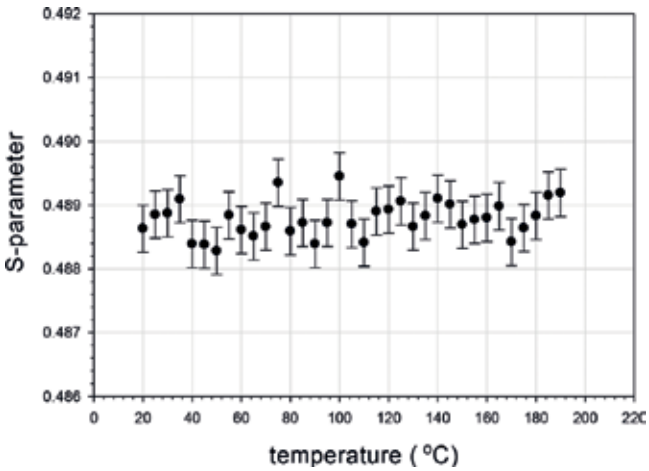

Figure 3. The value of the S-parameter as the function of the temperature obtained in the isochronal annealing measurements for pure bismuth. Each point was measured during 2 h.

equal to 18% [20]. Two components were resolved in the measured positron lifetime spectrum, the value of the first one is equal to 0.178 ± 0.001 ns, the intensity of this component is about (46 ± 5)% and the value of the second one equal to 0.309 ± 0.001 ns the intensity of (54 ± 5)%. Thus, in this process monovacancies or divacancies can be generated, because this value is close to the theoretical values, i.e., 0.293 or 0.334 ns, **Figure 2**. However, the lack of positron trapping at thermally activated monovacancies excludes them.

Creation of such a defect is supported by the fact that the plastic deformation is associated with the movement of dislocations which may cross each other and the jogs on their lines occur. The drag of dislocations with jogs generates monovacancies and interstitial atoms. The latter due to high mobility even at low temperature annihilate with monovacancies. Vacancies are mobile at room temperature too but they can associate creating divacancies or larger clusters. Such a mechanism is commonly accepted. Large vacancy clusters can be presented also at grain boundaries, which are created during the compression in great amount.

For comparison of results obtained for different compression, we apply the commonly accepted robust parameter, i.e., the mean positron lifetime equal to:

$$\bar{\tau} = \tau_1 I_1 + \tau_2 I_2, \tag{1}$$

where $\tau_{1,2}$ are the positron lifetimes resolved from the positron lifetime spectra and $I_{1,2}$ are their intensities (note: $I_1 + I_2 = 1$). The mean positron lifetime does not depend on the number of components resolved in the positron lifetime spectra, however, it is still sensitive to all parameters corresponding to the annihilation states and properties of the sample at the atomic level. The S-parameter and the mean positron lifetime are complementary parameters.

In **Figure 4**, the dependency of the mean positron lifetime for bismuth samples exposed to compression is depicted [21]. On the x-axis, the thickness reduction or strain of the compressed bismuth samples is indicated. This value increases starting from the bulk value, i.e.,

http://dx.doi.org/10.5772/intechopen.75269

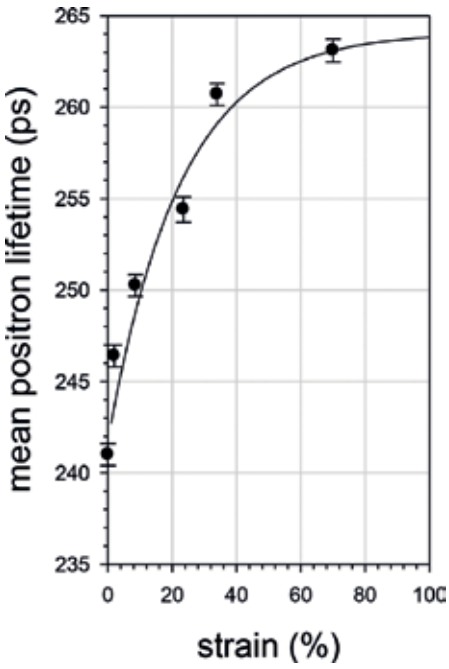

Figure 4. The measured values of the mean positron lifetime vs. thickness reduction or strain of compressed pure bismuth samples [21]. The solid line represents the best fit of Eq. (2), see text.

0.241 ± 0.0006 ns and it saturates at the value of about 0.263 ± 0.0007 ns for the thickness reduction of about 73%. This dependency can be well explained. With the increase in plastic deformation, that is, the increase in stress and strain, a large number of dislocations in shear bands and accompanying them point defects are created. However, at a certain level of defect concentration, all implanted positrons after thermalization and random walk are trapped in these defects. This is reflected in saturation of the positron annihilation characteristics, like mean positron lifetime. Further increase of the deformation and generation of new defects does not affect the positron trapping. This happens at the strain of about 50–60% in bismuth, **Figure 4**. In other metals, saturation occurs already with less deformation about 10% [22].

The obtained dependency in **Figure 4** can be described using a following analytical formula:

$$\bar{\tau} = \tau_{sat} + (\tau_{bulk} - \tau_{sat}) \exp(-c\varepsilon), \tag{2}$$

where ε is the thickness reduction in percent. The solid line in **Figure 4** represents the best fit of this simple function and the values of the adjustable parameters are as follows: τ_{sat} = 0.264 ± 0.003 ns, c = 0.044 ± 0.017.

The obtained value of the bulk lifetime equals to τ_{bulk} = 0.243 ± 0.002 ns. In comparison to other metals, the value of the *c* parameter for bismuth is about one order lower. For instance in copper c = 0.212 ± 0.010 [22]. This can be explained by the fact that in bismuth the mobility of point defects or other defects must be much higher than in copper which melting point is much higher, i.e. 1084°C. This is also clearly visible in the positron lifetime spectra, where for

the highly deformed bismuth sample, the value of the first lifetime is close to the bulk value, i.e., 0.241 ns, which indicates the presence of almost perfect bulk regions. These regions can result from recrystallization process, which can undergo also at room temperature. This can be visible in the following measurements.

4.3. Thermally activated recovery process

The isothermal measurements at room temperature were performed for the bismuth sample after thickness reduction of about 80% in compression. In **Figure 5a**, the obtained dependency of the S-parameter value as the function of time is depicted. The value of the S-parameter decreases and for the time above 10 h, its value ceases decreasing. This indicates that even at room temperature deformed bismuth samples undergo changes at the atomic scale. The recovery and recrystallization process can explain this behavior. This is clearly visible in the isochronal annealing experiment. The bismuth sample after thickness reduction of about 80% was located in the spectrometer, and the value of the S-parameter was measured with the sequenced increase in temperature. Each measurement was done within 2 h, to obtain a suitable accuracy. In **Figure 5b**, the dependency was depicted. Indeed above 40°C, the value of the S-parameter starts gradually decreasing up to the temperature of about 140°C and then saturates. Such a dependency is attributed to the recrystallization process, as we have shown for other metals, i.e., iron, gold or silver [23].

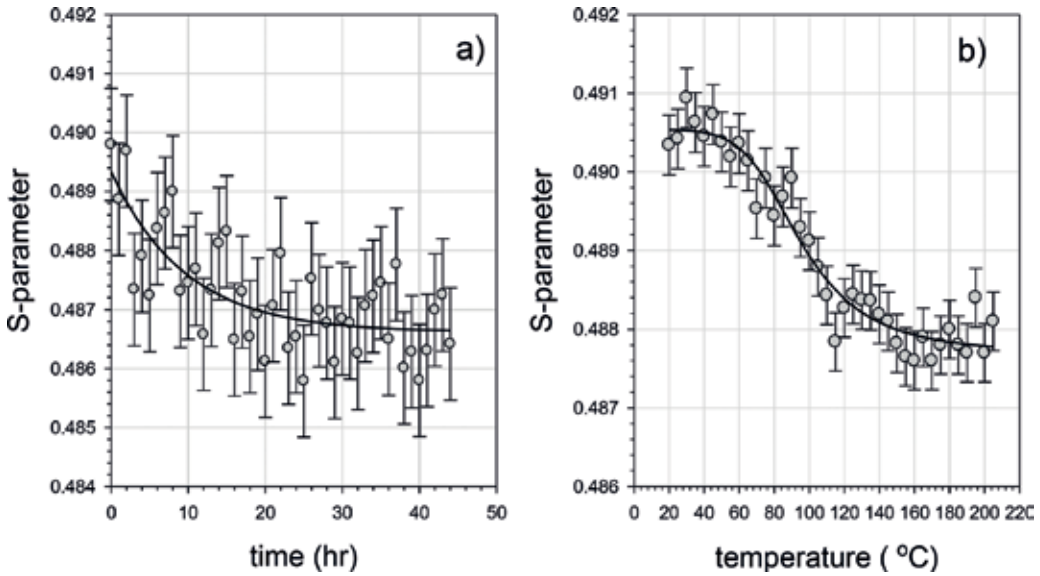

Figure 5. The results of the isothermal measurements of the S-parameter at the room temperature of the bismuth sample after plastic deformation (a). The solid line represents the following function, which is the best fit to the experimental points: $S = 0.486 + \exp(-t/9.5)$, where t is time in hours. The isochronal annealing measurements of the S-parameter for the bismuth samples exposed previously to the plastic deformation (b). The solid line represents the best fit of the function obtained from the positron diffusion trapping model, including the grain boundary migration in the recrystallization process.

http://dx.doi.org/10.5772/intechopen.75269

The migration of the grain boundaries causes an increase in the size of the new almost defects free grain. Hence, less positrons annihilate at grain boundaries. They contain a great number of defects including vacancy cluster which are traps for positrons. The results from **Figure 5b** can be described within the positron diffusion model, which takes into account not only the positron diffusion but also the model of grain expansion. This allows us to estimate the activation energy for grain boundary migration, which is responsible for this [23]. The solid line in this figure represents the best fit of this model to the experimental points. The obtained value of the grain boundary migration activation energy is equal to $Q = 0.84 \pm 0.11$ eV. We can state that the recrystallization temperature in bismuth is about 90°C, this is the temperature of the middle of the drop of the S-parameter which corresponds the temperature of half-complete recrystallization within a specified time.

5. The subsurface zone in bismuth

The fact that bismuth undergoes recrystallization at room temperature can be reflected in the properties of the subsurface zone generated during dry sliding. To find this the virgin bismuth samples were exposed to dry sliding against the rotating disc made from martensitic steel disc with the speed of about 5 cm/s. In order to obtain the defect depth profile the worn samples were sequentially: etched in a 25% solution of nitride acid in distilled water and after the measurement of positron lifetime spectrum was performed. The layer of about 15 μm thick was removed in every step. The accuracy of a digital micrometer screw used in the thickness measurement was 1 μm.

Two-lifetime components: τ_1 and τ_2 were resolved in each spectrum, and their values as a function of depth from the worn surface are depicted in **Figure 6**. For this sample, the duration of the sliding test was 1 min and applied load was about 10 N. In **Figure 6a**, the mean positron lifetime values are shown. Its value decreases with the increasing depth and exponential decay of this value is clearly visible. This kind of dependency was observed in other metals, e.g. iron [24].

Nevertheless, we have noticed another interesting feature. The value of the first- lifetime component increases and the value of the second-lifetime component remains almost constant with the increasing depth. The explanation can be found in the positron diffusion or standard trapping model [23]. The first-lifetime value lower than the bulk value indicates the fact that the subsurface zone contains almost defects free regions, presumably recrystallized grains. However, the second lifetime, which value is much higher indicates the positron trapping at grain boundaries. The average value of about 0.442 ± 0.058 ns is close to the theoretical value of 0.422 ns for positron trapped at the vacancy cluster which consists of five or more vacancies, **Figure 2**.

Taking into account Eq. (1) which links the strain with the mean positron lifetime, we can calculate the local strain at different depths. The right y-axis in **Figure 6a** represents the results of such calculations. It can be noticed that near the surface, the strain has the value of about 70% and then decay with the depth increase, but even at the depth of 150 μm, it has the value of 5%.

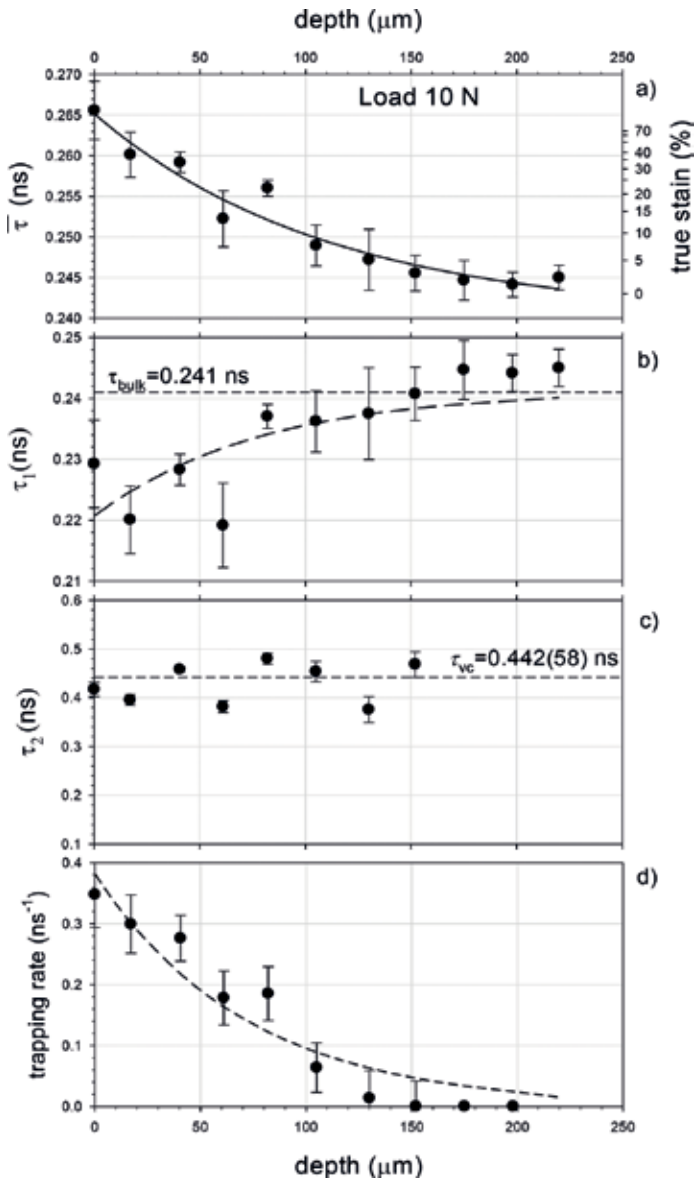

Figure 6. The values of τ_1 (b) and τ_2 (c) resolved from positron lifetime spectra as the function of depth from the worn surface of the sample which was exposed to sliding with the applied normal load equal to 10 N during 1 min [20]. The mean positron lifetime calculated from Eq. (1) and the trapping rate values calculated from Eq. (7) are presented in (a) and (d), respectively. The solid line in (a) and short-dashed line in (d) present the exponential decay functions fitted to the points in each figure. The long-dashed line in (b) presents calculated the value of τ_1 from Eq. (4) taking into account the exponential decay function for the trapping rate, Eq. (8).

To simplify the analysis of the data from **Figure 6**, we use the standard positron trapping model instead of diffusion trapping model mentioned above [10]. It neglects diffusion of positrons but takes into account the trapping at vacancy clusters. In this model, it is assumed that a positron can annihilate from the free state in the bulk or the bound state for instance in the

http://dx.doi.org/10.5772/intechopen.75269

vacancy cluster where it can be trapped with a certain rate. The average positron lifetime in both states are constant and equal to τ_{bulk} and τ_{vc}, respectively. The transition from the free to the bound state is described by the positron trapping rate which is equal to:

$$\kappa_{vc} = \mu C_{vc}, \tag{3}$$

where C_{vc} represents the concentration of the vacancy clusters which bind positrons and μ is the positron trapping efficiency rate. According to this model the first lifetime component in the spectrum is as follows:

$$\tau_1 = \frac{\tau_{bulk}}{1 + \tau_{bulk}\kappa_{vc}}, \tag{4}$$

and the second-lifetime component:

$$\tau_2 = \tau_{vc}. \tag{5}$$

The mean positron lifetime is given by:

$$\overline{\tau} = \frac{1 + \tau_{vc}\kappa_{vc}}{1 + \tau_{bulk}\kappa_{vc}}\tau_{bulk}. \tag{6}$$

It is also convenient to express the trapping rate as a function of the mean positron lifetime defined in Eq. (1):

$$\kappa_{vc} = \frac{1}{\tau_{bulk}}\frac{\overline{\tau} - \tau_{bulk}}{\tau_{vc} - \overline{\tau}}. \tag{7}$$

From Eqs. (4) and (5), it is well visible that the increase of the trapping rate and hence the concentration of the vacancy cluster which trap positrons causes the decrease of the first-lifetime component. The second component does not vary.

The average value of the second-lifetime component is 0.442 ± 0.058 ns, **Figure 6c**, and this value corresponds to the annihilation of positrons trapped at a vacancy cluster, which consists more than five vacancies, **Figure 2**. Taking into account the mean positron lifetime Eq. (1) and the average value of the second-lifetime component, we can calculate from Eq. (8) the positron trapping rate as the function of the depth. In **Figure 6d**, we depicted the obtained dependency, which exhibits the exponential decay with the depth increase, represented by a dashed line.

Identical dependencies were observed also for other samples exposed to dry sliding with other values of the applied load, not presented here. The values of the evaluated trapping rate as the function of the depth for various loads applied are depicted in **Figure 7**. For a description of the data from this figure, the following function is proposed:

$$\kappa = b\exp\left(-\frac{d}{d_0}\right), \tag{8}$$

with two b and d_0 adjustable parameters. This function describes well the obtained dependencies. The solid lines in **Figure 7** represent the best fits of Eq. (8) to the experimental points. In **Table 1**, the values of the adjustable parameters are given. It can be stated that with the increasing load the average depth of vacancy cluster distribution, which is represented by the d_0 parameter increases. For the highest load, i.e. 50 N the total depth of the subsurface zone is about 320 ± 20 μm. Like in other pure metals the determined total depth of the subsurface zone is ranged from 140 to 320 μm and it depends on the applied load in the sliding treatment, **Table 1**. The concentration of the vacancy clusters at the worn surface, represented by the b parameter also increases with the applied load.

For determination of the absolute value of the vacancy cluster concentration, the value of the positron trapping efficiency rate: μ, which describes the transition rate from the free to the trapped state is necessary, Eq. (3). This value in metals is ranged from 5×10^{14} to 5×10^{17} s^{-1} [25], however, because of experimental difficulties, it is rarely reported. In turn, the theoretical calculations of this quantity require knowledge about the mechanism of energy transfer from the trapped positron to the host, and this is also difficult to point out it in particular case [26].

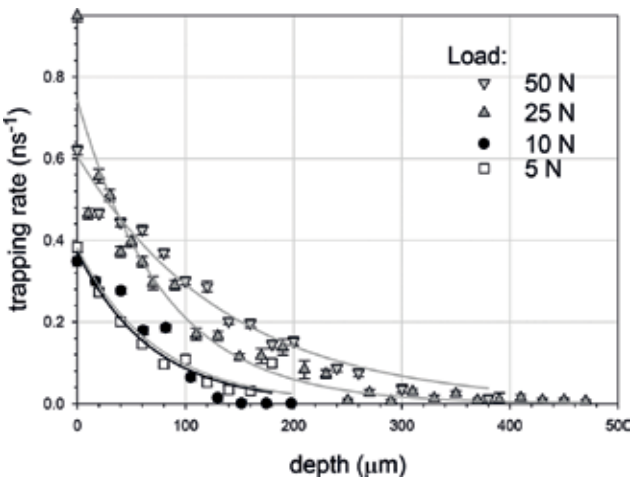

Figure 7. The trapping rate obtained from the positron lifetime spectra, i.e. Eq. (7) as the function of the depth from the worn surface for different loads applied during the test [20]. The tribo test lasted for 1 min for all samples. The solid lines represent the best fit of Eq. (8) to the experimental points, and the adjustable parameters are given in **Table 1**.

Load [N]	d_0 [μm]	b [ns^{-1}]	Total depth of the subsurface zone [μm]
5	68.4 ± 7.5	0.37 ± 0.02	140 ± 20
10	71.9 ± 1.2	0.38 ± 0.04	200 ± 20
25	79.2 ± 7.7	0.74 ± 0.04	280 ± 20
50	136.8 ± 7.7	0.60 ± 0.02	320 ± 20

In the last column, the value of the total depth of the subsurface zone defined as the depth, where the only single value of the positron lifetime equal to the bulk value is resolved.

Table 1. The values of the adjustable parameters from Eq. (8) which was fitted to the experimental points in **Figure 7**, where the trapping rate as a function of depth is depicted [20].

http://dx.doi.org/10.5772/intechopen.75269

Unfortunately, the lack of data regarding the positron trapping efficiency rate for pure bismuth excludes calculations of the absolute value of the vacancy cluster concentration in the subsurface zone. Nevertheless, we can state that concentration of vacancy clusters decreases exponentially with the depth increase.

6. The workhardening zone in bismuth

The microhardness profile on the cross section of the bismuth sample exposed to dry sliding allows us to detect the workhardening zone. The Vickers microhardness was measured using Zeiss (Neophot 30) microscope at the load of 10 g at different depths from the worn surface.

The only small increase of the microhardness in the layer adjoined the worn surface is observed, **Figure 8**, which only slightly exceeds the error bar. Additionally, the total depth profile is shallower than those detected by positrons, **Figure 7**. The microhardness profile range is less than 150 μm, **Figure 6a**, whereas the range detected by positrons, **Figure 7**, is about 200 μm. This difference can occur as a result of the fact that the microhardness indenter interacts with large regions of the sample in comparison to the atomic scale and is insensitive to the presence of point defects. One should emphasize very week increase of the microhardness in the layer adjoining the worn surface in comparison for example to the case of stainless steel [27] or iron [24]. In the former, the microhardness increases by the factor of about two in comparison to the bulk region. Probably this is the reason that bismuth is not used in frictional junctions, however, recent observations have shown that aluminum alloy containing dispersed bismuth nanoparticles exhibits better wear resistance and frictional properties than aluminum alloy with embedded lead nanoparticles [28]. Both are promising as bearing material.

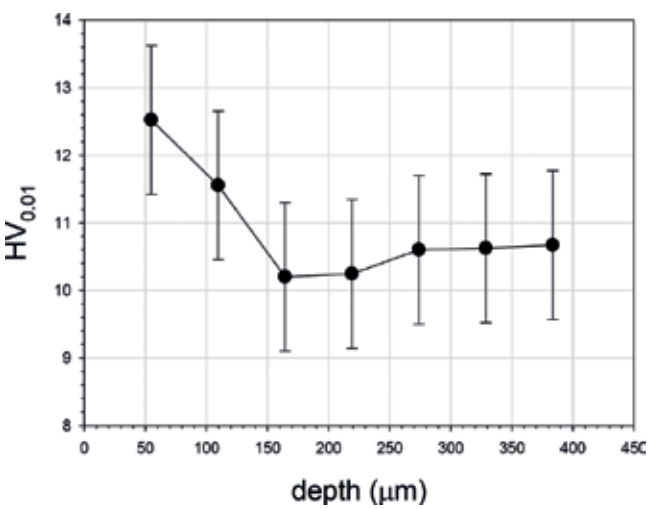

Figure 8. The depth profile of the Vickers microhardness measured on the cross section of the bismuth sample exposed to dry sliding against the rotating disc with the load of 15 N [21].

Acknowledgements

The author wishes to express his gratitude to K. Siemek for *ab inition* calculations presented in this text.

Author details

Jerzy Dryzek

Address all correspondence to: jerzy.dryzek@ifj.edu.pl

Institute of Nuclear Physics PAN, Kraków, Poland

References

[1] Zum Gahr K-H. Microstructure and Wear of Materials. Amsterdam, New York, Tokyo: Oxford, Elsevier; 1987

[2] Horodek P, Dryzek J, Wróbel M. Positron annihilation study of defects induced by various cutting methods in stainless steel grade 304. Tribology Letters. 2012;**45**:341-347. DOI: 10.1007/s11249-011-9890-7

[3] Bowden FP, Tabor D. Friction and Lubrication of Solids. Vol. 2. Oxford, Clarendon Press; 1950

[4] Carbone G, Bottiglione F. Asperity contact theories: Do they predict linearity between contact area and load. Journal of the Mechanics and Physics of Solids. 2008;**56**(8):2555. DOI: 10.1016/j.jmps.2008.03.011

[5] Wert JJ. The role of microstructure in subsurface damage induced by sliding contact. Key Engineering Materials. 1989;**33**:101-134

[6] Dryzek J, Dryzek E, Suzuki T, Yu R. Subsurface zone in pure magnesium studied by positron lifetime spectroscopy. Tribology Letters. 2005;**20**:91-97. DOI: 10.1007/s11249-005-7796-y

[7] Kennedy Jr FE. Plastic analysis of near-surface zones in sliding contacts of metals. Key Engineering Materials. 1989;**33**:35-48

[8] Horodek P, Siemek K, Dryzek J, Wróbel M. Positron annihilation and complementary studies of copper sandblasted at different pressures. Materials. 2017;**10**:1343. DOI: 10.3390/ma10121343

[9] Dryzek J, Horodek P. Positron annihilation studies of the near-surface regionsof niobium before and after wear treatment. Tribology Letters. 2017;**65**:117. DOI: 10.1007/s11249-017-0902-0

[10] Krause-Rehberg R, Leipner HS. Positron Annihilation in Semiconductors. Springer-Verlag; 1999

[11] Yoon H, Sheiretov T, Cusano C. Tribological evaluation ofsome aluminium-based materials in lubricant/refrigerant mixtures. Wear. 1998;**218**:54-65

[12] Robles JMC, Ogando E, Plazaola FJ. Positron lifetime calculation for the elements of the periodic table. Journal de Physique. 2007;**19**:176222-176220. DOI: 10.1088/1742-6596/265/1/012006

[13] Dryzek J, Singleton D. Implantation profile and linear absorption coefficients for positrons injected in solids from radioactive sources ^{22}Na and ^{68}Ge/^{68}Ga. Nuclear Instruments and Methods in Physics Research Section B. 2006;**252**:197-204. DOI: 10.1016/j.nimb.2006.08.017

[14] Blöchl PE. Projector augmented-wave method. Physical Review B. 1994;**50**:17953-17979

[15] ABINIT code. 2000-2017. Available from: http://www.abinit.org

[16] Triftshauser W. Positron trapping in solid and liquid metals. Physical Review B. 1975;**12**:4634

[17] Szymański C, Chabik S, Pajak J, et al. Temperature-dependence of the positron annihilation in liquid and solid bismuth and gallium. Physica Status Solidi A. 1980;**60**:375-380

[18] Shah N, Catz AL. Temperature dependence of positron annihilation in tin. Physical Review B. 1984;**30**:2498

[19] Chabik S, Rudzińska W, Szuszkiewicz M, et al. Positron annihilation in solid and liquid $Bi_{40}Sn_{60}$ alloy. Acta Physica Polonica A. 1999;**95**:479-482

[20] Dryzek J. Positron studies of subsurface zone created in sliding wear in bismuth. Tribology Letters. 2010;**40**:175-180. DOI: 10.1007/s11249-010-9654-9

[21] Dryzek J. The annealing studies of the subsurface zone induced by friction in bismuth detected by positron lifetime technique. Tribology Letters. 2014;**54**:229-236. DOI: 10.1007/s11249-013-0232-9

[22] Dryzek J, Nojiri S, Fujinami M. The positron microscopy studies of the wear tracks on the copper surface. Tribology Letters. 2014;**56**:101-106. DOI: 10.1007/s11249-014-0389-x

[23] Dryzek J, Wróbel M, Dryzek E. Recrystallization in severely deformed Ag, Au and Fe studied by positron annihilation and XRD method. Physica Status Solidi B. 2016;**253**:2031-2042. DOI 10.1002/pssb.201600280

[24] Dryzek J. Positron studies of subsurface zone in pure iron induced by sliding. Tribology Letters. 2011;**42**:9-15. DOI: 10.1007/s11249-010-9742-x

[25] Schaefer H-E. Investigation of thermal equilibrium vacancies in metals by positron annihilation. Physica Status Solidi A. 1987;**102**:47-65

[26] Dryzek J. Scattering and trapping of positrons at vacancies in solids. Journal of Physics: Condensed Matter. 1995;**7**:L383

[27] Dryzek J, Horodek P, Wróbel M. Use of positron annihilation measurements to detect the defect beneath worn surface of stainless steel 1.4301 (EN) under dry sliding condition. Wear. 2012;**294-295**:264-269. DOI: 10.1016/j.wear.2012.07.006

[28] Bhattacharya V, Chattopadhyay K. Microstructure and tribological behaviour of nano-embedded Al-alloys. Scripta Materialia. 2001;**44**:1677-1682. DOI: 10.1016/S1359-6462(01)00864-8

Edited by Ying Zhou, Fan Dong and Shengming Jin

Bismuth (Bi) is a post-transition metal element with the atomic number of 83, which belongs to the pnictogen group elements in Period 6 in the elemental periodic table. As a heavy metal, the hazard of Bi is unusually low in contrast to its neighbors Pb and Sb. This property, along with other typical characteristics like strong diamagnetism and low thermal conductivity, makes Bi attractive in industrial applications. There are more than 100 commercial bismuth products, from pharmaceutical to industrial catalysts. Based on the wide applications of Bi materials, this book goes further and mainly focuses on the potential uses of Bi-based materials, which consist of nine chapters. In addition, a special chapter concerning the defect in bismuth is also presented.

Published in London, UK

IntechOpen

ISBN 978-1-83881-528-8